Single laser pulse switching in RE-based multilayers without Gd

Yi Peng

Single laser pulse switching in RE-based multilayers without Gd

THESE

présentée et soutenue publiquement le **7 November 2023**
pour l'obtention du
Doctorat de l'Université de Lorraine
(en Physique)
par

Yi PENG

Composition du jury

Présidentrice de soutenance :		
	Liliana BUDA-PREJBEANU	Université Grenoble Alpes
Raporteurs :	Christine BOEGLIN	Université de Strasbourg
	André THIAVILLE	Université Paris-Saclay
Examinateurs :	Michel VIRET	Université Paris-Saclay
	Liliana BUDA-PREJBEANU	Université Grenoble Alpes
Directeur de thèse :	Michel HEHN	Université de lorraine
Co-Directeur de thèse :	Stéphane MANGIN	Université de lorraine

Institut Jean Lamour
UMR 7198 - Université de Lorraine - CNRS
Equipe 101 : Nanomagnétisme et Electronique de Spin

Commutation d'aimantation à l'aide d'une impulsion laser unique dans des multicouches à base de terre rare sans Gadolinium

La commutation de l'aimantation d'une nanostructure magnétique par une impulsion laser unique représente la capacité d'inverser l'aimantation d'une nanostructure avec une rapidité non égalée sans aucun champ magnétique appliqué. Depuis les premières expériences de commutation réalisées sur des alliages amorphes GdFeCo, ce phénomène n'a été étendu que récemment à quelques autres matériaux, les alliages MnRuGa et les multicouches Tb/Co avec une gamme très spécifique d'épaisseur et de composition.

Dans le cadre de ce travail de thèse, nous démontrons qu'il est possible d'obtenir une commutation à impulsion unique pour une large gamme de multicouches de terres rares et de métaux de transition, ce qui rend ce phénomène beaucoup plus général. L'étude peut être divisée en 3 sous parties: la première partie porte sur l'étude des alliages CoLu, la seconde partie porte sur les multicouches Co_xY_{1-x}/MT où Y est une terre rare et MT est un métal de transition, la troisième partie porte sur des multicouche Co/Ho.

0.1 Les alliages CoLu

La commutation ultrarapide de l'aimantation à l'aide d'un pulse laser femtoseconde unique est largement rapporté dans la littérature dans les alliages ou les multicouches à base de Gd. Dans ces composés, les modèles sont capables de reproduire ce comportement en considérant deux sous-réseaux d'aimantation couplés par échange antiferromagnétique et des temps de relaxation différents pour chaque sous-réseau. À cet égard, le Gd semble être un ingrédient clé compte tenu de son faible temps de relaxation qui résulte du faible couplage spin-orbite du Gd (avec L = 0) et de son couplage antiferromagnétique avec le métal de transition. En recherchant d'autres terres rares, RE, ayant un faible moment angulaire orbital comme dans le Gd ($[Xe].4f^7.5d^1.6s^2$), seuls Lu ($[Xe].4f^{14}.5d^1.6s^2$) et La ($[Xe].4f^0.5d^1.6s^2$) possèdent également L = 0 et, en outre, S = J = 0. Dans les deux cas, seules quelques publications ont fait état de leurs propriétés magnétiques. De surcroit, aucun test de renversement de l'aimantation à l'aide d'un pulse laser unique n'a été effectué sur TM_xLu_{1-x} ou TM_xLa_{1-x} jusqu'à présent.

Nous avons entrepris l'étude pour le système Co_xLu_{1-x}.

Des couches Verre/Ta(5)/Pt(4)/Co_xLu_{1-x}/Pt(2) (épaisseur en nanomètres) ont été produites par pulvérisation magnétique RF (Co) et DC (Ta, Pt, Lu) avec une pression de base inférieure à 3×10^{-8} mbar. Le substrat de verre transparent a été utilisé pour la géométrie pompe/sonde, la couche tampon Ta(5)/Pt(4) et la couche de protection Pt(2) sont utilisées pour promouvoir l'aimantation perpendiculaire au plan du film dans le Co_xLu_{1-x}. La couche supérieure de Pt sert également de couche de protection contre l'oxydation. La concentration de Lu a été variée entre 18% et 40%.

Pour une concentration de Lu inférieure à 20%, l'aimantation se situe dans le plan de l'échantillon. Un cas particulier a pu être observé pour une concentration de Lu de 22% pour laquelle une courbe d'hystérésis multidomaine perpendiculaire au plan du film a pu être mesurée. Pour des concentrations supérieures à 22%, le cycles d'hystérésis sont carrés avec une rémanence égale à un, ce qui prouve l'existence d'une anisotropie magnétique perpendiculaire (PMA). L'aimantation à saturation, Ms, calculée en utilisant l'épaisseur nominale de Co_xLu_{1-x} et la surface de l'échantillon, diminue linéairement de 830 kA/m à 18% à 400 kA/m à 40%.

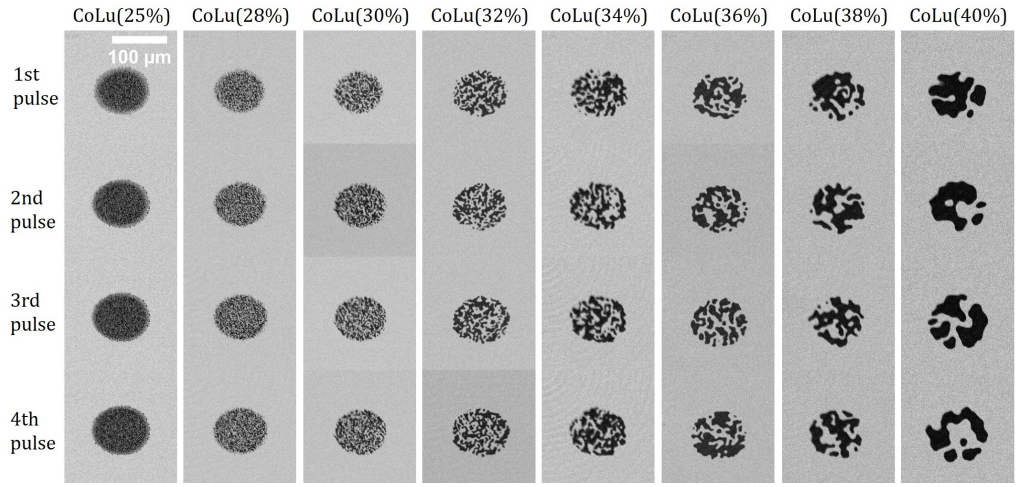

Figure 1: Structure en domaines stabilisée après une, deux, trois et quatre impulsions laser de 50fs avec une fluence de 6.7 mJ/cm^2. De gauche à droite, augmentation de la concentration en Lu. De haut en bas, 1 impulsion, 2 impulsions, 3 impulsions et 4 impulsions.

Des expériences de renversement avec une impulsion unique ont été entreprises sur des couches continues qui possèdent une aimantation perpendiculaire (Figure 1). La fluence critique inférieure pour laquelle des domaines apparaissent est de 2.1 mJ/cm^2, tandis que la limite supérieure de fluence pour laquelle les échantillons brûlent est d'environ 27.1 mJ/cm^2. Dans la figure 1, nous présentons l'évolution typique de la taille des domaines pour une fluence fixée à 6.7 mJ/cm^2, la même tendance a été observée pour des fluences comprises entre 2.1 mJ/cm^2 et 27.1 mJ/cm^2. L'analyse de la structure des domaines n'a pas permis d'extraire de signe d'inversion d'aimantation avec une impulsion unique. L'une des raisons possibles est que les domaines sont plus petits que la taille du spot. En effet, l'observation du renversement de l'aimantation tout optique exige que la taille d'équilibre des domaines magnétiques se formant pendant le processus de refroidissement soit plus grande que la taille du spot laser. Ceci ne semble pas être le cas ici. Cependant, une nette augmentation de la taille des domaines se produit lorsque la teneur en Lu passe de 25 % à 40 %. Ce résultat peut être attribué à la diminution de l'aimantation à saturation, comme le prévoit la théorie des domaines dans les matériaux avec PMA.

Nous avons donc réalisé des plots avec des tailles latérales microniques. Pour des plots de taille latérales inférieures à $3\mu m$, des plots de configuration monodomaine ont pu être obtenus. Après une seule impulsion laser, l'état de domaine unique a pu être préservé, mais l'inversion ne se produit pas après chaque impulsion. Il semble que 50 % des plots inversent leur aimantation à chaque impulsion. Le renversement n'est donc pas déterministe. A l'aide d'un modèle atomistique, nous montrons que le moment magnétique du Lu n'est pas suffisant pour apporter suffisamment de moment angulaire pour renverser le sous réseau de Co.

L'ensemble de ces résultats sont rapportés dans la publication **Laser single-shot magnetization reversal in Co_xLu_{1-x} nanostructures,** Y. Peng, G. Malinowski, W. Zhang, D. Lacour, F. Montaigne, S. Mangin, and M. Hehn, Physical Review B 107, 214415 (2023).

0.2 Les multicouches Co_xY_{1-x}/MT

Dans cette partie de la thèse, nous démontrons qu'il est possible d'obtenir une commutation à impulsion unique pour une large gamme de multicouches de terres rares et de métaux de transition, ce qui rend ce phénomène beaucoup plus général.

Comme point de départ de notre étude, nous considérons les multicouches magnétiques $[Tb/Co]_5$ et $[Tb/Fe]_4$, similaires à celles utilisées par Avilés-Felix et al. Ces multicouches présentent une forte anisotropie magnétique perpendiculaire à température ambiante et l'aimantation des couches de Tb et de Fe ou de Co est couplée par échange antiferromagnétique à l'interface. Comme le montre la figure 2a, la commutation d'aimantation d'un seul domaine magnétique est observée pour une excitation d'une durée d'impulsion de 50 fs et une faible fluence de 1.9 mJ/cm^2. Plus intéressant encore, pour une fluence laser supérieure à 2.6 mJ/cm^2, une structure annulaire commence à apparaître avec des directions magnétiques opposées dans les anneaux adjacents.

L'augmentation de la fluence laser se traduit par un plus grand nombre d'anneaux. Comme le montre la figure 2b, le domaine central est alternativement inversé et ce jusqu'à la fluence la plus élevée (7.0 mJ/cm^2) pour laquelle un état multidomaine est stabilisé. Ce comportement frappant a été étudié systématiquement en fonction de la durée de l'impulsion laser, ce qui nous permet d'établir un diagramme d'état complet (durée de l'impulsion en fonction de la fluence) présenté à la figure 2c.

Ce diagramme d'état ne ressemble ni au diagramme d'état observé dans le cas du renversement dans le GdFeCo, ni au diagramme d'état observé dans le cas de la commutation dépendante de l'hélicité optique à impulsions multiples. Il est surprenant de constater que les fluences nécessaires pour inverser et stabiliser un nombre donné d'anneaux dépendent très peu, voire pas du tout, de la durée des impulsions laser. La commutation de l'aimantation induite par une seule impulsion laser est observée pour des durées d'impulsion allant jusqu'à 12 ps, la plus longue durée d'impulsion atteignable dans notre équipement laser ultrarapide. Les multicouches Tb/Co et Tb/Fe se comportent de manière similaire, présentant toutes deux des structures en anneaux et une faible dépendance des fluences d'inversion par rapport à la durée de l'impulsion laser. Ces deux caractéristiques ont été examinées afin de déterminer les conditions d'obtention de l'inversion et de discuter du mécanisme possible à l'origine de celle-ci.

La structure sous forme d'anneaux, la dynamique de renversement de l'aimantation ou de réorientation de l'aimantation, l'analyse de la position en énergie des parois de domaines (qui n'en sont pas d'ailleurs), l'indépendance des fluences d'apparition

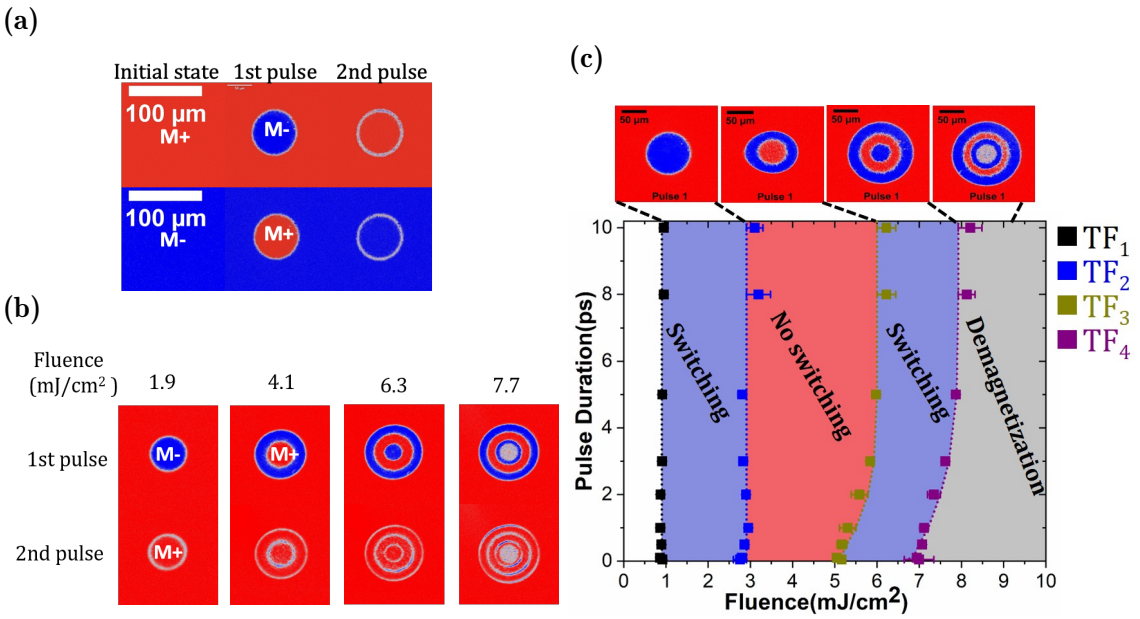

Figure 2: Commutation par impulsion unique et diagramme d'état pour la multicouche $[Tb(1.31\ nm)/Fe(1.89\ nm)]_4$ sous un champ appliqué nul. M+ (respectivement M-) correspond à une aimantation pointant perpendiculairement au plan du film, le long de +z (resp. -z) en rouge (resp. en bleu). (a): Images soustraites du fond après chaque impulsion unique avec une impulsion laser de 1.9 mJ/cm^2 à 50 fs, à partir de l'état M+ ou M-. (b): Images soustraites du fond après la première impulsion unique avec une impulsion laser de 50 fs de fluence différente. (c): Diagramme d'état de la durée de l'impulsion d'inversion en fonction de la fluence. TF_1 est la frontière pour la commutation ; TF_2 est la frontière vers l'état à deux domaines (c'est-à-dire un anneau) ; TF_3 est la frontière vers l'état à trois domaines (c'est-à-dire deux anneaux) ; TF_4 est la frontière vers l'état multidomaine au centre (c'est-à-dire trois anneaux). Les lignes en pointillé servent de guide pour les yeux.

des parois en fonction du temps de pulse nous ont permis de montrer les ingrédients nécessaires à l'obtention de ce renversement et de montrer que le mécanisme le plus probable est un renversement précessionnel.

Connaissant les ingrédients, nous avons pu designer divers échantillons où le renversement précessionnel a pu être observé. La plupart des échantillons étudiés (numéros 3 à 19 dans le tableau 1) sont constitués d'une multicouche (alliages TM-RE / FM) (TM: métal de transition / RE: terre rare). D'après la littérature, on sait que les alliages TM-RE sont amorphes, tandis que les couches FM sont polycristallines ou texturées lorsqu'elles sont déposées à température ambiante sur des couches amorphes, avec des tailles de grain typiques de 20 à 30 nm. Alors que les alliages TM-RE présentent une PMA, nous nous attendons à une distribution locale de la direction de l'anisotropie liée à la nature polycristalline des couches FM. La réduction rapide puis la récupération de l'anisotropie avec la température dans l'alliage TM-RE, liée à la très faible Tc du RE, conduit à l'orientation de l'aimantation de la couche FM dans le plan et à sa précession. L'ingrédient clé du renversement est la persistance de l'aimantation de la couche FM en raison de sa Tc élevée (puisqu'elle est constituée d'une couche pure de Co, Fe, Py, CoFeB). Dans le cas d'un grain ou d'un couple de grains magnétiques (identifiés comme grains "magnétiques") se comportant de manière indépendante, l'aimantation progresse autour de l'axe d'anisotropie local qui est distribué d'un grain à l'autre.

En partant d'un axe proche de la perpendiculaire, la précession se produit autour de cette anisotropie locale et lorsque le plan équatorial du film est traversé,

	Stacks		
1	[Tb(wedge)/Fe(wedge)]*4		
2	[Tb(wedge)/Co(wedge)]*5 (Cross wedge)		
3	$[Tb_{40}Co_{60}(x)/Co(wedge)]*3$	x = 1	
4		x = 2	
5		x = 3	
6		x = 4	
7		x = 5	
8		x = 7,5	
9	$[Dy_yCo_{100-y}$ (4) /Co(wedge)]*3	y = 25	
10		y = 30	
11		y = 35	
12	Pt(5) /Co(wedge)/ $Tb_{32}Co_{68}$ (4)		
13	Pt(5) /Co(wedge)/ $Tb_{32}Co_{68}$ (8)		
14	Pt(5) /Co(wedge)/ $Tb_{32}Co_{68}$ (16)		
15	$Dy_{35}Co_{65}$ (4) /Co(wedge)/ $Dy_{35}Co_{65}$ (4)		
16	$Tb_{32}Co_{68}$ (4) /Co(wedge)/ $Tb_{32}Co_{68}$ (4)		
17	$Tb_{32}Co_{68}$ (4) /CoFeB(wedge)/ $Tb_{32}Co_{68}$ (4)		
18	$Tb_{55}Fe_{45}$ (4) /Co(wedge)/ $Tb_{55}Fe_{45}$ (4)		
	Thickness of the TM layer	0.8 nm 1.2 nm 1.6nm 2.0 nm 2.4 nm 2.8 nm 3.2 nm	
19	$Tb_{32}Co_{68}$ (4) /Permalloy (wedge)/ $Tb_{32}Co_{68}$ (4)		
		2.0 nm 2.6 nm 3.2nm 3.8 nm 4.4 nm 5.0 nm 5.6 nm	

Table 1: Séries d'empilements étudiées dans cette étude : 1-11 sont des multicouches, 12-14 sont des bicouches et 15-19 sont des tricouches. La couleur rose pâle indique la gamme d'épaisseur de la couche TM (y compris Co, Fe, CoFeB, Permalloy) qui a été étudiée dans cette étude, tandis que la couleur bleue indique la région de l'épaisseur de la couche TM où la commutation en un pulse unique se produit dans les différents empilements. Notez que l'échantillon 1 est un échantillon à double wedge dans la même direction, tandis que l'échantillon 2 est un échantillon à wedge croisé. Les nombres indiqués entre parenthèses correspondent à l'épaisseur des couches en nanomètres.

l'inversion se produit. Le temps de précession est directement lié à l'énergie apportée par le faisceau laser, définissant des régions, toujours situées à la même énergie, dans lesquelles l'aimantation des grains peut soit arrêter sa précession selon l'orientation de départ, soit l'inverser. Ceci définit la position des limites des anneaux et également les zones où la densité de petits domaines est la plus élevée. Parfois, à l'intérieur des anneaux, les petits domaines ne sont pas inversés et se trouvent certainement à des positions pour lesquelles les grains magnétiques n'ont pas la configuration d'anisotropie appropriée. En se rapprochant du centre, la densité de petits domaines dans l'anneau augmente. À des fluences plus élevées, l'inversion implique des commutations multiples qui sont plus sensibles à toute distribution de propriétés comme l'axe d'anisotropie effectif.

En conclusion, la commutation de l'aimantation d'une multicouche magnétique à l'aide d'impulsion unique a été étendue à de nombreux matériaux différents avec une durée d'impulsion laser allant jusqu'à 10 ps. Il s'agit d'un phénomène relativement omniprésent dans les multicouches dont la conception est optimisée. L'image d'un renversement précessionnel émerge en raison de l'évidence que l'aimantation doit se réorienter dans le plan avant que l'aimantation ne s'inverse. Le diagramme d'état qui

en résulte ne ressemble ni au diagramme d'état observé dans le cas de la commutation dans le GdFeCo, ni au diagramme d'état observé dans le cas de la commutation à impulsions multiples avec un laser polarisé et démontre l'existence d'un nouveau type de commuation. En termes de temps de renversement, cette commutation précessionnelle à impulsion unique possède des échelles de temps typiques entre celles du GdFeCo et de Co/Pt à impulsions multiples. Alors que la réorientation de l'aimantation dans le plan est indubitablement prouvée et constitue un ingrédient clé, une précession à l'échelle d'un grain ou d'un couple de grains dans le TM, qui conserve une aimantation importante grâce à son Tc élevé, conduit à l'inversion dans une structure de domaine en forme d'anneau. C'est le deuxième ingrédient clé nécessaire, qui manque si l'on utilise uniquement l'alliage RE-TM.

L'ensemble de ces résultats sont rapportés dans la publication **In-plane reorientation induced single laser pulse magnetization reversal**, Y. Peng, D. Salomoni, G. Malinowski, W. Zhang, J. Hohlfeld, L. D. Buda-Prejbeanu, J. Gorchon, M. Vergès, J. X. Lin, D. Lacour, R. C. Sousa, I. L. Prejbeanu, S. Mangin and M. Hehn, Nature Communications 14:5000 (2023).

0.3 Les multicouches Co/Ho

Dans cette étude, nous démontrons expérimentalement un renversement de l'aimantation à l'aide d'une impulsion laser unique dans des empilements multicouches [Co/Ho] avec une anisotropie magnétique perpendiculaire. De manière surprenante, bien que le couplage spin-orbite soit plus important que dans le Tb et le Dy, ce qui devrait augmenter la dissipation du moment angulaire dans le réseau, le diagramme d'état durée d'impulsion / fluence est plus proche de celui du système basé sur le Gd. L'étude de ce nouveau système pourrait permettre de rapprocher les processus d'inversion à impulsion unique observés d'une part dans les hétérostructures à base de Gd et d'autre part dans les hétérostructures à base de Tb ou de Dy.

Des multicouches de verre/Ta(5)/Pt(5)/[Co(wedge)/Ho(wedge)]N/Pt(1)/Ta(5) ont été fabriquées par pulvérisation cathodique magnétron, où N indique le nombre de répétitions des bicouches Co/Ho. Les wedges de Co et de Ho sont orientés dans la même direction, ce qui permet d'obtenir un rapport d'épaisseur Co/Ho constant sur l'ensemble du wedge. Dans la suite, l'épaisseur du Co et du Ho varie de 0.4 nm à 1.2 nm, et de 0.45 nm à 1.35 nm, respectivement, ce qui donne un rapport d'épaisseur de 1/1.1 entre l'épaisseur de la monocouche de Co et celle de la monocouche de Ho. Les cycles d'hystérésis des échantillons sont caractérisés par l'effet Kerr magnéto-optique statique (MOKE) à température ambiante avec un champ magnétique appliqué perpendiculairement au plan du film. Tous les échantillons ont une aimantation perpendiculaire au film et présentent des cycles d'hystérésis très carrés et une rémanence de 100%. Le signe positif de la rotation de kerr à un champ positif élevé montre que la multicouche est dominée par le sous-réseau Co, bien que l'épaisseur de la couche Ho soit supérieure à celle de la couche Co. Ceci est principalement dû à la faible température de Curie de l'élément Ho, qui est d'environ 19K.

La figure 3a montre le résultat de la mesure effectuée sur l'empilement [Co(0.46)/ Ho(0.52)]$_4$, dans lequel l'échantillon est exposé à quatre impulsions laser successives avec F = 5.22 mJ/cm^2. Nous pouvons clairement observer une zone de commutation après la première impulsion laser. Après la deuxième impulsion, les moments magnétiques s'inversent pour revenir à l'état initial, ce qui indique un bon signe de commutation de l'aimantation. Des résultats similaires sont obtenus dans des

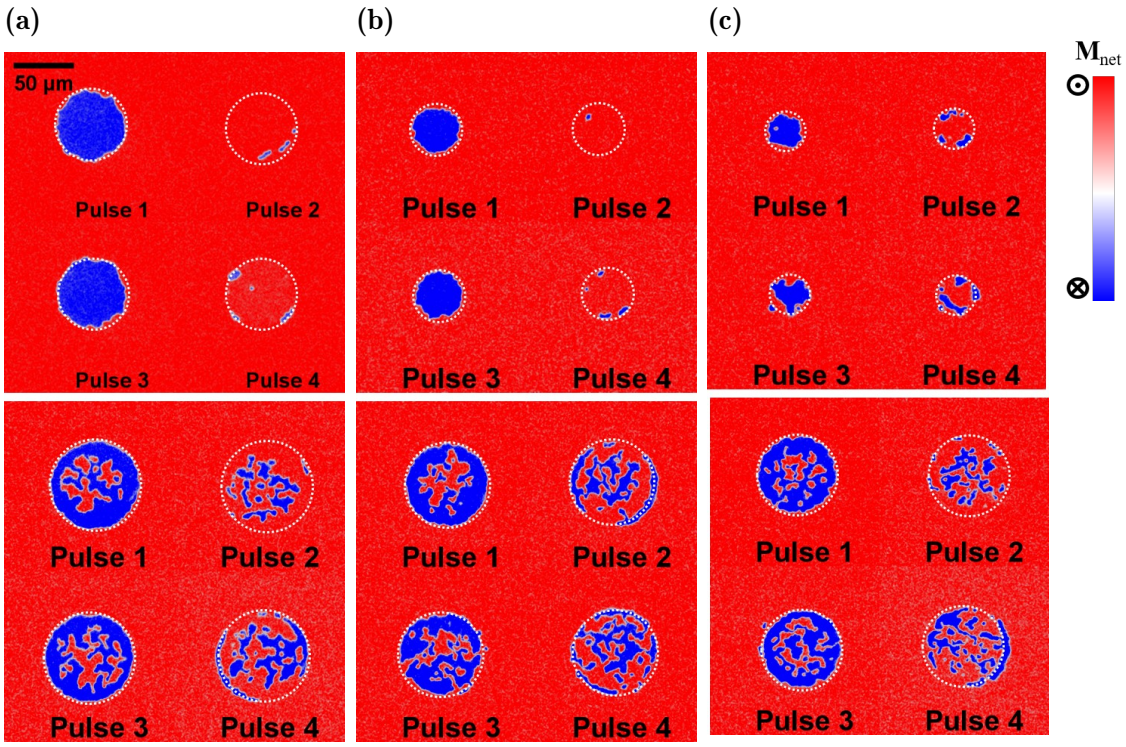

Figure 3: Mesures de la structure en domaines réalisées avec des pulses successifs sur des empilements $[Co/Ho]_4$ avec différentes épaisseurs de Co et de Ho. (a): $[Co(0.46)/Ho(0.52)]_4$; (b): $[Co(0.6)/Ho(0.7)]_4$; (c): $[Co(0.81)/Ho(0.91)]_4$ (épaisseur en nm). Les cercles en pointillés correspondent aux endroits où la structure est excitée par chaque impulsion laser (fluence de 3.75 mJ/cm^2(haut), 9.38 mJ/cm^2(bas), durée de l'impulsion de 50fs). Les couleurs rouge et bleue représentent l'aimantation nette pointant vers le haut et vers le bas.

échantillons légèrement plus épais (voir $[Co(0.6)/Ho(0.7)]_4$). En augmentant encore l'épaisseur de Co et Ho, la zone de commutation de l'aimantation après la première impulsion laser devient beaucoup moins lisse (voir $[Co(0.81)/Ho(0.91)]_4$). De plus, les impulsions laser suivantes conduisent à la formation d'une structure multidomaines, ce qui suggère la perte de la commutation de l'aimantation lorsque l'épaisseur de Co et Ho atteint 0,8 nm et 0,9 nm, respectivement. La forme du domaine après un nombre impair d'impulsions n'est pas un cercle bien défini à 100 % et quelques petits domaines au bord apparaissent après un nombre pair d'impulsions.

Nous montrons ici sans équivoque qu'un renversement peut être obtenu pour des couches de Co et de Ho inférieures à 0.8 nm et 0.9 nm, respectivement, lorsque le nombre de répétitions est égal à N = 4. Cette propriété est maintenue pour N allant de 3 à 5 (nous n'avons pas étudié l'effet pour N supérieur à 5).

Pour mieux comprendre la dépendance de la commutation de l'aimantation par rapport aux paramètres de l'impulsion laser, nous avons mesuré des diagramme d'état décrivant l'évolution de la fluence pour l'obtention du renversement de l'aimantation Fswitch et de la fluence pour l'obtention d'un état multidomaines F_{multi} en fonction de la durée de l'impulsion laser (figure 4). A 35fs, la fenêtre de fluence laser permettant la commutation est la plus large. En augmentant la durée de l'impulsion, Fswitch augmente, tandis que Fmulti est presque constante. La forme approximativement triangulaire de la zone de commutation est très similaire à celle rapportée dans les alliages GdFeCo, bien que les échantillons ne contiennent pas de Gd. Au contraire, les échantillons contiennent une terre rare lourde avec un fort couplage

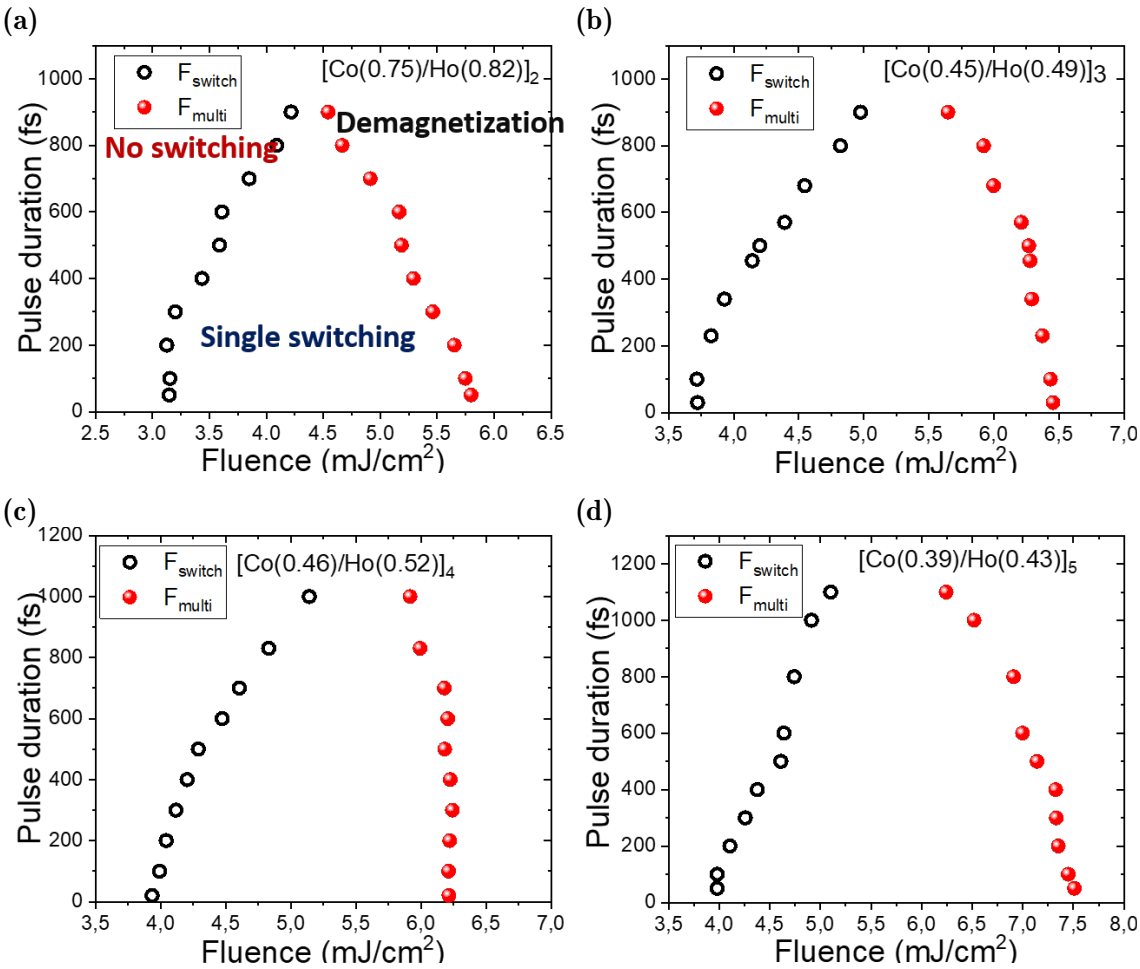

Figure 4: Diagramme d'état : fluence de commutation F_{switch} (cercle noir ouvert) et fluence multidomaine F_{multi} (cercle rouge plein) en fonction de la durée de l'impulsion pour une impulsion laser unique polarisée linéairement. (a): $[Co(0.75)/Ho(0.82)]_2$; (b): $[Co(0.45)/Ho(0.49)]_3$; (c): $[Co(0.46)/Ho(0.52)]_4$; (d): $[Co(0.39)/Ho(0.43)]_5$.

spin-orbite, similaire à Tb et Dy, mais le diagramme d'état de Co/Ho est significativement différent de celui rapporté dans les multicouches comprenant Tb, TbCo, DyCo, TbFe et une couche de métal de transition composée de Co, Fe, CoFeB et Py (voir ci-dessus).

Par conséquent, la compréhension actuelle du processus de renversement dans des échantillons à base de Gd, selon laquelle des matériaux à faible spin-orbite/amortissement sont nécessaires, ne décrit pas le comportement du Ho. Alors qu'avec l'utilisation de Ho, nous avons renforcé le couplage de l'orbite de spin et le moment angulaire total par rapport au Tb et au Dy, nous nous attendions à renforcer les caractéristiques de commutation dans les composés à base de Tb et de Dy (voir ci-dessus). L'étude plus approfondie des matériaux à base de Ho pourrait aider à comprendre la différence de comportement dans les matériaux à base de Gd d'une part et dans les hétérostructures à base de Tb ou de Dy d'autre part.

L'ensemble de ces résultats sont rapportés dans la publication **Single-Shot Helicity-Independent All-Optical Switching in Co/Ho Multilayers**, Y. Peng, G. Malinowski, J. Gorchon, J. Hohlfeld, D. Salomoni , L.D. Buda-Prejbeanu, R.C. Sousa , I.L. Prejbeanu, D. Lacour , S. Mangin, and M. Hehn, Physical Review Applied 20, 014068 (2023)

Résumé

Le domaine émergent de l'électronique à spin ultra-rapide intègre les idées et les concepts de la magnéto-optique et de l'opto-magnétisme avec les phénomènes de transport de spin, complétés par les possibilités offertes par la photonique pour une manipulation ultra-rapide à faible dissipation et le transport de l'information. La découverte de la commutation de magnétisation déterministe ultra-rapide entièrement optique a ouvert de nouvelles possibilités pour la manipulation de la magnétisation dans les dispositifs à l'aide d'impulsions laser femtosecondes. Le HI-AOS est principalement observé dans des alliages ou des multicouches ferrimagnétiques à base de terres rares (RE) à base de gadolinium ou de métaux de transition (TM). Il a récemment été observé dans des matériaux sans gadolinium, tels que le ferrimagnétique Mn_2Ru_xGa et la multicouche ferrimagnétique $[Tb/Co]_N$.

Dans ce travail, nous avons cherché à trouver de nouveaux matériaux capables de présenter une commutation optique entièrement optique (HI-AOS) indépendante de l'hélicité en un seul tir, et à comprendre le comportement de commutation, le mécanisme fondamental et le processus de commutation dans différents matériaux et structures. Par conséquent, trois principales parties de travail ont été réalisées dans cette thèse:

- Étude de l'alliage CoLu, où Lu a les mêmes propriétés que Gd avec un faible couplage spin-orbite (L=0). Une anisotropie magnétique perpendiculaire peut être obtenue dans 3 nm d'alliage $Co_{100-x}Lu_x$ avec x variant entre 22% et 42%. De plus, des mesures de commutation en un seul tir dans un film complet et un réseau de points de 3 m montrent qu'aucune commutation déterministe de la magnétisation ne peut être observée. Les résultats peuvent être attribués à la faible magnétisation et, par conséquent, à la faible quantité de moment angulaire transportée par l'élément Lu selon des simulations atomistiques.

- Commutation en un seul tir dans des multicouches [RE/TM]N, où la couche RE peut être un métal des terres rares avec un couplage spin-orbite plus important, comme Tb et Dy, et leur alliage avec des métaux de transition. À partir de multicouches $[Tb/Co]_5$ and $[Tb/Fe]_4$, la commutation en un seul tir a été étendue à diverses multicouches, bicouches et tricouches, en faisant un phénomène général dans les multicouches à base de Tb et de Dy, qui ont des propriétés sperimagnétiques couplées à des métaux transitoires. De manière intéressante, une structure complexe de cercles de directions de magnétisation opposées a été observée à haute énergie. Selon les mesures de pompage-sonde, nous avons essayé d'expliquer le mécanisme de commutation et les structures annulaires, qui pourraient être un mécanisme de précession de réorientation dans le plan.

- Commutation en un seul tir dans des multicouches $[Co/Ho]_N$, qui est un nouveau système de matériaux avec une attente de couplage spin-orbite plus élevé par rapport à Tb et Dy. Étonnamment, même si le couplage spin-orbite dans Ho (comme c'est le cas dans Tb et Dy) est plus important que celui de Gd, ce qui devrait augmenter la dissipation du moment angulaire dans la structure cristalline, le diagramme état de durée/fluence des impulsions est proche de celui du système à base de Gd. L'étude de ce nouveau système pourrait contribuer à combler les processus de retournement en un seul tir observés, d'une part, dans les hétérostructures à base de Gd, d'autre part, dans celles à base de Tb ou de Dy.

Mots-clés: Spintronique ultra-rapide, commutation en un seul tir, commutation de précession, réorientation dans le plan, alliage CoLu, multicouches, bicouches, tricouches, multicouches Co/Ho.

Abstract

The emerging field of ultrafast spin electronics integrates the ideas and concepts of magneto-optics and opto-magnetism with spin transport phenomena, supplemented with the possibilities offered by photonics for ultrafast low-dissipative manipulation and transport of information. The discovery of all-optical ultra-fast deterministic magnetization switching has opened up new possibilities for manipulating magnetization in devices using femtosecond laser pulses. Helicity-independent all-optical switching (HI-AOS) is predominantly observed in Gadolinium-based Rare Earth (RE) / Transition Metals (TM) ferrimagnetic alloys or multilayers. Notably, it has recently been witnessed in materials without Gadolinium, such as the ferrimagnet Mn_2Ru_xGa and the ferrimagnetic multilayer $[Tb/Co]_N$.

In this work, we tried to find new materials that can show single-shot HI-AOS and to understand the switching behavior, fundamental mechanism, and switching process in different materials and structures. Therefore, three main parts of work have been done in this thesis:

- Study the CoLu alloy, where Lu has the the small spin-orbit coupling (L=0) as Gd. Perpendicular magnetic anisotropy can be obtained in 3 nm of $Co_{100-x}Lu_x$ alloy with x varies between 22% and 42%. Besides, single-shot switching measurements in full film and 3 µm dots array show that no deterministic switching of the magnetization can be observed. The results can be attributed to the low magnetization and, consequently, too-small angular momentum carried by the Lu element by atomistic simulations.

- Single-shot switching in $[RE/TM]_N$ multilayers, where the RE layer could be rare-earth metal with larger spin-orbit coupling such as Tb and Dy, and their alloy with transition metals. Starting with $[Tb/Co]_5$ and $[Tb/Fe]_4$ multilayers, the single-shot switching has been extended to various multilayers, bilayers, and trilayers, making it a general phenomenon in Tb- and Dy-based multilayers, which have sperimagnetic properties coupled with transient metals. Interestingly, a complex structure of rings of opposite magnetization directions has been observed at high fluence. According to the pump-probe measurements, We tried to explain the switching mechanism and ring structures, which could be an in-plane reorientation precessional mechanism.

- Single-shot switching in $[Co/Ho]_N$ multilayers, which is a novel material system with the expectation of higher spin-orbit coupling compared to Tb and Dy. Surprisingly, even though the spin-orbit coupling in Ho (as it is in Tb and Dy) is larger than that of in Gd, which should increase the dissipation of angular momentum to the lattice, the pulse duration/fluence state diagram is close to

the Gd-based systems. Studying this new system could help bridge the single pulse reversal processes observed, on the one hand, in Gd-based, on the other hand, in the Tb or Dy-based heterostructures.

Keywords: Ultrafast spintronics, shingle-shot switching, precessional switching, in-plane reorientation, CoLu alloy, multilayers, bilayers, trilayers, Co/Ho multilayers

Acknowledgement

In the journey of completing my doctoral studies, I am deeply grateful to many individuals whose support and assistance have been instrumental in my successful completion of this significant academic milestone.

First and foremost, I extend my heartfelt thanks to my advisor, Michel Hehn. You have been an incredibly kind and patient mentor. Over the past three years, our delightful discussions, your meticulous guidance, and thoughtful discussions, coupled with your encouragement, have enabled us to efficiently carry out extensive working. Under your leadership, we continuously explored and delved into our research, creating unforgettable moments.

Next, I express my gratitude to my co-advisor, Stéphane Mangin. Your expertise, meticulous guidance, and encouragement have provided solid support for my research and thesis. Under your guidance, I have gained valuable experiences in both academia and my professional career, which will have a profound impact on my future development.

I would like to thank the collaborators at Spintec, including David and Liliana, for their excellent collaboration and in-depth discussions, which have been invaluable to my research.

Throughout the entire research process, my colleagues, especially Gregory and Julius, have been crucial in guiding and assisting me in MOKE experiments. Discussions with Jon, Junta, Leo, Yaohan, Quentin, Maxime, and others collegues in our Nanomagnetism and Spintronics team have been enlightening. Working with all of you has been a pleasure, and your motivation and collective effort have propelled the entire team forward.

Special thanks to Heloïse, with whom I spent three years sharing the same office. I am so impressive by your patience, pursuit of perfection, and the enviable brown curly hair. My daughter loves you and your hair so much. During the past three years, we jointly explored topics related to Sino-French studies, education, and culture, fostering mutual understanding and providing each other with steadfast support and encouragement. Thanks a lot for your warmly hug and words when I was down.

I am grateful to my husband, Wei, and my dear daughter Zining, as well as our five years together in France. Wei's steadfast support during my lowest points in completing my doctoral thesis, while taking care of our child and household, has been unwavering. In these five years, we have grown together, constantly adjusted, and become better individuals and partners. To my daughter, you are brave, intelligent, hardworking, and full of love. Because of your love, I can move forward with greater determination, stability, and confidence.

Lastly, I extend my gratitude to my family, including my parents, grandparents,

siblings, my husband's family, and friends, for their strong support both emotionally and spiritually. You will always be my tower of strength. Thank you for walking through this important journey of life with me.

Thank myself!

Contents

List of Figures

List of Tables

Chapter 1

Introduction

In this chapter, we briefly review the magnetization manipulation based on magnetic random access memory (MRAM). Then, we will introduce the ultrafast magnetization switching induced by pure laser pulses, including helicity-dependent all-optical switching (HD-AOS) and helicity-independent all-optical switching (HI-AOS). We mostly focus on the single-shot HI-AOS in different materials and its switching mechanism, which is the basis of this thesis.

1.1 General Introduction

In the modern era of information technology, magnetic recording stands as a crucial foundation that underpins our ability to store, access, and retrieve data. At its core, the magnetic record involves the manipulation of nanometric domains within materials to encode and store information. Introduced in 1956, the first commercial hard disk drive (HDD), with a data storage capacity of 3.75 Megabytes(MB), had been employed in computers for data storage purposes by IBM [6, 7]. Over the following decades, there has been a remarkable exponential growth in storage density (see Figure 1.1) [8–10], and magnetic materials, especially those in the shape, have been at the basis of much technological development. Simultaneously, memory devices have reduced in size. This increase in data storage capacity at reduced dimensions in part facilitates carrying information such as images and music in mobile phones and allows exchanging them online.

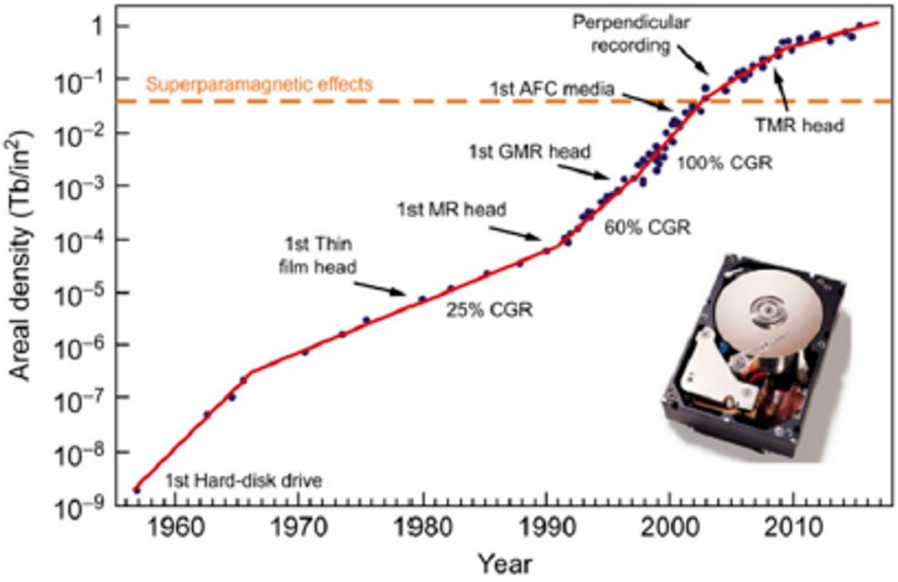

Figure 1.1: Time evolution of the areal bit density starting from the introduction of the first commercial magnetic hard drive disk in the late 1950s. The inset shows a top view of the IBM hard drive Ultrastar 36ZX developed in 1999 with the cover removed.

A hard disk drive (HDD) utilizes the magnetization direction of a ferromagnetic domain to store logical information. Each bit of information is recorded in a small part of the material, which has its magnetic moment aimed towards a certain direction or to the opposite, hence representing the two possible states of a binary code. The magnetization direction is conventionally manipulated by an external magnetic field generated by an inductive write head sliding over the recording medium [10]. With the decreasing bit size, high coercivity material has to be used to maintain the thermal stability for high-density storage, bringing challenges for the generated field of a magnetic head. An effective technology is Heat Assisted Magnetization Recording (HAMR) [11–13], a strategy that utilizes laser-induced heating to temporally lower the coercivity of the magnetic storage medium. This reduction in coercivity enables the facilitation of writing by an external magnetic field. Following the writing and eventual dissipation of the heat, the coercivity increases, and the 'written' bit becomes hard again. Another new technology is Microwave Assisted Magnetization Reversal (MAMR), where a microwave frequency field is applied to magnetic material and by resonantly exciting large angle precession succeeds in lowering its

reversal field [14–16].

HDDs can achieve high storage capacities at a relatively lower cost per gigabyte. However, physical limitations and areal density challenges are becoming more apparent as technology advances. Besides, HDDs require more power to operate due to the need for the spinning disks and the mechanical movement of the read/write heads. A non-volatile memory technology-Magnetic Random Access Memory (MRAM) uses the magneto-resistance changes of magnetic materials to store data [17–20]. It relies on the manipulation of magnetic moments to represent binary information.

A revolution in the recording industry is the discovery of giant magneto-resistance (GMR) phenomenon [21, 22] in the 1980s and later in the 1990s, with the invention of tunneling magneto-resistance (TMR) in a magnetic tunnel junction (MTJ). The observation of GMR is made independently by the groups of Grünberg [22] and Fert [21], who received the Nobel prize in 2007, playing a crucial role in developing Magnetoresistive Random-Access Memory (MRAM).

In MRAM, the reading is based on the magneto-resistance change of the high and low magnetic resistance. When the magnetizations of the two ferromagnetic layers are oriented in the same direction, the resistance will be lower due to the spin-dependent scattering of the minority electrons only. Conversely, when the magnetizations of the free and reference layers are anti-parallel to each other, both the minority and majority electrons will be scattered, resulting in a larger resistance state. The high and low resistance states represent the binary codes '1' and '0', corresponding to the antiparallel and parallel alignment of the two ferromagnetic layers, respectively. By sensing the resistance level, the information stored as parallel or antiparallel magnetic configurations can be read.

The writing in MRAM has been evolving and achieved using different methods in the past and the recent past, from conventional magnetic field-induced switching to current-induced switching and laser pulse-induced switching, with a drastic reduction not only in energy consumption but, more importantly, the reversal time scale of the magnetization leaps from microseconds to sub-picoseconds even femtoseconds.

1.2 Field-writing

One of the oldest methods used to write information is based on applying a magnetic field generated by current-carrying wires. This principle was used until a decade back, to achieve writing, which is also called switching of magnetization or simply switching. In this method, the MRAM architecture consists of a bit line and a word line (See Figure 1.2a). When a current is sent through the bit line and word line corresponding to a particular MRAM cell, two magnetic fields are produced orthogonal to each other. The current in the word line generates a magnetic field H_W along the easy axis, and the current in the bit line generates a magnetic field H_B in the transverse direction to the easy axis. Since field-assisted MRAMs were developed with in-plane magnetization, the easy axes in such MRAMs lie along the longer axis of the ellipsoid cells. After the downsizing of the read-heads and the development of out-of-plane magnetized media, the outdated in-plane longitudinal magnetic recording (LMR) technology was substituted by perpendicular magnetic recording (PMR) [23]. With the advances in PMR technology, data storage density has tremendously increased due to the fact that out-of-plane media has a lower demagnetizing field and allows much denser packing of magnetic bits [24, 25].

Under the Stoner–Wohlfarth switching mechanism, the threshold field required for resulting in magnetic field switching is given by $H_W{}^{\frac{2}{3}}+H_B{}^{\frac{2}{3}}=H_K{}^{\frac{2}{3}}$, where $H_K=\frac{2K}{\mu_0 M_s}$

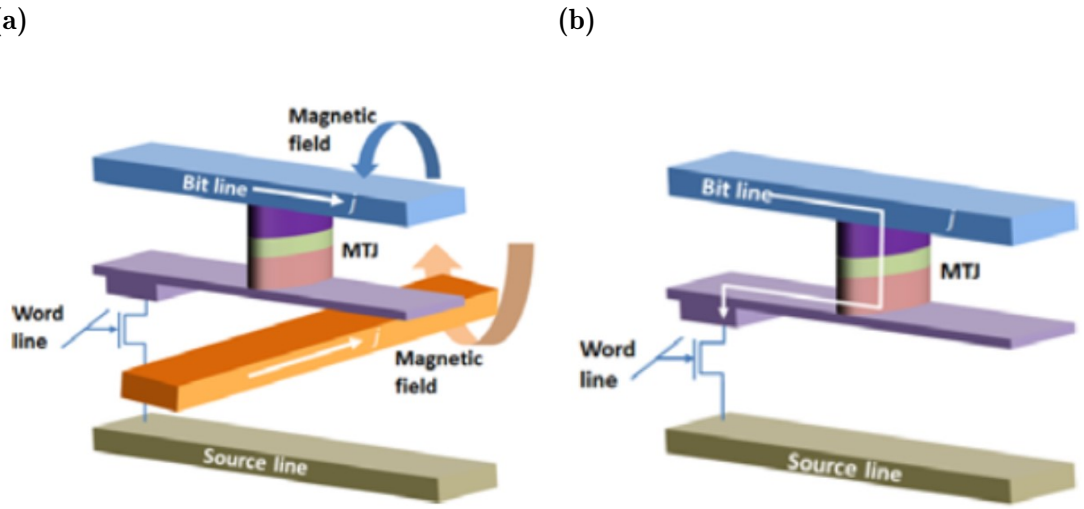

Figure 1.2: Schematic representation of (a) field-induced switching MRAM and (b) Spin Transfer Torque STT-MRAM. In the first case, the curling arrows represent the magnetic field direction generated by the electrodes. In STT switching, the current is sent through the MTJ, and the resultant structure is much less complex than that of field MRAM.

is the anisotropy of the MRAM cell. Switching occurs for any combination of fields for which the resulting field vector lies outside the asteroid. This enables the discerning alteration of a specific bit, attainable by selecting appropriate easy and hard axis fields.

The effective method in single-bit switching is demonstrated, but challenges arise in managing the dispersion of switching fields due to the influence of shape anisotropy. Minute deviations in shape and edge irregularities significantly impact field distribution, especially in extensive bit arrays. Besides, The current required for generating the magnetic field depends on the magnetic and morphological properties of the storing element. The switching field is inversely proportional to the area of the storing element. As a result, scalability toward smaller dimensions becomes a problem. Moreover, the external field creates a torque that acts on the spins in the magnetic medium and makes them precess about the direction of the applied field until the spins eventually point along this direction. The spin precession process, which drives the magnetic information writing, has a fundamental timescale of the order of nanoseconds, imposing a speed limit on the read-write event.

1.3 Current-writing

The electrons responsible for charge current in electronic circuits also possess intrinsic spins. In non-ferromagnetic materials, these spins exhibit random orientations with no impact on device behavior. However, when ferromagnetic components are incorporated into a device, the flowing electrons can be partially spin-polarized, and these spins can play an important role in device function. Due to spin-based interactions between the ferromagnets and electrons, the orientations of magnetization for ferromagnetic elements can determine the amount of current flow. By means of these same interactions, the electron spins can also influence the orientations of the magnetization, which is the so-called spin transfer torque [1, 26–28].

The discovery of spin-transfer torques has expanded the means available to manipulate the magnetization of ferromagnets. This discovery has led to the rapid

advancement of high-performance and high-density magnetic storage devices. Unlike a hard disk drive, which has to do mechanical movement, these new magnetic devices are all electronic and can be integrated with and add functionality to semiconductor devices.

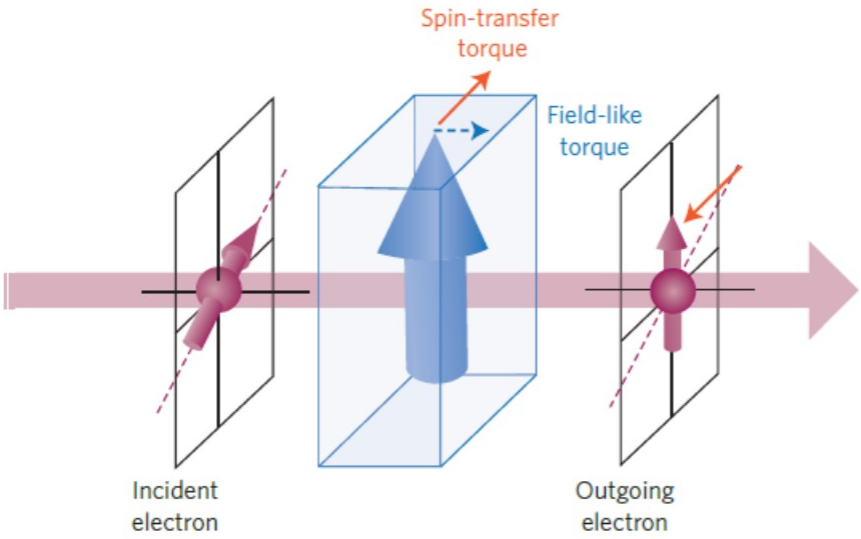

Figure 1.3: Illustration of current-induced spin-transfer torque. The interaction between the spin-polarized current and the magnetization causes a change in the spin direction of the outgoing electron compared with the incident electron when a spin-polarized current flows a ferromagnetic material. [1]

The spin current carries angular momentum, which can be transferred to the magnetization. Sloncwezski and Berger were the first to theorize about the existence of this phenomenon [29,30]. The torques result from an interaction between the spin-polarized itinerant electrons (spin current) in a ferromagnet and the magnetization. The interaction only occurs in regions with flowing spin currents, enabling precise directional control for applications. In fact, spin-transfer torques are not limited to ferromagnetic materials or antiferromagnets, and they also occur at interfaces of insulating magnetic materials such as in an MTJ [31, 32].

Another type of current-induced spin torque, spin-orbit torque (SOT), occurs in a material with strong spin-orbit coupling, inducing a transfer of angular momentum from the electron spin to its orbital motion [33]. The typical SOT device consists of a bilayer of non-magnetic metal (NM) and a ferromagnet (FM) capped by an oxide. When an electrical current flows in the plane of the NM thin film, a transverse spin current density at the bilayer interface is generated due to the spin-orbit coupling (SOC) effects at the bulk of the NM and/or the interface of NM/FM. This spin accumulation at the interface exerts the torque on the magnetization of the FM and subsequently has been proven to switch the magnetization of the FM, move domain walls inside the FM, and generate oscillations in an effective manner compared with conventional STT. Two main SOC phenomena that are attributed to generating spin accumulation are the spin Hall effect (SHE) [34] and the interface Rashba-Edelstein effect [35].

Both Spin-Transfer Torque (STT) and Spin-Orbit Torque (SOT) are fundamental concepts in the realm of spintronics, taking advantage of the fact that electrons have an intrinsic moment (spin) in addition to their charge. An important advance that spintronics provides is the ability to manipulate the magnetic moment of a ferromagnetic material in a purely electrical way. The major advantage of such

an electrical technique is device scalability and reduced power consumption over conventional magnetic field-based devices.

1.4 Laser-writing

The ever-increasing speed at which modern electronics operate, as well as the ever-increasing capacity for storing information, have prompted the search for faster ways to process and magnetically record information [36–46]. Writing information in a bit requires applying an external magnetic field in the opposite direction to reverse the magnetic moment. Much faster magnetization reversal can be obtained if the magnetic field is applied perpendicular to M via a precessional switching [36–40]. However, the speed of operation is fundamentally limited by the spin precession time no lon 10-100 ps. Such a time constraint severely limits the operation speed of the spintronic devices; Therefore, overcoming this problem is crucial for the future development of spintronics.

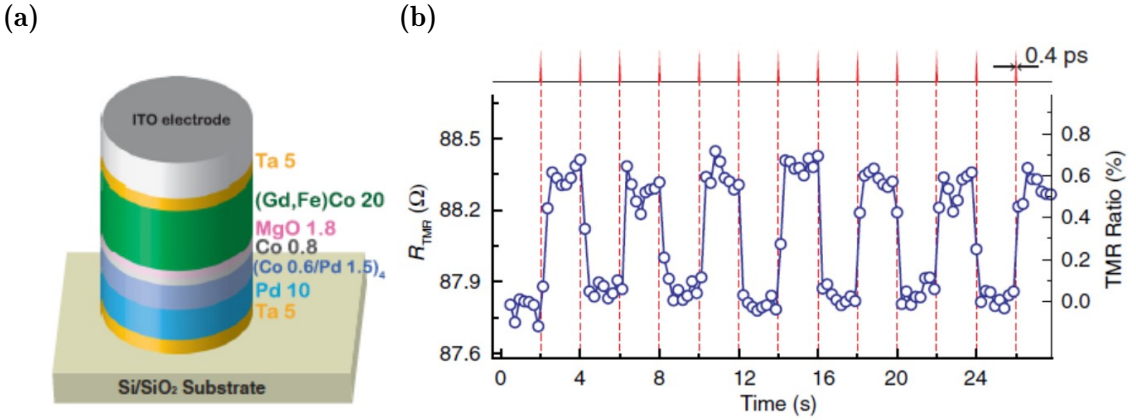

Figure 1.4: (a): Schematic of GdFeCo-based AOS-MTJ structure. (b): TMR of the MTJ device measured during AOS by 0.4-ps single laser pulses at 0.5-Hz repetition rate.

AOS features ultrafast and energy-efficient data writing, showing great potential toward integration with spintronic memories. In this regard, by integrating AOS with high-performance p-MTJs, an all-optical addressable MTJ device is envisioned, which will hold great promise for a unique class of integrated photonic spintronic memory devices with picosecond switching speed and low energy consumption. [47,48]. Chen et al. [49] demonstrated the first successful AOS operation of a micron-sized p-MTJ cell using a GdFeCo alloy storage layer, resulting in a small TMR ratio of 0.6%. It was later improved by Wang et al, who reported switching of Co/Gd bilayer tunnel junctions with cell sizes down to 3 μm lateral size and TMR ratio of 34.7% [50]. Before this improvement of TMR in an all-optical writing MTJ, Avilés-Félix reported the single-shot switching in Tb/Co multilayers and innovatively designed a Tb/Co multilayer coupled magnetically to the FeCoB interface of the storage layer, leading to an increased TMR up to 38% [51–53]. Recently, the TMR in Tb/Co multilayer-based MTJ has been largely improved up to 75% [54].

Ultrafast spin electronics is an emerging field of research that combines the ideas and concepts of magneto-optics and opto-magnetism with spin transport phenomena, supplemented with the possibilities offered by photonics for ultrafast low-dissipative manipulation and transport of information. Both light and spin currents can control magnetic order, though the mechanisms, as well as the corresponding time scales and energy dissipation differ. The project aims at the best of both

worlds, combining short time scales and non-dissipative propagation of light pulses with nanoscale selectivity and strong spin currents interactions to create novel data technology concepts. The ultimate goals are creating and implementing non-volatile, low-dissipative, and ultrafast functional elements. To reach these goals, two main objectives will be followed:

- Identifying new materials that can show single-shot helicity-independent all-optical switching (HI-AOS);
- Trying to understand the behavior and origin of their single-shot switching;

Therefore, three main parts of work have been done in this thesis:

- Study the CoLu alloy. Lu has the same properties as Gd (L=0). From scratch, we optimized the perpendicular anisotropy of CoLu alloy and tried to show single-shot reversal experiments.
- Single-shot switching in $[RE/TM]_N$ multilayers, where the RE layer could be rare-earth metal with larger spin-orbit coupling and their alloy with transition metals.
- Single-shot switching in $[Co/Ho]_N$ multilayers

1.5 Scope of this thesis

The work done in this thesis is guided by the directions outlined above. We studied the magnetic properties, and optimized the perpendicular anisotropy of the samples, and explored the single-shot switching behavior and its mechanism by means of magneto-optics on both static and ultrafast timescales.

This thesis is organized as follows:

In **Chapter 2** , we will introduce the history of ultrafast laser-induced switching, including multiple pulses helicity-dependent all-optical switching (HD-AOS) and single-shot helicity-independent switching (HI-AOS) in ferromagnetic, ferrimagnetic materials and their nanostructures.

Chapter 3 presents the experimental details of the experimental techniques that have been used in this thesis. A short introduction is made regarding sample growth, especially to introduce wedge film architectures and the thickness determination of wedge samples. A second part is devoted to describing our femtosecond laser setup and the ultrashort pulses characterization methods, including the magnetic property characterization and the static and dynamics AOS measurements based on the Magneto-Optic Kerr Effect (MOKE). Finally, we present the laser beam size and threshold fluences determination involving the energy Gaussian distribution of the laser pulse.

Chapter 4 presents the first work on CoLu thin film where Lu has zero orbits angular momentum, which is the same as Gd. The perpendicular anisotropy and magnetic properties have been optimized first. Then, single-shot switching measurements were done in full film and dense nanodots; consequently, domain properties were extracted from the MOKE images to determine the switching probability. By atomistic simulations, we proposed that the low magnetization and, consequently, the too-small angular momentum carried by the Lu element could be one of the reasons that no magnetization switching was observed in CoLu alloys.

Chapter 5 presents the shingle shot switching in a large variety of RE/TM multilayers, where the RE layer could be Tb and Dy or their alloys with transition metals (TM). Concentric ring domain structures are induced at high laser intensities, unveiling multiple fluence thresholds. These threshold fluences for switching are observed to be independent of the pulse duration, up to at least 10 ps or even longer. These striking switching features differ from those of HI-AOS in GdFeCo alloys. The picture of precessional reversal emerges due to the strong evidence concomitant with the demonstration of an in-plane reorientation of the magnetization, pointing towards an intrinsic precessional switching mechanism.

Chapter 6 reports some intriguing results obtained in TbCo/GdCo/TbCo trilayer. By decreasing the Gd concentration in the GdCo layer, we clearly observed the ultrafast toggle switching in Gd-based materials to the in-plane reorientation precessional switching in multilayers. Gd content is the key ingredient in ultrafast toggle switching, but magnetization and anisotropy are mainly responsible for the multidomain creation and the precessional switching.

Chapter 7 presents single shot-switching in $[Co/Ho]_N$ multilayers, which is a novel material system with the expectation of higher spin-orbit coupling compared to Tb and Dy. Single-shot switching behavior in Co/Ho multilayers with varying monolayer thicknesses depending on the repetition numbers of the bilayer has been observed. Interestingly, the total thickness of the multilayer played a crucial role in determining the switching capability. The switching behavior of Co/Ho multilayers resembles that of GdFeCo alloys, deviating from that observed in Tb-based and Dy-based multilayers.

Chapter 8 summarizes and concludes this thesis work and gives some perspectives.

Chapter 2

Utrafast demagnetization and all-optical switching

In this chapter, we will introduce the history of ultrafast laser-induced switching, including multiple pulses helicity-dependent all-optical switching (HD-AOS) and single-shot helicity-independent switching. Then, we focus on the single-pulse all-optical switching and its mechanism in different materials. It is intended to serve as a reference and comparison for discussing subsequent work.

The development of ultrafast laser pulses has opened up the possibility of exploring magnetic dynamics on picosecond and femtosecond timescales. In 1996, Beaurepaire et al. Experimentally demonstrated ultrafast demagnetization of a 20 nm thick Ni continuous film with a single 60 fs laser pulse [2]. It shows that the decay of the magneto-optical signal is already within 50 fs, three orders of magnitude shorter than any conventional demagnetization process. This is difficult to explain because none of the interactions, such as magnetic dipoles, Zeeman interactions, or even precession, play a significant role in such a short period of time. This discovery not only raises several questions about the fundamental physics of ultrafast magnetic manipulation but also opens up the possibility of its technological applications.

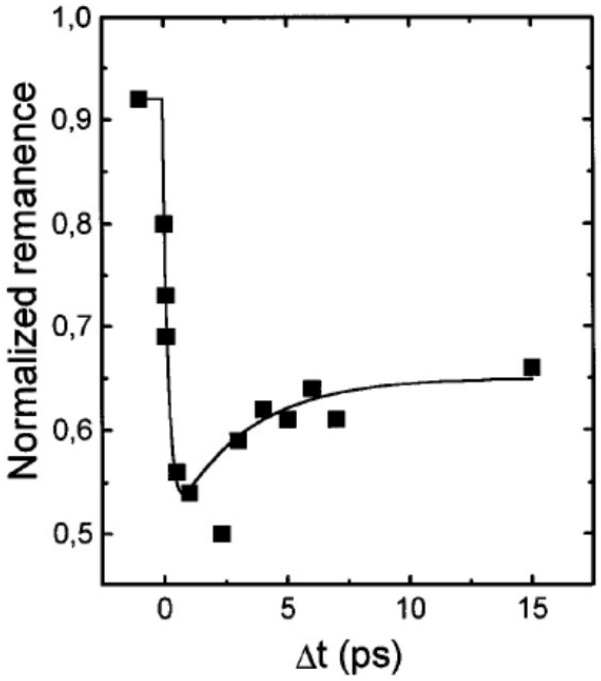

Figure 2.1: Ultrafast demagnetization in Nickel. The curve is obtained by measuring the remanent MOKE signal.

2.1 Ultrafast demagnetization

2.1.1 Standard magnetization dynamics

Spin systems involve organized magnetic arrangements, with spin angular momentum being an intrinsic quantum property absent in classical physics [55]. When materials are exposed to a magnetic field, they acquire a magnetic moment or magnetization. These materials are normally made up of domains, which exhibit long-range ordering that causes the spins of the atoms to line up parallel to each other in a domain. The fundamental interactions underlying magnetism originate from spin-spin exchange interactions generated by overlapping electron wave functions [56]. Additional influences on magnetic structures encompass magnetocrystalline anisotropy, applied magnetic fields, demagnetization fields, biquadratic exchange, and various weaker interactions. Drawing on phenomenological considerations, Landau and Lifshitz [57] introduced a foundational dynamical equation, integrating these interactions, to describe magnetization or spin behavior in bulk materials, where the effect of relativistic interactions was also included as a damping term. In 1954, Gilbert

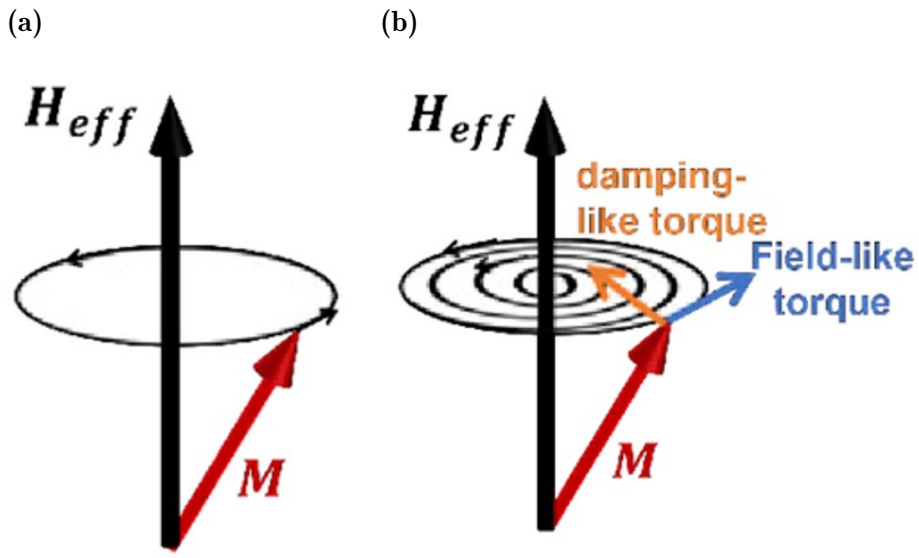

Figure 2.2: (a) Precession of magnetization without damping corresponding to the first term of the right side in Eq. 2.1, (b) Precession of magnetization with Gilbert damping corresponding to Eq. 2.1.

[58] introduced a more convincing form for the damping term based on a Lagrangian approach, and the combined form is now called the Landau–Lifshitz–Gilbert (LLG) equation, which is a fundamental dynamical system in applied magnetism:

$$\frac{\partial M}{\partial t} = -\gamma(M \times \mu_0 H_{\text{eff}}) + \frac{\alpha}{|M|} M \times \frac{\partial M}{\partial t} \tag{2.1}$$

where γ is the gyromagnetic ratio, μ_0 is the vacuum permeability, and α the Gilbert damping constant. The first term corresponds to the precession of the magnetic moment around the effective magnetic field (H_{eff}), comprising external and internal interactions, which is the case shown in Figure 2.2a. While employing the damping term, which is the second term of the right side, and the precession term, the magnetic moment process towards equilibrium.

To reverse magnetization, the antiparallel configuration's damping time is around nanoseconds, accelerating to approximately 100 picoseconds under an orthogonal field. [59]. However, the LLG equation doesn't account for thermal effects, making it unsuitable for scenarios involving laser excitation. The Langevin noise term [60,61] introduces thermal fluctuations, yet the LLG-Langevin model falls short at higher temperatures associated with laser excitation due to its omission of high-frequency spin waves, leading to overestimating the Curie temperature T_C [62, 63].

2.1.2 Microscopic three-temperature model (M3TM) of ultrafast laser-induced spin dynamics

In order to explain the ultrafast magnetization dynamics, many theoretical models highlight the role of laser heating in the demagnetization process and focus on the thermalization of spins via the absorption of laser pulses by the electronic system [64–66]. One of the representations is the phenomenological three-temperature model [2], which has been proposed to explain the demagnetization process and presents a thermodynamic description of the exchange of energy in the system and the evolution of the temperature. This 3TM is based on the interactions between three thermalized reservoirs, namely, the electrons, the lattice, and the spins. The 3TM takes the spin

system into account and is an extension of the two-temperature model (2TM), which describes the energy transferred from the laser-excited electrons only to the lattice [67].

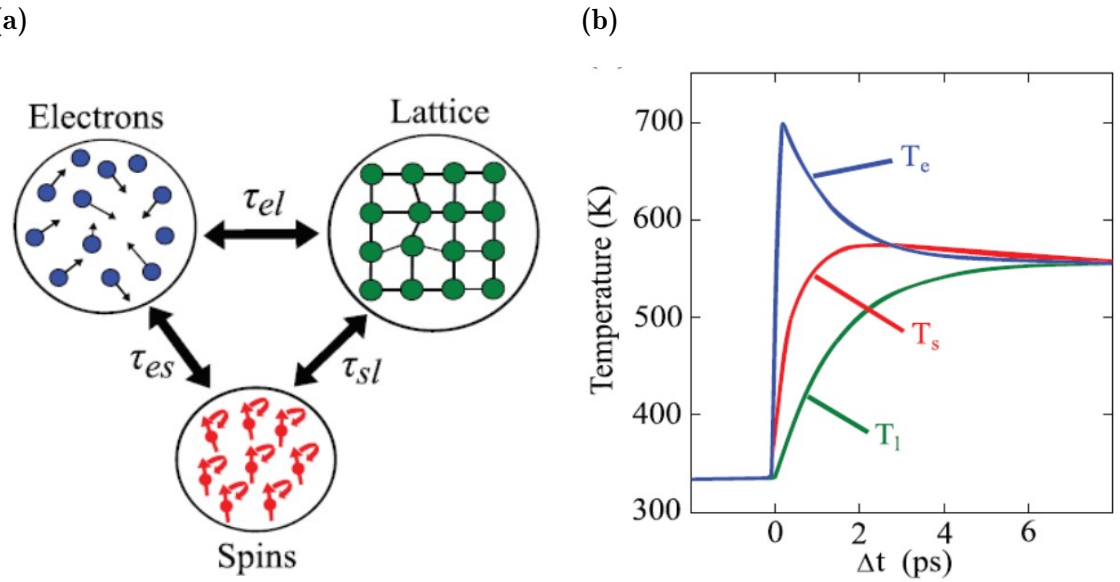

Figure 2.3: (a): Interacting reservoirs (spin, electrons, and lattice) in the 3TM model. The laser pulse is first absorbed by the electron bath, and then heat is transferred between the three-coupled reservoirs. (b) Evolution of spin T_s, electron T_e, and lattice T_l temperatures as a function of the delay time, as calculated by Beaurepaire et al. [2].

As depicted in Figure 2.3, each of these three coupled reservoirs has its own temperature and heat capacity. Taking into account the energy balance, the temporal evolution of the temperature in each reservoir can be expressed by the following coupled differential equations:

$$C_e(T_e)\frac{dT_e}{dt} = -G_{el}(T_e - T_l) - G_{es}(T_e - T_s) + P(t), \tag{2.2}$$

$$C_s(T_s)\frac{dT_s}{dt} = -G_{es}(T_s - T_e) - G_{sl}(T_s - T_l), \tag{2.3}$$

$$C_l(T_l)\frac{dT_l}{dt} = -G_{el}(T_l - T_e) - G_{sl}(T_l - T_s), \tag{2.4}$$

where G_{el}, G_{es} and G_{sl} are the coupling constants of electron-lattice, electron-spin, and spin-lattice, respectively. C_i and T_i are heat capacity and temperature, respectively, of i reservoirs. P(t) is the laser source term applying only to the electron term since the initial laser heating occurs only in the electron reservoir. These equations are coupled, meaning that the change in one temperature affects the changes in the others. For example, the electron temperature equation includes terms representing the transfer of energy to the lattice and spin subsystems, while the lattice temperature equation incorporates the energy received from the electrons. This interplay allows the model to track the energy flow and thermalization between the subsystems. The exciting laser pulse first deposits its energy in the electronic subsystem with the smallest heat capacity and rapidly heats up the electronic subsystem to high temperatures that are determined by the incident laser fluence. The heat is eventually redistributed to the spin and lattice subsystems at the characteristic coupling timescales, reducing the electron temperature and increasing the lattice and

spin temperatures until all three subsystems eventually attain thermal equilibrium.

Although such a simple phenomenological model successfully reproduced experimental electron and spin dynamics following laser excitation, several limitations must be pointed out. First of all, The 3TM assumes that the three subsystems (electron, lattice, and spin) start in equilibrium. However, in ultrafast processes induced by, for example, laser excitation, materials are often subjected to sudden and intense energy deposition. This leads to a highly non-equilibrium state where energy is not evenly distributed among the subsystems. Secondly, The 3TM completely ignores the conservation of angular momentum, which is at the origin of magnetization dynamics.

2.1.3 Conservation and transfer of angular momentum

During processes like ultrafast demagnetization, the excitation of electrons can lead to changes in their spin orientations, resulting in the transfer of angular momentum between the electron spins, the lattice vibrations (phonons), and the overall spin structure of the material. An excited electron can reverse its spin via different mechanisms in a ferromagnetic. These mechanisms involve intricate interactions between electrons, spins, and lattice vibrations in magnetic materials. One mechanism involves Stoner excitations, where an excited electron flips its spin due to interactions with other electrons [68]. This process can contribute to the redistribution of angular momentum within the material during ultrafast demagnetization. Another mechanism is the scattering of inelastic electron-spin waves [69–72]. Electrons can exchange angular momentum with spin waves, which are collective excitations of the spins in the material. This interaction can result in the transfer of angular momentum and contribute to the demagnetization process. Koopmans et al. explored the dissipation of angular momentum into the lattice upon laser irradiation, employing a microscopic model based on the Elliot-Yafet scattering mechanism to describe the probability of electron spin-flip events upon emission or absorption of phonons [64]. This type of electron scattering was also used to theoretically explain the rapid equilibrium of the magnetic order in a ferromagnet at a few hundred femtoseconds after laser pulsed irradiation [73]. Moreover, XMCD measurements done on Ni thin film [74] and Co thin film [75] suggested that the only possible way for the angular momentum to be dissipated is into the lattice, which is, therefore, consistent with an Elliot-Yafet spin-flip model.

2.2 All-optical magnetization switching

The ultrafast demagnetization observed in Ni thin films with femtosecond laser pulses introduced a novel approach to manipulate magnetization without an external magnetic field. While the potential for technological applications was conceptual, as complete magnetization reversal wasn't achieved, the breakthrough came with the discovery of all-optical switching (AOS). This was demonstrated in a GdFeCo alloy, where full magnetization reversal was induced by femtosecond laser pulses, paving the way for ultrafast magnetization recording.

2.2.1 Multiple pulses helicity-dependent all-optical switching

In 2007, Stanciu et al. demonstrated for the first time deterministic switching with circularly polarized fs laser pulses in a 20 nm-thick $Gd_{22}Fe_{74.6}Co_{3.4}$. A GdFeCo

amorphous ferrimagnetic alloy was chosen to perform the all-optical response measurements since it is widely used in magneto-optical recording [76] and is known for its strong magneto-optical effects [77]. Regeneratively amplified pulses, from a Ti:

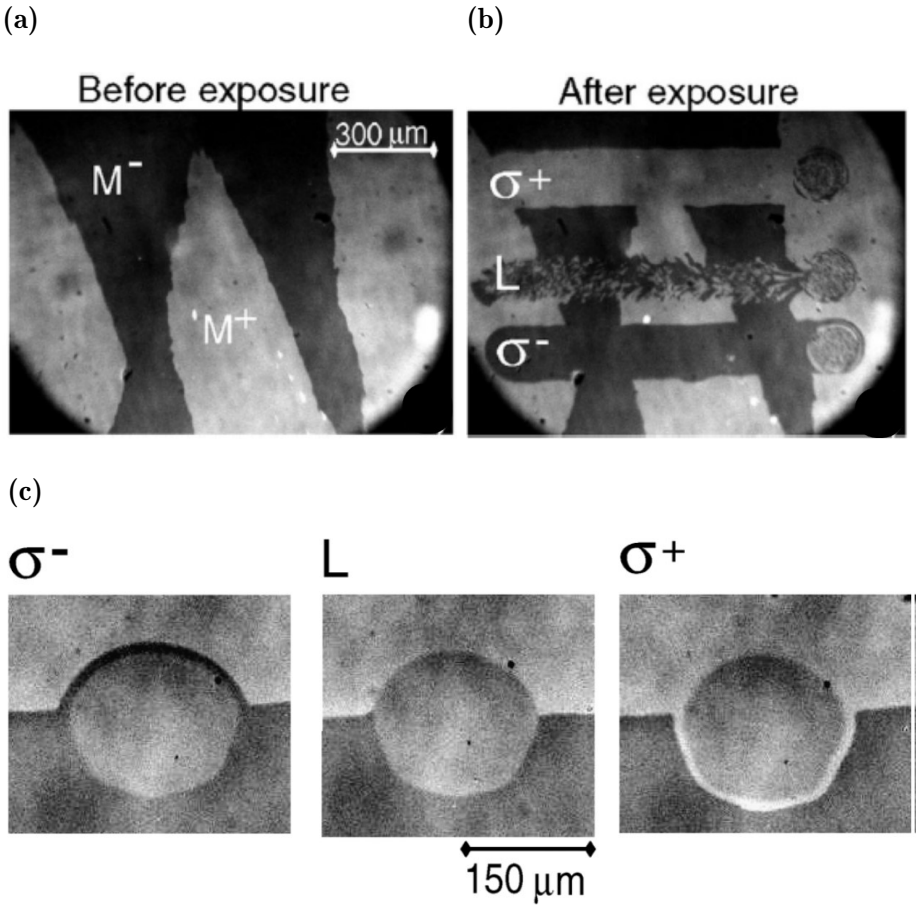

Figure 2.4: The effect of ultrashort polarized laser pulses on magnetic domains in $Gd_{22}Fe_{74.6}Co_{3.4}$. (a) Magneto-optical image of the initial magnetic state of the sample before laser exposure where White and black areas correspond to "up" (M_+) and "down" (M_-) magnetic domains, respectively. (b) Domain pattern resulting from sweeping the sample at low speed ($30\mu m/s$) with linear (L), right-handed (σ^+), and left-handed (σ^-) circularly polarized beams across the surface of the sample, with a laser fluence of about 11.4 mJ/cm^2. (c) A linearly- and circularly polarized laser beam is focused onto a domain wall boundary and kept static. Independently of the laser polarization, the central part of the beam shows a random distribution of up- and down-magnetic domains due to excessive heating. Figure adapted from [3].

sapphire laser with a wavelength of 800 nm and a repetition rate of 1 kHz, were used to excite the material, and were incident normal to the sample surface. Each pulse had a Gaussian intensity profile, with a pulse width at half maximum of 40 fs. The beam was swept over the sample surface with linear (L), right-handed (σ^+), and left-handed (σ^-) circularly polarized beams across the surface of the sample, with a laser fluence of about 11.4 mJ/cm^2. It was found that the pulses with σ^+-polarization (resp. σ^-) lead to the reversal of the M^- domain (resp. M^+ domain) while leaving the M^+ domain (resp. M^-) unchanged. In contrast, linearly polarized light creates only a demagnetized area. It is clear that the reversal is deterministic and depends on light helicity. On the contrary, linearly polarized light generates solely a demagnetized region. It's evident that the reversal process is deterministic and contingent upon the light helicity.

They also focused the laser beam onto a domain wall and recorded the MOKE images ***during*** the laser pulse excitation with different polarizations of the laser beam, σ^+, L and σ^-. As depicted in Figure 2.4c, the central regions show a demagnetization due to the strong heating in the central part of the Gaussian laser beam. However, a "switching rim" of opposite magnetization contrast can be observed for left- and right-circular polarizations, which is not the case for linear polarized laser pulses. It is noticed that this is a multiple-pulses laser-induced magnetization switching since the laser with 1 kHz repetition rate is always on during the recording of the images. Accompanying the fact that the magnetization switching depends on the helicity of light instead of the initial magnetic state, this laser-induced switching is called helicity-dependent all-optical switching (HD-AOS).

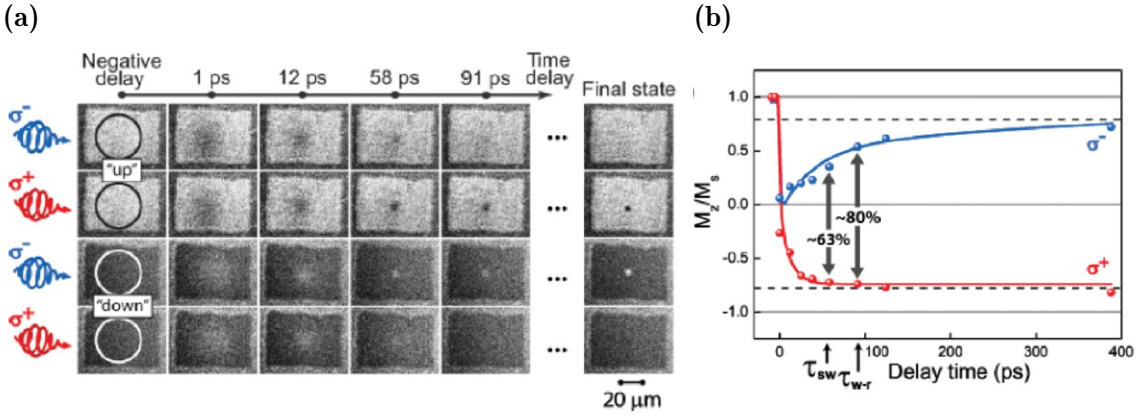

Figure 2.5: (a) The magnetization evolution in $Gd_{24}Fe_{66.5}Co_{9.5}$ after the excitation with σ^+ and σ^- circularly polarized pulses at room temperature. The domain is initially magnetized up (white domain) and down (black domain). The last column shows the final state of the domains after a few seconds. The circles show areas actually affected by pump pulses. (b) The averaged magnetization in the switched areas ($5\mu m$)after σ^+ and σ^- laser pulses, as extracted from the images in (a) for the initial magnetization up. Figure adapted from reference [4].

Vahaplar et al. studied the dynamics process Using time-resolved single-shot pump-probe microscopy in 20 nm GeFeCo alloy films with perpendicular anisotropy by a circularly polarized laser pulse [4]. They demonstrate that the reversal does not involve precession but has a linear character via a strong nonequilibrium state.

The pump pulses of both helicities bring the originally magnetized medium into a strong nonequilibrium state with no measurable net magnetization within a few hundred femtoseconds. Over the next tens of picoseconds, the medium either relaxes back to its initial state or forms a small domain with reversed magnetization. It's clear that the switching process occurs via a nonequilibrium demagnetized state, different from the conventional precessional motion, and the final state is determined by the helicity of the pump pulse. The metastable state corresponding to reversed magnetization is reached within 60 ps [1] after σ^+ and σ^- excitation. The switching time is, in fact, surprising because, in contrast to heat-assisted magnetic recording [78], the reversal time is much longer than the effective light-induced magnetic field pulse H_{eff}. Phenomenologically, this is very similar to the inverse Faraday effect. The feasibility of both all-optical recording and reading on an ultrashort time scale was demonstrated using two single subpicosecond laser pulses. The magnetic information

[1]The characteristic time of switching τ_{sw} is identified as the time required to reconstruct 63% $(1 - e^{-1})$ the difference between the metastable state. For example, in Figure 2.5b, $\tau_{sw} = 60$ ps.

was recorded by a subpicosecond laser pulse in a $5\mu m$ domain and readout by a similarly short pulse within 30 ps, which is the fastest write-read event demonstrated for magnetic recording so far.

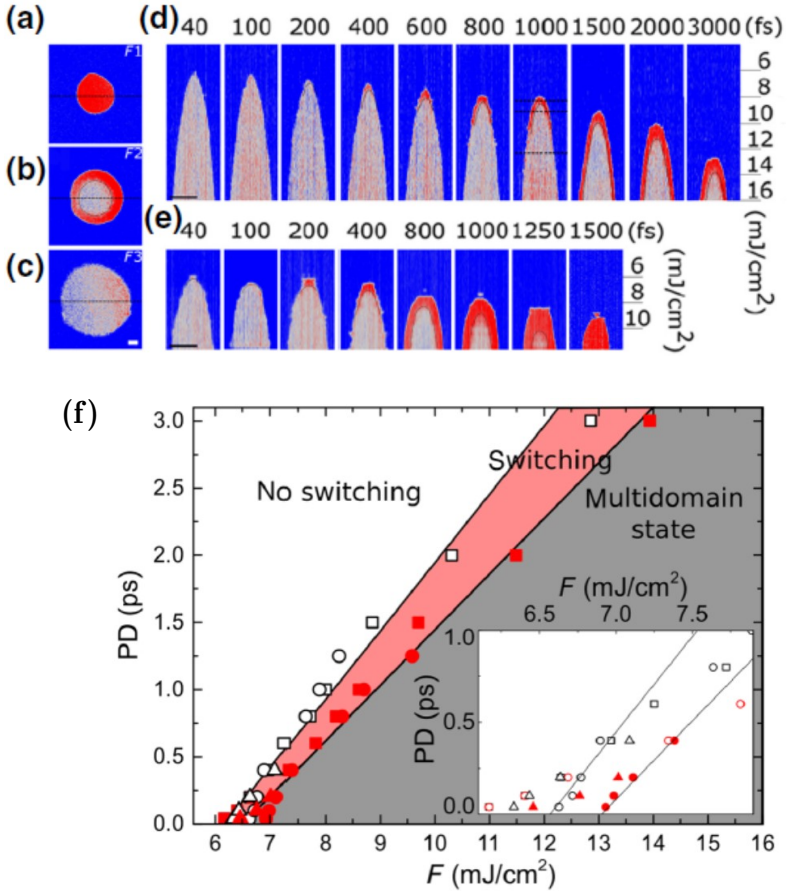

Figure 2.6: (a)–(c) Magneto-optical Kerr images obtained after exposing the Co/Pt sample to 600 laser pulses with a pulse duration of 1 ps, a σ^+ polarization, and laser fluences of (a): 8.3 mJ/cm^2, (b): 9.1 mJ/cm^2, and (c): 12.3 mJ/cm^2. The red and blue contrasts represent the opposite magnetization directions out of the paper film. (d)–(e) Cross section of the laser-excited area for laser fluences between 4 and 18 mJ/cm^2 due to the laser pulse Gaussian distribution and various pulse durations, the beam diameter is (d): 104 μm and (e): 168 μm. (f): Magnetization state diagram as a function of the laser fluence and the pulse duration for a circularly polarized static beam illuminating a Co/Pt thin film. The beam size differs for each curve: 84 μm for triangles, 104 μm for squares, and 168 μm for dots. For a given pulse duration, the maximum (minimum) fluence for which HD-AOS occurs is plotted as filled (open) symbols. The inset shows the zoom-in of the diagram for the short pulse durations.

After its observation in GdFeCo [3], HD-AOS in other amorphous RE-TM ferrimagnetic alloy films like TbCo [79, 80] and TbFe [81] have been reported, making this phenomenon a generic phenomenon, not restrict to Gd-based materials. Then Mangin et al. engineered a large variety of ferrimagnetic materials ranging from amorphous alloys, multilayers, and heterostructures to rare-earth-free synthetic ferrimagnets [82]. In order to observe HD-AOS, they tried to tune the magnetic properties, such as the exchange coupling and the compensation temperature T_{comp}. The underlying similarity among various RE-TM structures demonstrating HD-AOS is the presence of two ferrimagnetic sublattices with distinct temperature dependencies that can be magnetically compensated at a certain temperature. Further, the RE-

free Co–Ir-based synthetic ferrimagnetic heterostructures that mimic the magnetic properties of RE–TM alloys also exhibit HD-AOS. To conclude, this comprehensive study on material dependence provides compelling evidence that a wide variety of materials can be engineered for HD-AOS, which would allow the designing of complex structures with tunable properties, catering to diverse technological applications.

G. Kichin et al. [83] Studied the influence of laser pulse parameters such as pulse duration, beam size, fluence, and number of pulses on magnetization switching and demagnetization in Ferromagnetic Co/Pt multilayers. a state diagram that elucidates the magnetization state of the thin ferromagnetic film subsequent to laser exposure, contingent upon laser fluence and pulse duration, was constructed. The MOKE images are recorded after sending 600 circularly polarized pulses to the Co/Pt sample. The minimum fluence below which nothing observable happens on the sample, and the maximum fluence above which the multidomain state could be observed in the central region. As shown in Figure 2.6, when the pulse duration is below 400 fs, no magnetization occurs, and only a multidomain state is observed. A very narrow ring showing switching can be observed with a longer pulse duration. Obviously, the minimum and maximum fluences increase with longer pulse duration. However, the minimum fluence increases slightly faster than the maximum fluence, resulting in a larger fluence range to show HD-AOS. Furthermore, optimization of laser pulse characteristics has enabled the realization of full magnetization switching following 50 pulses and substantial switching effects after just 10 pulses. For a single laser pulse experiment, it shows that it is possible to obtain 10% switching if only sending one single pulse. Those experimental results allow us to conclude that the HD-AOS cannot be adequately elucidated by magnetic circular dichroism in isolation. Combining the experimental results and the three-temperature model, the criteria to observe switching is that enough heating is injected into the sample so that the spin temperature can reach a value close to the spin-ordering temperature, at which a moderate angular momentum transfer is expected from the circularly polarized light to the magnetic material and should be sufficient to generate the switching. This conclusion agrees with the theoretical prediction provided by Oppenner et al.[84, 85].

2.3 Helicity Independent All-Optical Switching (HI-AOS)

In 2011, employing the X-ray magnetic circular dichroism (XMCD), an element-specific detection technique, I. Radu studied the spin reversal dynamics in GdFeCo alloy [86]. The sample was excited with 60 fs laser pulse on a timescale relevant to the characteristic time of the exchange interaction between Gd and Fe spins. First, both sublattices experience a fast reduction in net magnetization. However, whereas the net magnetization of Fe has collapsed and crossed 0 within 300 fs, the demagnetization of Gd takes as long as 1.5 ps, which is much slower than the Fe sublattice. Despite the antiferromagnetic coupling of the ground state between Gd- and Fe-sublattices, a transient ferromagnetic-like state was formed in which the magnetic moment of Gd and Fe align in the same direction temporarily. Following this, the magnetizations of both sublattices undergo a reversal of directions by crossing the zero signal level and rebuilding their net magnetic moments. Notably, the net Fe and Gd moments in the transient ferromagnet-like state reach rather large values, up to 25% of the equilibrium magnetization. This observation and the substantial temperature rise induced by the laser indicate a notable transient alignment of the

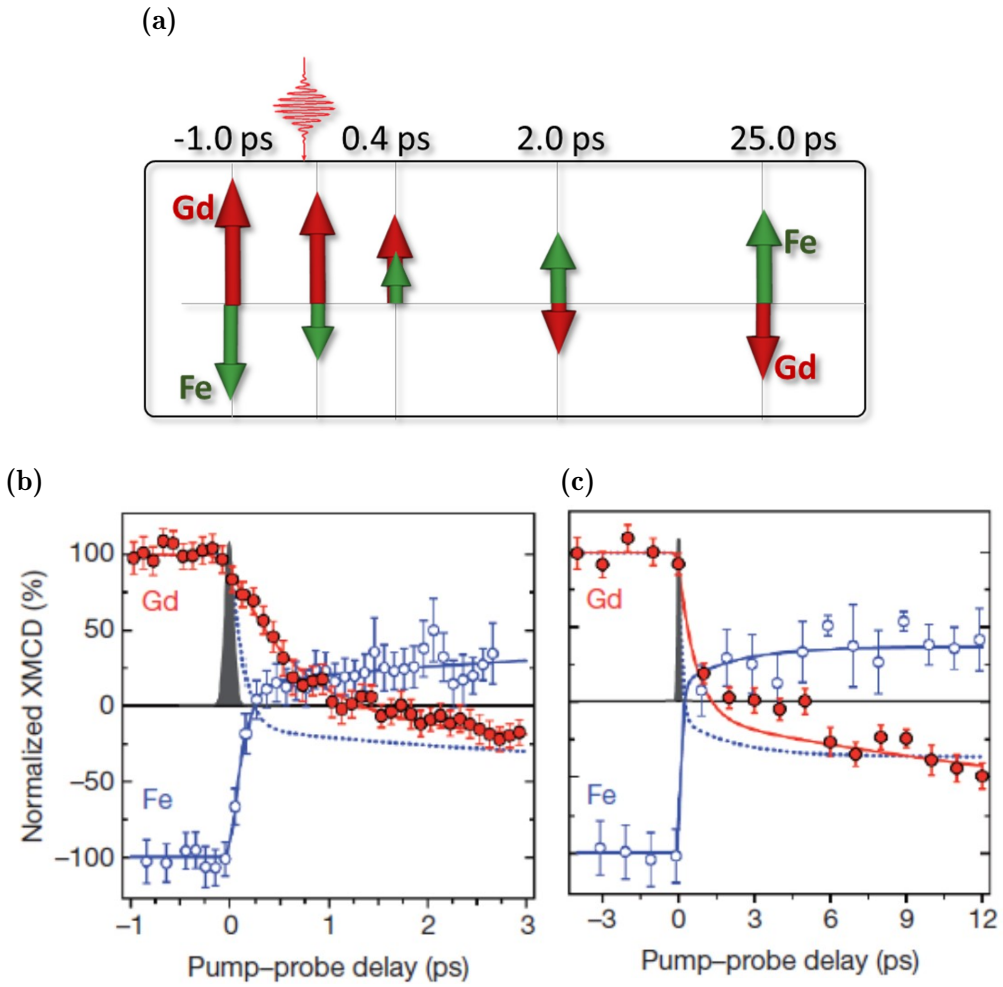

Figure 2.7: Cartoon-like illustration of the non-equilibrium dynamics of the Fe and Gd magnetizations with respect to an external magnetic field H. The lengths of the arrows are scaled to the magnitude of the transient XMCD signals. (a): Transient dynamics of the Fe (open circles) and Gd (filled circles) magnetic moments measured within the first 3 ps. (b): same As (a) but on a 12 ps timescale.

Fe and Gd moments in parallel orientation.

Additionally, the agreement between experimental findings and numerical simulations employing an atomic model coupled to the temperature of the electron thermal bath [63, 87] was obtained, where the simulations qualitatively reproduced the demagnetization timescales for each sublattice. Interestingly, adjusting the Gd–Gd exchange interaction strength in the simulations to match the Fe–Fe interaction does not introduce substantial changes in the dynamics of the Fe and Gd sublattices. Furthermore, despite neglecting differences in electron temperature and damping constants between Gd and Fe in the model, a noteworthy level of consistency between experimental results and simulations is maintained. This is a strong indication that the novel magnetization dynamics reported in this reference are an intrinsic property of the spins in a ferrimagnet excited by an ultrashort stimulus.

Later, T.A. Ostler [88] experimentally verified this switching mechanism in $Gd_{24}Fe_{66.5}Co_{9.5}$ by recording the images obtained on a MOKE microscopy. After excitation by a single 100 fs laser pulse, the magnetization switches from one direction to another and switches back by the second pulse. Every such pulse thereafter triggers this reversal. The observed sequence of switching occurs independently of the polarization of the laser pulses and without any use of the magnetic field. Thus,

this laser-induced switching is called helicity-independent all-optical switching (HI-AOS).

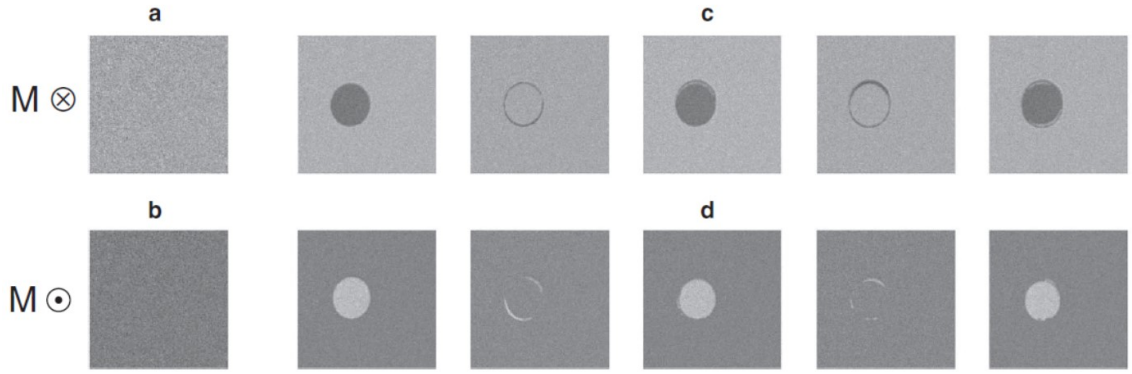

Figure 2.8: The MOKE images obtained in $Gd_{24}Fe_{66.5}Co_{9.5}$ amorphous alloy film after sending a sequence of 100 fs laser pulses. The sample was saturated in two opposite directions (a): 'up' (light grey) and (b): 'down' (dark grey), as represented by the circled dot and cross, respectively. (c) and (d): The film after excitation with N (N = 1,2,3,4,5) pulses with a fluence of 2.30 mJ/cm^2. Each laser pulse was sent to the same circle region of the film.

2.3.1 HI-AOS in Gd-based materials

As a follow-up to the two landmark experiments above, HI-AOS in GdFeCo with perpendicular magnetic anisotropy has been extensively investigated [89–94]. GdFeCo exhibits a phenomenon of magnetization compensation when the Gd content is around 25%, where the coercivity diverges. Although the concentration of Gd at the compensation point is slightly shifted under different thicknesses of the GdFeCo thin film, the single-shot reversals occur within 5% of the compensation point [92, 94]. Only multidomain instead of single shot switching was observed with either too large or too low Gd concentration [95, 96]. For the case of perpendicular magnetic anisotropy, the in-plane demagnetizing field has a large influence on domain formation when far from the compensation point. This is not the same case with in-plane anisotropy, where the single-shot switching occurs with a larger Gd concentration range, that is, between 7.5% and 27.5% [97].

Furthermore, the reversal of spins in both sublattices can be attributed to the transfer of angular momentum between them. However, the transfer of angular momentum might not be sufficient to achieve spin reversal if the Gd concentration deviates (either too large or too low) significantly from the angular momentum compensation point, located close to but distinct from the magnetization compensation point. Zhang et al. [98] and Ceballos et al. [99] respectively studied the single-shot switching behavior and dynamics by dopping Tb rare earth element into GdCo alloy. Increasing Tb content in the GdTbCo alloy leads to the disappearance of magnetization switching due to large damping from Tb. Moreover, the dynamics in TbGdCo alloy, in comparison to GdCo alloy, exhibit a slower behavior attributed to large damping arising from larger spin-orbit coupling in Tb. In terms of spin relaxation following laser-pulse irradiation in RE elements (Gd and Tb), it can occur via different channels. Firstly, spin angular momentum is directly dissipated via scattering between spins and lattices, depending on the value of the orbital moment. Additionally, spin angular momentum can be an indirect transfer between RE (Gd Tb) and TM (Co) sublattices. Consequently, angular momentum can be effectively

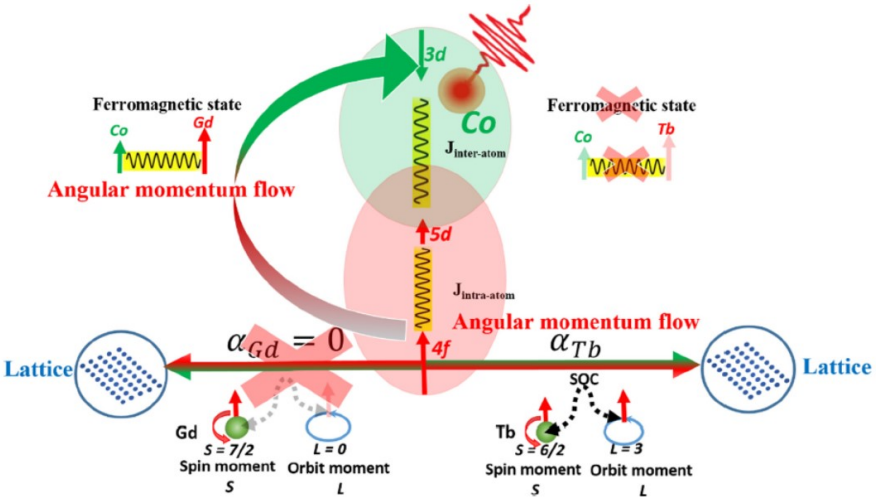

Figure 2.9: Schematic for spin angular momentum dissipation process in RE-TM alloys after infrared laser excitation. Spin angular momentum can be dissipated by lattice, but it depends on the orbital quantum number L. For Gd, this channel is greatly reduced due to L = 0 compared to Tb, where L = 3. Besides, the interaction between RE and TM facilitated by intra-atomic exchange energy provides another spin angular momentum transfer channel.

transferred from Gd to Co, enabling magnetization switching. However, for Tb, dissipation occurs through the lattice due to significant spin-orbit coupling rather than transferring between Tb and Co.

Indeed, thermal single-pulse switching is not limited to ferrimagnetic alloys but is also possible in Gd-based ferrimagnetic multilayers, such as Gd/Co and $[Co/Ni]_N/Gd$ [5,100–106]. More importantly, the single-shot switching observed in synthetic ferrimagnetic bilayers is unaffected by a potential compensation temperature, whereas, in ferrimagnetic alloys, the compensation temperature plays a crucial role. The switching can be observed with a large range of Co layers in the bilayer structure. This is because the magnetic moment switching in the bilayer structure does not occur simultaneously. The inset in Figure 2.10c shows that the Co layers exhibit sequential switching, commencing with the layers closest to the Co/Gd interface. The dynamics of the first Co monolayer are notably influenced by the exchange field originating from the slowly demagnetizing Gd layer. Consequently, the second Co monolayer undergoes switching first. Subsequently, the switch propagates throughout the Co layer, driven by exchange scattering between neighboring Co monolayers. With a front of reversed Co magnetization propagating away from the interface, this successive switching mechanism can succeed independently of the number of Co monolayers and explains why the Co/Gd bilayer can be switched for a relatively large Co thickness. The newfound shows more robust single-pulse switching in synthetic ferrimagnets compared to ferrimagnetic alloys. This highlights the potential of Pt/FM/Gd synthetic ferrimagnets as highly promising candidates for integrating single-pulse AOS in future data storage devices.

Similar to HD-AOS, the state diagram [94], which is the threshold fluences plotted as a function of pulse duration, allows us to optimize the pulse duration and the energy needed to switch a Gd-Fe-Co magnet. As shown in Figure 2.11, the state diagram shows a triangle shape, accompanying lower fluence (F_{switch}) is needed to switch the magnetization with a short laser pulse duration, while the F_{switch} increases with longer pulse duration. However, the multidomain fluence keeps a constant value and is independent of the pulse duration. Thus, single-shot switching can no longer

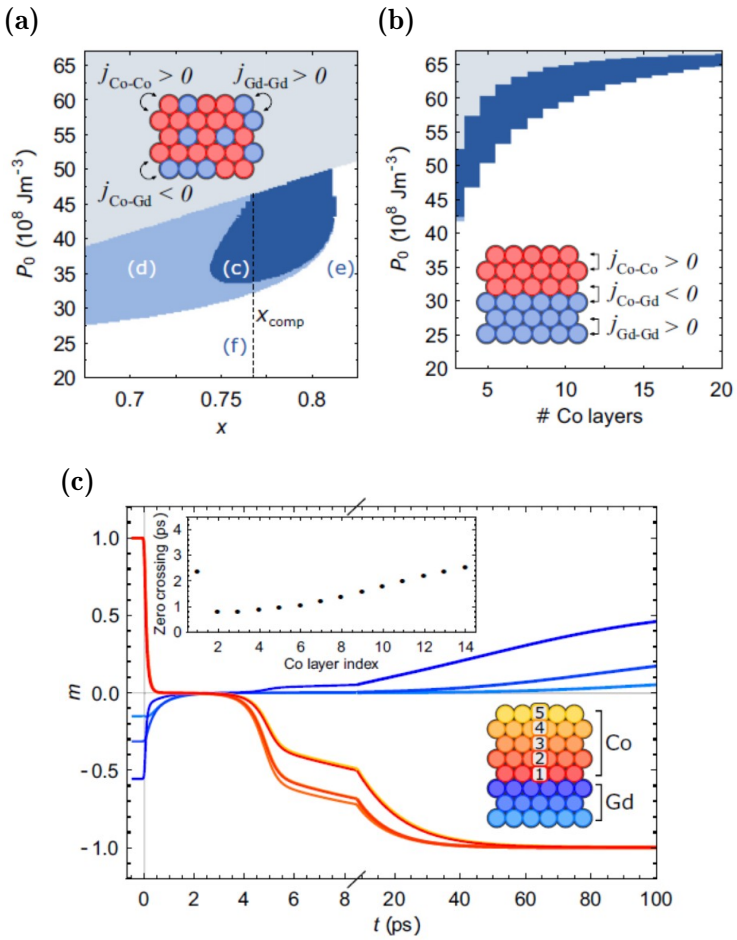

Figure 2.10: Simulated Phase diagram for AOS for (a): $Gd_{1-x}Co_x$ alloy, and (b): Co/Gd bilayer. (c): Laser-induced magnetization dynamics of all atomic monolayers in a Co/Gd bilayer consisting of 5 Co monolayers and 3 Gd monolayers. The inset shows the time at which the magnetization of each Co monolayer is reversed for a system of 14 Co layers and 3 Gd layers. Figure adapted from reference [5]

be observed when the switching fluence reaches the value of multidomain fluence at a certain pulse duration. This maximum pulse duration to show single switching is around 3 ps for GdFeCo alloy. Steil et al. suggested, by performing AO-HIS with 13 ps single laser pulse, that putting the electrons and phonons strongly out-of-equilibrium is not crucial. Gorchon et al. claimed an upper limit of 1 ps for $Gd_{24}(FeCo)_{76}$ against 15 ps for $Gd_{27}(FeCo)_{73}$ [90]. According to them, the slow energy transfer rates between the sublattices were responsible for the short pulse length limit for the lowest concentration of Gd.

2.3.2 HI-AOS in ferromagnets

Since the first observation of single-shot switching in GdFeCo alloy, this type of ultrafast switching has been restricted to ferri-magnetic GdFeCo films for a long period of time. However, by designing the stacks of nanostructure, we can achieve single-shot switching in ferromagnets. For instance, in 2016, Gorchon [90] demonstrated the magnetization switching induced by a single laser pulse in various ferromagnetic Co/Pt multilayers grown on GdFeCo by exploiting the exchange coupling between the two magnetic films. Despite using thick (up to 5 nm) metallic Pt spacers to separate a Co/Pt multilayer from a GdFeCo layer, single-shot AOS of the ferromag-

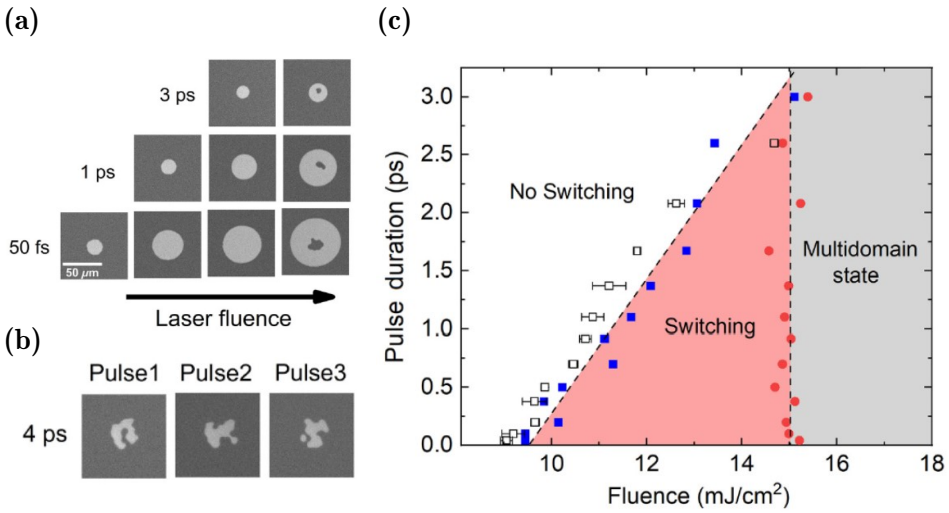

Figure 2.11: Magneto-optical images and all-optical helicity-independent switching state diagram for a 20-nm $Gd_{24}(FeCo)_{76}$ film. MOKE images after exposure to a single linearly polarized laser pulse with (a): pulse durations 50 fs, 1 ps, 3 ps and (b): 4 ps and with various fluences. (c) HI-AOS state diagram: switching fluence F_{switch} and multidomain fluence F_{multi} as a function of the pulse duration. The open squares are the fitting results obtained via the method proposed by Liu et al. [28].

netic layer can still be achieved. When a more conductive space layer such as Cu is employed, the Co/Pt magnetization can still undergo reversal with a larger spacer thickness [95, 107, 108]. In this case, the two magnetic layers are decoupled; thus, the switching in Co/Pt can not be attributed to the short-range exchange coupling.

Choi [109] demonstrated that the ultrafast demagnetization of TM and RE sublattices generate +z and -z spins, and the spin generation rate is proportional to the magnetization decay $-\frac{dM}{dt}$. The spins accumulate in the adjacent non-magnetic layer. As shown in Figure 2.12, the spin accumulation in GdFeCo and TbFeCo alloy show two opposite peaks; one positive peak corresponds to the demagnetization of the ferromagnet, and another negative peak corresponds to the demagnetization of the RE sublattice and spin-dependent Seebeck effect. Remy [95] pointed out that, at short time scales (below 1 ps), the laser heating due to hot carriers coming from other layers [110] will cause the demagnetization of the Co/Pt multilayer. The spin current, whose polarization is set by the Gd magnetization sublattice, interacts with and switches the ferromagnetic layer [109] when the Co/Pt multilayer is demagnetized. It is worth pointing out that the fastest dynamics happen during the demagnetization; thus, no full magnetization reversal of GdFeCo is needed to generate the spin current.

Just this year, Igarashi et al. [111] reported a very exciting result: single laser pulse-induced magnetic moment switching can be achieved in rare-earth-free archetypal spin valves of [Pt/Co]/Cu/[Co/Pt], which is commonly used for current-induced STT switching. Two types of switching have been obtained depending on the laser fluence. At high fluence, a reversal from the antiparallel (AP) to the parallel (P) configuration of the free [Co/Pt] layer (Figure 2.13 middle), while at low fluence, switching from the P state to the AP state was successfully established. In terms of AP to P switching, it can be explained by the spin current generated by the demagnetization of the reference layer, whose sign is opposite to the free layer. Surprisingly, a full switching of the free layer is observed when starting from a P state. Simple angular momentum conservation arguments cannot explain the observation.

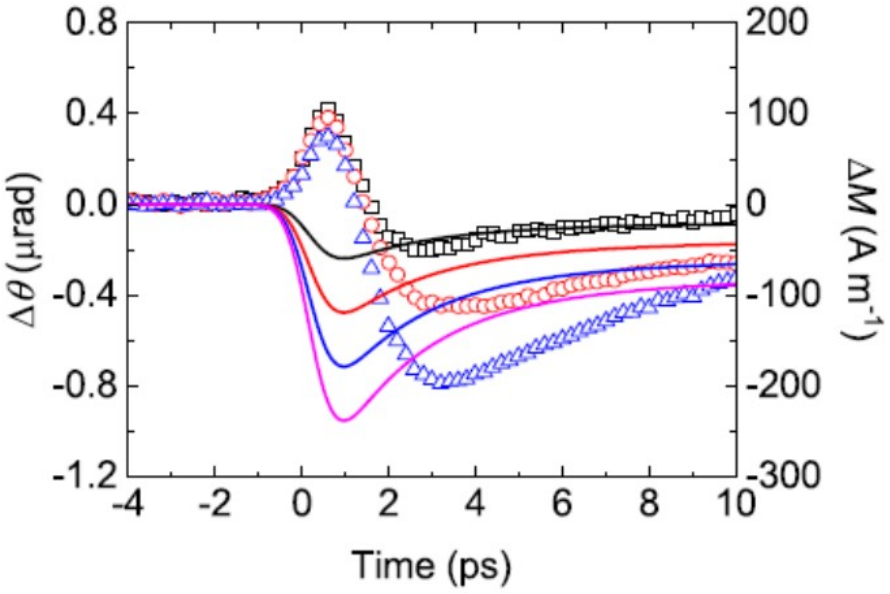

Figure 2.12: Spin accumulation on non-magnetic layer (NM). TR-MOKE measures spin accumulation on the Cu surface of $Tb_{20}Fe_{62}Co_{18}$/Cu (black squares), $Gd_{22}Fe_{68.5}Co_{9.5}$/Cu (red circles), and $Gd_{25}Fe_{65.5}Co_{9.4}$/Cu (blue triangles) samples. Solid lines are from spin diffusion calculation with spin generation from spin-dependent Seebeck effect (SDSE): black, red, blue, and purple lines are results with effective spin-dependent Seebeck coefficient S_S of 4, 8, 12, and 16 $\mu V/K$.

The mechanism for P-to-AP switching is clearly different from the framework of current AOS, and it must be due to some dynamical long-range coupling-spin current, which results in the injection of an opposite spin density (minority spins) into the free layer. The minority spins could originate from the free layer itself and be back-reflected at the interface with the reference layer. such a reflection mechanism is similar to the one observed in current-induced STT switching [112].

2.3.3 HI-AOS in Gd-Free ferrimagnetic materials

In 2020, Banerjee et al. [113] reported the shingle-shot toggle switching in Mn_2Ru_xGa half-metallic ferrimagnetic Heusler alloys, breaking the limitation of achieving single-pulse reversal only within Gd-based materials over a decade since the first observation of HI-AOS. In MnRuGa (MRG), the Mn atoms occupy two inequivalent positions 4a and 4c, with antiferromagnetic coupling between the sublattices [114]. At low temperatures, the magnetization is dominated by Mn(4c), but as temperature increases, it falls faster than that of the Mn(4a) sublattice, leading to a compensation temperature T_{comp}. By changing the Ru content in the alloy, the value of T_{comp} can be varied.

As depicted in Figure 2.14a, the irradiation by a series of laser pulses leads to a toggling of the direction of the magnetization starting from both opposite saturated directions. Although MRG possesses a low net magnetization, hence, a high anisotropy field, toggle switching can be obtained even with a coercivity over 1 T. The dynamic behavior indicates that MRG switches within 2 ps. In GdFeCo, single-shot switching can be obtained when the Gd concentration is near the compensation point, that is, the T_{comp} is near room temperature, both above and below. Partially differing from GdFeCo, switching occurs in MRG only when the starting temperature T_0 is below T_{comp}. Of course, if the starting temperature is

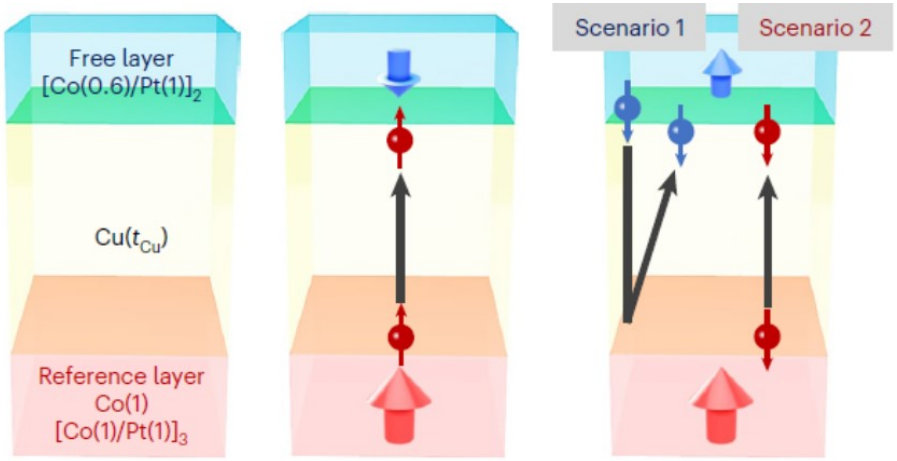

Figure 2.13: Left: Sample structure and schematic illustrations of the switching observed [Co/Pt]/Cu/[Co/Pt]. Values in parentheses are the layer thicknesses in nanometres. Middle and right: Schematic illustration of the process for magnetization reversal starting Middle: from the AP state and Right: from the P state. Blue (red) spin-polarized electrons are generated in the free (reference) layer. Dark grey arrows indicate the direction of electron flow.

room temperature, the switching occurs only in the samples with T_{comp} above room temperature. This can be attributed to the almost the same atomic moments of the two sublattices. Thus, they should not have drastically different response times to laser excitation. If $T_0 < T_{comp}$, the equilibrium thermal dependence of MRG implies $|S_{4a,0}| < |S_{4c,0}|$. Thus the equal demagnetization rates cause equal changes in S_{4a} and S_{4c} ($|\Delta S_{4a}| = |\Delta S_{4c}|$ in Figure 1.18c) and so S_{4a} crosses zero first, with S_{4c} soon to follow. If instead $T_0 > T_{comp}$, we obtain from $|S_{4a,0}| > |S_{4c,0}|$. The pulse-induced 1 : 1 demagnetization rates instead now cause S_{4c} to cross zero before S_{4a}, generating a transient "ferromagnetic-like" state but with reversed polarity. Net switching cannot emerge from this nonequilibrium state because $J_{4c\text{-}4c}$ is three times weaker than $J_{4a\text{-}4a}$; the sublattice with weaker intrasublattice coupling (S_{4c}) cannot drive the sublattice with a stronger intrasublattice coupling (S_{4a}) across the state with zero net magnetization [115, 116].

Also, in 2020, at almost the same time, Avilés-Félix reported the single-shot switching in Tb/Co multilayer-based electrodes with both femtosecond and picosecond laser pulse [51,52]. Interestingly, this single-shot switching was restricted to the Co-dominant region with specific Tb and Co thicknesses. Since the Tb-based material has large anisotropy, it can be a good candidate for future magnetic recording medium. However, as we discussed above, only partial switching of magnetization by a single laser pulse has been obtained in TbCo alloy [117] since the large spin-orbit coupling in Tb, which allows the angular momentum to dissipate to the lattice instead of transfer between Tb and Co sublattices. But with a multilayer structure, we can obtain very nice switching; this may tell us that the switching mechanism in a multilayer structure differs from the one in a Gd-based alloy. Most of this thesis is a continuation of this work, aiming to figure out the ingredients, behaviors, and mechanisms of switching in multilayer structures.

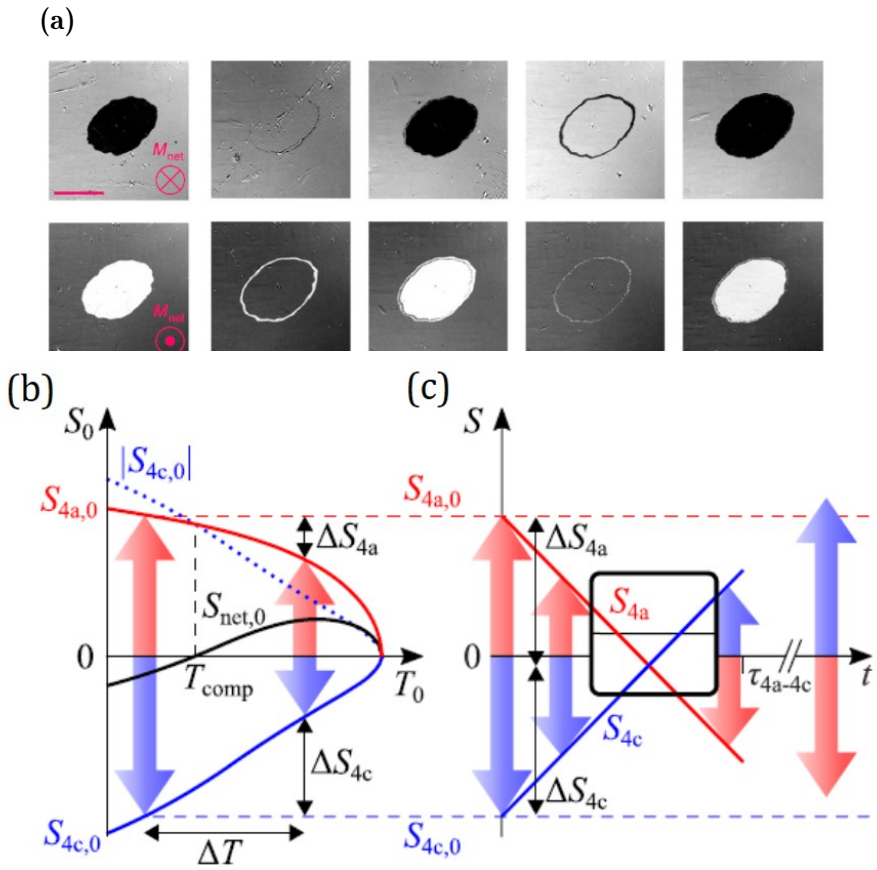

Figure 2.14: (a): Toggle switching of the magnetization in $Mn_2Ru_{1.0}Ga$ with 200 fs single laser pulse, a fluence of 11.6 mJ/cm^2. (b:) Representative equilibrium thermal dependence of angular momentum S in MRG, showing the change in angular momentum of the 4a (red) and 4c (blue) sublattice as the temperature (T_0) varies in equilibrium. (c): The nonequilibrium exchange-driven process of magnetic switching triggered by the 100-fs laser pulse at $T_0 < T_{comp}$.

2.4 Conclusion

We start this chapter by introducing laser-induced ultrafast magnetization demagnetization. After reviewing the conventional magnetization dynamics, we introduced two types of laser-induced magnetization switching, from multiple pulses HD-AOS to HI-AOS. Then, we focus on the single-pulse all-optical switching and its mechanism in different materials. It is intended to serve as a reference and comparison for discussing subsequent work.

Chapter 3

Methodology

This chapter outlines the experimental techniques employed in this thesis. It begins with an introduction to sample growth techniques, emphasizing wedge film architectures and determining wedge sample thickness. The second section covers the femtosecond laser setup and characterization methods for ultrashort pulses. This includes examining magnetic properties, as well as static and dynamic AOS measurements using the Magneto-Optic Kerr Effect (MOKE). The chapter ends with discussing the determination of laser beam size and threshold fluences, which involves analyzing the energy Gaussian distribution of the laser pulse.

3.1 Sample deposition and charactorization

All the samples except the $[Tb/Co]_N$ cross-wedge multilayer used in chapter 4 were grown by the Physical Vapor Deposition (PVD) method in an AJA machine by Professor Michel Hehn. $[Tb/Co]_N$ cross-wedge multilayer was deposited on the silicon substrate in Spintec due to our collaboration UltraFast Opto-magneto-spintronics (UFO) project. Here, I will briefly introduce the PVD techniques, including thermal evaporation, electron beam evaporation, and sputtering.

3.1.1 Physical vapor deposition

Ultra-high vacuum systems are used to deposit thin layers of ultra-high purity materials onto samples and substrates. In order to condense on the surface only the atoms coming from the source of interest made of high-purity materials, deposition is done in high vacuum systems. So, removing the air from the chamber in which the film deposition is done using vacuum pumps is necessary. The atoms come from an ultra-high purity material, which is called the source, and atoms from this source travel through the vacuum in the vacuum chamber and are deposited onto the surface of the substrate. This process is called physical vapor deposition (PVD) and requires the vacuum environments with pressures under 10^{-8} Torr or equivalently 1.3 times 10^{-4} Pascals. High-purity source materials, typically 99.9% or even better, are also required. Three main PVD techniques are thermal evaporation, electron beam evaporation, and magnetron sputtering, depending on how the solid source becomes atoms for deposition.

The first of the three PVD techniques is known as thermal evaporation, which uses heat to evaporate the source from solid to gas. Thermal evaporation is typically used most for metals since its low melting point and produces a pretty steady deposition rate. A large electrical current is used to heat up the source, which is called resistive heating. Once the source material is melted and evaporated, the atoms travel through the vacuum and condense onto the substrate. Thermal evaporation is relatively straightforward and cost-effective, but its lack of precise energy control can lead to variations in film thickness and quality.

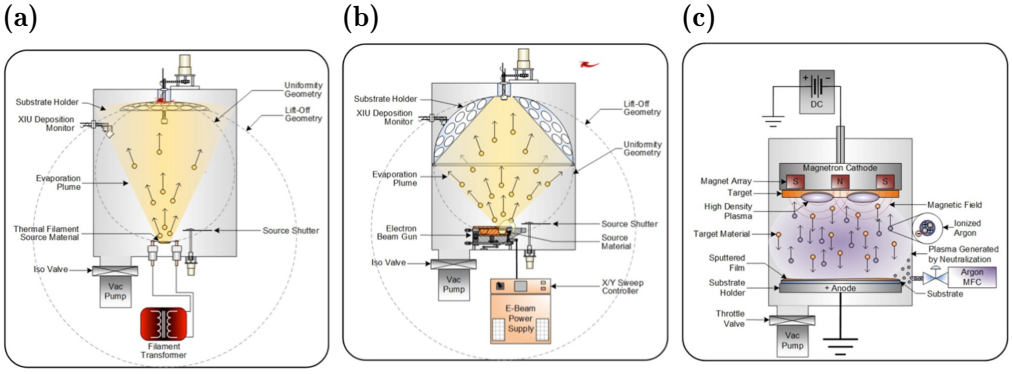

Figure 3.1: Scheme of three main PVD techniques (a): thermal evaporation, (b): Electron beam (Ebeam) evaporation and (c): magnetron sputtering (Here is a up-side-down scheme of magnetron sputtering).

Electrical beam (Ebeam) evaporation is similar to thermal evaporation, but the source material is heated up by a stream electron or an electron beam focused on the source material. One of the advantages of Ebeam evaporation is that we can rotate the different source materials into the path of the electron beam so that we can

deposit multiple materials sequentially without opening the vacuum system. The key advantage of Ebeam evaporation lies in its ability to finely tune the energy of the electron beam, enabling precise modulation of deposition rate and thickness uniformity. This technique is well-suited for applications demanding precise thickness and high film quality, such as semiconductor and optical coatings.

Another PVD technique is sputtering, which is entirely different from the evaporation technique. Sputtering uses energized atoms to hit the source, which is in the form of a plate which is called a target. After pumping the chamber to a high vacuum, typically around 5×10^{-8} Torr, a noble gas such as argon (Ar), is introduced into the vacuum chamber. An electric field is applied in the vacuum chamber, causing the gas to ionize and create a plasma that consists of ions and electrons. Introducing a magnetic field behind the target material effectively confines electrons close to the target surface. The Ar ions are attracted to the target and have enough energy to physically knock off the individual atoms or a group of atoms of the target material. Magnetron sputtering is versatile and can deposit a wide range of materials, and is well-suited for coating complex geometries.

3.1.2 Thickness determination of wedge samples

The samples used in Chapter 5, 6, 7 are wedged samples in thickness or concentration. The wedge samples are deposited by stopping rotating the substrate, resulting in a gradient of thickness or concentration.

Here, we show how to determine the thickness of an elemental layer in a wedge sample. A calibration of the thickness as a function of position has been done beforehand, which allows us to determine the thickness in a calculation way instead of measuring each sample later. The calibration has been done in Glass/Ta(3)/Cu(5)/Gd_{22} $(FeCo)_{78}$(10) /Cu(200, wedge)/Pt(5). Here, the unit of the value in brackets is nanometer (nm), and the thickness for each layer except the Cu layer is uniform everywhere, and the total thickness except the Cu layer is 23 nm. The wedge-shaped Cu sample was deposited on two pieces of glass substrat spanned 25 mm each. At the position of 25mm, the thickness is targeted to be 200 nm. Thus, the total thickness at 25 mm is 223 nm. Using atomic force microscopy (AFM), we measured the total thickness as a function of the position and plotted it in Figure 3.2b. Then, we subtract the total thickness of other layers and fit the plotting linearly. The variation of the Cu thickness of Cu was fitted as

$$t_{\mathrm{Cu}} = 100.9 + 3.83x$$

where x is the position in mm, and the t_{Cu} is in nm. Thus, the thickness t in the wedge can be obtained by

$$t(x) = \frac{100.9}{200} \times t_{25\mathrm{mm}} + t_{25\mathrm{mm}} \times \frac{3.83}{200} \times (50 - x)$$

where $t_{25\mathrm{mm}}$ is the targeted thickness at 25 mm. The certainty of the thickness is thus

$$\Delta t_x = t_{25\mathrm{mm}} \times \frac{3.83}{200} \times \Delta x$$

where Δx is the uncertainty of the position. Δx is estimated to be 0.1 mm, Therefore, $\Delta t_x \approx 0.002 \times t_{25\mathrm{mm}}$. Since the variation of thickness spanning 25 nm is less than 5 nm, thus $\Delta t_x < 0.01$ nm. So, the layer thicknesses are quoted to hundredths of nanometers.

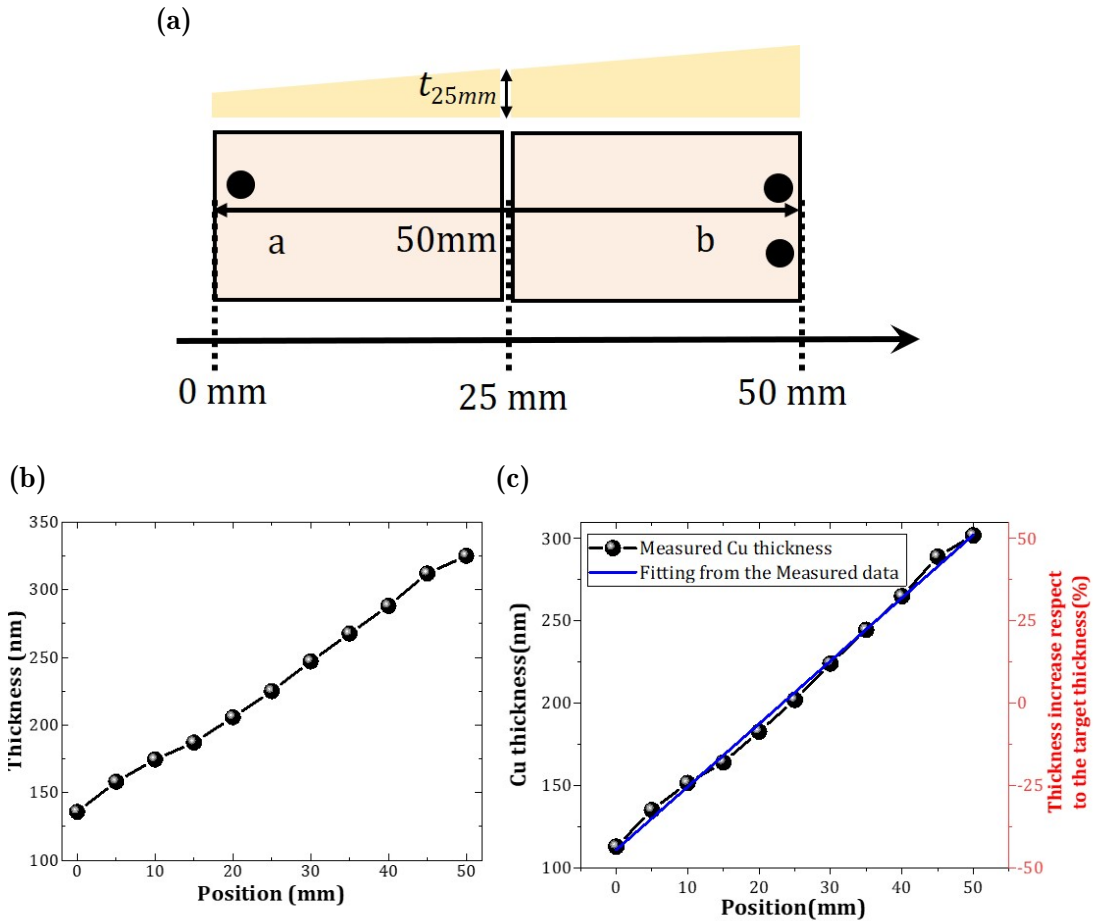

Figure 3.2: Calibration of the wedge deposition thickness. (a): Scheme of thickness wedge sample; (b): measured total thickness of Glass/Ta(3)/Cu(5)/$(CoFe)_{78}Gd_{22}$(10)/Cu(200 nm, wedge)/Pt(5); (c): Variation of the thickness of a thick Cu wedge as a function of position.

Next, let's look at the determination of the concentration gradient. Here, I will show an example of Glass/Ta(5)/Pt(5)/($Tb_{32}Co_{68}$(4)/GdCo(2nm, wedge in concentration around 10/90)/$Tb_{32}Co_{68}$(4)/Ta(5)/Pt(1). The thickness of GdCo alloy and Gd concentration at 25 mm are around 2nm and 10%, respectively. First, we must know the deposition time and deposition rate of each element. For this sample, the deposition time is 22.6 s; the deposition rate for Gd and Co elements are 0.021022 nm/s and 0.06666 nm/s, respectively. So, the thicknesses of Gd and Co at 25 mm are 0.475 nm and 1.507 nm [1]. Thus, the Gd and Co thickness as a function of position can be estimated as:

$$t_{\mathrm{Gd}}(x) = \frac{100.9}{200} \times t_{25\mathrm{mm,\ Gd}} + t_{25\mathrm{mm,\ Gd}} \times \frac{3.83}{200} \times x$$

$$t_{\mathrm{Co}}(x) = \frac{100.9}{200} \times t_{25\mathrm{mm,\ Co}} + t_{25\mathrm{mm,\ Co}} \times \frac{3.83}{200} \times x$$

Then, the volume percentage of Gd and Co, $vl_{\mathrm{Gd}}(\%)$ and $vl_{\mathrm{Co}}(\%)$ can be determined by using their thicknesses divided by the total thickness since the area of the

[1] Note that the thickness is an equivalent single Gd or Co layer.

cross-section for Gd and Co are the same.

$$vl_{\mathrm{Gd}}(\%) = \frac{t_{\mathrm{Gd}}}{t_{\mathrm{Gd}} + t_{\mathrm{Co}}} \times 100$$

$$vl_{\mathrm{Co}}(\%) = \frac{t_{\mathrm{Co}}}{t_{\mathrm{Gd}} + t_{\mathrm{Co}}} \times 100$$

Thus, the atomic percentages of Gd and Co are:

$$at_{\mathrm{Gd}}(\%) = \frac{vl_{\mathrm{Gd}}(\%)/\beta_{\mathrm{Gd}}}{vl_{\mathrm{Gd}}(\%)/\beta_{\mathrm{Gd}} + vl_{\mathrm{Gd}}(\%)/\beta_{\mathrm{Co}}}$$

$$at_{\mathrm{Co}}(\%) = \frac{vl_{\mathrm{Co}}(\%)/\beta_{\mathrm{Co}}}{vl_{\mathrm{Gd}}(\%)/\beta_{\mathrm{Gd}} + vl_{\mathrm{Gd}}(\%)/\beta_{\mathrm{Co}}}$$

where the β^{Gd}= 19.9 $\times$ 10^{-6} m^3/mol and β_{Co}= 6.67 $\times$ 10^{-6} m^3/mol are the molar volume of Gd and Co, respectively.

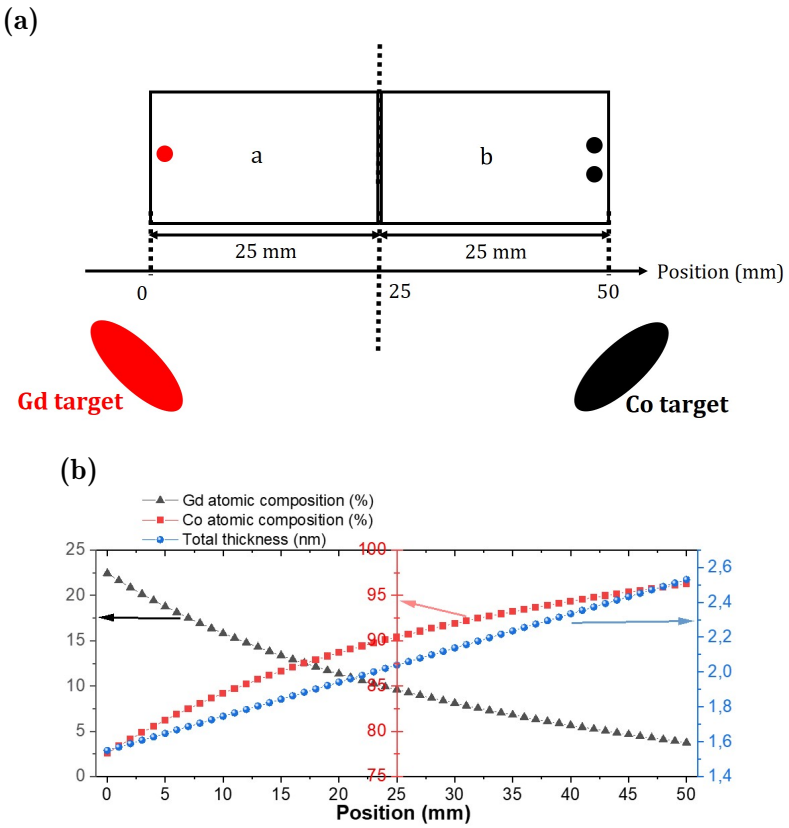

Figure 3.3: (a): Scheme of thickness and concentration wedge sample; (b): Variation of the thickness and concentration of Gd and Co as a function of position in Glass/Ta(5)/Pt(5)/($Tb_{32}Co_{68}$(4)/GdCo(2nm, wedge in concentration around 10/90)/$Tb_{32}Co_{68}$(4)/Ta(5)/Pt(1).

The Gd and Co atomic percentage and the thickness of the GdCo alloy thin film can be calculated and shown in Figure 3.3b. The Gd concentration varies from 22.4% on the left side to 3.7% on the right side, while the total thickness linearly increases from 1.55 nm to 2.54 nm.

3.2 Magneto-optical Kerr effect

The Magneto-Optical Kerr Effect (MOKE) is a phenomenon in physics involving light interaction with magnetic materials. This effect was first discovered by Scottish scientist John Kerr in the 19th century [118, 119] and is particularly widely used in studying magnetic properties. Many of the techniques used in this thesis are based on the Kerr effect.

Much like the Faraday effect, the Kerr effect occurs when light encounters a magnetic material. While the Faraday effect describes transmitted light, the Kerr effect describes the physical effect on the reflected light. The linearly polarized light, which is reflected from the magnetic surface, becomes ellipsoidally polarized, and a rotation of the polarization's principal axis occurs. The rotation of this axis is referred to as the Kerr rotation and is proportional to the magnetization of the reflecting surface.

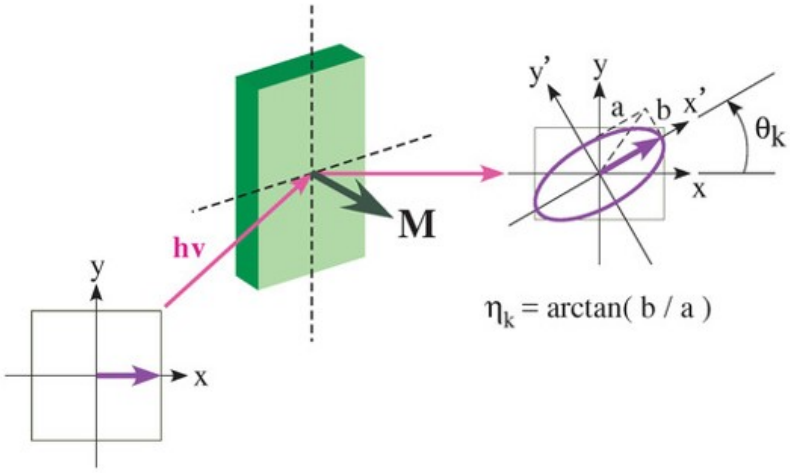

Figure 3.4: Illustration of the (polar) magneto-optical Kerr effect (MOKE). Linearly-polarized light with a photon energy of hv becomes elliptically polarized after reflection from a magnetized material with magnetization (M), and the main polarization plane is tilted by a small angle θ_k with respect to that of the incident light. The ellipticity of the reflected light is quantified using $\eta_k = \arctan \frac{b}{a}$.

The orientation of the magnetization vector can be obtained using different components of the MOKE [120]. The three basic configurations of the magnetization vector with respect to the input light polarization, the plane incidence, and the sample plane are usually distinguished as follows: (i) the polar MOKE (P-MOKE), where the component of the magnetization is perpendicular to the sample plane; (ii) the longitudinal Kerr effect (L-MOKE), where the in-plane component of the magnetization is parallel to both the sample plane and the plane of incidence of the light; (iii) the transverse Kerr effect (T-MOKE), where the in-plane component of the magnetization is perpendicular to the plane of incidence. The polar MOKE and longitudinal MOKE are based on polarization analysis because the polarization of the reflected light rotates, and its ellipticity changes. The transverse MOKE involves intensity measurements and is based on the fact that the polarization states of the reflected light do not change from the corresponding states of the incident light.

3.2.1 MOKE magnetometer

The MOKE magnetometer is very convenient used to characterize the coercivity and magnetic anisotropy. For all the samples studied in this thesis, we focus on perpen-

Name	(a) Polar	(b) Longitudinal	(c) Transverse
Geometry	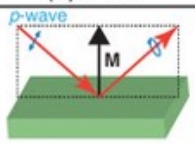	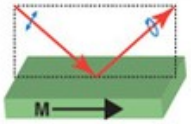	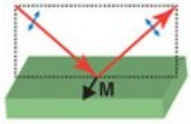
Detection	Out-of-plane	in-plane	in-plane
Polarization Variation	Rotation Ellipticity 		None 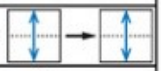
Measurement	Polarization Analysis		Intensity measurement

Table 3.1: Schematic diagram of MOKE measurement geometry for p-polarized incident light. The dashed line in the geometry row expresses the incident plane. In the polarization variation row, the changes in the polarization state that are projected in the plane that lies perpendicular to the direction of the travel of the light are shown for both incident (left) and reflected light (right).

dicular magnetic anisotropy (PMA); thus, a polar MOKE magnetometer shown in Figure 3.5 is employed to demonstrate the magnetic properties.

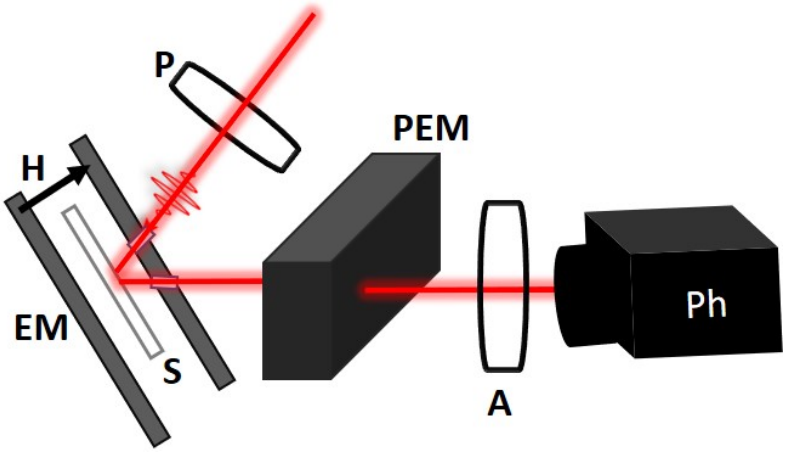

Figure 3.5: Scheme of polar MOKE magnetometry setup with the following elements: electromagnet (EM); polarizer (P); sample (S); photoelastic modulator (PEM); analyzer (A) and photodetector (Ph).

A helium-neon (He-Ne) laser generates a linearly s-polarized beam, which is reflected by the sample and then passed through a photoelastic modulator (PEM) with a vibration axis parallel to the table. Subsequently, the beam traverses an analyzer set at a 45° angle to the PEM axis before being detected by a photodetector. The PEM frequency is 50kHz and is used as a reference frequency for a lock-in amplifier. The photodetector signal is fed into the input of the lock-in amplifier. By varying the external magnetic field using an electromagnet, hysteresis loops can be measured. Notably, the lock-in amplifier outputs a complex signal, but only the real part (X signal) is utilized, with the possibility of adjusting the lock-in internal phase to optimize signal reception, facilitating precise analysis and characterization of the magnetic properties.

In the investigation of ferrimagnetic alloys, where the determination of whether a signal should be positive or negative for a given external magnetic field is ini-

tially uncertain due to the monitoring of transition metal (TM) alone, a calibration approach is adopted. The phase of the lock-in is calibrated with a ferromagnetic [Co/Pt] multilayer or a GdFeCo alloy, for example, well below its compensation composition, such that the output signal is positive at positive external magnetic fields.

More importantly, most of the samples studied in this thesis are wedge samples with a gradient in thickness. Thus, the MOKE magnetometer is a very convenient tool to characterize the magnetic properties by moving the sample in space within millimeters (mm).

3.2.2 MOKE microscopy

MOKE microscopy is a specialized imaging technique that combines the principles of the Magneto-Optical Kerr Effect with microscopy to visualize and study the magnetic properties and domain structures of materials at the microscale and nanoscale. Combining with a laser source, we can observe the laser-induced magnetic domains with MOKE microscopy.

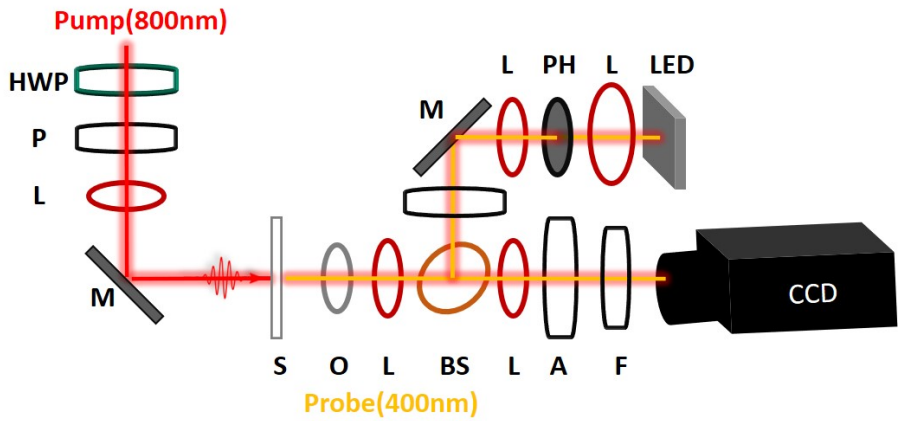

Figure 3.6: Scheme of MOKE microscopy set-up with the following elements: half wave-plate (HWP); polarizer (P); lens (L); mirror (M); sample (S); objective (O); beam splitter (BS); analyzer (A); filter (F); pin hole (PH); light emitting diode (LED) and charge-coupled device (CDD). The scheme shows a transmission mode, where the pump laser excitation was sent on one side, while the probe laser was on the other side.

Ti:sapphire femtosecond-laser source and regenerative amplifier were used for the pump laser beam in AOS measurement. The wavelength and repetition rate of the femtosecond laser are 800 nm and 5 kHz, respectively. A pulse picker is employed to direct a single laser pulse, previously linearly polarized, through a half-wave plate and a polarizer, allowing precise control over the laser pulse fluence. The focused laser pulse interacts with the sample, while a light-emitting diode (LED) light probe source with a wavelength of 628 nm is used for capturing MOKE images. The emitted light is collected through a Fresnel lens and directed through a field diaphragm, followed by collimation by a lens. After linear polarization via a polarizer and transmission to the microscope objective via a beam splitter and lens, the light reflects off the magnetic sample, acquiring Kerr rotation and ellipticity. It retraces its path, partially passes through the beam splitter, and is refocused on the objective with a lens. To prevent laser light from reaching the Charge Coupled Device (CCD), a filter is inserted, along with an analyzer placed before the filter to complete the MOKE measurement. Crucially, the polarizer and analyzer must be nearly perpendicular

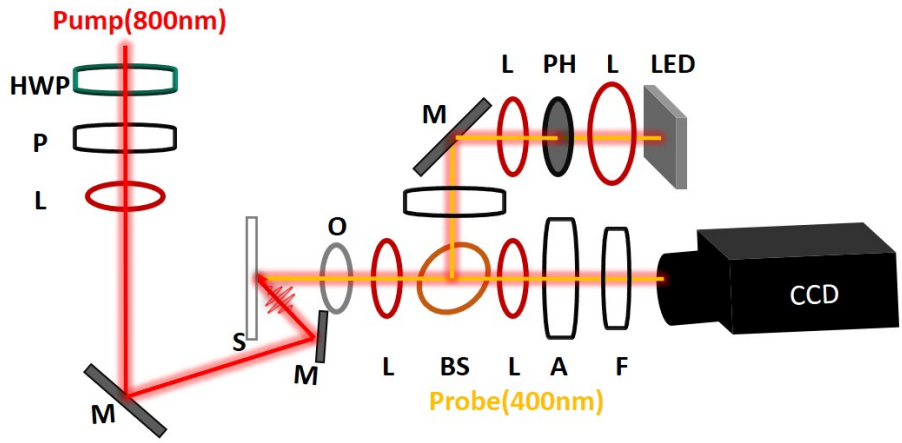

Figure 3.7: Scheme of MOKE microscopy set-up with reflection mode, where the pump laser excitation and probe laser were on the same side.

to prevent undesired light, unaffected by Kerr rotation, from reaching the CCD. No light will be transmitted to the CCD if the polarizer and analyzer are perfectly crossed [121].

3.2.3 Time-Resovled MOKE

Time-resolved MOKE is based on the pump-probe technique, which involves using two precisely timed laser pulses—an initial "pump" pulse and a delayed "probe" pulse to study fast and transient processes in a sample. The pump pulse excites the sample or triggers a specific event, while the probe pulse is used to monitor the consequences or changes induced by the pump pulse. A typical pump-probe setup includes an ultrafast laser source that generates both the pump and probe pulses. The pump pulse is modulated to excite the sample, while the probe pulse is delayed by a variable time interval and directed onto the sample. Changes in the probe pulse are measured using detectors. By varying the time delay between the pump and probe pulses, researchers can create time-resolved data to investigate the dynamics of interest.

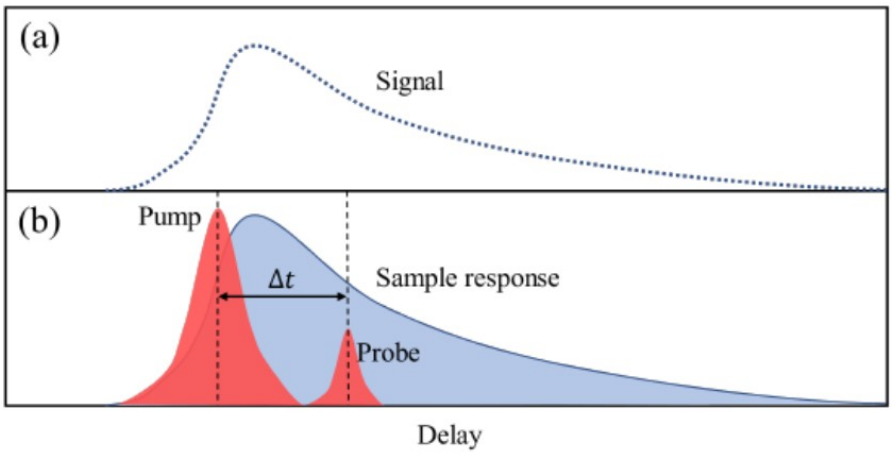

Figure 3.8: The idea of pump-probe technique for TR-MOKE, the magnetization dynamics can be detected by changing the delay time δt between the pump pulse and probe pulse.

Time-resolved MOKE combines the principles of the MOKE with ultrafast laser technology to investigate and capture the dynamics of magnetization in materials

on extremely short timescales, normally femtosecond and nanosecond time scales.

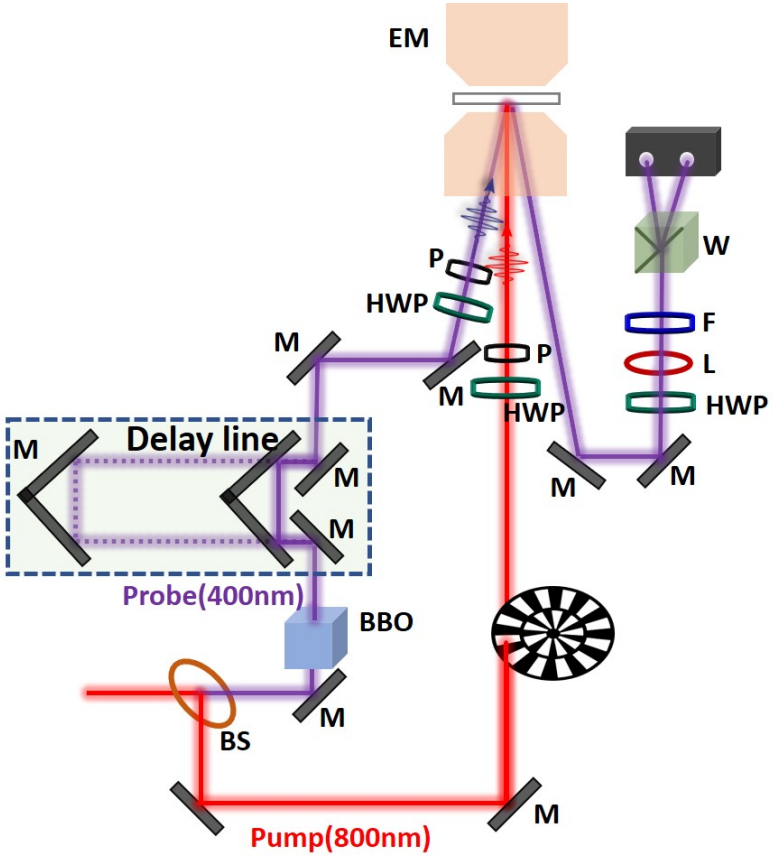

Figure 3.9: TR-MOKE setup with the following elements: half wave-plate (HWP); polarizer (P); chopper (C); sample (S); electromagnet (EM); mirror (M); lens (L); filter (F); Wollaston prism (W); balanced photodiodes (BP). The beam splitter separates the original beam 800 nm into two beams. The probe beam 400nm is generated via second harmonic generation with a barium borate crystal (BBO). The probe angle of incidence has been exaggerated for the purpose of illustration.

The laser continuously sends pulses at a repetition rate of 5kHz, which are then split into two beams via a beam splitter. Allowing one beam to travel a different distance from the beam splitter to the sample makes it possible to introduce a time delay between the arrival of one pulse on the sample and the other. Subsequently, one pulse serves as the "pump", initiating out-of-equilibrium magnetization dynamics, while the other acts as the "probe", capturing the dynamics. The probe beam 400nm is generated via second harmonic generation with a barium borate crystal (BBO). The high-energy pump beam is modulated by changing the rotation speed of the chopper. A half-wave plate and a polarizer are used to control the pump and probe beam powers. The probe power is fixed by the balanced photodiode linear response power threshold, while the pump power varies depending on the measurement. Both beams are focused on the sample, at nearly normal incidence, using spherical mirrors such that the beam spot of the pump is roughly ten times higher than the probe beam spot. This ensures that the probed area corresponds to a roughly uniform pump fluence. The probe signal is then collected and collimated using another spherical mirror and subsequently focused onto a balanced photodiode with a lens and a Wollaston prism. Using the Wollaston prism allows for the separation of the s and p components of the electric field, and a half-wave plate is employed to balance the signal on the photodiodes. The output differential signal is transformed

into a digital signal after the frequency-selective filtering of a lock-in amplifier, and collected by the computer in the end.

3.2.4 Time-resovled MOKE microscopy

Another setup has been used on the Yb laser, which is similar to the standard TR-MOKE setup except that it is also spatially resolved [122, 123]. Compared to standard TR-MOKE, (i) an analyzer and camera replace the balanced detector to obtain spatially resolved domain contrast images; (ii) the probe beam is defocused so as to be much larger than the pump spot, such that pump-induced contrast changes can be observed relative to an unperturbed background. The insertion of two OPAs (Optical Parametric Amplifier) allows us to tune the wavelengths of both the pump and probe beams; the pump laser pulse has a wavelength of 800 nm, while the probe laser pulse has a wavelength of 515 nm. The repetition rate is adjustable with a maximum frequency of 100 kHz. To avoid the accumulation of heat in the sample and consequent damage resulting from several pump-probe pulse pairs incident on the same spot and to get the best contrast simultaneously, we usually set a certain repetition frequency and then continuously irradiate the sample for more than 30 minutes without adding a magnetic field. In practice, both OPAs provide ultrafast laser pulses whose duration ranges from 100 fs to 200 fs, depending on the wavelength.

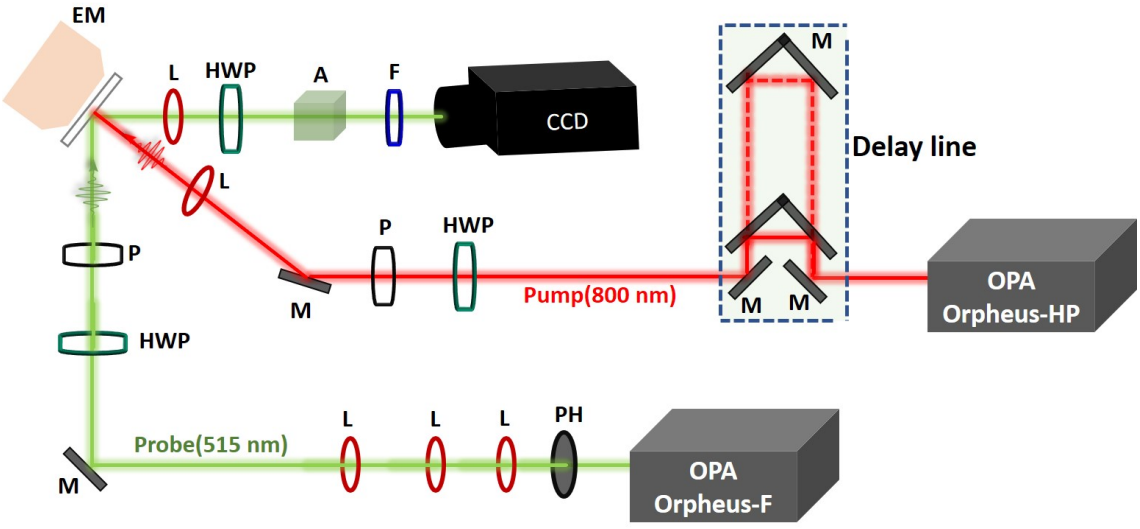

Figure 3.10: TR-MOKE microscope setup with the following elements: half wave-plate (HWP); polarizer (P); sample (S); electromagnet (EM); mirror (M); lens (L); filter (F), charge-coupled device (CCD); pin hole (PH).

This TR-MOKE microscopy is a combination of TR-MOKE and MOKE microscopy, allowing for both time-resolved dynamic observations and static measurements within a single experimental setup. Besides, the probe beam angle of incidence is around 45 degrees, which makes it sensitive to both in-plane and out-of-plane magnetization components, allowing us to investigate the laser-induced magnetization switching with in-plane anisotropy [97]. Moreover, one of the main advantages of TR-MOKE microscopy is that we can have access to a complete set of fluence-dependent dynamics in one measurement according to the spatial Gaussian distribution of the pump beam profile.

3.3 Data analysis

Now, let's look at how we analyze the data obtained on the MOKE microscopy and TR-MOKE microscopy. For static single laser switching measurements, the sample was saturated using a strong external magnetic field and was recorded as the raw background. Raw images and subtracted images obtained after sending femtosecond laser pulses on a $Gd_{22}(FeCo)_{78}$(15 nm)/Cu(4 nm)/[Co(0.6 nm)/Pt(1 nm)]×3 [2], which exhibits AO-HIS, are shown in Figure 3.11. In order for readers to see the magnetic domain image more intuitively, only the background-subtracted images will be shown in the rest of the thesis. The scale bars are determined thanks to a prior calibration using patterned samples with known dimensions.

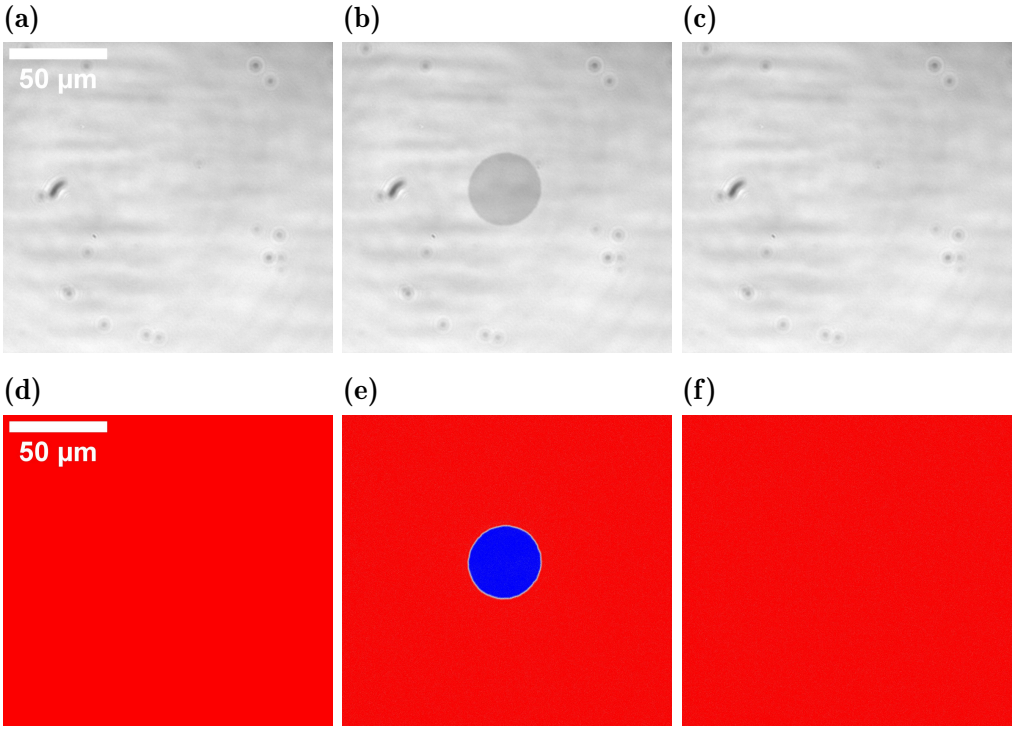

Figure 3.11: (a-c): Raw images and (d-f): subtracted images observed by MOKE microscopy in Si/SiO/Ta(5)/Cu(20)/Ta(5)/Cu(5)/$Gd_{22}(FeCo)_{78}$(15)/Cu(4)/[Co(0.6)/Pt(1)]×3/Ta(5). Unit of the value in the brackets is nm. The images are recorded after being saturated by a magnetic field (a) and (c), after sending the first (b) and (e), and second (c) and (f) 50 fs laser pulse with the energy of 0.9 µJ.

3.3.1 Laser spot size determination

The Gaussian beam size was determined in two ways: by directly observing the beam at the focal plane of the microscope's lens (Used for imaging) and by using the domain size vs. pulse energy fit. For samples grown on the glass substrate, pump laser excitation was done on one side of the sample, and MOKE microspore observation was on the other side (Transmission configuration, see Figure 3.6). Both

[2]The MOKE hysteresis loop of this spin valve structure shows perpendicular anisotropy and only one step switching of the magnetization with the magnetic field up to 2000 Oe. Considering the anisotropy of Co/Pt multilayer and GdFeCo alloy, the two layers on both sides of Cu show the same coercivity. Thus, we couldn't distinguish which layer switched. However, it is not important here since we just use this sample to show how we record the images and how we determine the threshold fluence and beam size later.

methods make it possible to determine the beam size and provide consistent results. The pump and probe light are both on the sample side (Reflection configuration, see Figure 3.7) for samples grown on the silicon substrate. In this case, the beam size was only obtained by fitting the domain size vs. pulse energy.

3.3.2 Observation with a microscope.

A typical beam spot, corresponding to a fixed distance z, observed using the microscope setup is shown in Figure 3.12a. The light intensity can be extracted and plotted as a function of spatial distance, shown in Figure 3.12b. The spatial intensity can be fitted with the Gaussian formula

$$y = y_0 + Ae^{-(\frac{x-x_c}{\sigma})^2}$$

which confirms the spatial Gaussian distribution of the laser pulse.

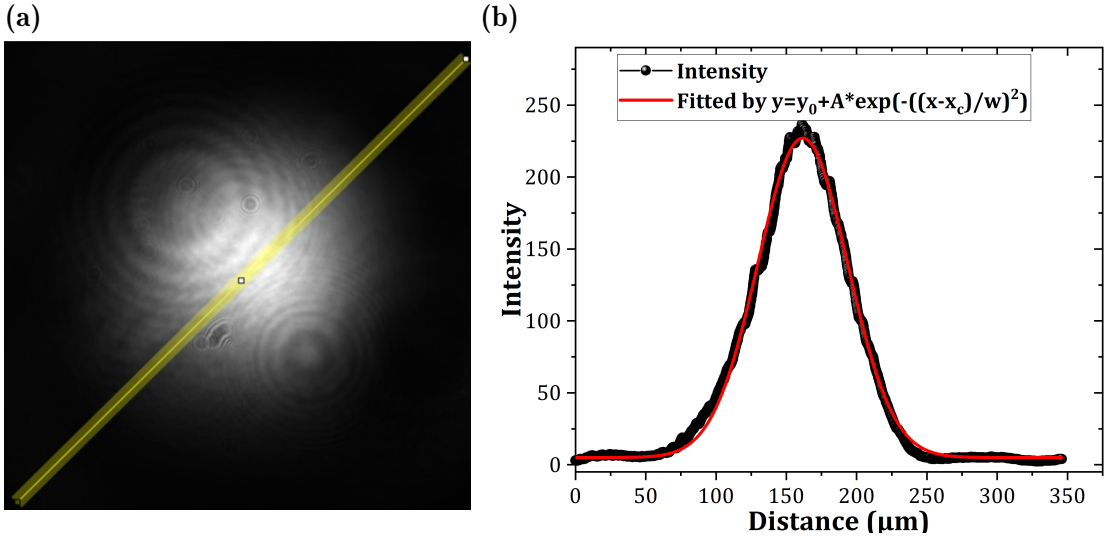

Figure 3.12: (a): Beam spot observed with a microscope. The diffraction fringes come from dust on the optics. (b): Spatial Intensity.

Considering a two-dimensional standard Gaussian energy spatial distribution of an ultrafast laser pulse, it is typically described by the following equation, which represents the spatial intensity profile of the laser beam:

$$I(x,y) = I_0 e^{-(\frac{x}{2\sigma_x})^2-(\frac{y}{2\sigma_y})^2} \tag{3.1}$$

Where:

- *I(x,y)* is the intensity at coordinates (x, y) within the beam profile;
- I_0 is the peak intensity at the center of the beam;
- σ_x and σ_y are the standard deviations that determine the width of the beam in the x and y axes (long and short axes). The beam shape is round if $\sigma_x = \sigma_y$, while it is elliptical is $\sigma_x \neq \sigma_y$

Let's consider the case when $\sigma_x = \sigma_y$, the energy profile is:

$$I(x) = I_0 e^{-(\frac{x}{\sigma_x})^2} \tag{3.2}$$

Using $\int_{-\infty}^{+\infty} e^{-a(x+b)^2} dx = \sqrt{\frac{\pi}{a}}$, the total energy of the laser pulse is obtained by integrating the energy distribution:

$$E_{total} = \int_{-\infty}^{+\infty} I_0 e^{-(\frac{x}{\sigma_x})^2} dx = I_0 \sigma_x \sqrt{\pi} \tag{3.3}$$

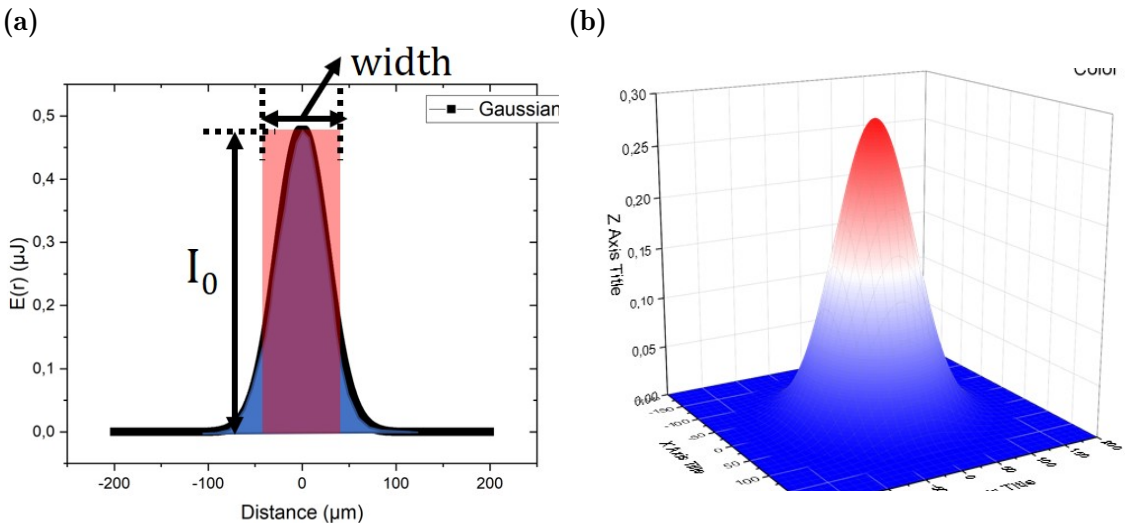

Figure 3.13: (a): One- and (b): two-dimensional Gaussian laser beam. The beam size is defined by making the integration of the Gaussian profile (blue area) equal to the area of rectangular (red area) where its height is the peak intensity I_0.

The width of the rectangular area (red area) is determined by making the integration of the Gaussian profile (blue area) equal to the area of the rectangular where its height is the peak intensity I_0.

$$width = \sigma_x \sqrt{\pi} \tag{3.4}$$

Considering a two-dimensional Gaussian profile, the area covered by the rectangle corresponds to the size of the laser beam, namely:

$$S = \sigma_x \sqrt{\pi} \times \sigma_x \sqrt{\pi} = \pi \sigma_x^2 = \pi \sigma^2 \tag{3.5}$$

where S is the beam area. Thus, σ is the beam radius of a round shape Gaussian. While

$$S = \pi \sigma_x \sigma_y \tag{3.6}$$

if $\sigma_x \neq \sigma_y$ with an elliptical beam shape.

It's important to emphasize that variations in the coefficients of the exponential function will impact the value of sigma in the Gaussian equation. Therefore, when applying the Gaussian formula for fitting, it's essential to maintain a coefficient of 1 for the exponential function. However, when dealing with a specific intensity distribution, the full width of half maximum (FWHM) remains constant, regardless of the coefficient value, as long as the distribution adheres to the Gaussian formula.

$$\frac{I_0}{2} = I_0 e^{-(\frac{\frac{FWHM}{2}}{\sigma})^2} = I_0 e^{-(\frac{FWHM}{2\sigma})^2} \tag{3.7}$$

Thus,

$$\sigma = \frac{FWHM}{2\sqrt{\ln 2}} \tag{3.8}$$

***Remember that FWHM is the full width of half maximum of the laser profile, and σ is the radius of the laser beam.**

In the case of Figure 3.12, the beam radius σ obtained with the camera is $46.9 \pm 0.4\mu m$.

3.3.3 Fitted threshold fluence and beam size.

This method assumes that something happens once the energy is above a certain threshold fluence (or threshold energy). Because of the spatial Gaussian beam profile, the material does not receive the same amount of energy everywhere. Magnetization will only reverse where the local energy exceeds its threshold energy.

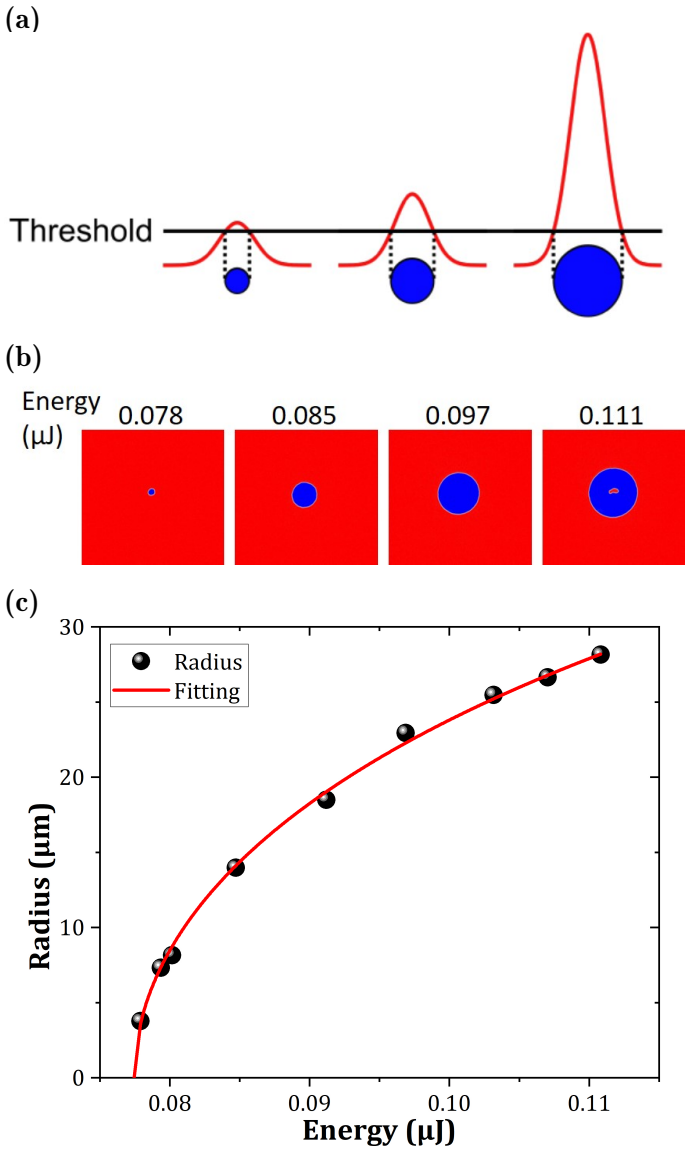

Figure 3.14: (a): Illustration of the reversed domain above a threshold energy. (b): reversed domains when the amplitude of the Gaussian intensity profile increases. (c): Reversed magnetic domain radius as a function of the incident laser pulse energy. Domains obtained in the sample $Gd_{22}(FeCo)_{78}$(15 nm)/Cu(4 nm)/[Co(0.6 nm)/Pt(1 nm)]×3.

The measured laser incident fluence was calculated using

$$F = \frac{P}{fS} \tag{3.9}$$

where P is the measured power, f is the repetition rate of the laser ($f = 5$ kHz), and S is the beam spot area. For transmission configuration, the beam spot area is

$$S = \pi R^2 \tag{3.10}$$

where $R = \sigma$ is the radius of the beam spot and equals $\frac{FWHM}{2\sqrt{\ln 2}}$, where FWHM is the laser spatial full-width of half-maximum. So, the measured fluence F is defined such that the power of the laser is divided by a factor e^2 at a distance from the center of the beam:

$$\overline{F} = \frac{P}{f\pi R^2} \tag{3.11}$$

The fluence profile has the following form:

$$F(r) = 2\overline{F}e^{-(\frac{r}{R})^2} \tag{3.12}$$

where r is the domain radius. The peak value is then twice its measured value. A magnetic domain appears as soon as the fluence peak value exceeds a certain threshold value $\mathrm{F_{th}}$. When this happens, one would measure a fluence $\overline{F} = \frac{F_{th}}{2} = \overline{F}_{th}$. The domain radius must verify the following equation:

$$F(r) = F_{th} \Longleftrightarrow r = R\sqrt{\ln(\frac{\overline{F}}{\overline{F}_{th}})} \tag{3.13}$$

Considering equation 3.11, the threshold powers, as well as beam spot radius, can be extracted as a fitting parameter:

$$r = R\sqrt{\ln(\frac{P}{f\pi R^2 \cdot \overline{F}_{th}})} \tag{3.14}$$

For the reflection configuration, the domains as well as the beam spot, are elongated due to an angle of incidence of 45°. We use the following equation to extract the threshold powers and beam spot area as a fitting parameter:

$$a = S\ln(\frac{P}{fS\overline{F}_{th}}) \tag{3.15}$$

where a is the domain area, while S is the beam area.

If our sole objective is to determine the threshold fluence $\overline{F}_{th}$, we can employ either the magnetic domain radius or the magnetic domain area and fit it using Equation 3.15. However, when aiming to characterize the energy distribution, we must employ the magnetic domain radius for fitting the spot size. Furthermore, in cases of an elliptical spot, such as in a reflection configuration, we can rewrite Equation 2.14 as follows:

$$r_{x/y} = R_{x/y}\sqrt{\ln(\frac{P}{f\pi R_x R_y \cdot \overline{F}_{th}})} \tag{3.16}$$

where $R_x = \sigma_x$, $R_y = \sigma_y$ correspond to the beam spot radius along x and y directions, respectively.

As shown in Figure 3.14b and 3.14c, the domain radius has been extracted and plotted as a function of energy. Using Equation 3.14 [3], the beam radius can be derived as a fitting parameter of $47.1 \pm 0.4 \mu m$, which agrees with the value obtained by observation.

3.4 Nanofabrication

The nanofabrication of the dense dot array studied in Chapter 4 was done by Dr. Danny Petty Gweha Nyoma using the same techniques in his thesis [93].

3.5 Conclusion

The chapter presented the methodology that involves this work. We first explain the three mains of physical vapor deposition techniques. Then, we introduced the thickness determination of wedge samples, including thickness wedge and concentration wedge. After that, four MOKE characterization setups have been briefly introduced. Finally, we show the details of laser characterization, especially the spatial energy distribution and the laser beam size.

[3] Equation 3.14 was rewritten as $r = R\sqrt{\ln(\frac{E}{\pi R^2 \cdot \overline{F}_{th}})}$ with energy.

Chapter 4

Laser single shot reversal in CoLu nanostructures

This chapter presents the first work on CoLu thin film where Lu has zero orbits angular momentum, which is the same as Gd. The perpendicular anisotropy and magnetic properties have been optimized first. Then, single-shot switching measurements were done in full film and dense nanodots; consequently, domain properties were extracted from the MOKE images to determine the switching probability. By atomistic simulations, we proposed that the low magnetization and consequently, the too-small angular momentum carried by the Lu element could be one of the reasons that no magnetization switching was observed in CoLu alloys. [1]

[1] This work has been published: PENG et al., Laser single-shot magnetization reversal in $Co_{1x}Lu_x$ nanostructures, *Physical Review B*, **107**, 214415 (2023)

In the case of Gd-based alloys, models can replicate HI-AOS behaviors by considering two antiferromagnetically exchange-coupled magnetization sublattices with different relaxation times for each sublattice [88, 101]. In this respect, Gd seems to be a key ingredient in most materials, considering its low relaxation time arising from the small spin-orbit coupling of Gd (with L = 0) [124] and its antiferromagnetic coupling to transition metal. The theoretical results also suggest that engineering the element-specific damping in the alloy can open up new classes of materials that exhibit low-energy, ultrafast AO-HIS [99]. In the quest for other RE elements with low orbital angular momentum similar to Gd ($[Xe].4f^7.5d^1.6s^2$), it has been found that only Lu ($[Xe].4f^{14}.5d^1.6s^2$) and La ($[Xe].4f^0.5d^1.6s^2$) also possess L = 0 and furthermore S = J = 0. Nevertheless, only a few publications have reported on their magnetic properties, and no tests of HI-AOS have been conducted on TM-Lu or TM-La alloys thus far.

Previous studies have examined the crystallographic and magnetic properties of $Co_{1-x}Lu_x$. Paramagnetic behavior has been observed in Lu_3Co, Lu_4Co_3, $LuCo_2$, whereas ferromagnetism has been observed in $LuCo_3$ and Lu_2Co_{17} [125]. Partial substitution of aluminum for cobalt in $LuCo_2$ leads to itinerant metamagnetism at first (partial concentration of Al<0.08) and then to the appearance of ferromagnetism [126]. In the case of FeLu alloys, magnetization measurements between 2 K and 850 K have revealed ferromagnetic characteristics in $LuFe_2$, $LuFe_3$, Lu_6Fe_{23}, and Lu_2Fe_{17}, and Lu_2Fe_{17} has a particular behavior: it is ferromagnetic below 100 K and, at 270 K, the magnetization in a 100 Oe field shows a peak characteristic of a Néel temperature. The transition occurs, therefore, between a ferromagnetic and an antiferromagnetic state. On the other hand, measurements at 300 K using X-ray magnetic circular dichroism (XMCD) showed that $LuFe_2$ is ferrimagnetic [127]. In this case, the magnetic moment of Lu is carried by the 5d electrons and is antiparallel to the Fe 3d moment [128]. The magnetic moment of Lu, μ_{Lu} = -0.41 μ_B, is much weaker than the one of Fe, μ_{Fe} = 1.63 μ_B. It is, therefore, not possible to reach the magnetic compensation at room temperature. Nevertheless, previous studies have successfully reversed magnetization in GdFeCo alloys using a single pulse, even in regions dominated by the CoFe phase and far from magnetic compensation. In this chapter, we investigate and optimize the magnetic properties of CoLu to test if AO-HIS occurs in this material. Indeed, a necessary pre-requisite for our study is the achievement of perpendicular to film plane magnetization at zero applied field (PMA). The latter is more easily obtained with a Co/Pt interface when the thickness of the layer is thin.

4.1 Sample optimization

As a starting point, two groups of samples were grown by RF and DC-magnetron sputtering in an AJA sputtering tool with a base pressure lower than 3×10^{-8} mbar. Glass/Ta(5)/Cu(5)/CoLu(15, X)/Pt(2)(Thickness in nanometers), where Lu concentration X is 14%, 18.2% and 21.8% was group one. Glass/Ta(5)/Pt(5)/CoLu(t,14%) /Pt(2) was group two. The transparent glass substrate was used for the future pump/probe geometry. The buffer layer Ta(5)/Cu(5) was chosen for group one, and Ta(5)/Pt(5) was chosen for group two, in which both the Cu/Co interface and Pt/Co interface provide good perpendicular anisotropy [129, 130]. The capping layer Pt(2) was also used to promote perpendicular anisotropy to the film plane in $Co_{1-x}Lu_x$ alloy. The top Pt layer also acts as a protective layer against oxidation.

The hysteresis loops with a magnetic field perpendicular to the film plane for

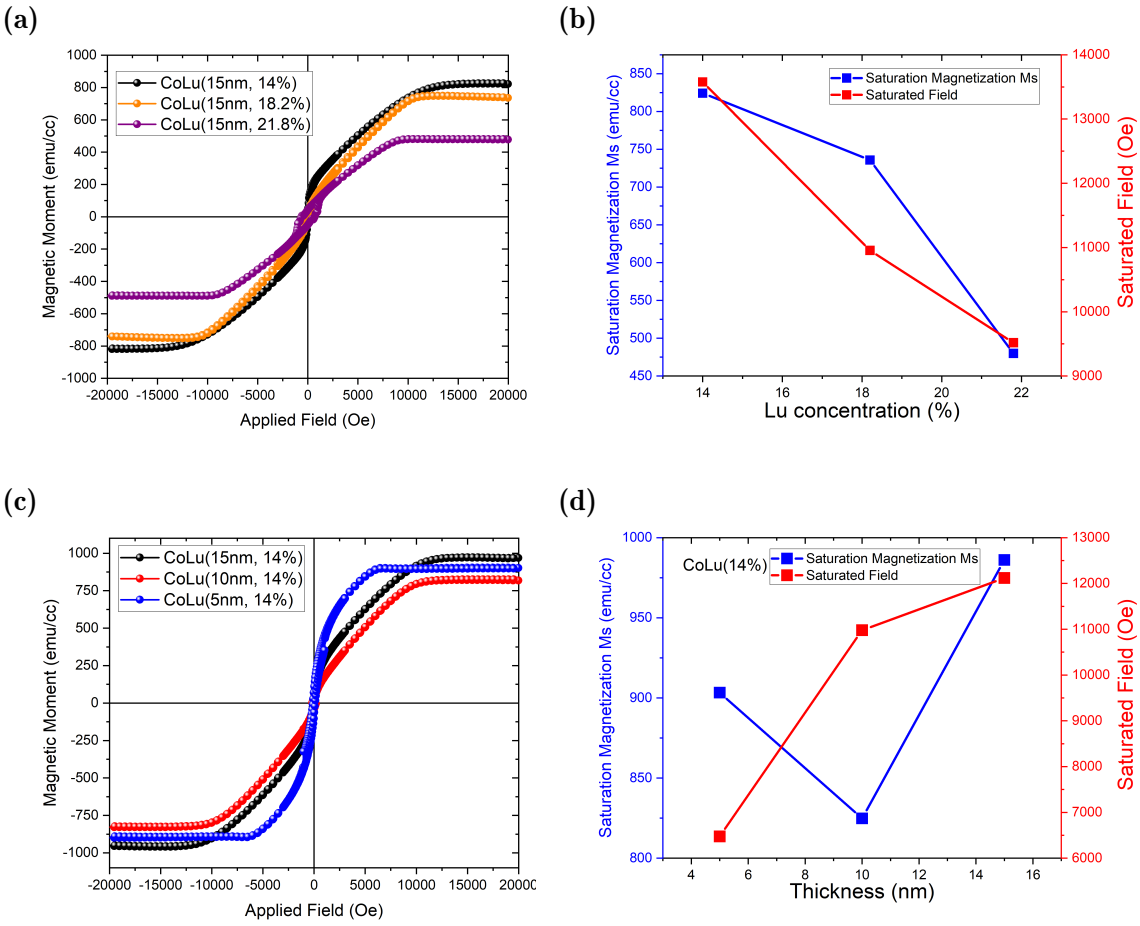

Figure 4.1: Magnetic properties of CoLu thin film. The hysteresis loops were measured by SQUID with a magnetic field perpendicular to the film plane. (a) and (b): $t = 15$ nm with different Lu concentrations; (c) and (d): Different CoLu thicknesses with 14% of Lu. The hysteresis loops are measured by applying a magnetic field that is perpendicular to the film.

group one are shown in Figure4.1a and 4.1b. All the hysteresis loops exhibit an in-plane magnetization instead of perpendicular anisotropy. The saturation magnetization M_s and saturation field H_{sat} can be extracted from the hysteresis loops. The saturation magnetization decreases due to the much lower atomic magnetic moment of Lu compared to Co when the Lu concentration increases. The saturation field H_{sat} is around 1.35 T with 14% of Lu, while it decreases to 0.95 T with 21.8% of Lu. The decrease in the saturation field is due to the decrease in M_s where the saturation field is proportional to the $4\pi M_s$. For another group of samples, the Lu concentration was fixed at 14% while the thickness was varied from 15 nm to 5 nm. Similar to the previous group, these samples also exhibit in-plane magnetization, and the saturation magnetization M_s remains relatively unchanged. However, the saturation field decreases significantly to 0.6 T as the thickness decreases to 5 nm, indicating a better perpendicular anisotropy with lower CoLu thickness. According to the two groups of samples, lower thickness and higher Lu concentration are favorable for CoLu alloy to show perpendicular anisotropy. Thus, a series of samples with Lu concentration varies from 18% to 40% were deposited, with thickness decreases down to 3 nm.

Typical hysteresis loops measured in the polar MOKE configuration with a per-

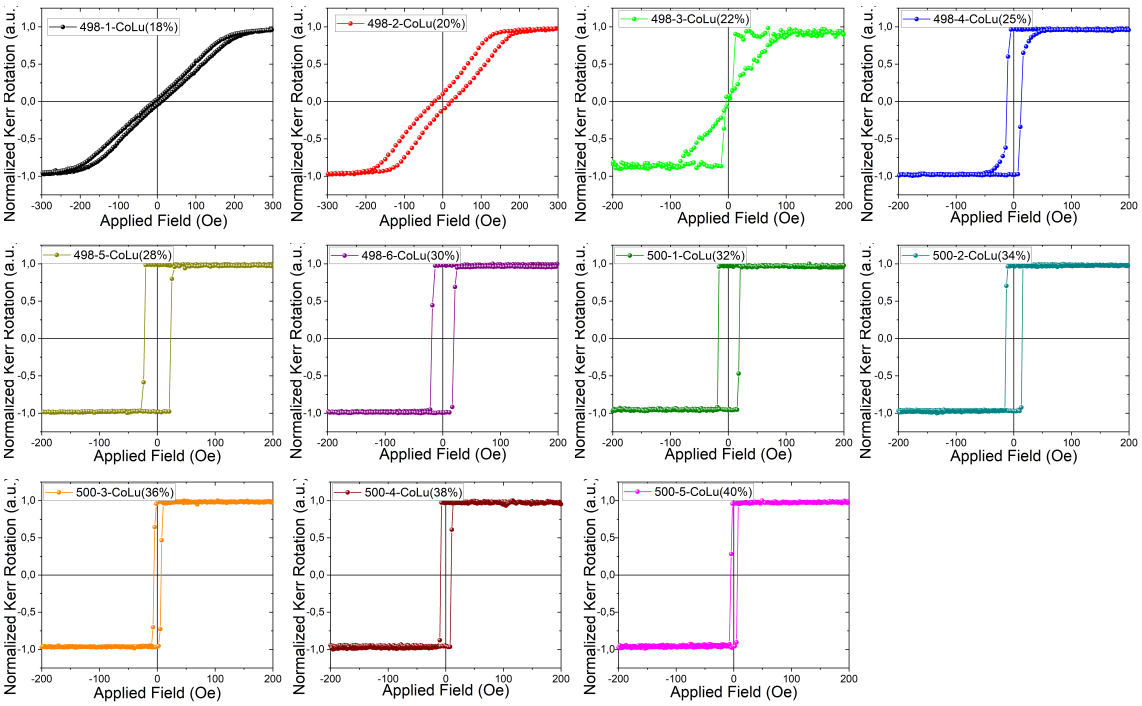

Figure 4.2: Polar MOKE hysteresis loops of CoLu alloy with Lu concentration varies from 18% to 40%. The thickness of CoLu thin film is 3nm.

pendicular magnetic field for different Lu concentrations are reported in Figure 4.2. The magnetization lies in the film plane for a Lu concentration lower than 20%. For 22% of Lu concentration, the magnetization reverses at a positive field with remanence equals 0, which is related to the nucleation of multidomain structures such as vortex, bubbles, strips or skyrmion[131–133]. The square hysteresis loops with a remanence equal to one indicate the presence of perpendicular magnetic anisotropy (PMA) of the CoLu thin films when Lu concentration is above 22%. Moreover, the positive Kerr rotation at a positive high magnetic field agrees with the fact that Co-sublattice dominates the net magnetization(See 3.2.1).

4.2 Magnetic properties

The saturation magnetization M_s and coercivity H_c can be obtained by measuring the hysteresis loops by SQUID VSM. Figure 4.3a shows saturation magnetization and coercivity as a function of Lu concentration at room temperature. The saturation magnetization M_s is 830 emu/cc with 18% of Lu and linearly decreases as increasing the Lu concentration. The saturation magnetization M_s decreases down to 400 emu/cc when the Lu concentration is up to 40%, resulting in a 52% reduction. This effective value of M_s includes the proximity-induced magnetism in both top and bottom Pt through the magnetic proximity effect. Indeed, element-resolved x-ray magnetic measurements showed that the proximity-induced moment in Pt was parallel to the TM sublattice rather than the RE or the net moment in Pt/RE-TM ferrimagnetic alloys [134, 135]. Considering the low thickness of the CoLu layer, the magnetism contribution of the Pt layer to the total magnetic moment must be significant.

Besides, the variation of the saturation magnetization versus temperature for CoLu alloys with the concentration of 28%, 34%, and 40% clearly shows that, for temperatures ranging between 10K and 400K, the saturation magnetization

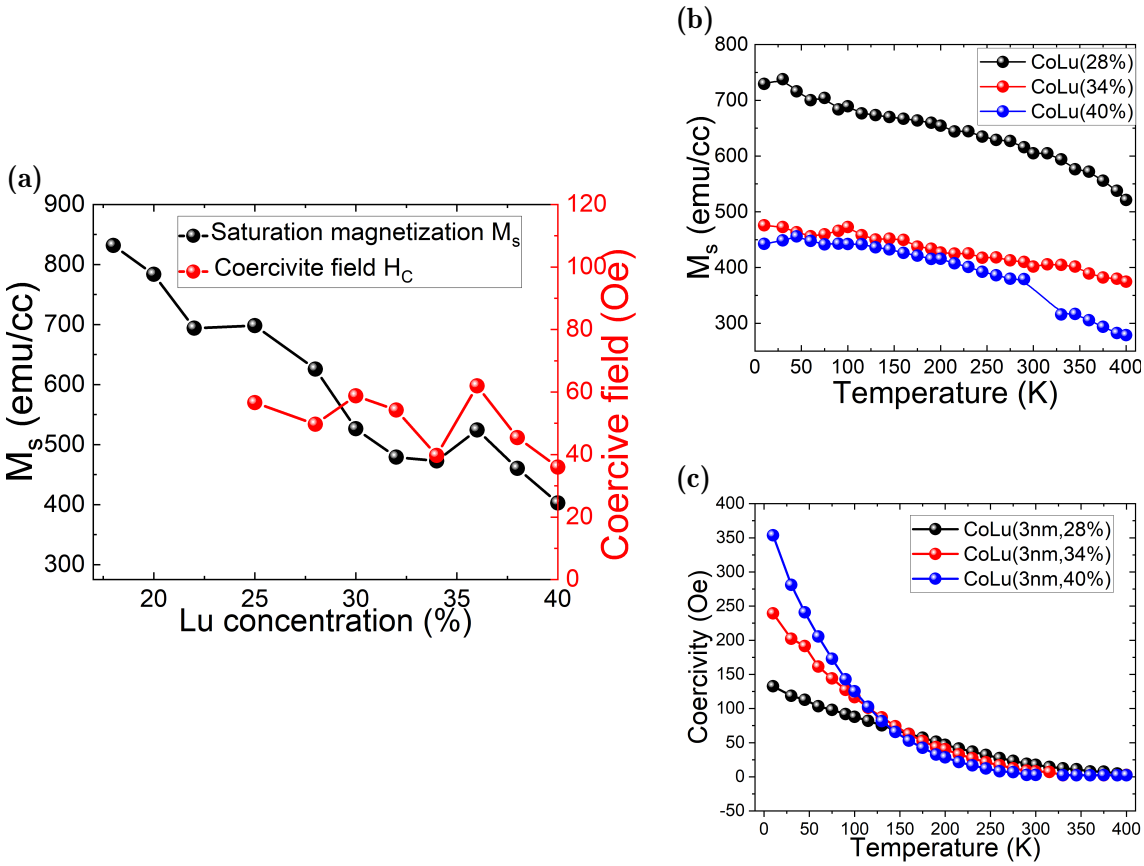

Figure 4.3: Lu concentration-dependent and temperature-dependent saturation magnetization M_s and coercivity H_c.

monotonously decreases, without the presence of compensation temperature. Considering the much lower atomic moment of Lu than that of Co, the magnetic moment in Lu can not compensate for the magnetic moment in Co, with Lu concentration varying between 18% and 40%. Thus, the CoLu magnetization is dominated by Co-sublattice; consequently, the compensation temperature must be below room temperature if it exists. However, the monotonously decreasing temperature-dependent saturation magnetization and coercivity depict the absence of magnetic compensation.

4.3 Single switching in full film

Single-shot reversal experiments have been performed on all full film samples with perpendicular anisotropy. Here, we look at the sample with 40% of Lu, as shown in Figure 4.4. One can see that only a multidomain state could be observed after being exposed to a single 50fs laser pulse with 6.7 mJ/cm^2. The domain area ratio, which compares the area of the actual domains to that of a perfect circle (shown by the black dashed circle), has been reported and remains consistent after each pulse. Specifically, the ratios observed for the first, second, third, and fourth pulses are 0.58, 0.56, 0.59, and 0.55, respectively, suggesting no helicity-independent switching occurs. As the fluences increase to 11.9 mJ/cm^2, it is still multidomain, while the area showing the multidomain (Indicated by a white dash circle in Figure 4.4b) is larger. The domain pattern doesn't change until the sample is burned in the

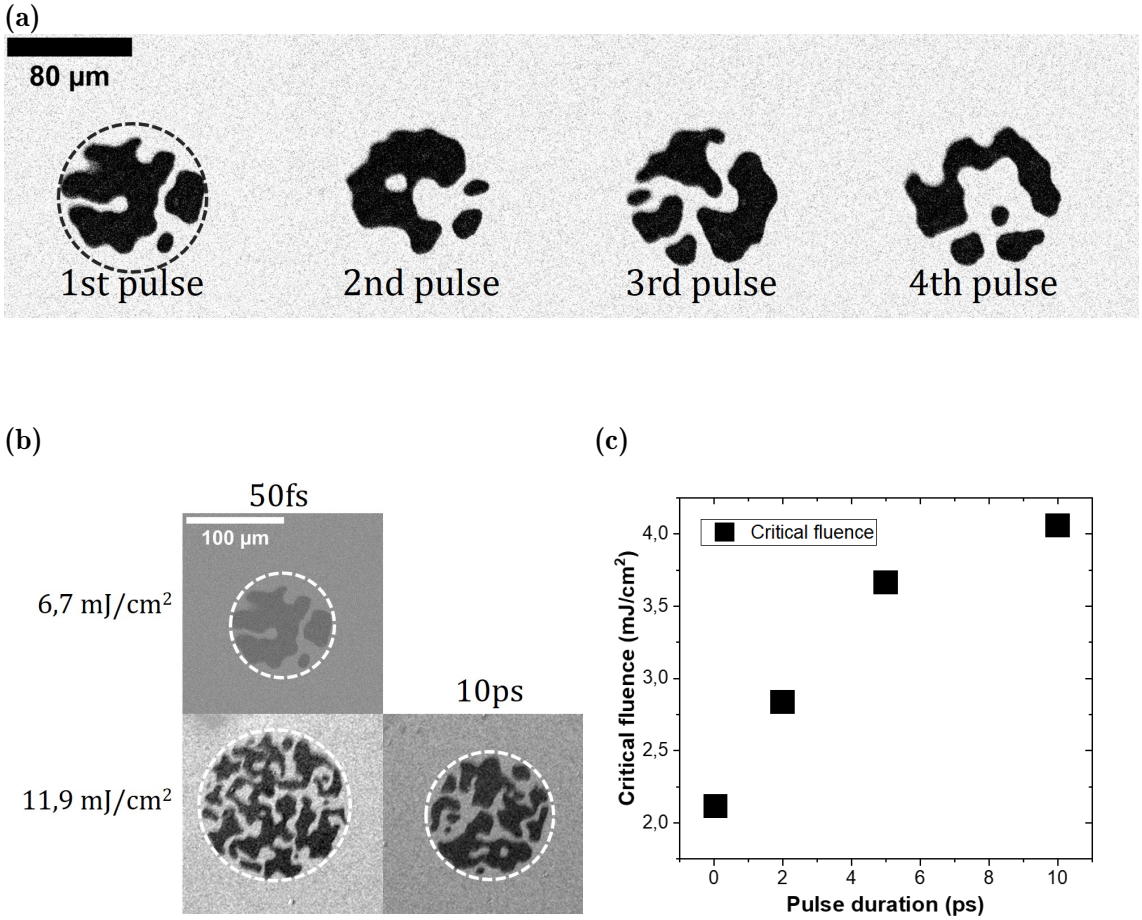

Figure 4.4: (a): Domain structure stabilized after 50fs laser pulses with fluence 6.7 mJ/cm^2 in 40% of Lu concentration. The domain areas ratio, which compares the area of the actual domains to that of a perfect circle (shown by the black dashed circle), has been reported after each pulse; first pulse: 0.58; second pulse: 0.56; third pulse: 0.59; fourth pulse: 0.55. (b): MOKE images obtained after exposure to a single laser pulse with different pulse durations and fluences. (c) Critical fluence $F_{critical}$, below which nothing happens on the thin film, above which multidomain could be observed, as a function of pulse duration. The images are subtracted by the background, which is saturated by a magnetic field.

center, indicating that there is no all-optical helicity-independent switching again. Even though there is no AO-HIS, a critical fluences $F_{critical}$, below which nothing happens on the thin film, above which multidomain could be observed, still exists. The critical fluence for 50fs pulse duration is 2.1 mJ/cm^2. Comparing the two images in Figure 4.4b bottom row, where the fluence is fixed at 11.9 mJ/cm^2 while the pulse duration is 50 fs and 10 ps, respectively, the multidomain area for 10 ps is smaller than the one for 50 fs. Considering Gaussian laser energy distribution, the smaller multidomain area corresponds to higher critical fluence(See 3.3 Data analysis). The critical fluence is plotted as a function of pulse duration. The critical fluence increases with the increase of pulse duration when the pulse width is below 5ps, while it doesn't increase much for a longer pulse duration.

For other Lu concentrations, no AO-HIS has been observed either. However, a clear increase in the domain size occurs when the Lu content increases from 25% to 40%. Since the mean domain size is hard to define from Figure 4.5, the total domain wall length has been extracted by averaging the states obtained for 4 pulses. An increase in domain wall length is obviously associated with a decrease in domain

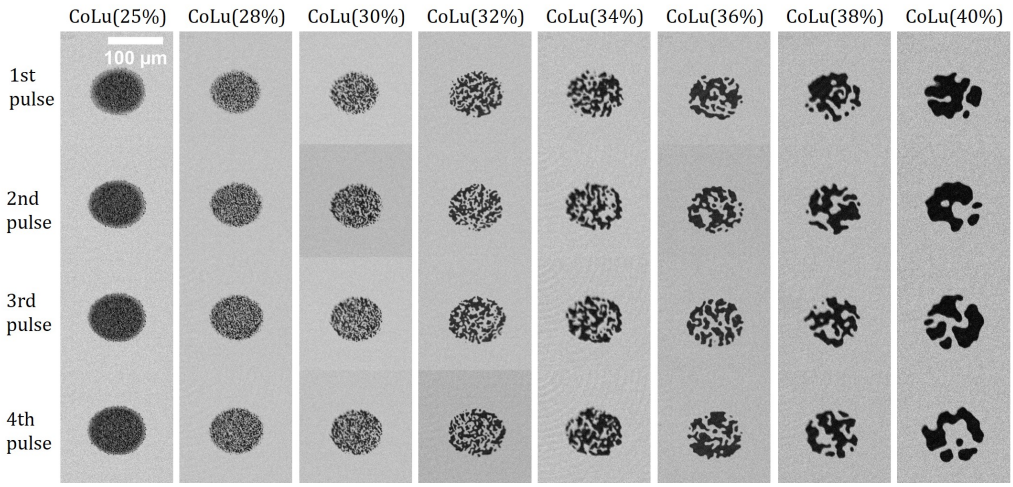

Figure 4.5: Domain structure stabilized after 50fs laser pulses with fluence 6.7 mJ/cm^2 in the samples with Lu concentration varies from 25% to 40%. The images are subtracted by the background, which is saturated by a magnetic field. From left to right, increasing the Lu concentration. From top to bottom, exposed by 1st pulse, 2nd pulse, 3rd pulse, and 4th pulse.

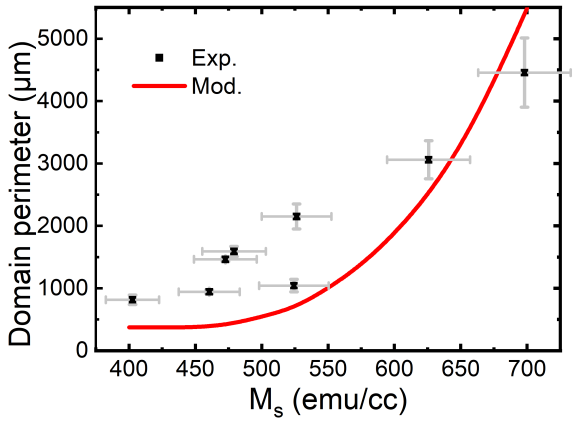

Figure 4.6: Analysis of the domain perimeter averaged over the 4 pulses versus saturation magnetization. Comparison with the theory of stable domain size versus saturation magnetization in stripe domains.

size. Using the expression of the domain period in parallel stripe domains [136], the domain wall length in a circular region with a diameter of 95 μm, which is the size of the region where domains are stabilized after the laser pulse shot, was theoretically estimated. Since the M_s is obtained from the SQUID measurements, the domain wall energy per unit area (σ_{DW}) is needed. According to the classical Heisenberg model, in mean field one expects that the exchange constant is proportional to the square of saturation magnetization,

$$A = \frac{2}{3}\mu_0 {M_\mathrm{s}}^2 \tag{4.1}$$

Using the dependence of exchange constant on the saturation magnetization for a ferromagnet[137, 138],

$$\frac{A(Lu\%)}{A(0)} = (\frac{M_s(Lu\%)}{M_s(0)})^2$$

where $A(0)$ and $M_s(0)$ are the exchange constant and saturation magnetization for 0% of Lu, while $A(\text{Lu}\%)$ and $M_s(\text{Lu}\%)$ are the exchange constant and saturation magnetization for a certain Lu concentration. The domain wall energy per unit area (σ_{DW}) of a strip domain wall can be expressed as follows:

$$\sigma_{\text{DW}} = 4\sqrt{AK_{\text{u}}} \tag{4.2}$$

Introducing equation 4.1 into equation 4.2, a linear variation of the domain wall energy with saturation magnetization was taken into account,

$$\frac{\sigma_{\text{DW}}(M_s)}{\sigma_{\text{DW}}(400)} = \frac{M_s}{400} \tag{4.3}$$

here, $\sigma_{\text{DW}}(400) = 0.23 J/m^3$, which is the domain wall energy with $M_s = 400$ emu/cc, while $\sigma_{\text{DW}}(M_s)$ is the domain wall energy with a certain value of M_s. Considering the very crude approximation made in our model with a constant value of K_u, a good agreement between theory and experiments, where the size of magnetic domains is inversely proportional to the saturation magnetization of the material, could be obtained.

4.4 Single switching in dots

The next step consisted of patterning dot arrays in the full film in order to bring the structure's size below the equilibrium size of magnetic domains. Therefore, E-beam lithography and dry Ar etching were used to pattern dot arrays with a 3 µm diameter and 3.3 µm period, as shown in Figure 4.7a. We chose the sample with 40% of Lu concentration corresponding to the largest equilibrium domains. After patterning, the 3 nm thick and 3 µm diameter $Co_{60}Lu_{40}$ kept its PMA.

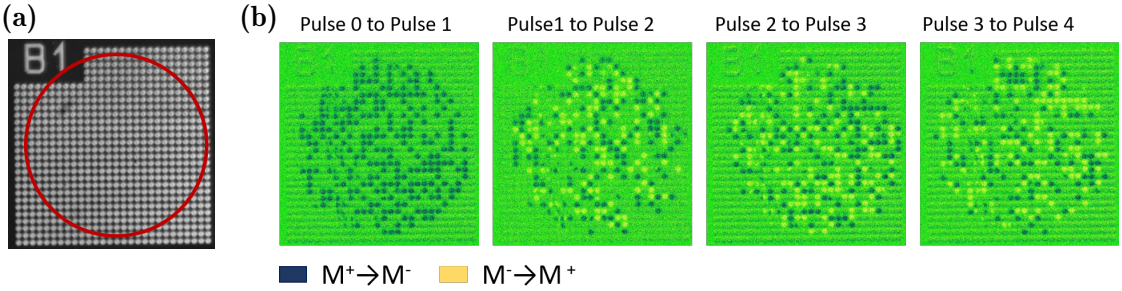

Figure 4.7: Single pulse reversal on nanodot structure with 3 µm of the dot diameter. (a): nanodot arrays of the sample with 40% of Lu concentration. The area enclosed by the red circle is the region where the fluence is above the critical fluence; (b): from left to right are the pictures which are subtracted by the previous one; for example, pulse 0 to pulse 1 is image pulse 1 subtracted by background, pulse 1 to pulse 2 is image pulse 2 subtracted by image pulse 1. Blue represents the dot that switched from the M+ state to M- state, and yellow represents the dots that switched from M- state to the M+ state. Experiments were done with a fluence of 9.3 mJ/cm^2.

As shown in Figure 4.7a, 531 dots are located in the region where the fluence is above the critical fluence. After saturating the sample with a magnetic field, we shined a 50fs laser pulse, then counted how many dots had their magnetization

	M^+ to M^-	M^- to M^+	Total	Switching rate
Pulse 0 to pulse 1	263	0	531	49.5%
Pulse 1 to pulse 2	139	114	531	47.6%
Pulse 2 to pulse 3	145	133	531	52.4%
Pulse 3 to pulse 4	143	129	531	51.2%

Table 4.1: Statistic of the single switching of nanodot structure based on Figure 4.7

switched. After the first pulse, the magnetization of 263 dots switched from M^+ state to M^- state, namely 49.5% of dots have been switched by the femtosecond laser pulse. Meanwhile, 268 dots stay in the M^+ state. The second pulse makes 139 dots switch from M^+ state to M^- state, and 114 dots switch from M^- state to M+ state simultaneously, namely 47.6% of dots switched. Thus, 243 dots stay in M^+ state, and 288 dots stay in M^- state after pulse 2. As shown in Figure 4(b) and Table 1, more dots switch from M^+ state to M^- state, but fewer dots switch from M^- state to M^+ state. As a result, compared to CoFeGd, for which 100% of dots reverse, only roughly 50% of dots can be switched by each laser pulse. Furthermore, each CoLu dot's magnetization does not switch after each pulse.

4.5 Discussion

The magnetic properties of CoLu alloys were promising to get a single-shot reversal. Decreasing the thickness down to 3 nm, magnetization could be stabilized in the out-of-plane configuration. Increasing the Lu content, saturation magnetization could be decreased, allowing to stabilize micrometer size domains and so single domain in dots with 3 µm in diameter, but the compensation point was never reached. After a single laser pulse, the single domain state could be preserved, but reversal does not occur after each pulse. It appears that around 50% of the dots reverse their magnetization by each pulse.

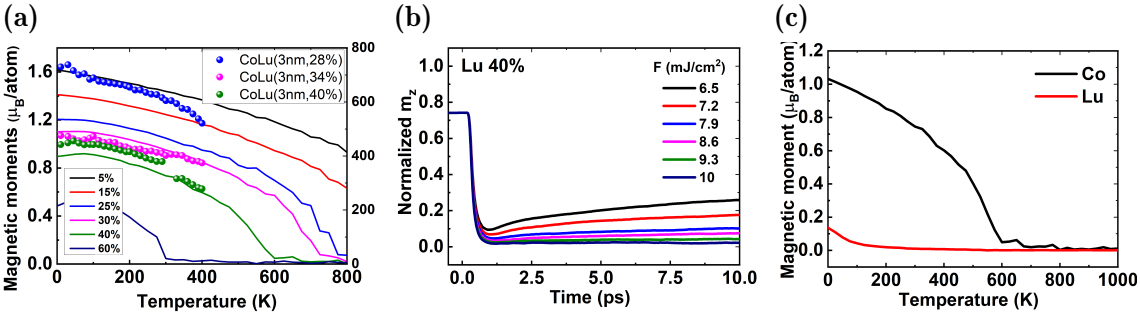

Figure 4.8: (a) Magnetic moment versus temperature for CoLu alloys with various concentrations. Sphere: experiments; lines: simulations; (b) Simulations of the Co demagnetization dynamics for the $CoLu_{40\%}$ alloy as a function of laser power. (c) Simulations of the magnetic moment versus temperature for both Co and Lu subnetworks in the case of $CoLu_{40\%}$.

In order to shed light on this behavior, atomistic simulations done by Dr. Wei ZHANG have been performed that predict the switching behavior in Gd-based ma-

terials. Since the magnetic parameters of Lu are not well known, in the first step, static magnetization versus temperature has been computed to adjust the magnetic parameters. The energy terms taken into account are the exchange energy given by a Heisenberg spin model and effective anisotropy energy. We used the magnetic moment close to the one found in literature, $\mu_{Lu} = 0.34\ \mu_B$/atom, and change the exchange constant $J_{Lu\text{-}Lu}$. $J_{Co\text{-}Lu}$ has been fixed to -3×10^{-22} J and $J_{Co\text{-}Co}$ to 4.8×10^{-21} J. Figure4.8a shows the temperature-dependent magnetization evolution, from which the Curie temperature of CoLu can be extracted for various Lu concentration (the polarization of Pt was not considered here). The evolution of magnetization as a function of the temperature could be reproduced using $J_{Lu\text{-}Lu} = 6 \times 10^{-23}$ J. The dynamics of the spin system were then computed based on the Langevin dynamics of the Landau-Lifshitz-Gilbert equation, and the temperature of the spin system was estimated with a two-temperature model which couples the spin and electron [88,94]. By means of the time integration of the LLG equation through the VAMPIRE software package [Vam], we can obtain the temporal evolution of a system of spins for different pulse fluence. Figure 4.8b shows the laser fluence-

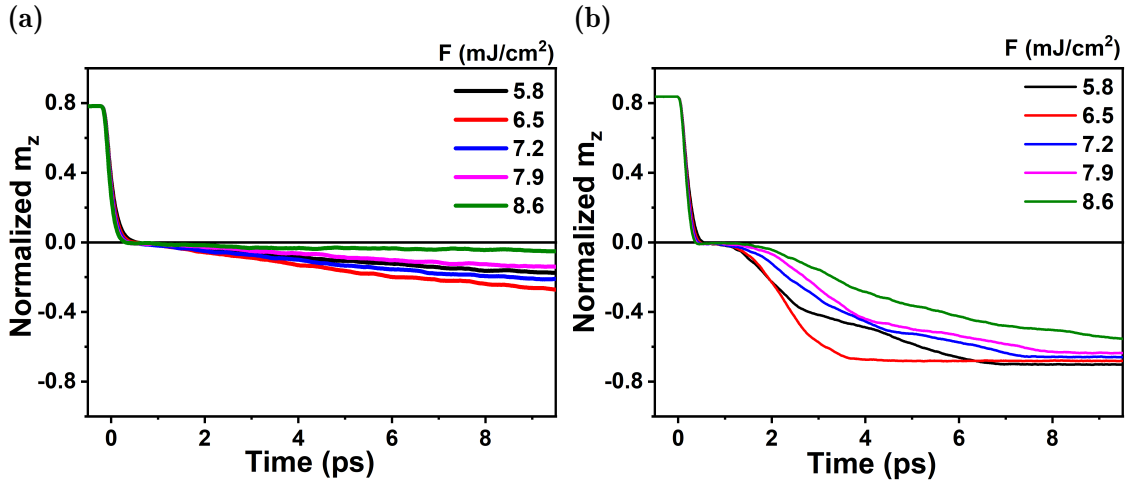

Figure 4.9: (a): Demagnetization dynamics for $J_{Lu\text{-}Lu}$ equal to 6×10^{-22} J when $\mu_{Lu} = 4.34\ \mu_B$/atom as a function of fluence. (b): Demagnetization dynamics for $J_{Lu\text{-}Lu}$ equal to 6×10^{-21} J when $\mu_{Lu} = 3.34\ \mu_B$/atom as a function of fluence.

dependent magnetization dynamics for $Co_{0.6}Lu_{0.4}$ with laser fluence changing from 6.5 to 10 mJ/cm^2. We can see that for all laser fluences, only demagnetization of the alloy could be obtained, as observed experimentally. A close analysis of magnetic moment versus temperature shows that when temperature increases, the Lu moment experiences a strong decrease and is close to zero, while the moment of Co only shows a decrease of 20%. As a result, for temperatures for which the reversal of Co could be activated, the transfer of angular momentum is not efficient; thus, no deterministic reversal can happen.

In the simulations, the magnetic parameters of Lu (μ_{Lu} and $J_{Lu\text{-}Lu}$) have been varied in order to check if a reversal could be observed. When $J_{Lu\text{-}Lu} = 6 \times 10^{-23}$ J, the single shot switching behavior can not be observed, whatever the magnetic moment. By increasing $J_{Lu\text{-}Lu}$ to 6×10^{-22} J, a value which remains two times lower than $J_{Gd\text{-}Gd}$ [94], magnetization switching occurs until $\mu_{Lu} = 4.34\ \mu_B$/atom as is shown in figure 4.9a. Further increasing of $J_{Lu\text{-}Lu}$ leads to a decrease of this threshold. For example, Figure 4.9b shows the magnetization switching behavior for $\mu_{Lu} = 3.34\ \mu_B$, when $J_{Lu\text{-}Lu} = 6 \times 10^{-21}$ J. As a result, with its low magnetic moment

per atom and its low Curie temperature, Lu cannot transfer enough angular moment or spin current to the Co subnetwork, leading to a non-deterministic magnetization reversal of the 3 µm size dots.

4.6 Conclusion

In conclusion, we prepared a series of CoLu thin films with various thicknesses as well as concentrations. The static magnetic properties were carefully studied, including saturated magnetization and coercivity as a function of temperature, sample thickness, and concentrations. As a result, we achieved a good PMA when the CoLu samples had a low thickness and proper concentrations with low M_S. Then, the single-shot laser pulse-induced switching was investigated, and only the laser pulse-induced multidomain states were obtained. Furthermore, the film has been fabricated into nanodots to bring the structure size below the domain size. Still, non-deterministic magnetization reversal can be achieved with 3 µm diameter dots. By atomistic simulations, we proposed that the low magnetization, and consequently the too-small angular momentum carried by the Lu element, could be one of the reasons that no magnetization switching was observed in CoLu alloys.

Sample list

- 459-1 V/Ta(5)/Cu(5)/CoLu(15, 14%)/Pt(2)
- 459-2 V/Ta(5)/Cu(5)/CoLu(15, 18.2%)/Pt(2)
- 459-3 V/Ta(5)/Cu(5)/CoLu(15, 21.8%)/Pt(2)
- 460-1 V/Ta(5)/Pt(5)/CoLu(15, 14%)/Pt(2)
- 460-2 V/Ta(5)/Pt(5)/CoLu(10, 14%)/Pt(2)
- 460-3 V/Ta(5)/Pt(5)/CoLu(5, 14%)/Pt(2)
- 498-1 V/Ta(5)Pt(4)CoLu(3, 18%)Pt(2)
- 498-2 V/Ta(5)Pt(4)CoLu(3, 20%)Pt(2)
- 498-3 V/Ta(5)Pt(4)CoLu(3, 22%)Pt(2)
- 498-4 V/Ta(5)Pt(4)CoLu(3, 25%)Pt(2)
- 498-5 V/Ta(5)Pt(4)CoLu(3, 28%)Pt(2)
- 498-6 V/Ta(5)Pt(4)CoLu(3, 30%)Pt(2)
- 500-1 V/Ta(5)Pt(4)CoLu(3, 32%)Pt(2)
- 500-2 V/Ta(5)Pt(4)CoLu(3, 34%)Pt(2)
- 500-3 V/Ta(5)Pt(4)CoLu(3, 36%)Pt(2)
- 500-4 V/Ta(5)Pt(4)CoLu(3, 38%)Pt(2)
- 500-5 V/Ta(5)Pt(4)CoLu(3, 40%)Pt(2)

Chapter 5

Single switching in Tb and Dy-based multilayer

This chapter presents the single switching in various multilayers, bilayers, and trilayers. And found that the helicity-independent switching is a general phenomenon in Tb- and Dy-based multilayers, which have sperimagnetic properties coupled with transient metals. Interestingly, a complex structure of rings of opposite magnetization directions has been observed at high fluence. According to the pump-probe measurements, We tried to explain the switching mechanism and ring structures, which could be an in-plane reorientation precession mechanism.[1]

[1]This work has been published: PENG et. al, In-plane reorientation induced single laser pulse magnetization reversal, *Nature Communications* **14**(1):5000, 2023

In 2020, Avilés-Felix and co-workers reported reliable helicity-independent switching of the magnetization was observed using both femtosecond and picosecond laser pulse in a Tb/Co multilayer-based electrode, whose anisotropy is large enough to preserve magnetically stable information bits at small diameters in a magnetic tunnel junction and maintains its perpendicular anisotropy even after a 250°C annealing process [51, 52]. Using a crossed-wedge multilayer structure, they showed that the switching occurs within a specific range of Tb and Co thickness combinations in Co-dominate compositions. These significant findings potentially pave the way for integrating them into scalable magnetic tunnel junctions. However, the switching behaviors haven't been studied systematically; thus, the mechanism leading to single-pulse AO-HIS in those samples remains unknown. In this chapter, by combining material science static and dynamic measurements of more than 200 samples, we give a credible mechanism of reversal that differs from the one in Gd-based materials.

5.1 $[Tb/Fe]_4$ multilayers

5.1.1 Magnetic properties and single laser pulse switching

Avilés-Felix reported that single-pulse helicity-independent switching was observed in $[Tb/Co]_N$ multilayer alone and for the multilayer coupled to a CoFeB electrode as well. To test whether this phenomenon is specific to $[Tb/Co]_N$ multilayer, a Fe layer, also a transition metal, was used to replace the Co layer. An opposite double wedge $[Tb(0.9\text{ nm, wedge})/Fe(0.9\text{ nm, wedge})]_4$ multilayer, where the thickness of Tb and Fe increase in the opposite directions, was deposited to find the magnetic compensation point. As shown in section 3.1, the thicknesses of the two layers vary over a length of 50 mm, while 0.9 nm for both Tb and Fe are the thickness at the position of 25 mm. Thus, the thicknesses of the two layers span $0.45\text{ nm} < t_{Fe} < 1.35\text{ nm}$ and $1.35\text{ nm} > t_{Tb} > 0.45\text{ nm}$.

The MOKE hysteresis loops have been measured on a spatially resolved basis across the opposite double-wedge samples, enabling us to identify nanolayer thickness combinations. The magnetic field was applied perpendicular to the film plane, employing a maximum field of up to 7 kOe. For the case of $[Tb(0.1.19)/Fe(0.67)]_4$, where the thickness of Tb is much larger than that of Fe, the magnetization is dominated by Tb-sublattice. While the Tb thickness decreases to 0.76 nm and Fe thickness increases to 1.1 nm, the hysteresis loop is inverted, and the magnetization is dominated by Fe-sublattice. The two inverted hysteresis loops with different thickness combinations indicate the existence of the magnetic compensation point, where the magnetic moment of Tb and Fe align in opposite directions and compensate to each other, resulting in a 0 net magnetization. By plotting the coercivity obtained by the MOKE hysteresis loops with different thickness combinations as a function of Fe (Tb) thickness, we find that the coercivity diverges with $[Tb(0.98\text{ nm})/Fe(0.87\text{ nm})]_4$, while decreases with larger and lower Fe thickness (lower and larger Tb thickness). The divergence of the coercivity further confirms that the magnetic compensation occurs with $[Tb(0.98\text{ nm})/Fe(0.87\text{ nm})]_4$.

We now look at the results of sending single laser pulses on such $[Tb/Fe]_4$ with different thickness combinations. The sample was exposed to a 50 fs laser pulse after being saturated by a magnetic field. In the Tb-dominate region (see Figure 5.2c with $[Tb(1.19\text{ nm})/Fe(0.67\text{ nm})]_4$), only multidomain state can be observed, indicating the absence of AO-HIS. Similarly, in the Fe-dominate region and further away from the magnetic compensation point, exemplified by [Tb(0.5 nm)/Fe(1.36

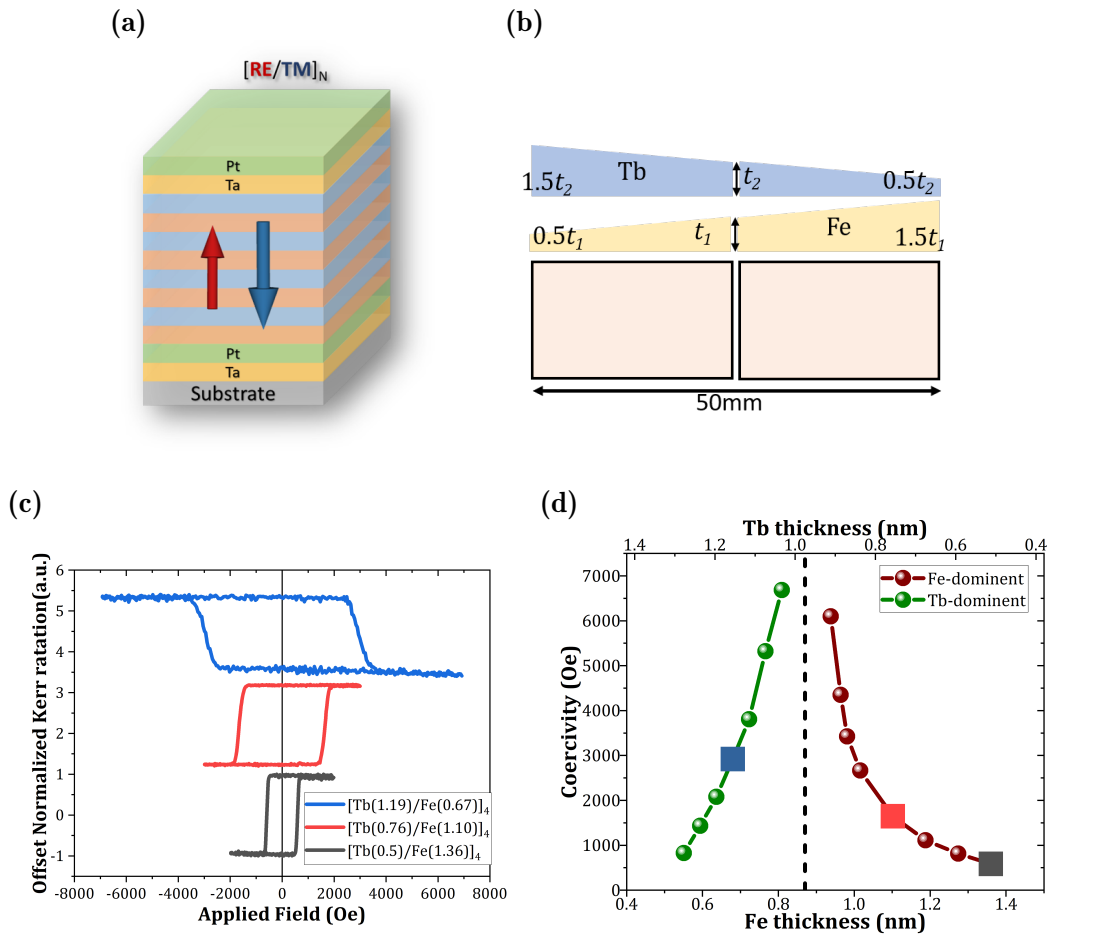

Figure 5.1: (a): Schematic of the $[RE/TM]_N$. (b): schematic of the opposite double-wedge [Tb(0.9 nm, wedge)/Fe(0.9 nm, wedge)]$_4$ multilayers where the thicknesses of the Tb layer and Fe layer increase in opposite directions. The thicknesses of Tb and Fe vary over a length of 50 mm, and $t_1 = 0.9$ nm and $t_2 = 0.9$ nm are the thicknesses at the position of 25mm for Fe and Tb layer, respectively, spanning 0.45 nm $< t_{Fe} <$ 1.35 nm and 1.35 nm $> t_{Tb} >$ 0.45 nm. (c): MOKE hysteresis loops for different thickness combinations. (d): The coercivity as a function of Fe (Tb) thickness.

nm)]$_4$, no AO-HIS was observed. However, for the case of [Tb(0.76 nm)/Fe(1.1 nm)]$_4$, which is in the Fe-dominate region and is close to the compensation point, partial magnetization switching to the opposite direction occurred after the first pulse and then switched back after the second pulse. Although the magnetization of the sample cannot be completely switched to the opposite direction by each laser pulse, it still shows partial switching in response to the single laser pulse with this specific thickness combination. These results are similar to the results in Tb/Co multilayers.

Based on the test above, a double-wedge sample was deposited where the thickness of both Tb and Fe was increased in the same direction, resulting in a 1:1.44 thickness ratio. The MOKE hysteresis loops show that all the samples are in the Fe-dominate region. The observation of these Fe-dominant states in the hysteresis loops can be attributed to the proportional increase in the thickness of Tb and Fe in the double-wedge sample, consequently, resulting in a nearly constant coercivity throughout the different thicknesses.

This double-wedge sample [Tb(0.9 nm, wedge)/Fe(1.3 nm, wedge)]$_4$ allows us to investigate the single switching in a large range of thickness. As shown in Figure

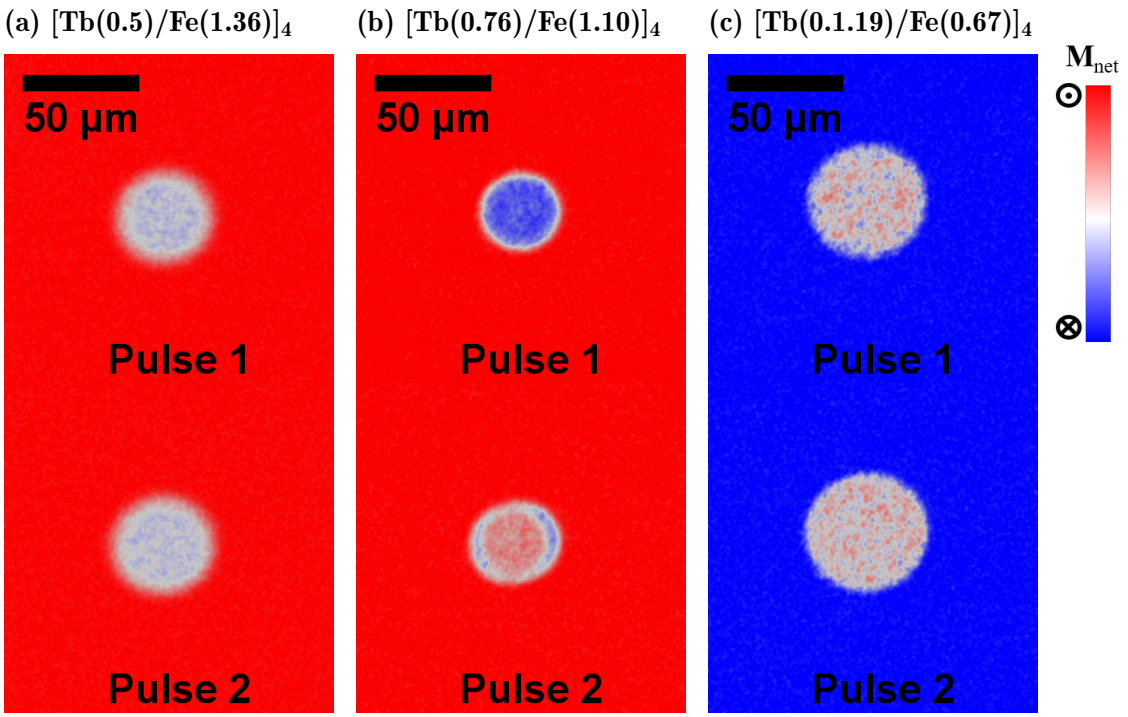

Figure 5.2: AOS measurements performed on $[Tb/Fe]_4$ multilayers with different thickness combinations using a pulse duration of 50fs. The fluences are (a): 1.93 mJ/cm^2, (b): 1.41 mJ/cm^2, and (c): 3.44 mJ/cm^2, respectively. (The unit of the thickness in brackets is nm)

5.2b, partial switching has been observed with this thickness combination [Tb(0.76 nm)/Fe(1.1 nm)]$_4$. As a result, we expect the single switching in either larger or lower thickness in this sample [Tb(0.9 nm, wedge)/Fe(1.3 nm, wedge)]$_4$. Thus, the AOS measurements have been performed in three samples where the thicknesses are either above or below [Tb(0.76 nm)/Fe(1.1 nm)]$_4$.

Figure 5.4c shows the multidomain state of the sample [Tb(0.5)/Fe(0.72)]$_4$, which is in the low thickness region, using a 50 fs single laser pulse with a fluence of 6.93 mJ/cm^2. The 0 normalized contrast in the laser exposure area after the first pulse confirms that there is no AO-HIS. When the Tb and Fe thickness proportionally increase to [Tb(1.15)/Fe(1.67)]$_4$, the MOKE images after the first and second pulse clearly show the switching of the magnetization. However, after the first pulse, the magnetization switches from +1, which indicates the positive direction, to -0.8, leading to a 90% of switching. After the second pulse, the magnetization switches back to +0.7, which indicates that the magnetization doesn't completely switch back to the initial state. Further increase in the thicknesses of both layers leads to a very nice magnetization switching by each single laser pulse. These results indicate that a higher thickness of the Tb and Fe layer is better for showing single switching with the thickness range we studied so far.

No matter the partial or nice switching of the magnetization, a quite narrow ring area is left after the second laser pulse. This narrow ring area may come due to many reasons: 1) shifting of the laser spot; 2) small domains at the edge of the large blue and red areas. Hu [117] analyzed the average size of the domain induced by fs laser pulse in TbCo alloy, which is around 700 nm. It is reasonable that the edge of the blue and red areas consists of hundreds, even thousands of small domains. Thus, the behavior of the edge area is always demagnetization. The MFM images shown in Figure 5.25 confirm this point. Another possibility is that the threshold fluences for switching are different when the sample is saturated in opposite directions. This

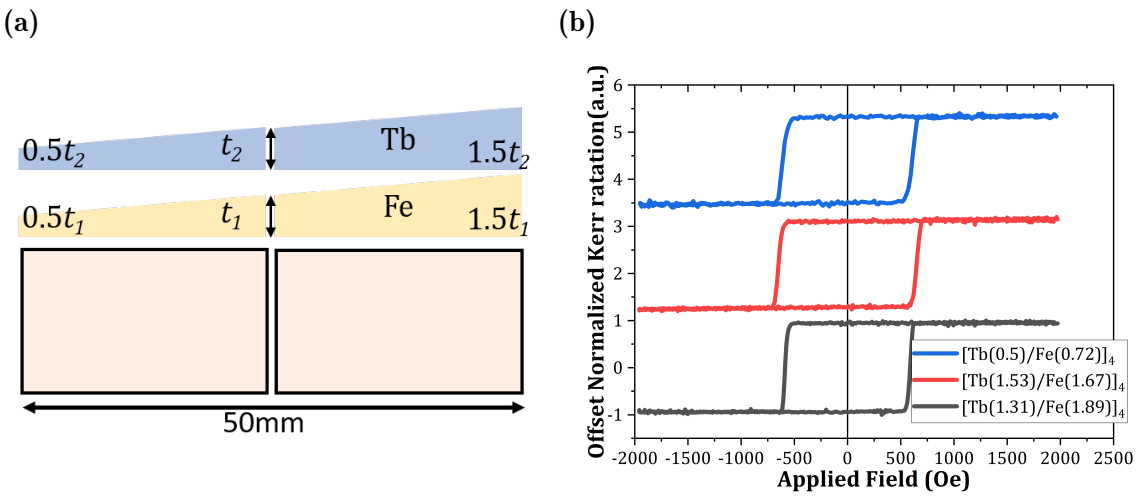

Figure 5.3: (a): Schematic of the [Tb(0.9 nm, wedge)/Fe(1.3 nm, wedge)]$_4$ double-wedge multilayer where the thicknesses of Tb and Fe increase in the same direction, resulting in a certain thickness ratio t_{Tb}:t_{Fe} = 1:1.44. (b): MOKE hysteresis loops for different thickness combinations with a thickness ratio of 1:1.44.

behavior differs from the case of GdFeCo.

5.1.2 Impact of the laser fluence

We now look at the switching behavior when we increase the incident laser fluence. Very surprising and interesting results have been observed with the thickness combination [Tb(1.31 nm)/Fe(1.89 nm)]$_4$, where the magnetization can be switched by each pulse 100%.

In the case of GdFeCo, the laser pulse exhibits distinct effects on the magnetic moment depending on the fluence applied. When the fluence is below a specific threshold value, the laser pulse lacks the necessary energy to switch the magnetic moment, and this threshold is defined as switching fluence F_{switch}. Conversely, when the power exceeds another critical value, it is multi-domain instead of switching due to the heating, leading to demagnetization. This threshold is referred to as the multi-domain fluence F_{multi} or demagnetization fluence F_{demag}. As depicted in Figure 5.5, toggle switching of a single magnetic domain is observed for excitation with a pulse duration of 50 fs and a low fluence of 1.9 mJ/cm^2. More interestingly, for laser fluence larger than 4.1 mJ/cm^2, the central region of the exposure spot stays in the red, indicating no switching of the magnetization. Subsequently, after the second pulse, the magnetization in the switching ring switches back to its initial state, signifying toggle switching in this region. Notably, the magnetization in the central region appears unaffected and remains in its initial state. With further increases in fluence, the magnetization in the central region switches again, resulting in the emergence of a captivating bullseye structure with adjacent rings exhibiting opposite magnetic directions. This behavior, where the central domain experiences alternating reversals or remains unchanged as the fluence increases until a certain threshold, is a stark departure from the behavior observed in GdFeCo.

5.1.3 Impact of the laser pulse duration

The laser pulse duration is also an important parameter to investigate the AO-HIS. The AOS measurements for 50 fs and 10 ps of pulse duration are shown in Figure 8.1a

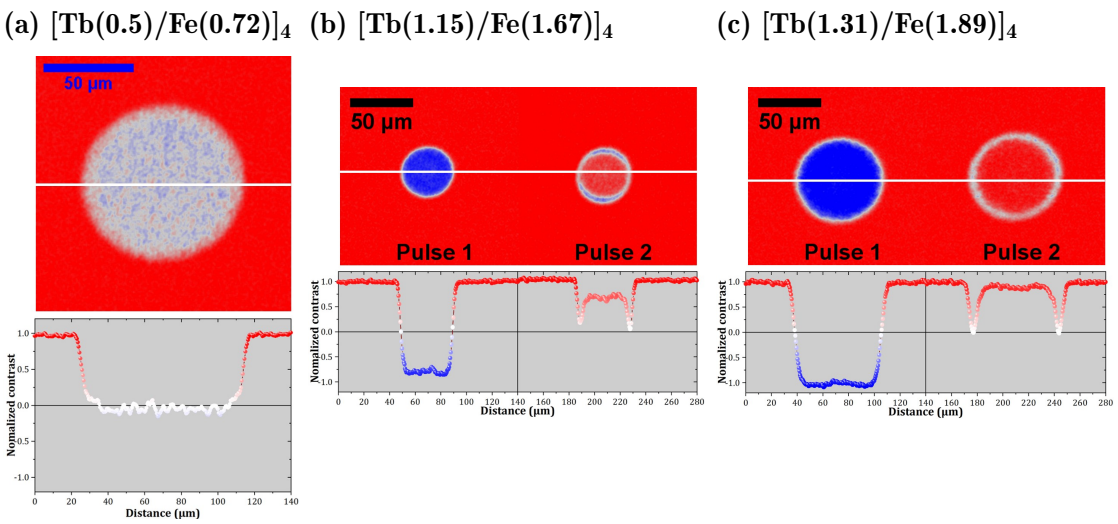

Figure 5.4: AOS measurements performed on $[Tb/Fe]_4$ multilayers with different thickness combinations with a 1:1.44 Tb and Fe thickness ratio using a pulse duration of 50fs. The fluences are (a): 6.93 mJ/cm^2, (b): 1.51 mJ/cm^2, and (c): 2.68 mJ/cm^2, respectively. (Thickness in nm)

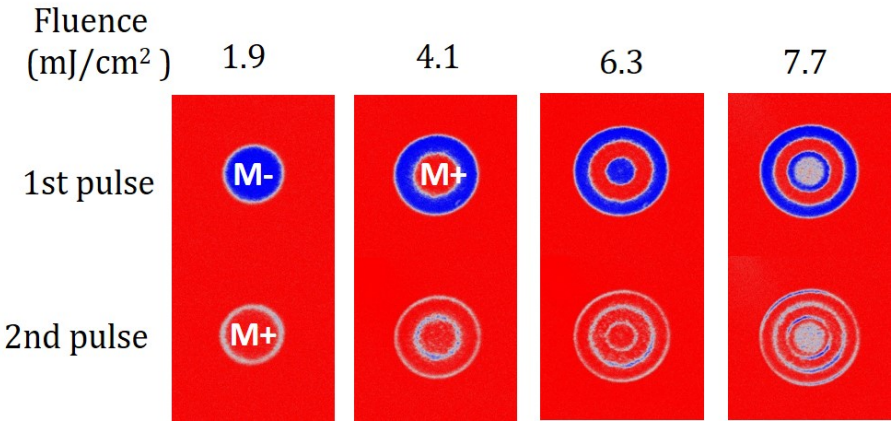

Figure 5.5: Single pulse switching for $[Tb(1.31\ nm)/Fe(1.89\ nm)]_4$ multilayer with different fluences of a 50 fs laser pulse under zero applied field. M+ (respectively M-) corresponds to magnetization pointing perpendicular to the film plane, along +z (resp. -z) in red (resp. in blue).

and 8.1b. Surprisingly, the single switching can be observed when the pulse duration is up to 10 ps. Besides, the switching behavior with 10 ps laser pulse does not differ too much from that of 50 fs. We still observe the bullseye ring structure. Because of the bullseye structure with opposite magnetic directions in adjacent rings, we have multiple threshold fluences instead of only two as it is for Gd-based materials. Each switching ring corresponds to two threshold fluences. Thus, the outermost switching ring corresponds to TF_1 and TF_2, the second outer ring corresponds to TF_3 and TF_4.....

The state diagram can be obtained by plotting each threshold fluences as a function of pulse durations. In the case of $Tb(1.31\ nm)/Fe(1.89\ nm)]_4$ multilayers, there are two switching rings until we see the multidomain in the central region. Consequently, we can extract four threshold fluences, namely TF_1, TF_2, TF_3 and TF_4 from the recorded images. These four thresholds effectively divide the state diagram into five distinct regions, each holding unique magnetic responses:

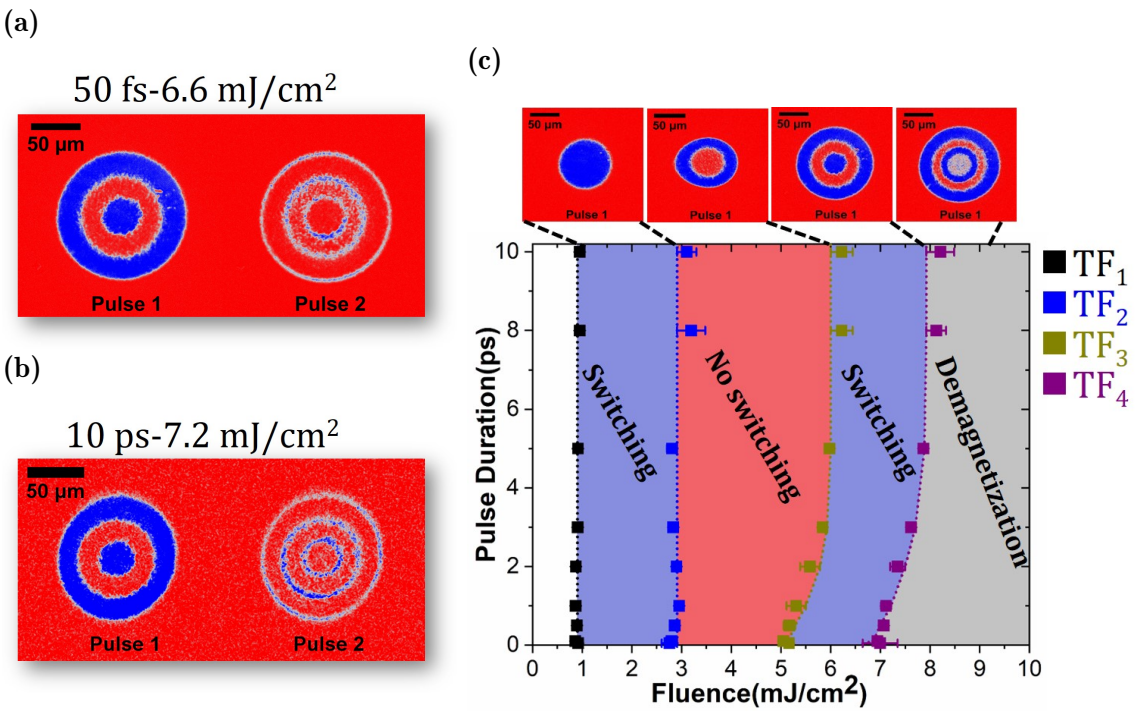

Figure 5.6: AOS measurements and State diagram in [Tb(1.31 nm)/Fe(1.89 nm)]$_4$ multilayers. AOS measurements with (a): 50 fs and (b): 10 ps of pulse durations with similar fluence. (c): State diagram of reversal pulse duration versus fluence. TF1 is the border for switching; TF2 is the border to two domains state (i.e., one ring); TF3 is the border to three domains state (i.e., two rings); TF4 is the border to a multidomain state at the center (i.e., three rings). The dotted lines are a guide for the eyes.

- Below TF$_1$ (also defined as F$_{switch}$), nothing happens, representing a state where no switching occurs.
- Between TF$_1$ and TF$_2$, we observe the first switching region.
- The region between TF$_2$ and TF$_3$ corresponds to the no-switching region, where the magnetization remains in its initial state.
- Between TF$_3$ and TF$_4$ represents the second switching region.
- Above TF$_4$, we observe demagnetization, where the sample ends as a multidomain state. This threshold is also identified as F$_{multi}$ or F$_{demag}$ here.

These five regions represent the final state of the central regions of the shooting spot we observe when given the corresponding fluence, while the images of the entire shooting spot we observe are at the upper of the state diagram.

This state diagram resembles neither the state diagram observed in the case of AO-HIS in GdFeCo[94] nor the state diagram observed in the case of multiple pulses All Optical Helicity Dependent Switching (AO-HDS)[83]. Here, TF$_1$ and TF$_2$ show complete independence on the pulse duration, while TF$_3$ and TF$_4$ increase with increasing pulse duration up to 3 ps, after which they remain constant for longer pulse durations. The fluences required to reverse and stabilize a given number of rings depend very little or not at all on the duration of the laser pulses.

In order to check the switching behavior in [Tb/Co]$_5$ multilayer, a cross double-wedge sample has been deposited. Similarly, [Tb/Co]$_5$ multilayer also shows bulls-eye ring structures when we applied a larger fluence. However, we can see two

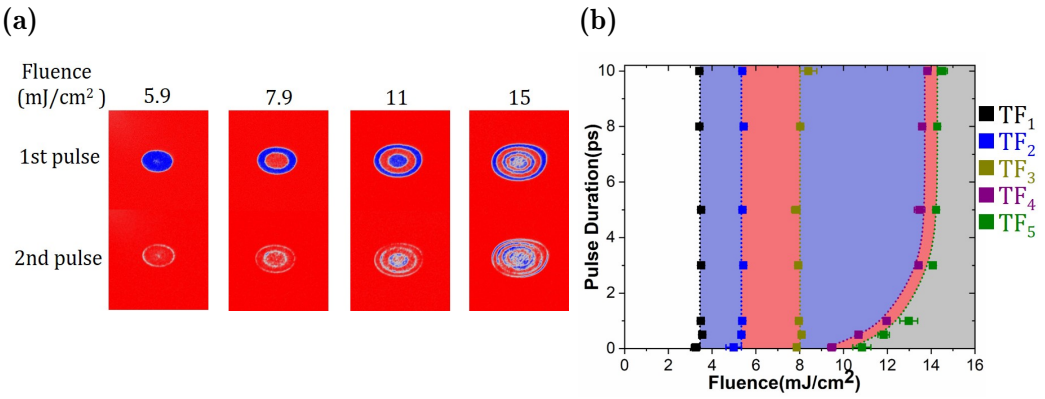

Figure 5.7: Single switching and state diagram in $[Tb(1.06\ nm)/Co(1.78\ nm)]_5$ multilayers. (a) Background subtracted images after the first single with 50 fs laser pulse of different fluence. (b) State diagram pulse duration versus laser fluence. TF1 is the border for switching; TF2 is the border to two domains state, one ring; TF3 is the border to three domains state, two rings; TF4 is the border to four domains state, three rings; TF5 is the border to multidomain state at the center and four rings. The dotted lines are a guide for the eyes.

switching and two no-switching rings until demagnetization in the central region. Consequently, we have five threshold fluences, and TF_5 is the F_{demag} in this case. Regarding the pulse duration vs. fluence state diagram, a similar shape was observed. However, the three lower threshold fluences, namely TF_1, TF_2 and TF_3 are independent of the pulse duration, while TF_4 and TF_5 increase as pulse duration increases up to 3 ps and remains a constant for longer pulse durations.

Since we have four threshold fluences for $[Tb/Fe]_4$ and five threshold fluences for $[Tb/Co]_5$, you may think that there is a link between the number of rings and the repetition of the bilayer. However, this is just a coincidence. We will talk about the impact of the laser thicknesses and some other parameters on the ring structure later.

Until now, we observed the single shot switching in both $[Tb/Co]_5$ and $[Tb/Fe]_4$ multilayers. Both Tb/Co and Tb/Fe multilayers behave similarly, both having ring structures and low dependence of the reversal fluences on the laser pulse duration. Both features will be considered to determine the conditions to obtain the reversal and to discuss the possible mechanism at its origin.

5.2 Test of the ingredients for single switching

In this section, some conditions or ingredients for single switching have been tested as follows:

- Magnetic structure of the multilayers on the switching;
- Anisotropy of Co and RE alloy layer on the switching;
- Direct exchange coupled RE/TM interface;
- .....

The magnetic structure of Tb-Fe films is divided into four regions; ferrimagnetically coupled Tb-Fe, ferromagnetic Fe, ferromagnetic Tb, and magnetically compensated Tb regions [139]. The ferrimagnetically coupled Tb-Fe region was observed

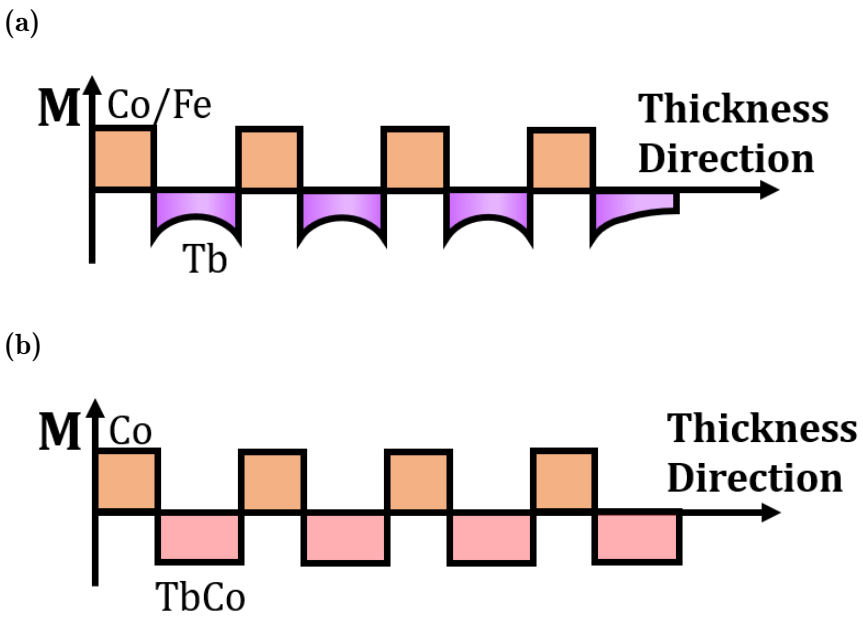

Figure 5.8: (a): Sketch of the magnetization profile in the Tb/Co(Fe) samples. In the Co(Fe) layers, the magnetization is considered constant, while in the Tb layers, the magnetization decays exponentially away from the interface. (b): Magnetic structure $[TbCo/Co]_N$ multilayers.

up to a Tb layer thickness of about 0.9 nm and an Fe layer thickness of about 1 nm from the Tb-Fe interface. Films with thicker layers of Tb and Fe are composed of ferrimagnetically coupled Tb-Fe, ferromagnetic Fe, ferromagnetic Tb, and/or magnetically compensated Tb regions. In the case of our Tb/Co and Tb/Fe multilayers, the thicknesses of Tb are generally more than 1 nm. As a consequence, the magnetic structure of the Tb layer contains not only the antiferromagnetically coupled interface but also the magnetically compensated Tb layer. This implies that the magnetism of the Tb layer exhibits non-uniformity in the thickness direction, where the magnetism is higher at the interface but gradually diminishes further away from it. Besides, it should be noted that the occurrence of sharp interfaces is not likely in the samples. During the sputtering process and afterward, over time, intermixing between the different layers can take place, resulting in the formation of an alloyed TbCo layer in between the Co and Tb layers, which increases the amount of Tb that is influenced by the proximity effect of the Co.

Thus, modifying its thickness will also lead to a variation of its anisotropy and its magnetic moment, consequently, a large change in magnetic properties. In order to check if thicknesses or the variation of the magnetic properties are key parameters in the process, and also we hope that the magnetic properties do not change too much with thickness, the Tb layer was replaced by a rare earth–transition metal (RE–TM) alloy with a high RE concentration so the net magnetization of the alloy layer points in the direction of the RE sublattice. Due to the high RE content, the alloy has a Curie temperature higher but close to room temperature[77] and possesses a perpendicular magnetic anisotropy (PMA).

5.2.1 $[\text{RE alloy/Co}]_N$ Multilayers

Firstly, a series of single-wedge $[Tb_{40}Co_{60}(X)/Co(2\text{ nm, wedge})]_3$ were deposited, where the $Tb_{40}Co_{60}$ is the replacement RE-TM alloy layer with a high Tb concen-

tration. X is the thickness of $Tb_{40}Co_{60}$ layer, which is fixed throughout the entire wedge and is 1 nm, 2 nm, 3 nm, 4 nm, 5 nm, and 7.5 nm, while the thickness of the Co layer spans 1 nm $< t_{Co} <$ 3 nm. When the thickness of the TbCo layer is too low, such as 1 nm and 2 nm, no magnetic compensation point is observed in the Co thickness range of 1–3 nm. Consequently, the samples across the entire Co thickness range exhibit Co-dominated behavior. When the thickness of TbCo reaches 3 nm, a magnetic compensation point emerges at 1.45 nm in the Co layer. As the thickness of TbCo increases, the magnetic moment of Co required to reach the magnetic compensation point also increases. Consequently, larger thicknesses of Co are necessitated to compensate for the magnetic moment of the Tb-sublattice.

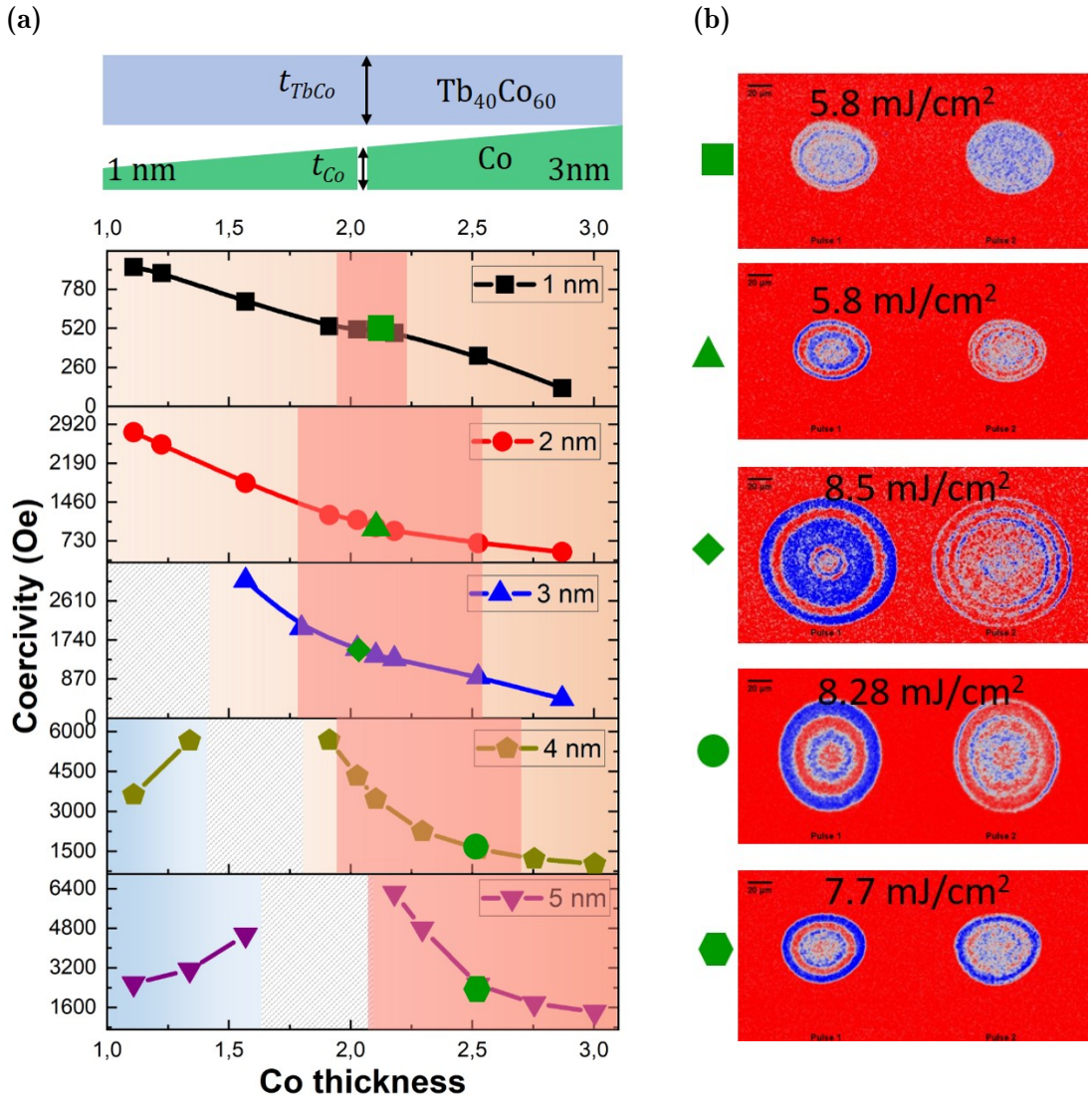

Figure 5.9: The magnetic and AOS measurements performed in [TbCo(X nm)/Co(2nm, wedge)]$_3$ multilayers, while the thickness of TbCo layer is 1 nm, 2 nm, 3 nm, 4 nm, and 5 nm respectively. (a): Coercivity as a function of Co thickness; (b): AOS results of the [TbCo(X nm)/Co]$_3$ multilayers corresponding to sample marked in (a). The blue color represents the Tb-dominate region, while the orange color represents the Co-dominate region. Besides, the light red color in (a) shows the region where single switching occurs.

The AOS measurements have been done throughout the entire wedge samples. The observation of single pulse switching for all samples is highly encouraging and highlights the robustness of our experimental results. In Figure 4.9a, the light red

color indicates the Co thickness range where switching behavior is observed. Notably, the thickness of Co undergoing switching is predominantly concentrated around 2 nm. Interestingly, as the thickness of TbCo increases, the minimum Co thickness required for switching becomes closer to the compensation point. It is fascinating that for some samples, once we cross the compensation point and enter into the Co-dominated region, we can see the ring structure, although these rings are composed of small magnetic domains instead of a single domain. We will discuss this point later when discussing the switching mechanism.

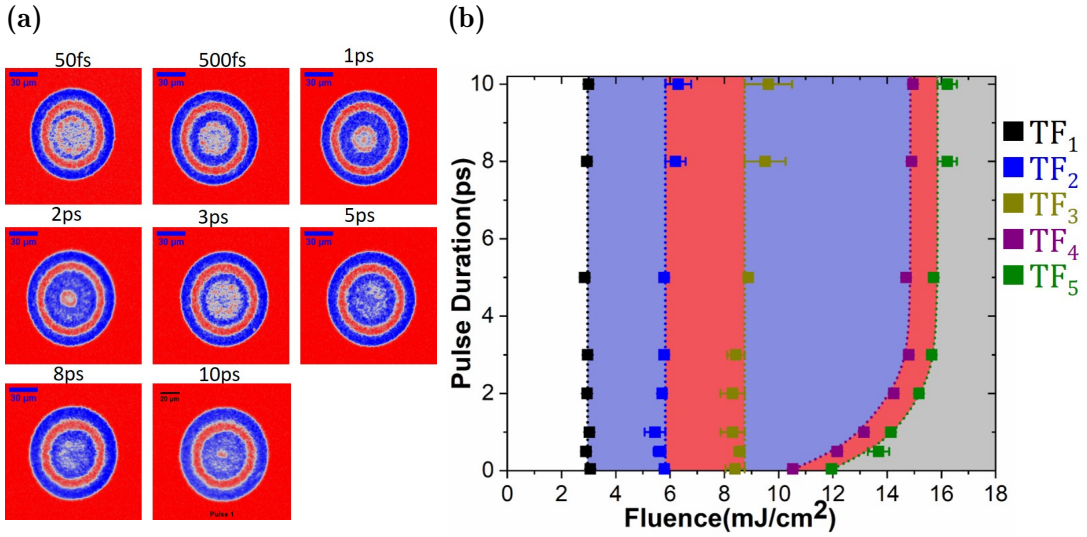

Figure 5.10: (a): AOS results with different pulse durations and (b): the state diagram of $[TbCo(4\ nm)/Co(2.5\ nm)]_3$

The AOS measurements have been done with different pulse durations up to 10 ps. One does not see any difference for the outermost blue and red rings (the first switching ring and no-switching ring) for all the pulse durations. It is obvious to see that the second switching ring (second blue ring) becomes larger and larger with an increase in pulse duration up to 2 ps. When the pulse duration increases to 3 ps, this switching ring does not continue to get larger but is split into two switching rings and a no-switching ring. As the pulse duration increases, each of the two rings changes. However, we do not show this in the phase diagram in figure 5.10b because the boundary between the two split rings is unclear, so it is impossible to extract the specific radius of the domain and, thus, the fluence value. In addition, new rings may appear in the gray area of the state diagram, representing demagnetization as the pulse duration increases. On the one hand, it may be due to physics reasons that new rings appear; on the other hand, it may also be because the energy distribution is not a very smooth Gaussian distribution (such as shown in Figure 3.12b), and the local peak of energy may lead to some very narrow rings. Therefore, we also did not take these narrow rings into account in the state diagram.

5.2.2 Single switching in Dy-based multilayers

In addition, Dy rare-earth elements were also considered due to the high spin-orbit coupling of its 4f electrons and the strong perpendicular anisotropy exhibited by its compounds with transition metals. Another series of single-wedge samples $[Dy_yCo_{100-y}(4\ nm)/Co(2nm,\ wedge)]_3$ multilayers are used to test the switching behavior, where the Dy concentration y in DyCo layer is 25, 30, 35 respectively. All

the samples exhibit perpendicular anisotropy with all the Co thicknesses. In addition, the magnetic compensation point occurs at 1.1 nm, 1.3 nm, and 1.5 nm for $[Dy_{30}Co_{70}(4\ nm)/Co(2\ nm,\ wedge)]_3$ and $[Dy_{35}Co_{65}(4\ nm)/Co(2\ nm,\ wedge)]_3$, and $[Dy_{40}Co_{60}(4\ nm)/Co(2\ nm,\ wedge)]_3$, respectively.

Only demagnetization has been observed for the samples with 40 of Dy concentration. For the samples of the other three concentrations of samples, the magnetization can be reversed by a single pulse within a certain range of Co thickness. For the Dy concentration Dy of 25 and 35, the sample shows single switching when the thickness range of Co is between 2 nm and 2.5 nm. When the composition of Dy is 30, the thickness of Co, where it shows single switching, is relatively large, ranging from 1.8 nm to 2.9 nm. This result once again shows that the single-shot switching that occurs in the multilayer film structure is related to the thickness of the single layer and further related to the magnetic properties of the multilayer film, such as magnetization and/or anisotropy.

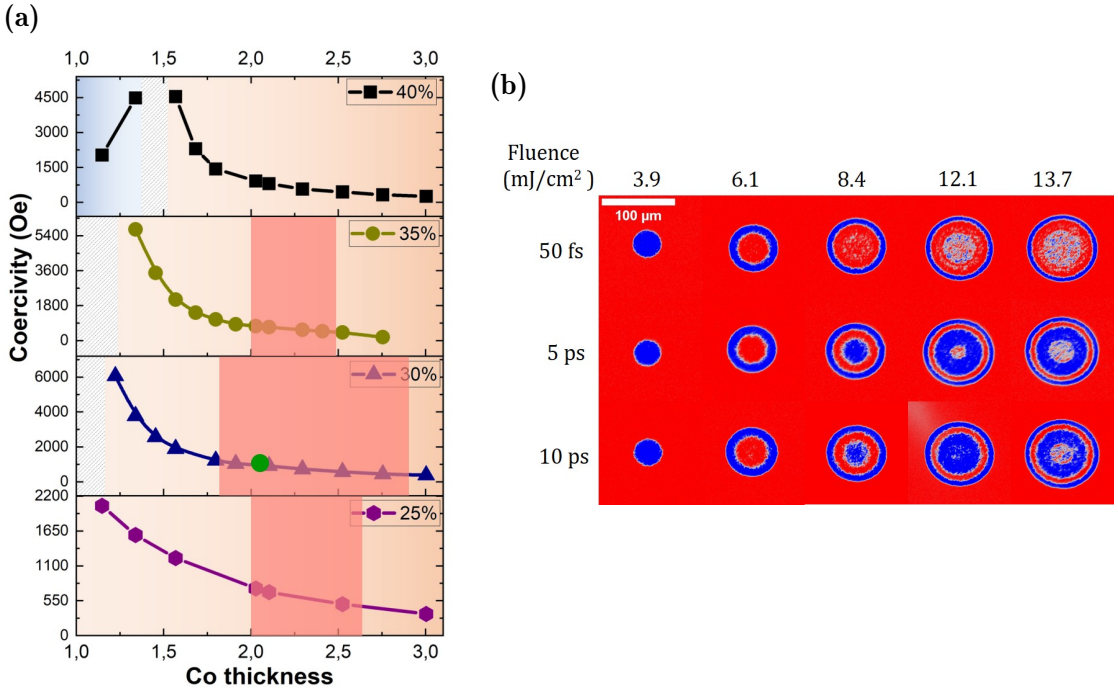

Figure 5.11: The magnetic and AOS measurements performed in $[Dy_yCo_{100-y}(4\ nm)/Co(2\ nm,\ wedge)]_3$ multilayers, where the Dy concentration y in DyCo layer are 25, 30, 35 and 40 respectively. (a): Coercivity as a function of Co thickness; (b): AOS results of the $[Dy_{30}Co_{70}(4\ nm)/Co(2.1\ nm)]_3$ multilayers corresponding to sample marked in (a). The light red color in (a) shows the region where single switching occurs.

The AOS images exhibit striking similarities to those of the Tb-based multilayers. When the fluence is 3.9 mJ/cm^2 and 6.1 mJ/cm^2, there is no difference in AOS images there are no discernible differences in the AOS images, regardless of the pulse duration used. But when the power is 8.4 mJ/cm^2, some white dots begin to form a distinctive ring in the inner red area of the images. Remarkably, as the pulse duration increases, this ring becomes more obvious and eventually becomes a fully switching domain. This magnetic behavior closely resembles what we observe in $[TbCo/Co]_3$ multilayer. But there is also a little difference: under larger pulse durations, the ring formed by small magnetic domains remains intact, and it does not split into two separate switching rings, as observed in $[TbCo/Co]_3$ multilayer.

As a conclusion for the section, Single-shot switching is not only observed in

rare earth/transition metal multilayers but also in rare earth alloy/transition metal multilayers, which indicates that the magnetic gradient or magnetic inhomogeneity in the rare earth layer is not the key point of switching. Nevertheless, the magnetic properties, as well as the magnetic anisotropy, seem to have some influence on the switching since the single-shot switching only occurs in the Co-dominate region within a certain thickness range.

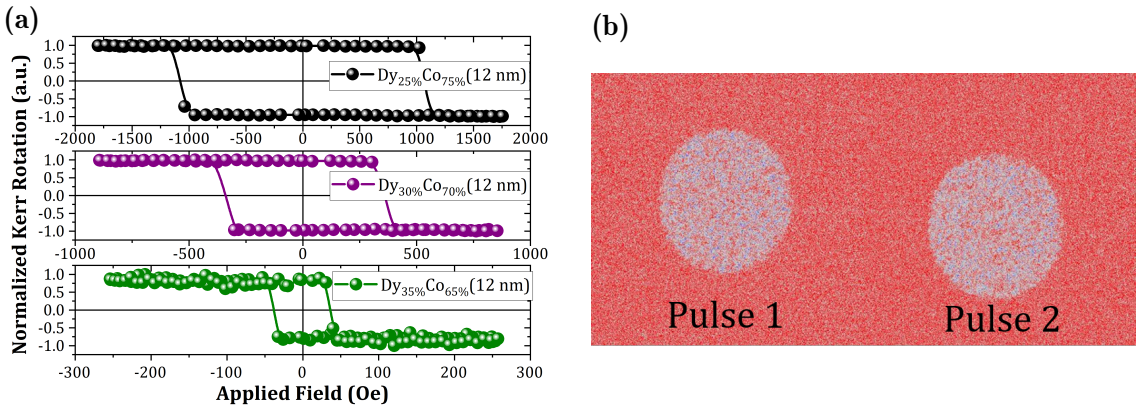

Figure 5.12: (a): The perpendicular MOKE hysteresis loops of 12 nm of DyCo alloy with different compositions. (b): AOS measurements performed in $Dy_{30}Co_{70}$

Based on the switching in RE alloy/TM multilayers, we then remove the TM layers to check the switching in the RE alloy layer. As shown in figure 5.12a, all the 12 nm of DyCo alloy with varying compositions exhibit perpendicular anisotropy and are dominated by Dy-sublattice. However, the AOS results didn't show single-shot switching in DyCo alloy; instead, a multidomain state was observed after each laser pulse.

To gain further insights, we compared our findings to a previous study on DyCo alloy [117], where single-pulse all-optical partial switching had been achieved. Notably, in our case, the DyCo alloy is dominated by the Dy-sublattice, leading to a compensation temperature above room temperature, which differs from Hu's work. This discrepancy could potentially explain the absence of switching in our rare earth alloy if the switching mechanism in Hu's work is similar to that in our multilayers. The compensation temperature might be a crucial factor in determining whether a single switching occurs or not. Furthermore, introducing a Co layer into the alloy to form a multilayer alters the sample's structure as the first notable change. However, the specific impact of the magnetic properties or structural characteristics of the Co layer on the switching process remains unclear at present. In-depth investigations are required to elucidate the precise influence of the Co layer on the overall switching behavior within the multilayer system.

5.2.3 Test of the anisotropy in Co layer

We have tested the Tb/Fe, Tb/Co, and TbCo/Co multilayers and found that the magnetism gradient in Tb layer does not play a role in the switching. Now, we consider the anisotropy of the Co layer.

Here, we deposited another series of samples with the RE alloy layer composition of $Tb_{32}Co_{68}$. According to the results of DyCo/Co multilayers with different Dy compositions in the DyCo layer, we have discovered the potential for a broad range of RE compositions to enable effective switching. Firstly, a series of bilayers Pt/Co(2 nm, wedge)/$Tb_{32}Co_{68}$(x) where the thickness of $Tb_{32}Co_{68}$ are 4 nm, 8 nm, and 16

nm, respectively. When the thickness of $Tb_{32}Co_{68}$ is 4 nm, the sample exhibits Co-dominate behavior throughout the entire wedge, in which the coercivity decreases as Co thickness increases. Conversely, it is Tb-dominate with 16 nm of $Tb_{32}Co_{68}$

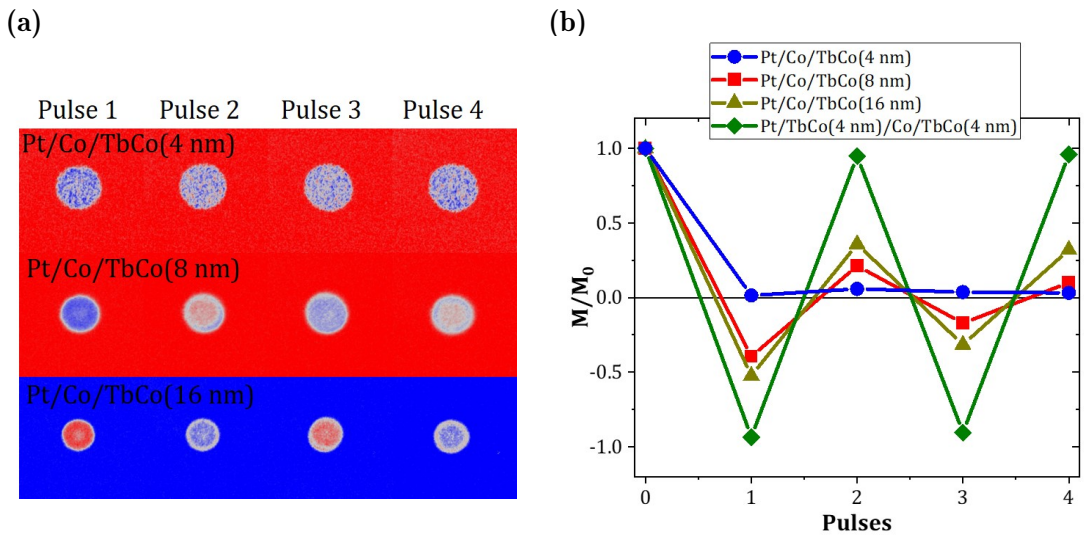

Figure 5.13: (a): Single pulse switching in Pt/Co(2.27 nm)/$Tb_{32}Co_{68}$(x) bilayer where x is 4 nm (top), 8 nm (middle) and 16 nm (bottom). (b): The changes of magnetization around the center of the spot, estimated from magnetic contrast, are plotted as a function of the number of pulses. The value of $Tb_{32}Co_{68}$(4 nm) /Co(2.27 nm)/$Tb_{32}Co_{68}$(4 nm) is given for comparison.

of the bilayer in which the coercivity increases as Co thickness increases. With 8 nm of $Tb_{32}Co_{68}$, the coercivity diverges where Co thickness is 1.2 nm, indicating a magnetic compensate point.

Let's look at the single switching in the bilayers. The switching images and the magnetization changes in the laser-exposed spot after each pulse are shown in Figure 5.13. For 4 nm of $Tb_{32}Co_{68}$, only a multidomain state can be observed after sending the 50 fs laser pulse; correspondingly, the Normalized M/M_0 changes from 1 to 0. After that, the net magnetization in the laser spot keeps a constant of 0, as shown in figure 5.13b. As the $Tb_{32}Co_{68}$ thickness increased to 8 nm within the Co-dominant region, Partial switching can be seen. The magnetization change value changes from 1 to -0.5 for the first laser pulse, alternating and attenuating between ± 0.5 for the consequent pulses. Interestingly, single switching has been observed in the Tb-dominate region with 16 nm of $Tb_{32}Co_{68}$, in which the magnetization change value surpassed even that of the case of 8 nm, indicating a better single switching.

A Ta(5)/Pt(5) buffer layer was used in all the stacks to provide strong perpendicular anisotropy due to the Pt/Co interface. As one can see in figure 5.13 and 5.14a, the magnetization in Pt/Co/TbCo bilayers can not be switched by the single laser pulse. However, If we change the stack to Pt/TbCo/Co with weaker anisotropy in the Co layer due to the absence of the Pt/Co interface, the magnetization can partially be switched by each single laser pulse. Encouraging switching has been observed in the Pt/TbCo/Co/TbCo trilayer by adding one TbCo layer on top of the Pt/TbCo/Co bilayer, leading to two TbCo/Co exchange coupled interfaces and reduced anisotropy in the Co layer. Similar AOS results were also been obtained in Co/DyCo bilayers and DyCo/Co/DyCo trilayers (See figures 5.16 and 5.17).

Comparing the response of the magnetic moment in bilayers and trilayers to the single laser pulse, it can be reasonably inferred that the anisotropy of Co should not

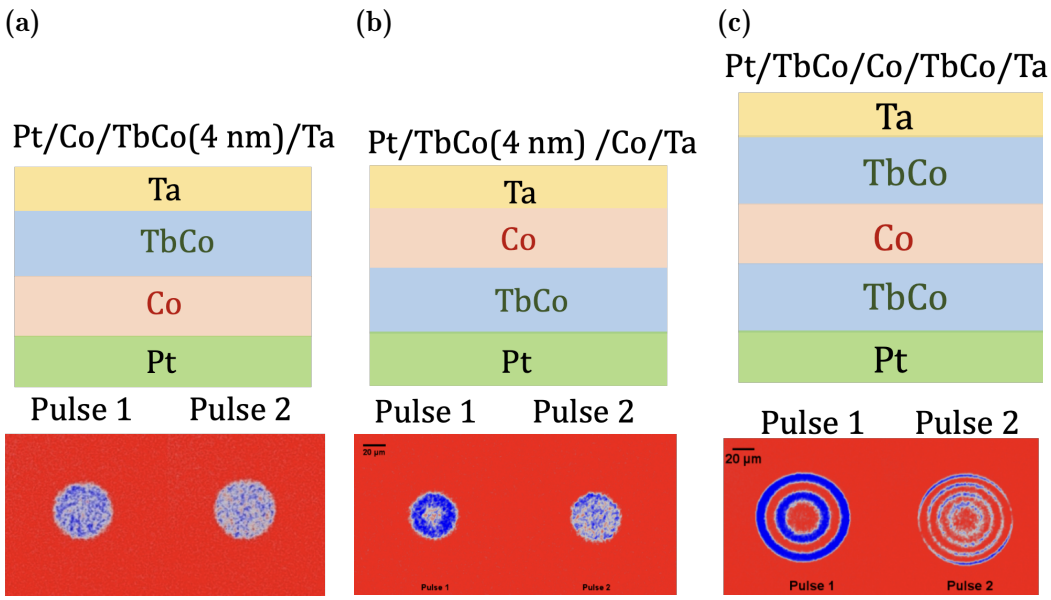

Figure 5.14: (a): Single pulse switching in Pt/Co(2.27 nm)/$Tb_{32}Co_{68}$(x) bilayer where x is 4 nm (top), 8 nm (middle) and 16 nm (bottom). (b): The changes of magnetization around the center of the spot, estimated from magnetic contrast, are plotted as a function of the number of pulses. The value of $Tb_{32}Co_{68}$(4 nm) /Co(2.27 nm)/$Tb_{32}Co_{68}$ (4 nm) is given for comparison.

be too strong in order to realize the single-pulse switching in our RE/TM system. Furthermore, multiple exchange coupling interfaces between RE(RE alloy) and TM become imperative for attaining individual switching events. By duplicating the RE (or RE alloy)/TM bilayer to construct a multilayer stack, two significant outcomes arise: firstly, the perpendicular anisotropy of the Co layer is reduced due to the absence of a Pt/Co interface, and secondly, the RE/TM exchange coupling interface is integrated. Consequently, this arrangement facilitates the attainment of single-pulse switching within a multilayer system.

In addition, a thin Cu layer was inserted at the RE/TM interface to study the effect of the direct exchange coupled RE/TM interface on the single switching. We formulated two distinct stack configurations for this purpose: one involved the insertion of a Cu layer at a single TbCo/Co interface in the $Tb_{32}Co_{68}$(4 nm)/Co(2 nm)/$Tb_{32}Co_{68}$(4 nm) trilayer, while the other entailed the insertion of a Cu layer at both interfaces.

When considering the presence of Cu at a single interface, clear instances of single switching become evident with a thin Cu layer thickness, for example, 0.5 nm. Even though the second pulse doesn't fully accomplish magnetic moment switching and leaves some magnetic domains unchanged, this doesn't hinder the observation of single-pulse switching. Nevertheless, as the Cu thickness increases to 1.25 nm, the single-pulse switching response disappears, replaced by a multi-domain state. However, when the thickness of Cu increases to 1.25 nm, the switching of the magnetic moment under the excitation of a single pulse can no longer be observed, and a multi-domain state replaces it. For the case of Cu at the two interfaces, even if the thickness of Cu is thin, some magnetic domains can be switched under the excitation of laser pulses, but compared with the Cu layer without any interface, the number of magnetic domains that do not switch is much more for trilayers without Cu. When the thickness of Cu increases to 1.2 nm, the whole system becomes Tb-dominated, which should be due to the RKKY exchange coupling effect, and only

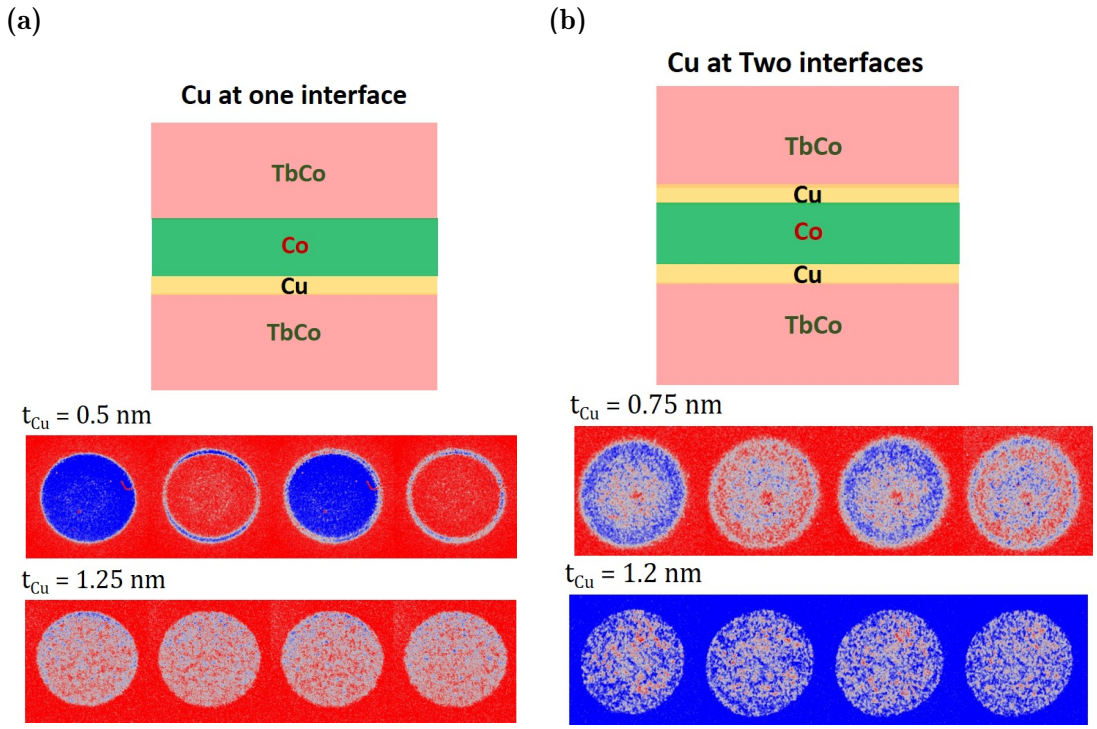

Figure 5.15: Single pulse switching in $Tb_{32}Co_{68}$/Co/$Tb_{32}Co_{68}$ trilayers with one Cu at the interface; (a): Cu at one interface and (b): Cu at two interfaces.

demagnetization was observed without any sign of switching.

5.2.4 Conclusion for switching ingredients

We qualitatively tested the effect of some conditions on whether the sample can undergo single-pulse switching so as to design the stacks to obtain better single-shot switching.

- Firstly, two antiferromagnetically coupled sublayers are necessary. One of these sublayers is RE-dominate, while the other is TM-dominate, which is Co in our case. The RE layer can comprise heavy rare earth metals like Tb or Dy or their respective alloys. In essence, the uniformity of the magnetic structure within the RE layer does not stand as a prerequisite for the occurrence of switching.

- The thickness of the Co layer should not be either too thick to maintain the perpendicular anisotropy or too thin to reduce its anisotropy.

- The exchange-coupled RE/Co interface also provides Co sublayer perpendicular anisotropy without the Co/Pt interface. At the same time, the interfacial pair magnetism is also non-negligible due to the antiferromagnetic exchange coupling. Although the magnetic structure of each sublayer is not the key factor for switching, the temperature-dependent magnetism and anisotropy of the whole system play a significant role.

- By duplicating the RE (or RE alloy)/TM bilayer to construct a multilayer stack, on the one hand, the perpendicular anisotropy of the Co layer is reduced due to the absence of a Pt/Co interface; on the other hand, the RE/TM exchange coupling interface is integrated.

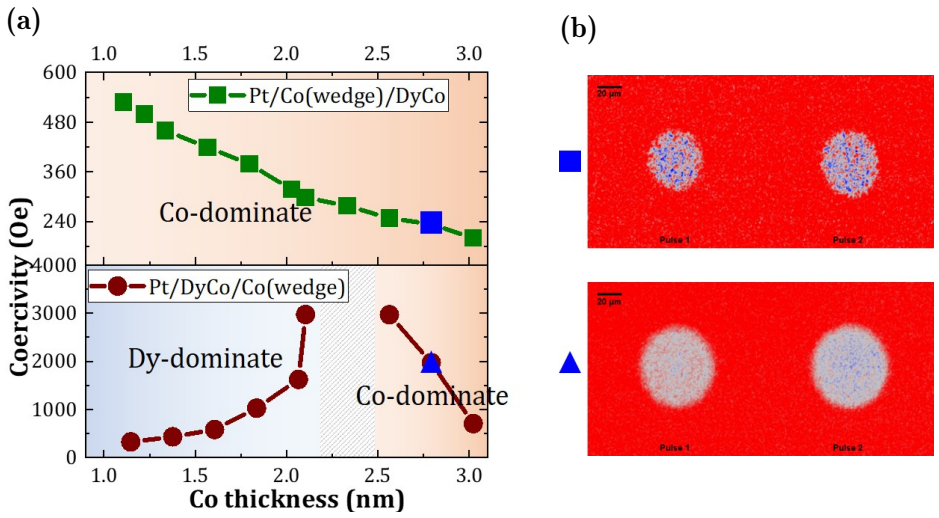

Figure 5.16: The magnetic and AOS measurements performed in Pt/Co(2 nm, wedge)/$Dy_{35}Co_{65}$(4 nm) and Pt/$Dy_{35}Co_{65}$(4 nm)/Co(2 nm, wedge) bilayers.

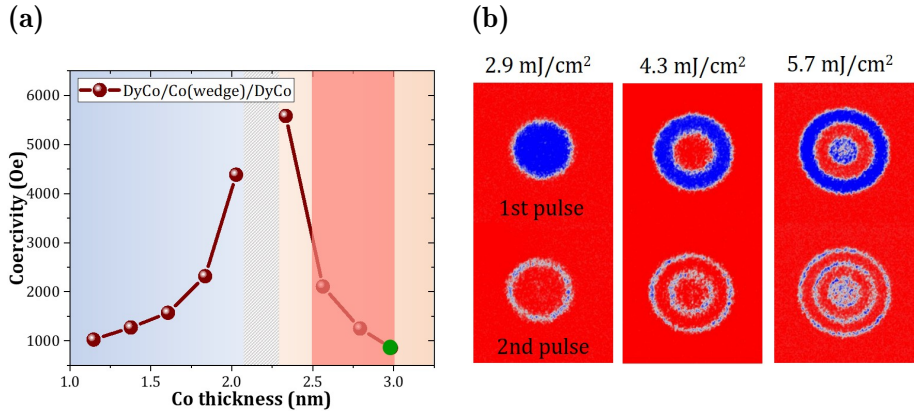

Figure 5.17: Single switching in $Dy_{35}Co_{65}$(4 nm)/Co(2 nm, wedge)/$Dy_{35}Co_{65}$(4 nm) trilayer. The light red color shows the region of Co thickness (2.41 nm $< t_{Co} <$ 3.02 nm) where single shot switching occurs; (b) AOS results after each 50 fs laser pulse with different fluences, where t_{Co} = 2.98 nm.

Based on those concepts and ingredients, we tested large varieties of samples, including [TbCo/Co], [TbCo/$Ni_{80}Fe_{20}$], [TbCo/$Co_{40}Fe_{40}B_{20}$], [DyCo/Co], [TbFe/Co] multilayers. In the following, $Ni_{80}Fe_{20}$ (respectively $Co_{40}Fe_{40}B_{20}$) is referred to as Py (respectively CoFeB). The complete study indicates that all those combinations of multilayers show a similar all-optical switching behavior, i.e., a single pulse magnetization reversal with a ring structure and pulse duration-independent threshold fluences. Besides, we are able to switch the magnetization in a multilayer structure with a total thickness of up to 30 nm. For most of the samples, the switching only occurs in the TM-dominant region. However, we also observed some partial switching in the Tb-dominant region when the TbCo layers are very thick, such as in the case of [TbCo(7.5 nm)/Co(wedge)]$_3$ and Pt/Co(wedge)/TbCo(16 nm). Within the large variety of samples, since the perpendicular anisotropy in TbCo, DyCo, or TbFe alloys is expected to disappear as the lattice temperature rises after the laser pulse, the simplest multilayers to characterize are then TbCo/X/TbCo (X = Co, Py, CoFeB), Y/Co/Y (Y = DyCo, TbFe) trilayers in which Co, Py and CoFeB, the perpendicular anisotropy are induced by its proximity with TbCo, DyCo or TbFe alloys without any Pt/TM interface.

	Stacks		Thickness of the TM layer
1	[Tb(wedge)/Fe(wedge)]*4		0.8 nm 1.2 nm 1.6nm 2.0 nm 2.4 nm 2.8 nm 3.2 nm
2	[Tb(wedge)/Co(wedge)]*5 (Cross wedge)		2.0 nm 2.6 nm 3.2nm 3.8 nm 4.4 nm 5.0 nm 5.6 nm
3	$[Tb_{40}Co_{60}(x)/Co(wedge)]*3$	x = 1	
4		x = 2	
5		x = 3	
6		x = 4	
7		x = 5	
8		x = 7,5	
9	$[Dy_yCo_{100-y}$ (4) /Co(wedge)]*3	y = 25	
10		y = 30	
11		y = 35	
12	Pt(5) /Co(wedge)/ $Tb_{32}Co_{68}$ (4)		
13	Pt(5) /Co(wedge)/ $Tb_{32}Co_{68}$ (8)		
14	Pt(5) /Co(wedge)/ $Tb_{32}Co_{68}$ (16)		
15	$Dy_{35}Co_{65}$ (4) /Co(wedge)/ $Dy_{35}Co_{65}$ (4)		
16	$Tb_{32}Co_{68}$ (4) /Co(wedge)/ $Tb_{32}Co_{68}$ (4)		
17	$Tb_{32}Co_{68}$ (4) /CoFeB(wedge)/ $Tb_{32}Co_{68}$ (4)		
18	$Tb_{55}Fe_{45}$ (4) /Co(wedge)/ $Tb_{55}Fe_{45}$ (4)		
19	$Tb_{32}Co_{68}$ (4) /Permalloy (wedge)/ $Tb_{32}Co_{68}$ (4)		

Table 5.1: Series of stacks that have been studied in this thesis: 1-11 are multilayers, 12-14 are bilayers, and 15-19 are trilayers. The light pink color shows the TM layer (including Co, Fe, CoFeB, and Permalloy) thickness range that has been studied in this paper, while the blue color shows the region of TM thickness where single shot switching occurs in different stacks. Note that stack 1 is a double-wedge sample in the same direction, while stack 2 is a cross-wedge sample. Numbers shown within the brackets are the layer thicknesses in nanometers.

5.3 Ring structure

The bullseye structure with opposite magnetic directions in adjacent rings is one of the striking behaviors of single-shot switching in multilayers. The ring-shaped magnetic texture resembles the observation by Davies et al. in reference [140] in the dielectric bismuth-substituted YIG. A nonlinear magnetization precession was triggered by a transient thermal modification of the growth-induced crystalline anisotropy. For the heat-assisted pump with a Gaussian profile, the heat-induced anisotropy modification showed a radial gradient; depending on the odd or even number of half-periods of the precession, alternate rings of up and down were stabilized. Whether the formation mechanism of the ring structure is the same as this remains unclear. Before delving into the specifics of the ring structure's formation, we initially assess whether certain factors influence its creation.

5.3.1 Laser spot size effect

The first thing to test is whether the size of the laser spot affects ring formation. We conducted tests using two distinct laser spot diameters, 75 µm and 110 µm, corresponding to total energy delivery of 0.6 μJ and 1.2 μJ, respectively. As depicted in Figure 5.18a and 5.18b, we obtained the same number of rings: two switching rings,

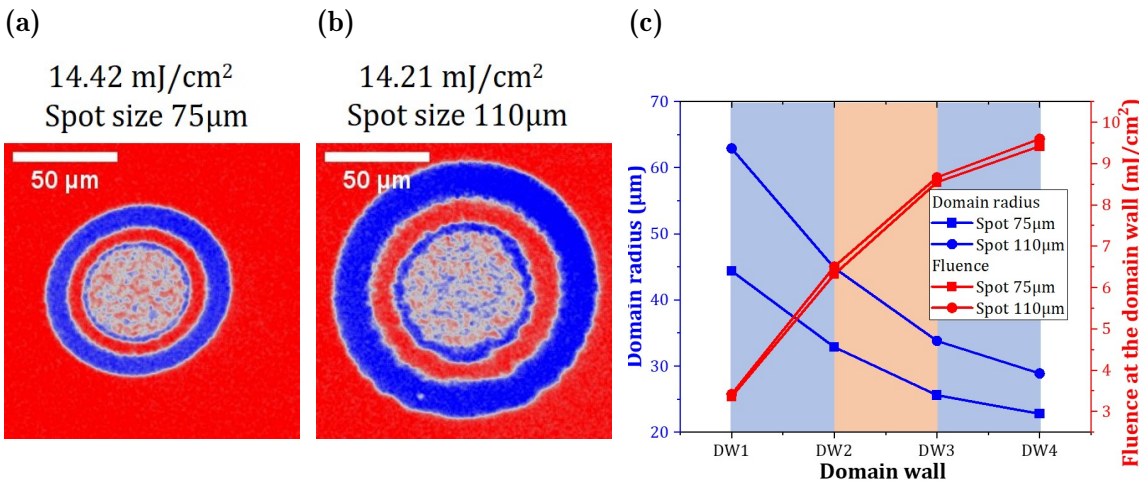

Figure 5.18: Test of influence of the laser spot size on the ring structure. The MOKE images were recorded after sending one single laser pulse with the laser spot diameter (a): 75 µm and (b): 110 µm. (c): The domain radius and the local fluences at each domain wall.

one no-switching ring, and demagnetization in the central region. Each switching ring corresponds to two domain walls (DW); for instance, the first switching ring corresponds to DW1 and DW2, and the second switching ring corresponds to DW3 and DW4. We extracted and compared the radius of each domain wall with different laser spot sizes. The radius with 110 µm of laser spot size is larger than those with 75 µm of laser spot size. The local fluences extracted according to the laser Gaussian profile at each domain wall are the same for different laser spot sizes.

While the size of the laser spot does not impact the emergence of the ring structure, the ring's dimensions are closely linked to the laser spot size. Moreover, the Gaussian energy distribution of the laser guarantees that a spatial point corresponding to any energy value within the range of 0 to the energy peak value can be identified. Consequently, the spatial distribution of laser pulse energy dictates the observing ring structures. For example, using a rectangular pulse, the outcome is contingent on the laser energy: the sample can solely undergo switching, no-switching, or demagnetization, but the simultaneous occurrence of all three outcomes is unattainable.

5.3.2 Dipolar effect

Two partly overlapping pulses have been sent to the sample to test if the dipolar field plays a role in forming the ring structure. The local magnetic state is found to be independent of the configuration of the neighboring first domains and depends only on the distance to the spot center, namely the local laser fluence. For the fluence used in the experiment shown in Figure 5.19a, region 2 experiences 2 reversals, one for each pulse, region 1 (respectively 1') experiences reversal for pulse 1 (respectively 2) and the state of region 0 does not change.

Besides, four successive pulses were sent to the sample saturated with the applied field. Toggle switching of the magnetization can be observed. Subsequent to this, continuous laser irradiation followed the four pulses. Due to continuous heating, the magnetic domain structure becomes random after the continuous laser stops. Taking this randomized domain configuration as the initial state, another set of four consecutive laser pulses was sent to the sample. This scenario is illustrated

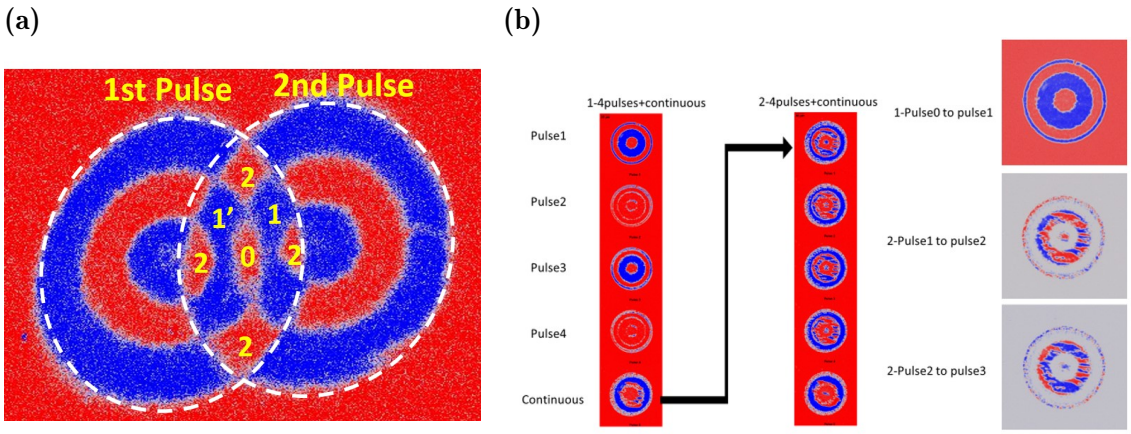

Figure 5.19: (a): Domain pattern obtained by sending 2 successive pulses: a first one and then, after moving the laser at a distance smaller than the spot size, a second one. The two spots are then overlapping. The experiments were done on a [Tb(1.31 nm)]/Fe(1.89 nm)]$_4$ multilayer. The color scale corresponds to magnetization pointing out of the plane: M+ (respectively M-) along the perpendicular to the film plane, along +z (resp. -z) in red (resp. in blue). The sample is initially saturated along the M+ direction. The laser pulse has a fluence of 5.2 mJ/cm^2 and a duration of 50fs. (b): Images recorded after twice of 4 pulses + continuous laser. The sample was only saturated with a magnetic field once. The difference between the two pulses is the image subtracted by the previous pulse.

as "2-4 pulses + continuous" in the second column of Figure 5.19b. After sending the first pulse on the saturated sample, the image is recorded as 1-pulse 0 to pulse 1. Furthermore, the images titled "2-pulse 1 to pulse 2" and "2-pulse 2 to pulse 3" capture the disparity between the 2-pulse 1 and pulse 2 and 2-pulse 2 and pulse 3, respectively. We found that the regions where the magnetization switches are the same as the switching regions on a saturated sample. This reaffirms that the creation of the ring structure is not a consequence of the dipole field but rather relies on the proximity to the center of the laser spot.

5.3.3 Laser fluence

Whether the sample can switch and the size of the switching area are closely related to the energy received by the sample. This connection is captured by the relationship between the switching domain radius r as a function of the beam radius R, pulse energy E and pulse energy threshold E_{th}:

$$r = R\sqrt{\ln\left(\frac{E}{E_{\text{th}}}\right)}$$

By extracting multiple magnetic domain radii and plotting them against pulse energies, we can employ the above function to fit the domain radius versus pulse energy curves. This procedure provides insights into both the beam size and the threshold energies for each domain wall. Once the beam radius is determined, the pulse energy profile can be expressed as:

$$E(r) = Ee^{(-\frac{r}{R})^2}$$

. Consequently, the local energy at each domain wall can be derived. As depicted in Figure 5.20c and 5.20d, regardless of the energy magnitude directed at the sample, the corresponding domain wall consistently maintains the same local energy level. Once again, the pivotal factor in determining whether the magnetic moment can be

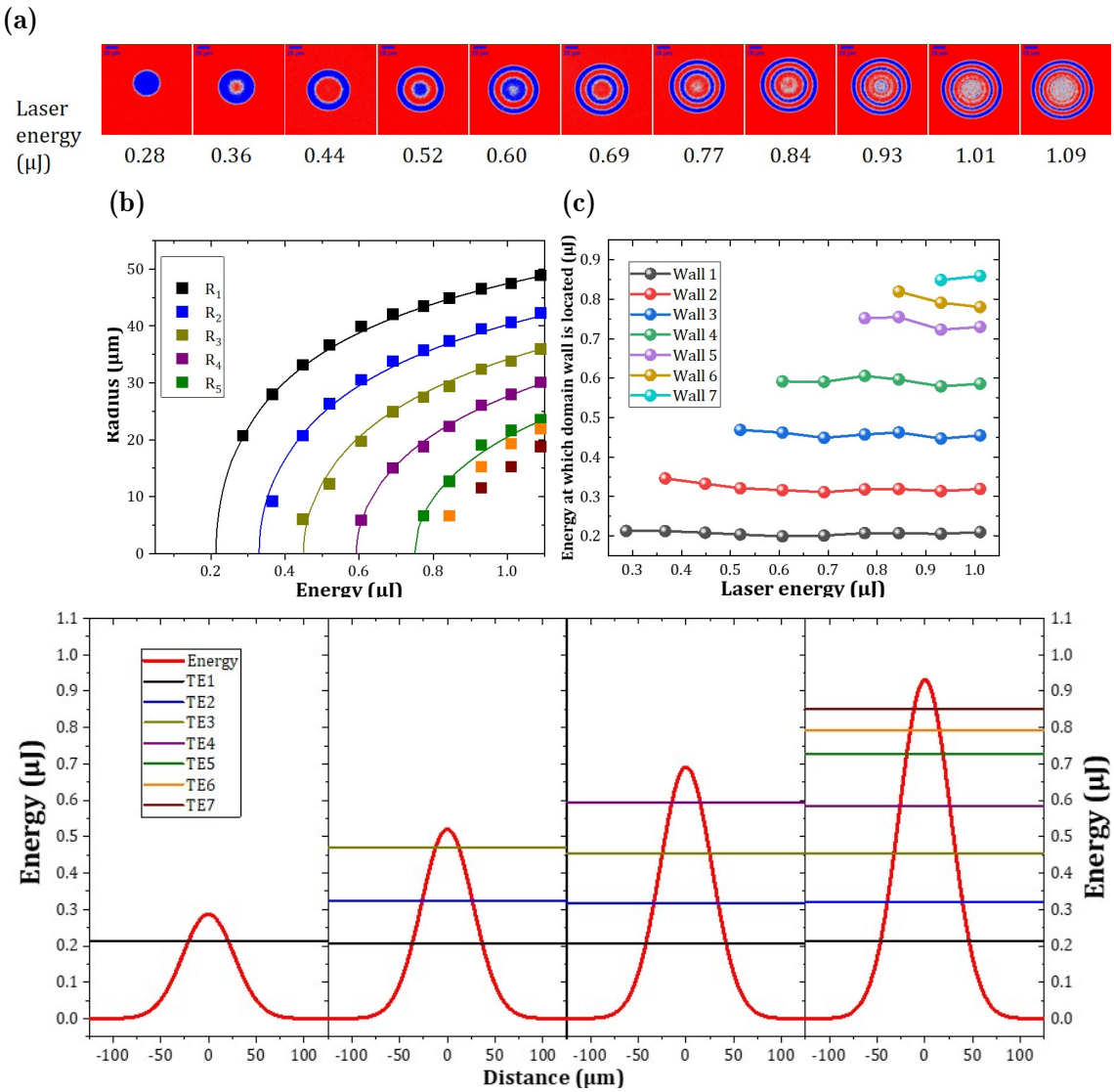

Figure 5.20: Analysis of the domain wall position of the ring structure, in space and energy, versus laser pulse energy in $Tb_{32}Co_{68}$(4 nm)/Co(1.52 nm)/$Tb_{32}Co_{68}$(4 nm) trilayer. (a): The images were recorded after sending a single laser pulse with different energies. (b): Ring radius versus energy. (c): Plot of the Gaussian laser profile for different laser energies and report of the ring radius. (d): Local energy of the domain walls and laser energy profile.

switched is the local energy, entirely unrelated to the laser spot size or the dipole field.

5.4 In-plane reorientation-induced magnetization precession switching mechanism

So far, we demonstrated the AO-HIS and ring structure in a large variety of multilayers and trilayers using static microscopy measurements. Previously, similar ring structures have been observed in ferrites, and they have been attributed to the reorientation of the magnetization from out-of-plane to in-plane followed by its precession [140, 141]. In metallic thin films[142], magnetization precession could be observed without magnetization reversal. In both cases, an in-plane magnetic field was applied for ferrites and metallic thin films, which is not the case in our study. Despite this, the magnetization reversal process involves an in-plane magnetization reorien-

tation and potentially a precessional mechanism. In the following, we will test the hypothesis of a spin reorientation accompanied by a precession.

5.4.1 Time-resovled MOKE dynamics

Time-resolved magneto-optic Kerr images (TR-MOKE images) were used to capture the dynamic behavior, involving recording a sequence of images for various time delays between the pump and probe pulses. The polar geometry employed in these measurements predominantly probes the component of transition metal magnetization perpendicular to the film plane. In this stroboscopic measurement setup, the magnetic configuration is reset after each pulse, necessitating the application of a continuous (DC) magnetic field during the measurement. Due to the laser-induced heating, the magnetic field required to initialize the magnetization is much lower than the coercivity. The laser repetition rate has been optimized to get the best contrast without changing the properties of the layers (annealing or burning). The images are recorded at a certain time delay of up to 1 ns. And we subtracted data for opposite external magnetic field directions.

The TR-MOKE images obtained in $[Tb_{40}Co_{60}(4\text{ nm})/Co(2.1\text{ nm})]_3$ multilayer with a fluence of 6.5 mJ/cm^2 are displayed in Figure 5.21a. The magnetic contrast changes from a bright, saturated background to the ultrafast appearance of a spot with darker contrast (at 0 ps) and gets darker and darker until 1 ps. Following this, an initial reduction of the laser-induced contrast change and then an increase starting at $\sim$ 3 ps until a homogeneous spot is eventually stabilized at $\sim$ 100 ps. Until 1 ns, the laser-induced spot seems to retain the same contrast, although its area decreases and its edges become better defined.

According to the Gaussian distribution of the laser pulse energy, the dynamics signal in spatial corresponding to fluence can be extracted from the TR-MOKE images. For the case of low-fluence excitation, for instance, 1.9 mJ/cm^2, after a fast demagnetization at a time scale of a few hundred femtoseconds, the first recovery of the magnetization occurs, similar to the conventional demagnetization/re-magnetization shown in various ferromagnetic and ferrimagnetic materials [2, 92, 143–145]. With increasing fluence following the preceding two stages, a reduction in magnetization becomes evident within a few tens of picoseconds. These findings align with the dynamic outcomes observed in Tb/Co multilayers [146], thereby corroborating each other. Similar to reference [146], the magnetization dynamics can be divided into three steps: (i) ultrafast demagnetization; (ii) fast, partial magnetization recovery, manifesting as an upturn in the detected signal; and (iii) slower evolution of magnetization to in-plane [2]. Increasing the fluence leads to larger ultrafast demagnetization and the degree of magnetization change in the third step.

The magnetization decrease in the third step cannot be attributed to the creation of a domain structure because, on the one hand, the Kerr microscope images do not reveal any domain formation; on the other hand, the experiment is done under an applied field which prevails over the possibility of a non-uniform magnetic configuration. Thus, this decrease is attributed to the reorientation of the magnetization in-plane of the layers. This has also been observed by Hennes et al. in a $Co_{88}Tb_{12}$ thin film [147]. The similar magnetization dynamics behaviors for some other different systems, the historical Tb/Co multilayer as well as TbCo/Co/TbCo

[2] In reference [146], the magnetization switching was observed in the third step, which is not the case with our measurements. This difference is mainly due to a magnetic field applied to initialize the magnetization in our dynamics experiments, so no reversal of the magnetic moment was observed.

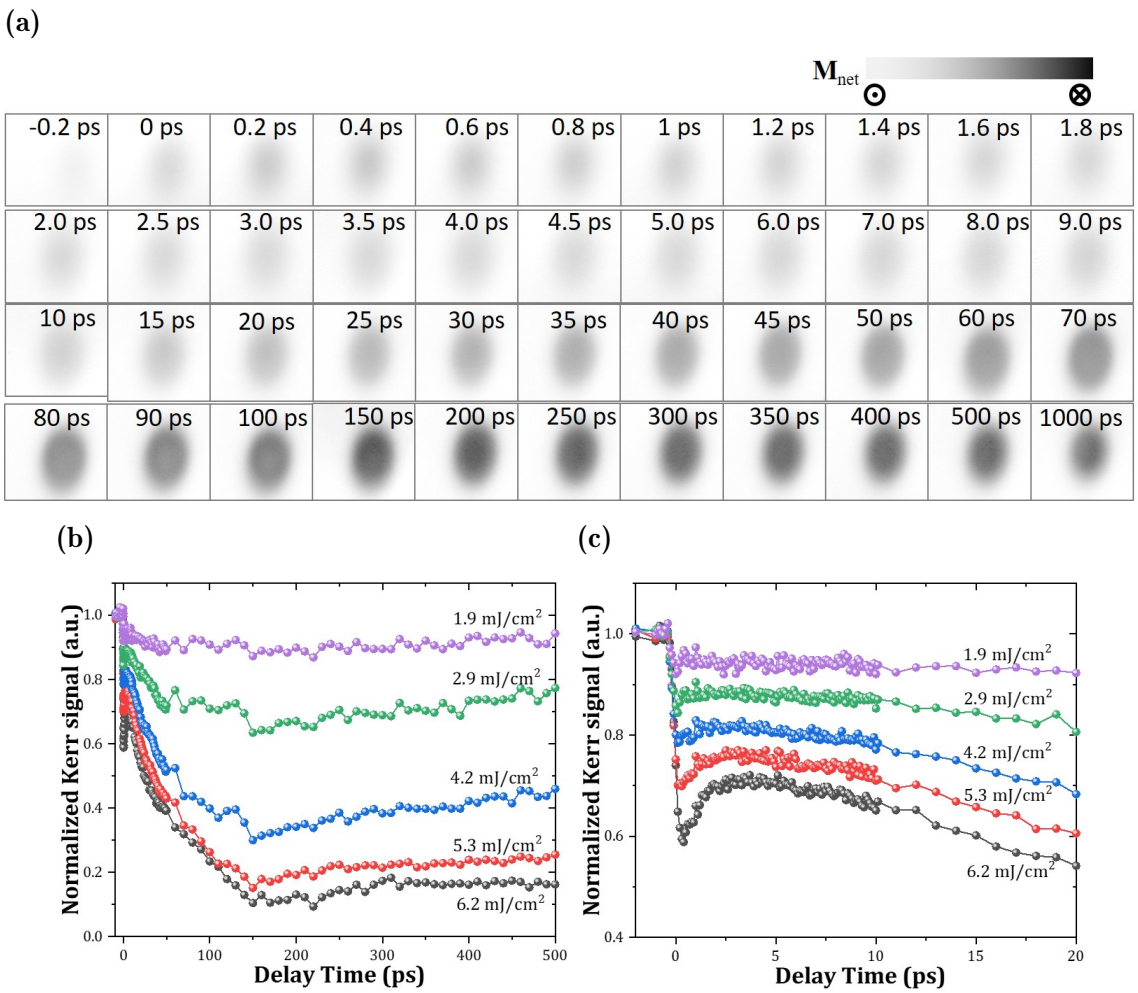

Figure 5.21: TR-MOKE measurements performed in $[Tb_{40}Co_{60}(4\text{ nm})/Co(2.1\text{ nm})]_3$ multilayers with different laser fluences. (a): TR-MOKE images recorded up to 1 ns. (b): 500 ps time scale. (c): zoom-in of the first 20 ps time scale. The DC magnetic field and laser repetition rates are 610 Oe and 10 kHz, respectively, shown in Table 5.2.

trilayers and $[TbCo/Co]_3$ and $[DyCo/Co]_3$ multilayers have been shown in Figure 5.22. This magnetization reorientation within the in-plane seems to be a common feature and supports the hypothesis of the possible precession of the magnetization.

To verify the in-plane reorientation in the third step, the hysteresis loops have been measured on pump-probe TR-MOKE set-up at different delay times with and without the pump. One can clearly observe that the hysteresis loop measured in the polar geometry is characteristic of an out-of-plane magnetization without any pump. At negative delay time, the amplitude is the same as the case without the pump. Notably, when the magnetic field is smaller than the coercivity, the field loop exhibits a switching behavior with a positive field and a plateau around 0 signal. This plateau corresponds to the average of the ultrafast switching of the magnetization between up and down states. The amplitude observed at longer delay times aligns well with the dynamics curves. Interestingly, the hysteresis loops at 10 ps and beyond (30 ps) reveal a distinct hard-axis behavior. This shift in behavior implies a temporal in-plane anisotropy, which serves as compelling evidence supporting our interpretation of in-plane reorientation. In essence, this suggests that the initially dominant out-of-plane anisotropy dynamically transforms into an in-plane anisotropy in response to the laser pulse.

Conversely, changing the magnitude of the reset magnetic field yields remark-

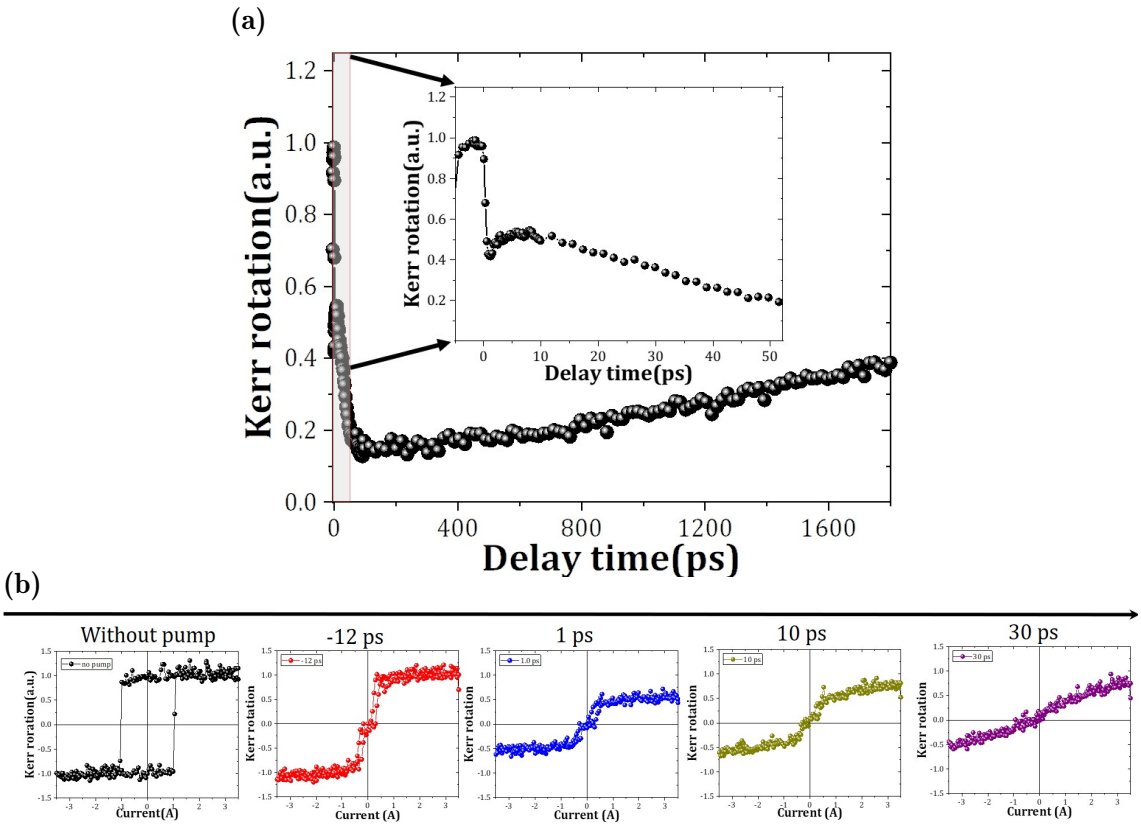

Figure 5.22: Hysteresis loops measured by pump-probe method at different delay time with pump fluence of 3.3 mJ/cm^2 for a sample with the composition TbCo(4 nm)/Co(2 nm)/TbCo(4 nm).

ably distinct dynamics. With a high magnetic field, the dynamics curve reveals an ultrafast demagnetization followed by a subsequent remagnetization back to the initial state. However, the in-plane reorientation in the third step can be observed as the magnetic field decreases to 3.77 kOe. Notably, at approximately 50 ps, the magnetization starts to return to its initial state. Further decreasing on the field makes the third step last longer and a larger change of the magnetization. These dynamics results show some oscillations, indicating the possibility of the precession mechanism. However, a well-defined precession frequency can not be observed. On the one hand, the existence of the DC field makes the precession difficult to be seen. On the other hand, the precession oscillation is strongly impacted by the materials damping. For instance, in the study of reference [148], it is shown that for in-plane magnetized $TbCo_2$/FeCo multilayers, oscillations were strongly damped and became undistinguished after two or even one period.

5.4.2 Discussion of the switching mechanism

Regarding in-plane reorientation, when considering the magnetization reorientation of the ferromagnetic layer (Py, CoFeB, or Co) as a pivotal element in promoting toggle switching in the whole multilayer stack, the perpendicular anisotropy in the FM layer has to vanish during the process. However, this isn't the scenario when Co, CoFeB, or Py layers come into contact with a Pt buffer or capping layer or when they are in contact with an insulating MgO layer; under these conditions, the anisotropy is strong. Hence, a key strategy for achieving robust All-Optical Switching involves either suppressing the source of anisotropy within the FM layer or diminishing its

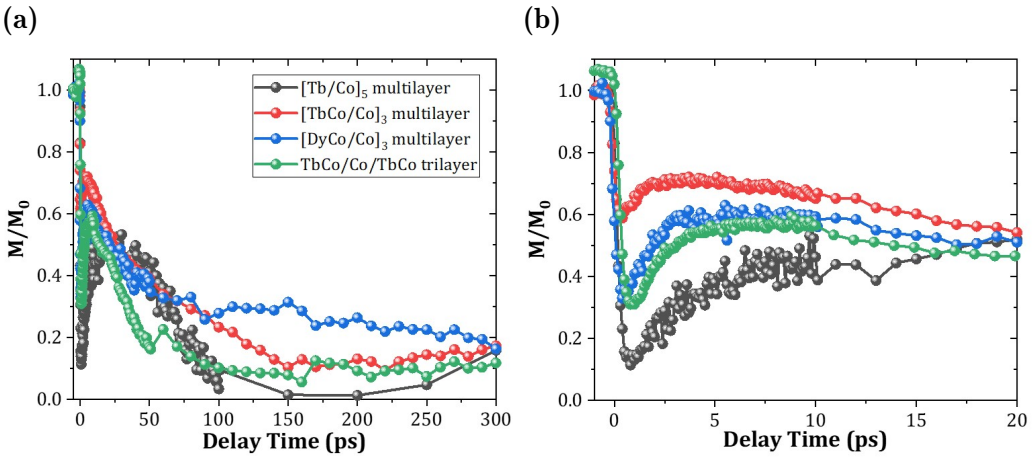

Figure 5.23: TR-MOKE measurements performed on the different multilayers showing single-pulse switching. (a): 300 ps time scale. (b): zoom-in of the first 20 ps time scale. The description of the stacks and conditions for TR-MOKE measurements have been shown in Table 5.2.

Stacks	Composition	Field (Oe)	Fluence(mJ/cm²)	Repetition rate(kHz)
$[Tb/Co]_5$ multilayer	t(Tb) = 1.06 nm t(Co) = 1.78 nm	550	6.32	0.2
$[TbCo/Co]_3$ multilayer	$t(Tb_{40}Co_{60})$ = 4 nm t(Co) = 2.10 nm	610	6.52	10
$[DyCo/Co]_3$ multilayer	$t(Dy_{30}Co_{70})$ = 4 nm t(Co) = 2.18 nm	570	3.83	1
TbCo/Co/TbCo trilayer	$t(Tb_{32}Co_{68})$ = 4 nm t(Co) = 2.24 nm	690	3.26	1

Table 5.2: Stacks and TR-MOKE conditions corresponding to Figure 5.23. The repetition rate has been optimized to get the best contrast without changing the properties of the layers.

contribution. Two strategies to achieve this have been explored: (i) in the trilayer or multilayer by removing the Pt/Co interface; (ii) by increasing the thickness of the RE alloy layer. We clearly show that, on the one hand, increasing the number of bilayers in the multilayer, and thus the number of Co layers that interact with the RE alloy layer, results in a higher quality of reversal; on the other hand, in a single TbCo/Co bilayer, the switching is favored when the thickness of TbCo is much larger compared to the Co layer. This allows obtaining a reversal in a multilayer with a record thickness of 30 nm. Since perpendicular anisotropy in TbCo, DyCo, or TbFe alloys is expected to disappear as the lattice temperature rises after the laser pulse, the simplest stacks to characterize are then TbCo/X/TbCo (X = Co, Py, CoFeB), Y/Co/Y (Y = DyCo, TbFe) trilayers in which the anisotropy of Co, Py, and CoFeB is induced by its proximity with TbCo, DyCo or TbFe alloys.

While the in-plane reorientation appears as a key condition for reversal, it is not sufficient to explain alone a precession-type reversal. An effective field around which the precession takes place has to be identified [140, 141]. One source of symmetry breaking that we can see in the system is the laser's Gaussian profile. Although the laser profile has cylindrical symmetry, exposure is not homogeneous. Therefore, lateral gradients of deposited energy are created in the film. However, as analyzed in section 5.3.3, We can observe that the walls are always located at the same local

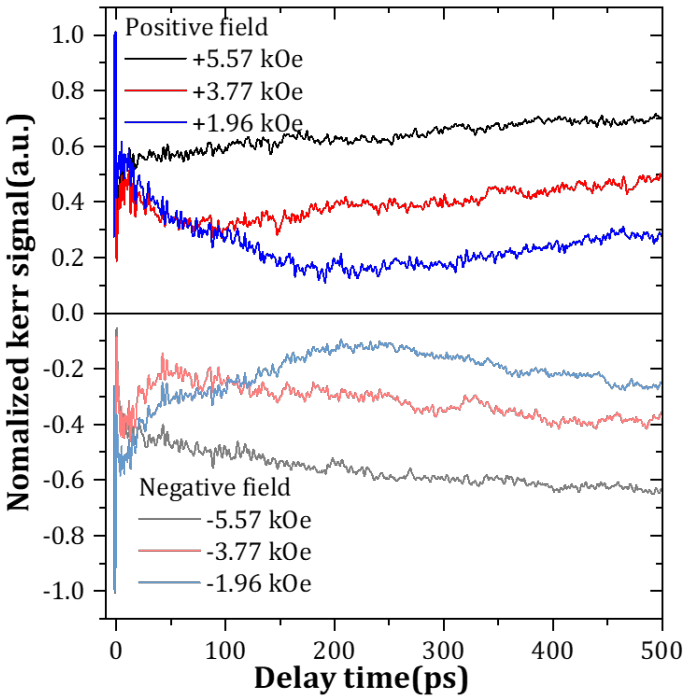

Figure 5.24: Dynamics of a [Co(2.1 nm)/($Tb_{40}Co_{60}$)(4)]3 multilayer. The dynamics are recorded using different applied fields in both opposite directions. In all those measurements, the fluence was kept constant at 5.0 mJ/cm^2.

threshold energy and do not depend on their distance to the Gaussian beam's center. The energy gradients do not seem to dominate the switching mechanism; the locally absorbed fluence does. We can, therefore, neglect dipolar interactions or lateral-induced strain as a possible source for this in-plane effective field. However, this observation is again compatible with a precessional reversal mode.

A close analysis of a Magnetic Force Microscopy image of the ring domain structure gives us a view of the process (Figure 5.25a). The process has to be considered at the scale of a grain or a couple of grains in the TM layer. First, the rings don't exhibit a distinct separation via sharp and clearly defined domain walls (as shown in Figure 5.25b). Instead, the separation is characterized by an amalgamation of small domains, densely clustered, especially at the separation (depicted in Figure 5.25e). In comparison, a domain wall located at the center of figure 5.25a (and exiting in the sample before laser irradiation), we notice that its sharpness is much more pronounced (Figure 5.25c). Second, we can clearly observe the presence of small domains, with sizes ranging between 100 to 300 nm inside the rings (Figure 5.25b and 5.25c, red circles). Their density increases upon increasing the fluence towards the center of the spot (Figure 5.25e).

Most of the samples studied (from number 3 to 19 in Table 1) are multilayers containing a RE alloy layer and an FM layer. It is known that TM-RE alloys are amorphous [149], while FM layers are polycrystalline or textured when deposited at room temperature on amorphous layers, with typical grain sizes of 20 to 30nm. We expect a local distribution of the easy axis directions linked to the polycrystalline nature of the FM layers. The consequences of this distribution are visible in the MFM image recorded in the area of the layer that has been saturated before the experiments (Figure 5.25d). The fast reduction followed by the subsequent recovery of anisotropy within the TM-RE alloy, attributed to the notably low Curie temperature (T_C) of the rare earth component, leads to the orientation of the magnetization

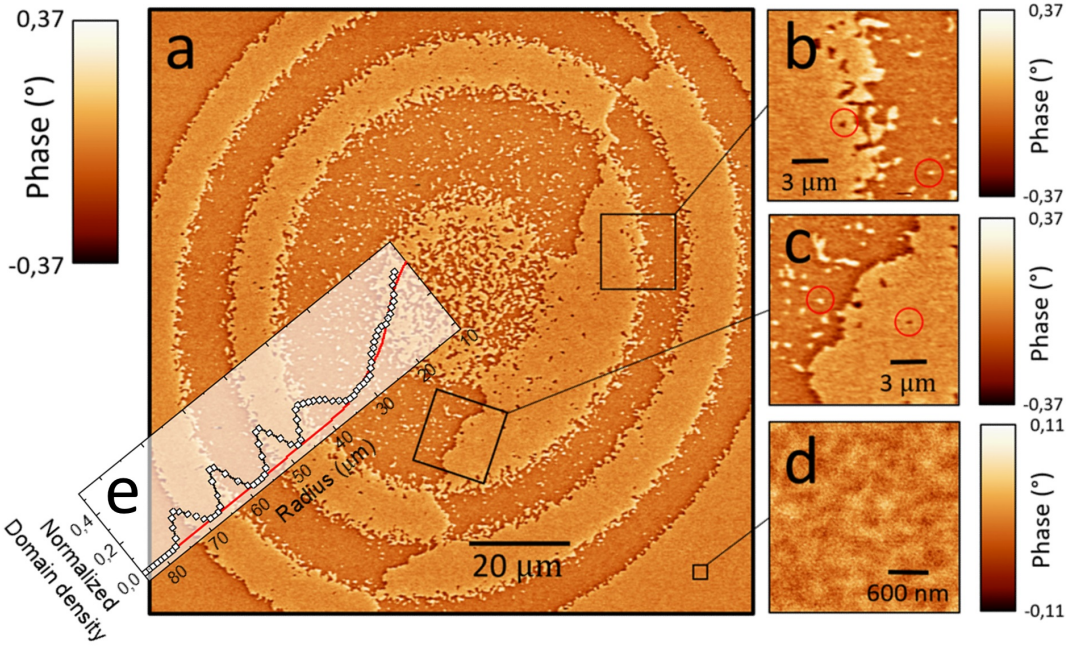

Figure 5.25: Magnetic force microscopy investigation of a characteristic ring structure. (a): A ring structure observed by MFM. (b): zoom on the region that separates two rings. (c): zoom on a domain wall. (d): zoom on a region outside the laser spot that has been saturated before the experiment. (e): annular analysis of the small domain density.

of the FM layer in-plane and its precession. The key ingredient for the reversal is the persistence of the magnetization of the FM layer due to its high (T_C), which arises from being composed of pure Co, Fe, Py, or CoFeB materials. In a scenario where magnetic grains or a couple of grains (identified as "magnetic" grains) behave independently, the magnetization exhibits precession around the local anisotropy axis, which is distributed from grain to grain.

Starting from the perpendicular axis, the magnetization precession would occur around the local anisotropy. Once the magnetization precesses and crosses the equatorial plane of the film, the magnetization switching occurs; otherwise, it goes back to the initial direction. Whether the magnetization can process across the equatorial plane depends on the precession time, which is directly linked to the energy distribution of laser beam-defining regions. Thus, depending on the range of energy absorption, the magnetization of grains can end up either reversed or not reversed. However, when approaching the critical energy threshold, whether its magnetization can finally reverse is extremely sensitive to the anisotropy distribution, which is the reason why the density of the small domains is the highest at the transition area. Occasionally, the absence of reversal within certain small domains contained within the rings is attributed to a lack of a suitable configuration in the magnetic grains. Going closer to the center of the laser spot, in addition to the above discussion, the heat can also affect the amplitude of the magnetic moment, thus increasing the uncertainty of the reversal, resulting in an increase in the density of small domains.

5.5 A macrospin model based on LLG equation

In the last section 5.4.2, we discussed the possibility of a precessional switching mechanism. In this section, we address the in-plane reorientation switching mechanism by developing a phenomenological macrospin model based on the LLG equation

to a two-temperature model (2TM) [53]. This model was developed by David SALOMONI in Spintec [54].

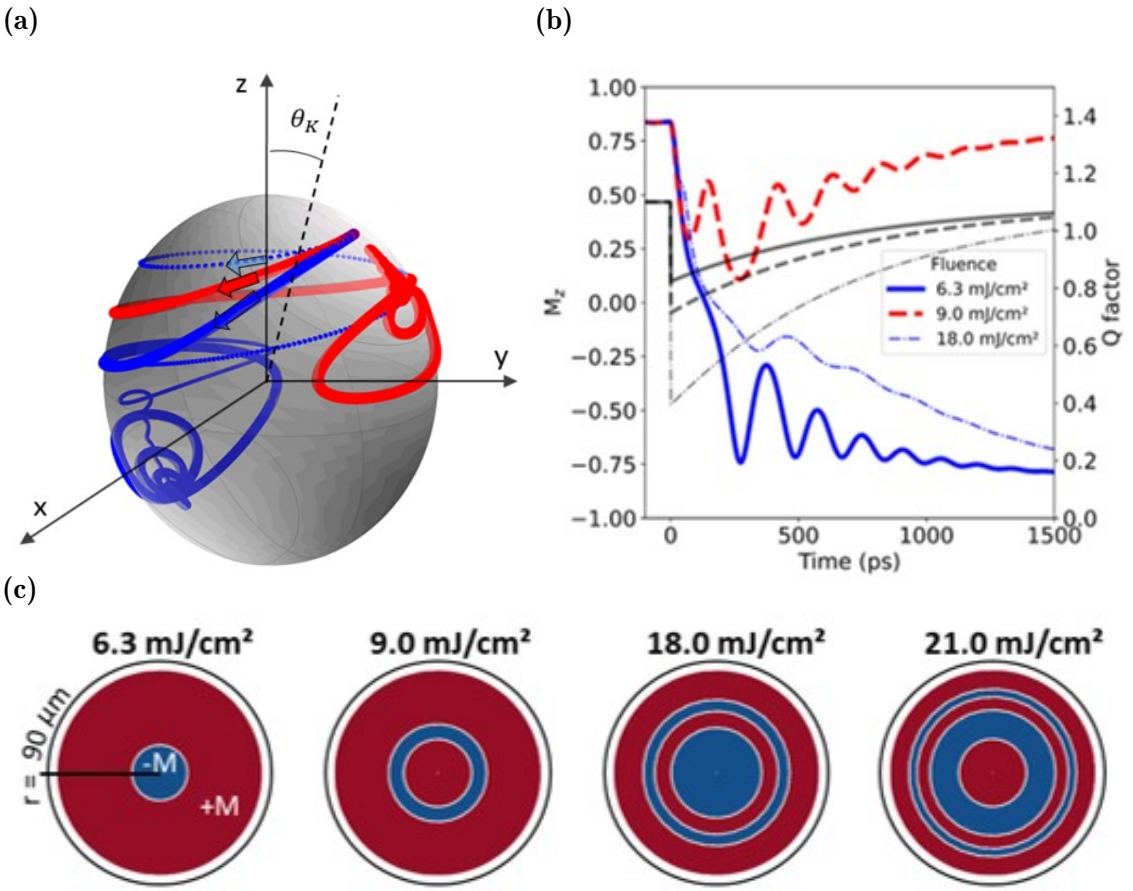

Figure 5.26: (a): 3D view of the magnetization dynamics as predicted by the macrospin model. (b): M_z and quality Q factor time traces for 3 different fluences 6.3 mJ/cm^2, 9.0 mJ/cm^2, 18.0 mJ/cm^2, 21.0 mJ/cm^2. c) Expected magnetization pattern after 100 fs for a single Gaussian-shaped laser pulse with peak fluence: 6.3 mJ/cm^2, 9.0 mJ/cm^2, 18.0 mJ/cm^2, 21.0 mJ/cm^2. Simulations in a),b) and c) were performed for $\theta_K = 5°$, M_s = 1:42 MA/m and $K_u(300K) = 1.1 \cdot \frac{1}{2}\mu_0 {M_S}^2$, damping $\alpha = 0.1$.

The model accounts for two key features: i) fast drop of the factor Q with increasing temperature.

$$K_u = QK_d \tag{5.1}$$

where K_d is the demagnetizing anisotropy:

$$K_d = \frac{1}{2}\mu_0 {M_S}^2 \tag{5.2}$$

Thus,

$$Q = \frac{2K_u}{\mu_0 {M_S}^2} \tag{5.3}$$

where K_u is the magnetocrystalline anisotropy, M_S is the saturation magnetization; and ii) a small tilt angle of the uniaxial anisotropy axis with respect to the out-of-plane direction $\theta_K > 5°$. Without this small title range of the easy axis, only demagnetization can be obtained under the excitation of the single laser pulse. With a small tilt angle, under the excitation of the laser pulse, the temperature on the sample increases rapidly, resulting in the fast reduction of the Q factor, which is

the first key assumption of this model. Consequently, the magnetization starts to process towards the in-plane due to the demagnetizing field. The anisotropy field recovers during the precession due to cooling. The precession time and the end-point of the magnetization before cooling depend on the energy absorption of the sample, that is, the fluence. For example, the tilt angle was set to have a deviation in the xz plane from the z-axis and has a $+x$ component. If the end-point of the magnetization before cooling has a $+x$ component, it processes back to the initial state, while if it has a -x component, the magnetization can cross the equatorial plane, leading to a reversal. Thus, the magnetization can end up as reversed or not reversed depending on the fluence, as shown in Figure 6.1.

Considering the two key features,

- What is the origin of the tilt angle?

  As we discussed in section 5.4.2, We expect a local distribution of the easy axis directions linked to the polycrystalline nature of the FM layers. The local easy axis of a grain or a couple of grains could be the origin of the tilt angle.

- The fast reduction of the Q factor.

  According to equation 5.3, The fast reduction of the Q factor can be either induced by the reduction of K_u or an increase in M_S, or both. Since the Q factor is inversely proportional to the square of M_S, changes in Ms have a greater impact on the Q factor. In our extensive sample testing, a noteworthy observation is that switching predominantly occurs in samples dominated by TM, in which the compensation temperature is below room temperature. Consequently, when the sample temperature begins to rise from room temperature, M_S experiences a fast increase, leading to a rapid reduction in Q. Conversely, in samples dominated by Tb, the compensation temperature is above room temperature. Consequently, as the temperature increases, M_S experiences a rapid decrease, resulting in a notable increase in the Q factor rather than a rapid decrease.

However, we also observed some partial switching in the Tb-dominant region when the TbCo layers are very thick, such as the case of 14 in Table 5.1 also in Figure 5.13. This might be due to the reduction of K_u is much larger than the reduction in M_s with increasing temperature.

5.6 Conclusion

In this chapter, we demonstrate that single-shot HI-AOS can be obtained for a large variety of RE/TM multilayers, expanding the range of potential materials that can exhibit this effect. Surprisingly, concentric ring domain structures are induced at high laser intensities, unveiling multiple fluence thresholds. These threshold fluences for switching are observed to be independent of the pulse duration, up to at least 10 ps or even longer. These striking switching features are in contrast to those of HI-AOS in GdFeCo alloys. The picture of precessional reversal emerges due to the strong evidence concomitant with the demonstration of an in-plane reorientation of the magnetization, pointing towards an intrinsic precessional switching mechanism. Regarding the reversal time, this single-pulse precessional-like AOS possesses typical time scales between those of GdFeCo and multiple-pulse HD-AOS. While the in-plane reorientation of the magnetization is undoubtedly proven and is one key

ingredient, a precession at the scale of a grain or a couple of grains in the TM, which keeps a sizable magnetization thanks to its high T_C, leads to the reversal in a ring shape domain structure. This is the second key ingredient needed, which is missing if only the RE-TM alloy is used.

Extended figures

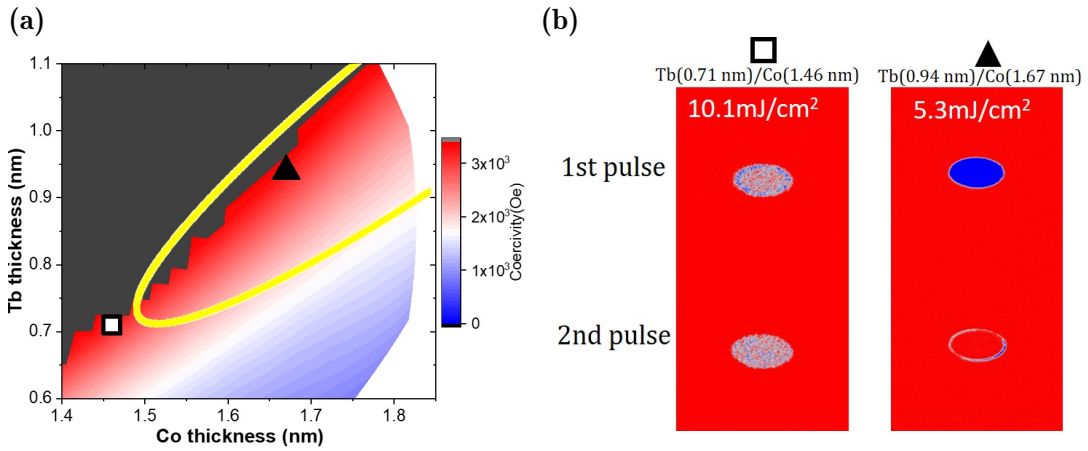

Figure 5.27: Single switching in $[Tb(wedge)/Co(wedge)]_5$ cross-wedge multilayer. (a): Coercivity map of $[Tb/Co]_5$ along the Tb and Co thickness wedges. The grey indicates the region where the applied field was insufficient to saturate the stack. The region shown by the solid yellow line indicates the Tb and Co thicknesses region where single switching occurs. (b): Single switching using a 50 fs laser pulse at two positions enclosed by the symbols in (a).

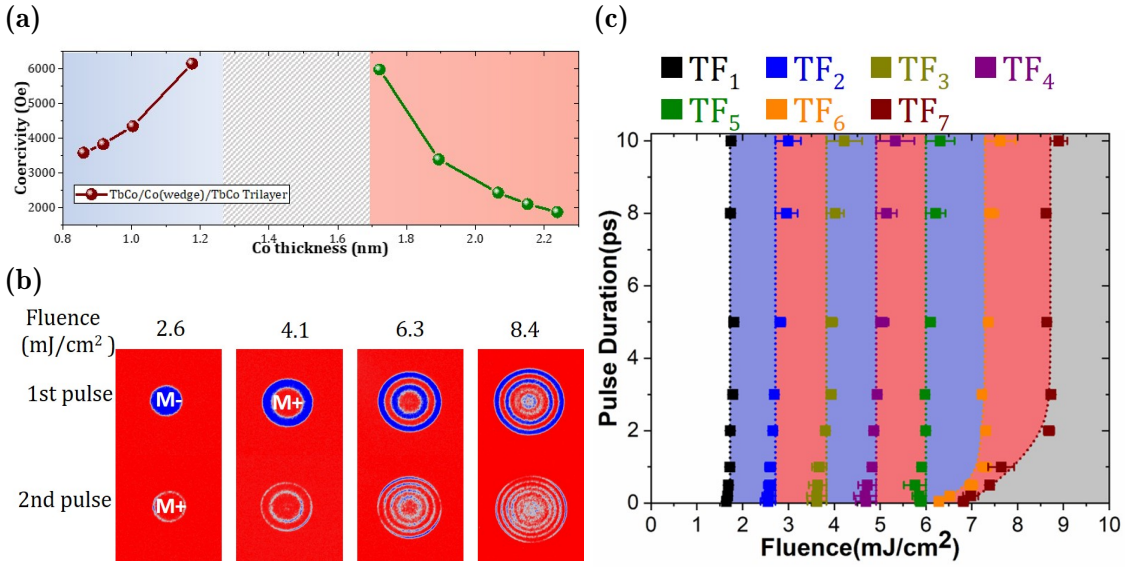

Figure 5.28: Single pulse reversal in $Tb_{32}Co_{68}$(4 nm)/Co/$Tb_{32}Co_{68}$(4 nm) trilayer. (a) Coercivity as a function of Co thickness. Light red color shows the region of Co thickness (1.68 nm $< t_{Co} <$ 2.27 nm) where single shot switching occurs. (b) Single pulse switching with 50 fs laser pulse and (c) State diagram with Co thickness of 2.2 nm.

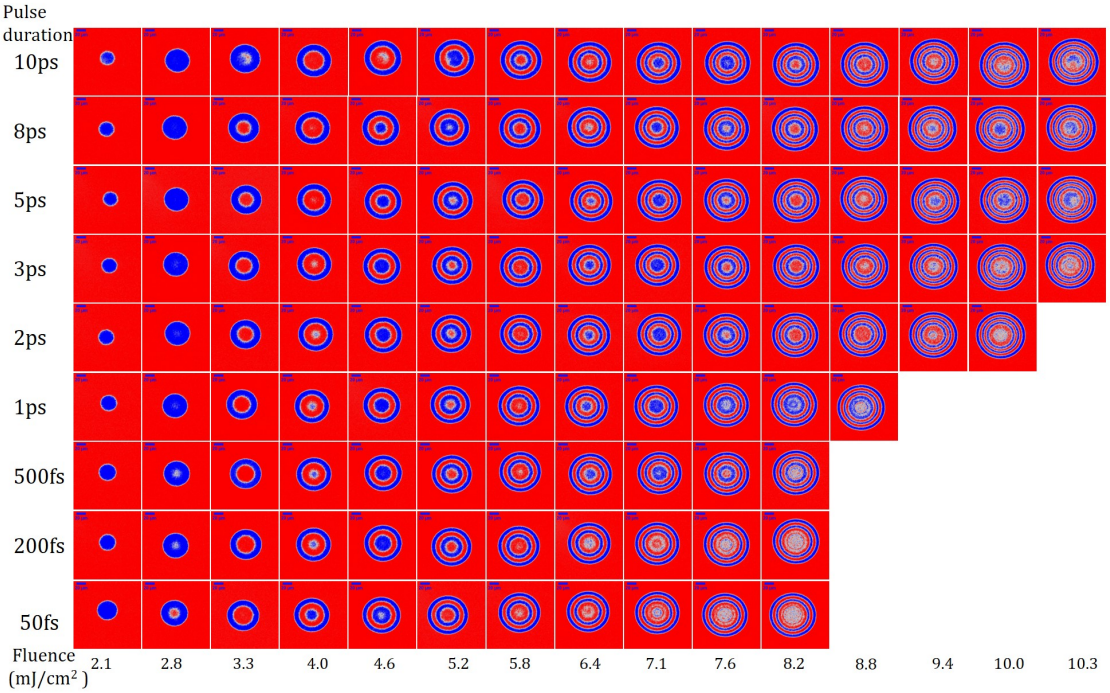

Figure 5.29: MOKE images for $Tb_{32}Co_{68}$(4 nm)/Co(2.2 nm)/$Tb_{32}Co_{68}$(4 nm) trilayer with different pulse duration and fluences.

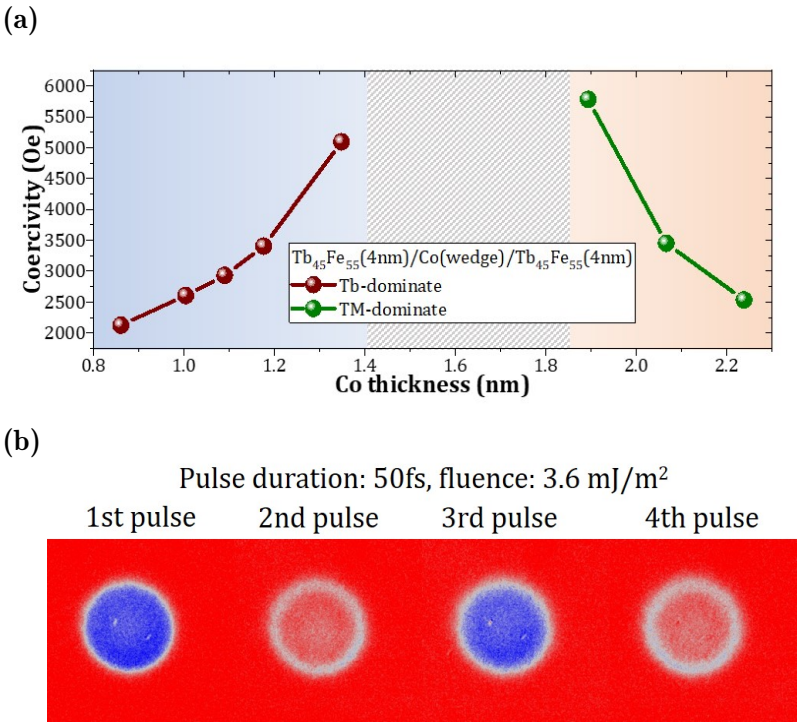

Figure 5.30: Single pulse reversal in $Tb_{45}Fe_{55}$(4 nm)/Co/$Tb_{45}Fe_{55}$(4 nm) trilayer. (a) Coercivity as a function of Co thickness. (b) Single pulse switching images with Co thickness of 2.2 nm.

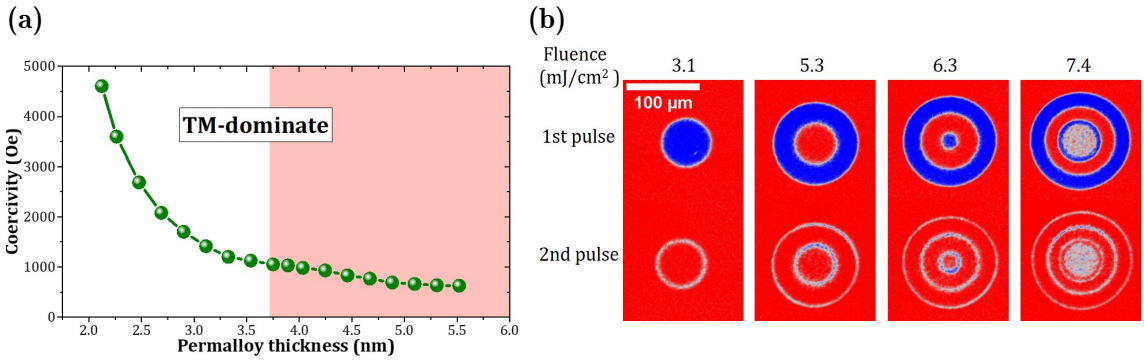

Figure 5.31: Single switching in $Tb_{32}Co_{68}$(4 nm)/$Ni_{80}Fe_{20}$(wedge)/$Tb_{32}Co_{68}$(4 nm) trilayer. (a): Coercivity as a function of $Ni_{80}Fe_{20}$ (permalloy, or Py). Light red color shows the region of Py thickness (3.89 nm $< t_{Py} <$ 5.60 nm) where single-shot switching occurs. (b) Background subtracted images after each 50fs laser pulse with different fluences measured at the green point position with $t_{Py} = 5.10$ nm.

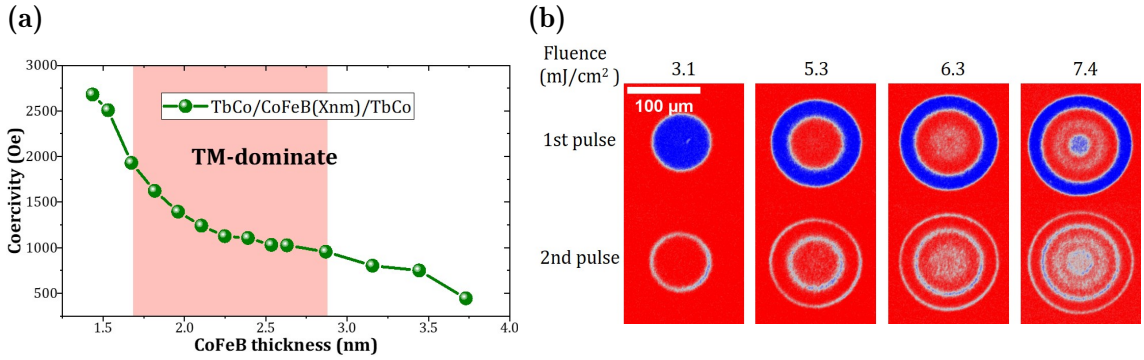

Figure 5.32: Single switching in $Tb_{32}Co_{68}$(4 nm)/$Co_{40}Fe_{40}B_{20}$(wedge)/$Tb_{32}Co_{68}$(4 nm) trilayer. (a): Coercivity as a function of $Co_{40}Fe_{40}B_{20}$ (CoFeB). Light red color shows the region of CoFeB thickness (1.67 nm $< t_{CoFeB} <$ 2.87 nm) where single-shot switching occurs. (b) Background subtracted images after each 50 fs laser pulse with different fluences measured at the green point position with $t_{CoFeB} = 2.25$ nm.

Sample list

- AV39-05 SiO2/Pt(2)Ta(2)[Co(wedge)/Tb(wedge)]$_5$Ta(3) (Cross double wedge)
- 605-5 V/Ta(5)Pt(5)[Fe(0.9, wedge)/Tb(0.9, wedge)]$_4$Pt(1)Ta(5) (Opposite double wedge)
- 606-4 V/Ta(5)Pt(5)[Fe(0.9, wedge)/Tb(0.9, wedge)]$_4$Pt(1)Ta(5) (Double wedge)
- 613 V/Ta(5)Pt(5)[Fe(1.1, wedge)/Tb(0.9, wedge)]$_4$Pt(1)Ta(5) (Double wedge)
- 614 V/Ta(5)Pt(5)[Fe(1.3, wedge)/Tb(0.9, wedge)]$_4$Pt(1)Ta(5) (Double wedge)
- 682 V/Ta(5)Pt(5)[Co(2nm, wedge)/(Co70Tb30)(3)Ta(5)Pt(1) (Bilayer)
- 695-3 V/Ta(5)Pt(5)[Co(2nm, wedge)/(Co60Tb40)(1)]$_3$Ta(5)Pt(1)
- 695-2 V/Ta(5)Pt(5)[Co(2nm, wedge)/(Co60Tb40)(2)]$_3$Ta(5)Pt(1)
- 695-1 V/Ta(5)Pt(5)[Co(2nm, wedge)/(Co60Tb40)(3)]$_3$Ta(5)Pt(1)
- 696-1 V/Ta(5)Pt(5)[Co(2nm, wedge)/(Co60Tb40)(4)]$_3$Ta(5)Pt(1)
- 696-2 V/Ta(5)Pt(5)[Co(2nm, wedge)/(Co60Tb40)(5)]$_3$Ta(5)Pt(1)
- 698-1 V/Ta(5)Pt(1)[Co(2nm, wedge)/(Co60Tb40)(4)]Ta(5)Pt(1)
- 698-2 V/Ta(5)Pt(5)[Co(2nm, wedge)/(Co60Tb40)(4)/Pt(2)]$_3$Ta(5)Pt(1)
- 699-5 V/Ta(5)Pt(5)[Co(2nm, wedge)/(Co70Tb30)(6)]$_3$Ta(5)Pt(1)
- 699-2 V/Ta(5)Pt(5)[Co(2nm, wedge)/(Co60Tb40)(7.5)]$_3$Ta(5)Pt(1)
- 711-1 V/Ta(5)Pt(5)[Co(2nm, wedge)/(Co65Dy35)(4)]$_3$Ta(5)Pt(1)
- 711-2 V/Ta(5)Pt(5)[Co(2nm, wedge)/(Co60Dy40)(4)]$_3$Ta(5)Pt(1)
- 711-3 V/Ta(5)Pt(5)[Co(2nm, wedge)/(Co70Dy30)(4)]$_3$Ta(5)Pt(1)
- 711-4 V/Ta(5)Pt(5)[Co(2nm, wedge)/(Co75Dy25)(4)]$_3$Ta(5)Pt(1)
- 711-5 V/Ta(5)Pt(5)[(Co65Dy35)(4)]$_3$Ta(5)Pt(1)
- 711-6 V/Ta(5)Pt(5)[(Co60Dy40)(4)]$_3$Ta(5)Pt(1)
- 711-7 V/Ta(5)Pt(5)[(Co70Dy30)(4)]$_3$Ta(5)Pt(1)
- 711-8 V/Ta(5)Pt(5)[(Co75Dy25)(4)]$_3$Ta(5)Pt(1)
- 711-9 V/Ta(5)Pt(5) (Co65Dy35)(4) Co(2nm, wedge) (Co65Dy35)(4) Ta(5)Pt(1)
- 715-1 V/Ta(5)Pt(5) Co(2nm, wedge) (Co65Dy35)(4) Ta(5)Pt(1)
- 715-2 V/Ta(5)Pt(5) (Co65Dy35)(4) Co(2nm, wedge) Ta(5)Pt(1)
- 726-2 V/Ta(5)Pt(5)[Co(1,5nm, wedge)/(Co67Tb32)(4)]$_3$Ta(5)Pt(1)
- 726-3 V/Ta(5)Pt(5)(Co67Tb32)(4)Co(1,5nm, wedge)(Co67Tb32)(4)Ta(5)Pt(1)
- 727-3 V/Ta(5)Pt(5)[Co(1,5nm)/(Co67Tb32)(4)]$_3$Ta(5)Pt(1)(with rotation)

- 727-4 V/Ta(5)Pt(5)Co(1,5nm, wedge)/(Co67Tb32)(8)]Ta(5)Pt(1)
- 727-5 V/Ta(5)(Co67Tb32)(4)Co(1,5nm, wedge)Ta(5)Pt(1)
- 728-1 V/Ta(5)Co(1,5nm, wedge)/(Co67Tb32)(8)]Ta(5)Pt(1)
- 728-2 V/Ta(5)Pt(5)(Co67Tb32)(4)Co(1,5nm, wedge)Ta(5)Pt(1)
- 728-3 V/Ta(5)Pt(5)Co(1,5nm, wedge)/(Co67Tb32)(16)]Ta(5)Pt(1)
- 742 V/Ta(5)Pt(5)(Fe45Tb55)(4)Co(1,5nm, wedge)(Fe45Tb55)(4)Ta(5)Pt(1)
- 761-4 V/Ta(5)Pt(5)(Co67Tb32)(4)Py(3,7, wedge)(Co67Tb32)(4)Ta(5)Pt(1)
- 769 V/Ta(5)Pt(5)(Co67Tb32)(4)CoFeB(2,5, wedge)(Co67Tb32)(4)Ta(5)Pt(1)

Chapter 6

From Gd-based single-shot switching to precessional switching

In this chapter, we will report some intriguing results obtained in TbCo/GdCo/TbCo trilayer. By decreasing the Gd concentration in the GdCo layer, we clearly observed the ultrafast toggle switching in Gd-based materials to the in-plane reorientation precessional switching in multilayers. Gd content is the key ingredient in ultrafast toggle switching, but magnetization and anisotropy are mainly responsible for the multidomain creation and the precessional switching.

6.1 Sample description and characterization

The sample structure consists of a trilayer stack of $Tb_{32}Co_{68}$(4 nm)/Gd_xCo_{100-x}(t)/ $Tb_{32}Co_{68}$(4 nm), where both the thickness and the Gd concentration of the GdCo layer vary gradually. To create these alloys, we employ a co-deposition process utilizing multiple sources arranged in a confocal geometry. The composition is adjusted by controlling the power applied to different cathodes. For all layers, except the Gd_xCo_{100-x}(t) layer, we achieve layer homogeneity by rotating the sample during deposition. In the case of the Gd_xCo_{100-x}(t) layer, we employ a co-sputtering technique using pure Co and Gd targets. The variation in thickness across this layer is achieved by stopping the rotation of the sample during the deposition process. Due to the diametrically opposed positioning of the Co and Gd sources, a natural concentration gradient forms. Additionally, because the deposition rates of Co and Gd differ, a thickness gradient also emerges in the final structure. The thickness and Gd concentration determination method has been shown in subsection 3.1.2 in Chapter 3.

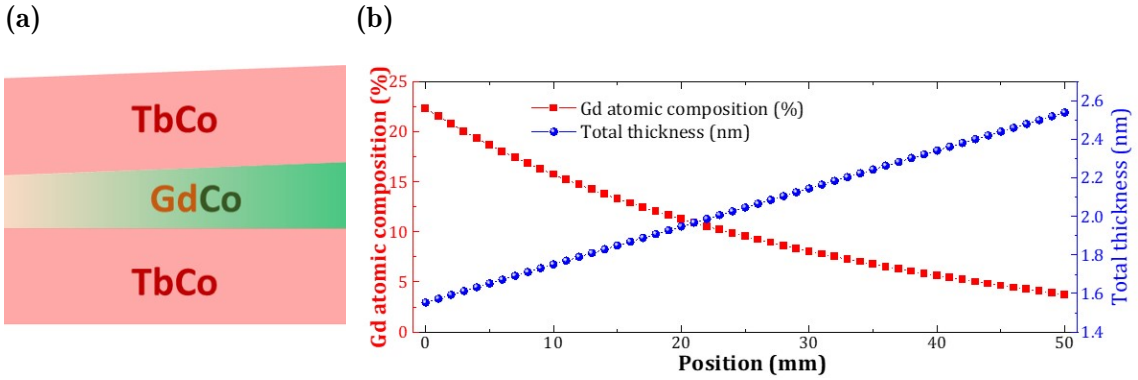

Figure 6.1: (a) schematic of the trilayer stack, where the thickness and Gd concentration of the GdCo layer are wedges, shown as a function of position in the thickness wedge sample in (b).

Figure 6.1b illustrates the variation in thickness and Gd concentration within the GdCo alloy layer as a function of position along the sample. The thickness of the GdCo alloy layer exhibits a linear variation, starting at 1.5 nm at one end of the sample and gradually increasing to 2.55 nm at the opposite end. In contrast, the Gd concentration within the GdCo alloy layer follows a nonlinear pattern. At the initial position, the Gd concentration stands at 21.6%, but it decreases more rapidly along the sample. The concentration curve shows a steeper slope initially, then gradually levels off as it approaches 3.6 % to the other end of the sample.

In $Tb_{32}Co_{68}$(4 nm)/Gd_xCo_{100-x}(t)/$Tb_{32}Co_{68}$(4 nm), the Co atoms are strongly ferromagnetically exchange coupled at the interface. Therefore, the magnetization subnetworks of Tb and Gd are parallel. We performed Kerr magnetometer hysteresis loops in the polar geometry to check PMA, coercivity, and subnetwork dominance. For 21.6% and 12.1% of Gd, the hysteresis loops are dominated by the RE, while the sample is dominated by Co with 5% of Gd. By checking the coercivity throughout the entire wedge, the coercivity diverges at 7% of Gd and 2.2 nm of the GdCo layer, where magnetization is compensated.

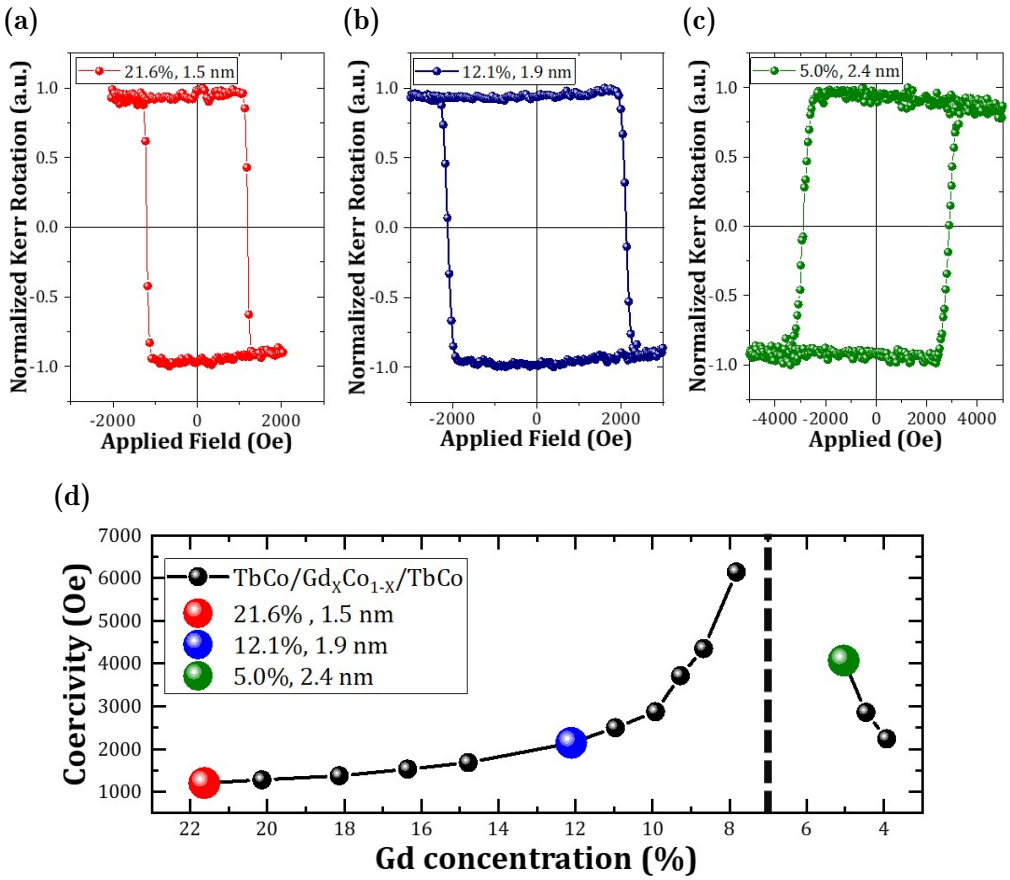

Figure 6.2: The MOKE hysteresis loops measured with (a): 21.6%; (b): 12.1% and (c): 5%. (d): The coercivity as a function of Gd concentration.

6.2 Static switching and dynamics

Single pulse reversal experiments have been done for concentration range x from 5 to 22%, and measurements performed for x = 5%, 12.1%, and 21.6% are reported in Figure 6.3a. When x=21.6%, a perfect single-shot switching is observed, where the magnetization can be switched by the first pulse and switched back by the second pulse. It is worth noticing that the domain wall is much smoother compared to the switching in Tb/Co multilayers shown in the last chapter. More importantly, the switching does not show ring structure with higher fluence (See the switching images in Figure 6.5a). The switching behavior observed with a Gd concentration of 21.6% appears to resemble the switching characteristics typically associated with Gd-based ferrimagnets. The state diagram confirms this point.

Regarding the state diagram of x=21.6% Iin Figure 6.3b, two threshold fluences can be defined: F_{switch} and F_{multi} that correspond to the fluence needed to get the switching and a multidomain state in the central region, respectively. Notably, the triangular shape of this state diagram is a distinctive feature typically associated with toggle reversal in Gd-based materials [90]. The dependence of F_{switch} on pulse duration suggests that the underlying mechanism is likely governed by the maximum electronic temperature, which decreases with increasing the pulse duration as discussed in references [90, 94]. The switching can only be obtained with a pulse duration below 1.6 ps. On the other hand, since F_{multi} depends only slightly on pulse duration, a link to both Curie temperature and energy transferred to the lattice is highly probable, as suggested in reference [90].

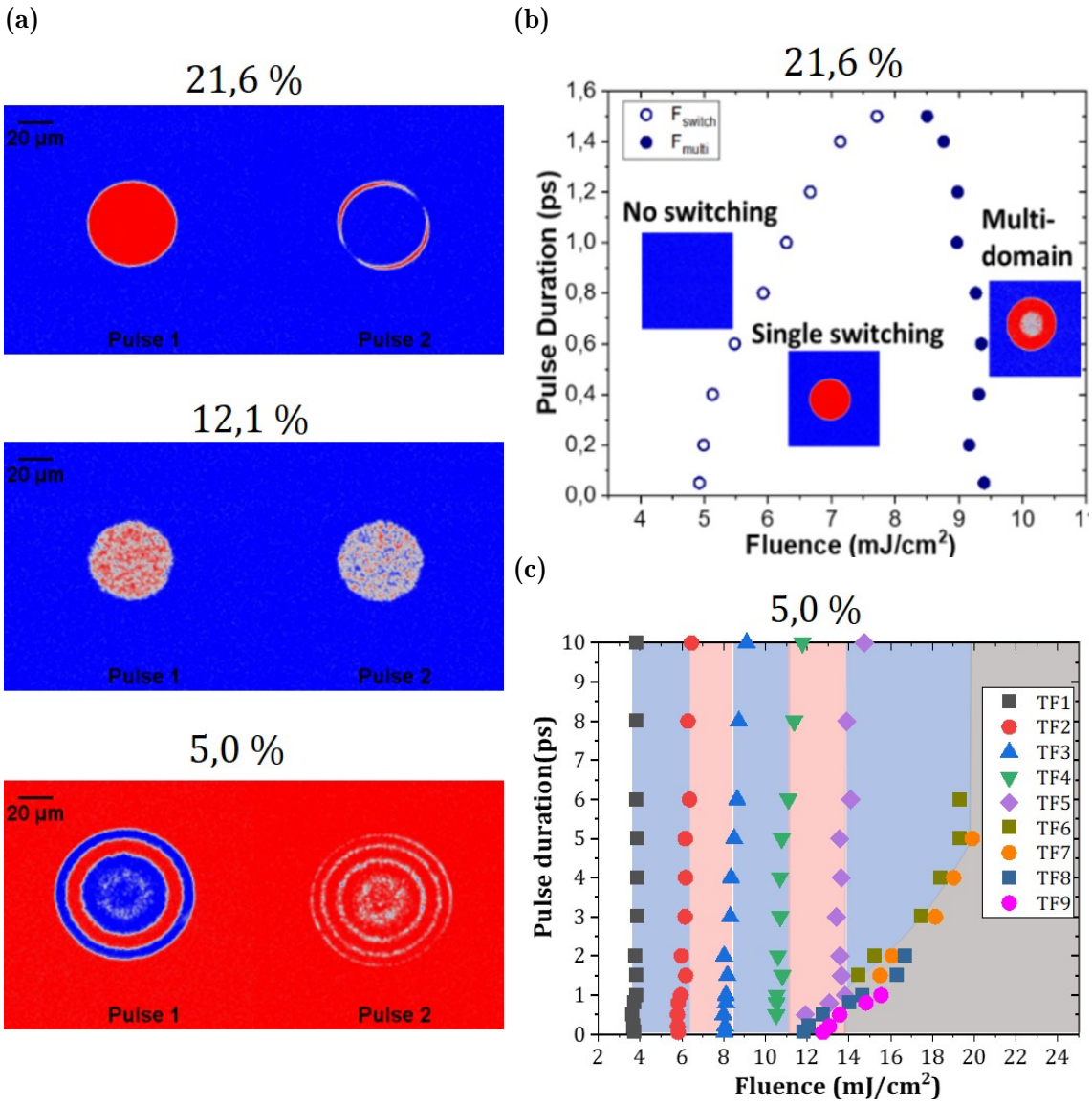

Figure 6.3: The switching images by 50 fs laser pulse in the sample with 21.6% (top), 12.1% (middle) and 5% (bottom) of Gd. (b) and (c): the pulse duration dependent threshold fluence state diagram.

At the other end, with 5% of Gd, the switching images show ring structure. In between, only a demagnetization state occurs, as seen for 12.1% of Gd. As far as the state diagram of x=5% is concerned, the ring structure results in multiple threshold fluences. The four lower threshold fluences (TF_1 - TF_4) are mostly independent of pulse duration. For TF_5, it increases with the pulse duration up to 1 ps, while it keeps a constant with a longer pulse duration. For TF_6 - TF_9, they increase until a longer pulse duration, for instance, 5 ps [1].

A deeper understanding of the reversal process is garnered through the examination of pump-probe measurements, as illustrated in Figure 6.4. In the case of the sample with x = 21.6%, the dynamics reveal a remarkably rapid demagnetization occurring within a few hundred femtoseconds (fs). Following this initial demagnetization process, there is a recovery towards the initial state, indicated by the increase in the Kerr signal with a fluence as low as 4.0 mJ/cm^2. This fluence is below the

[1]Note that TF_7 - TF_9 cannot be obtained until 10 ps, since the central region will be burned with too high fluence before demagnetization is observed in the central region.

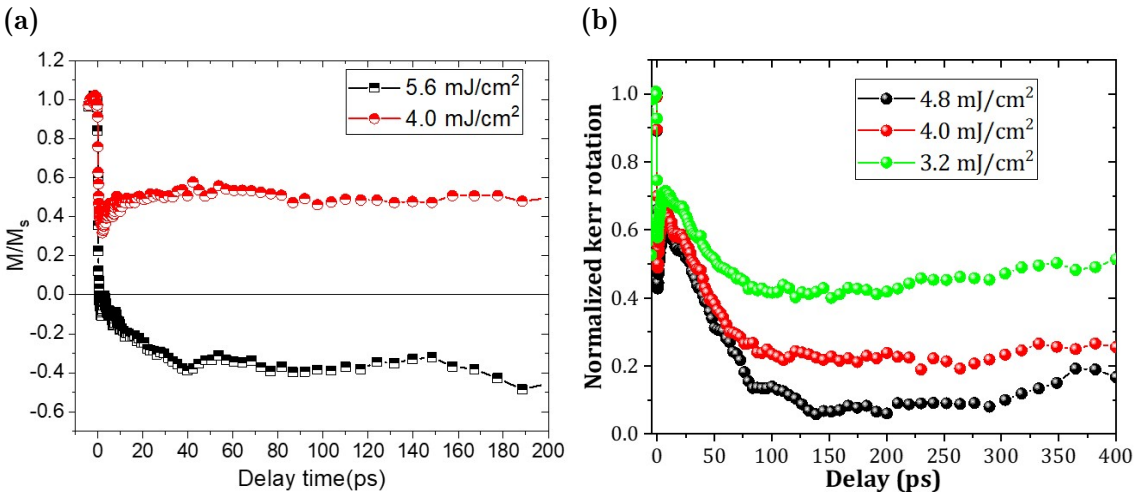

Figure 6.4: (a): Dynamics measured in sample with 21.6% of Gd with the fluence below and above F_{switch}; (b): Dynamics measured in sample with 5% of Gd

F_{switch} threshold when employing a 50 fs laser pulse. Upon increasing the fluence to 5.6 mJ/cm^2, typical demagnetization behavior occurs, and the magnetization crosses the zero point at approximately 600 fs. A full reversal occurs at 40ps before magnetization recovers at a longer time scale because of the applied field to reset the magnetization for the pump-probe experiments. The dynamic behavior is similar to the typical dynamics curves in GdFeCo [92, 98], as ultrafast toggle switching.

In the case of the sample with x = 5%, we observe a distinct set of dynamics. Initially, upon laser excitation, the magnetization undergoes an ultrafast demagnetization, followed by a fast recovery towards its initial state. This behavior resembles the conventional demagnetization and subsequent re-magnetization commonly observed in various ferromagnetic and ferrimagnetic materials. However, at a longer delay time scale, we observe a decrease in the Kerr signal. This decrease corresponds to the in-plane reorientation of the magnetization, a phenomenon previously discussed in Chapter 5.

6.3 Discussion

Based on the observed switching behavior, state diagrams, and dynamic curves of samples with varying Gd concentrations presented above, the magnetization switching induced by a single linearly polarized laser pulse can be categorized into two distinct types. The first category pertains to ultrafast toggle switching within Gd-based materials, and its switching mechanism is governed by the maximum electron temperature attained during laser excitation. The second category involves switching within multilayer structures, which aligns with the in-plane reorientation-induced precessional switching discussed in a prior chapter. This second category of switching leads to the formation of intricate ring structures.

Then, we carefully studied the switching throughout the entire wedge, which has been shown in Figure 6.5. For Gd concentration varies between 21.6% and 12.5%, the trilayer system switches like Gd-based materials without complex ring structure, and We tentatively define it as ultrafast toggle switching and referred to as type-I. While with the Gd concentration less than 7%, the switching behaves like the multilayer, and we call it in-plane reorientation-induced precessional switching and referred to as type-II. In between, only demagnetization can be observed, with the

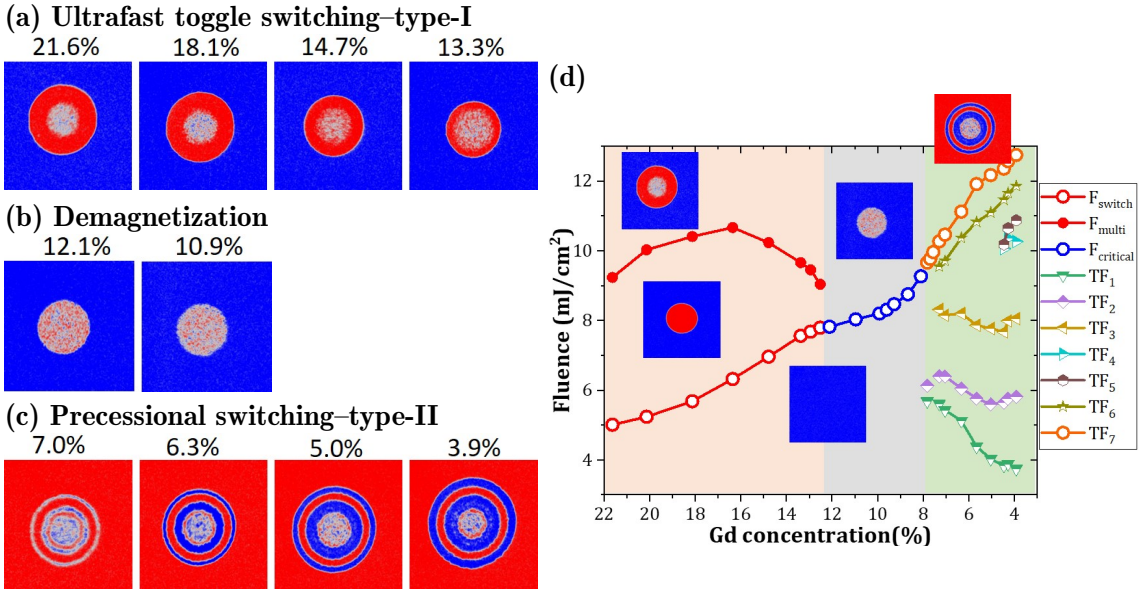

Figure 6.5: (a)-(c): The switching behaviors with different Gd concentrations. (a): Ultrafast toggle switching without complex ring structure with Gd concentration varies between 21.6% and 12.5%; (b): only demagnetization with Gd concentration varies between 12.1% and 7.5%; (c): In-plane reorientation induced-precessional switching with Gd concentration is less than 7.3%. The fluence for 21.6 % is 10.7 mJ/cm^2, and 12.4 mJ/cm^2 for Gd concentration in between 18.1% and 7%, 13.5% for Gd concentration is below 6.3%. (d): The threshold fluences as a function of Gd concentration. F_{switch} and F_{multi} correspond to the ultrafast toggle switching, $F_{critical}$ corresponding to the only demagnetization region, above which multidomain state can be observed in the laser shooting area, while below which nothing happens on the final state. TF_1-TF_7 correspond to the precessional switching with 50 fs laser pulse. More threshold fluences may appear under the excitation of laser pulse with longer pulse duration (See Figure 6.3c). The sample was saturated by a positive magnetic field; thus, the net magnetization aligned in the opposite direction for RE-dominated samples (blue background) and Co-dominated samples (red background).

Gd concentration varying between 12.1% and 7.5%.

The threshold fluence can be extracted using the method introduced in 3.3. For ultrafast toggle switching, threshold fluences can be defined as above: F_{switch} and F_{multi}. Below F_{switch}, nothing happens on the final state, while above F_{multi}, a multidomain state occurs in the central region. In between, a well-defined round shape of the switched domain is obtained. In the demagnetization region, we define a $F_{critical}$, above which a multidomain state will be obtained. For precessional switching, multiple threshold fluences can be extracted due to the ring structure.

It's quite astonishing that the F_{switch} for ultrafast toggle switching, the $F_{critical}$ of the demagnetization region, and TF_7, which also corresponds to F_{multi} for precessional switching, form a seamless continuous curve. This might unveil an inherent connection between these two switching mechanisms. To validate this assertion, we conducted similar measurements using a pulse duration of 1 ps. With a 1 ps pulse, the three curves exhibit a collective upward shift while preserving the same trends observed in the case of a 50 fs pulse, which increases as the Gd concentration decreases. The ultrafast toggle switching occurs when the Gd concentration is above 16.8%, which is higher than the case of 50 fs. It is possible that TbGdCo exists at the TbCo/GdCo interface. According to the single-shot switching in TbGdCo alloy [98, 99], the F_{switch} is higher with lower Gd concentration. Furthermore, the range of fluences at which single-shot switching occurs at 50 fs directly impacts the

magnitude of τ_{max}. In other words, a broader switching fluence range leads to a larger τ_{max}, and conversely, while a narrower range results in a smaller τ_{max} [94,98]. As depicted in Figure 6.5d, the fluence range for ultrafast toggle switching becomes narrower when the Gd concentration is below 16% due to the simultaneous increase in F_{switch} and decrease in F_{multi}. Consequently, a larger Gd concentration range shows demagnetization at 1 ps.

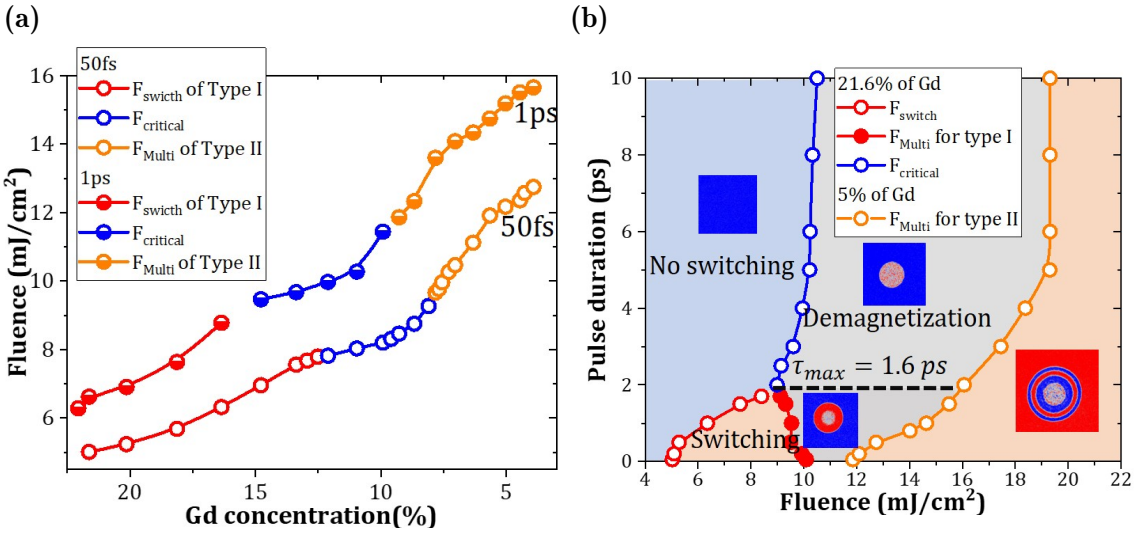

Figure 6.6: (a): F_{switch} for type-I, $F_{critical}$ and F_{multi} for type-II as a function of Gd concentration for 50 fs and 1 ps laser pulse, respectively. (b): F_{switch} and F_{multi} for type-I and $F_{critical}$ for type-I, but pulse duration is above maximum value to get switching (τ_{max} = 1.6 ps) for 21.6% of Gd; andF_{multi} for type-II, as a function of pulse duration.

Given that F_{switch} and F_{multi} exhibit parallel trends in their relationship with Gd concentration across varying pulse durations, one might question whether they also share a similar relationship with pulse duration when Gd content varies. Thus, we conducted state diagrams for Gd concentrations of 21.6% and 5% with pulse duration up to 10 ps, shown in Figure 6.6. As previously discussed, the state diagram for 21.6% Gd content exhibits a triangular shape, with F_{switch} increasing while F_{multi} decreasing as the pulse duration is longer. Consequently, the single-shot switching can not be seen if $F_{switch} = F_{multi}$, resulting in a maximum pulse duration τ_{max} = 1.6 ps. Only a multidomain state can be observed if the pulse duration is above τ_{max}. We extended our measurements up to 10 ps and extracted a $F_{critical}$, above which a multidomain state can be seen. Interestingly, the $F_{critical}$ vs. pulse duration curve appears to be an extension of F_{switch} rather than F_{multi}. More importantly, this F_{switch}, $F_{critical}$ curve demonstrates the same trend as F_{multi} for type-II, where fluence increases with shorter pulse durations and remains constant for longer pulse durations. Once again, these two sets of experimental results reaffirm the existence of inherent connections between the two switching mechanisms.

Let's revisit Figure 6.5d and Figure 6.4, considering F_{switch} for ultrafast toggle switching, the $F_{critical}$ of the demagnetization region, F_{multi} for precessional switching as components of a continuous curve denoted as F'_{switch} for ultrafast toggle switching. Below this F'_{switch}, ultrafast toggle switching does not occur, while it becomes possible only when the fluence exceeds F'_{switch}. However, precessional switching takes place below F'_{switch}. Regarding the dynamics when the fluence is below F'_{switch}, the magnetization undergoes ultrafast demagnetization followed by a recovery toward the initial state, shown in Figure 6.4a with 4.0 mJ/cm^2. Following this demagne-

tization and then the remagnetization process, the magnetization precesses toward the in-plane at a longer delay for 5% of Gd. This behavior arises because, under the excitation of the laser pulse, the temperature increases fast and heats the sample. The perpendicular magnetic anisotropy of the samples was reduced rapidly, causing a temporary shift in effective anisotropy to an in-plane orientation due to the demagnetization field.

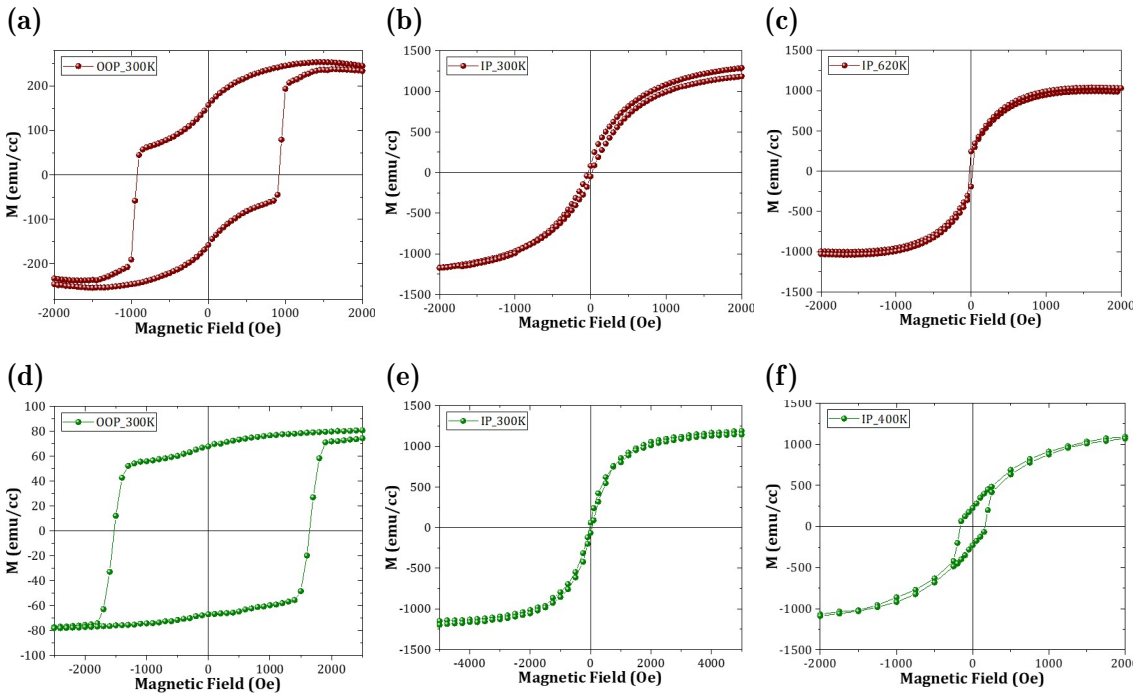

Figure 6.7: Temperature-dependent hysteresis loops for (a-c): 21.6 % of Gd and (d-f): 5% of Gd, measured by SQUID-VSM. (a): Out-of-plane (OOP), (b): In-plane (IP) hysteresis loops measured at 300 K, and (c): In-plane (IP) hysteresis loops measured at 620 K for the sample with 5% of Gd; (d): Out-of-plane (OOP), (e): In-plane (IP) hysteresis loops measured at 300 K, and (c): In-plane (IP) hysteresis loops measured at 400 K for the sample with 21.6% of Gd;

This point can be verified by measuring the hysteresis loops at different temperatures. As depicted in Figure 6.7, out-of-plane (OOP) and in-plane (IP) hysteresis loops have been measured at different temperatures by SQUID-VSM [2]. At 300K, both samples, one with x = 21.6% and the other with x = 5%, exhibit perpendicular anisotropy. Consequently, the in-plane hysteresis loops display the typical characteristics of hard-axis hysteresis loops. However, a notable transition occurs in the orientation of the easy axis. For the sample with x = 21.6%, this transition occurs at 620 K, which we have defined as the in-plane reorientation transition temperature. In contrast, for the sample with x = 5%, the in-plane reorientation temperature is much lower, at 400 K, in comparison to the case of x = 21.6%.

The higher in-plane reorientation transition temperature observed in samples with higher Gd content may be attributed to two primary factors. On the one

[2]The magnetic signal consists of all the signals, including the magnetic sample, the glass substrate, the glue or tape used to fix the sample, the sample holders, and so on. Therefore, the magnetic moment values depicted in the figure do not represent the actual values of the magnetic materials. Furthermore, in our SQUID-VSM measurements of ferrimagnets, a stage near zero field consistently exists, which is currently uncalibrated. This uncalibrated factor leads to a considerably higher saturation magnetization as well. However, the anisotropy and coercivity are not affected by these factors.

hand, the PMA in GdCo alloy may be less susceptible to the influence of rising temperatures, allowing it to persist PMA at higher temperatures. This PMA remains relatively stable as the temperature increases. On the other hand, since the trilayer system with higher content is RE-dominate, whose compensation temperature is above room temperature. This aspect enhances the PMA of the entire system at higher temperatures, resulting in a higher in-plane reorientation transition temperature.

Based on the comprehensive analysis of the static, dynamic, and temperature-dependent magnetic test results discussed above, we gain deeper insights into the two types of switching mechanisms and their associated processes. Within our TbCo/Gd_xCo_{100-x}/TbCo trilayer structure, we observe the presence of two distinct magnetization switching phenomena induced by a single laser pulse: ultrafast toggle switching and precessional switching. While these two mechanisms may coexist, one typically assumes a dominant role depending on Gd concentration. In scenarios where the Gd content is higher, ultrafast toggle tends to dominate the switching process, which occurs on a very short time scale, usually within a few ps. With less Gd content, due to the higher Co content, even though the Gd atoms are evenly distributed among the Co atoms, The aggregation of Co atomic clusters will also form grains, and the direction of its easy axis has local distribution. Therefore, under the excitation of the laser pulse, the magnetization precesses around the local easy axis and toward the in-plane, and finally, switches.

6.4 Conclusion

In this chapter, we reported the two types of switching by varying the Gd concentration in TbCo/Gd_xCo_{100-x}/TbCo trilayer. The system exhibits ultrafast toggle switching with higher Gd concentration, while it shows precessional switching with low Gd concentration. These two mechanisms may exist at the same time, but only one plays a dominant role. However, in precessional switching, the PMA changes to in-plane anisotropy with lower temperature and fluence than Gd-based materials. Consequently, in-plane reorientation-induced precessional switching occurs. This precessional switching occurs below the fluence needed for Gd-based switching.

Sample list

- 732-2 V/Ta(5)Pt(5)(Co67Tb32)(4)CoGd(2nm, wedge in concentration around 90/10)(Co67Tb32)(4)Ta(5)Pt(1)

Chapter 7

Observation of Single-shot Helicity-independent all-optical switching in Co/Ho multilayers

In this Chapter, we experimentally demonstrate AO-HIS in [Co/Ho] multilayer stacks with perpendicular magnetic anisotropy. Surprisingly, even though the spin-orbit coupling in Ho (as it is in Tb and Dy) is larger than that of in Gd, which should increase the dissipation of angular momentum to the lattice, the pulse duration/fluence state diagram is close to the Gd-based system's. Studying this new system could help bridge the single pulse reversal processes observed, on the one hand, in Gd-based, on the other hand, in the Tb or Dy-based heterostructures.[1]

[1]This work has been published: PENG et al., Single-Shot Helicity-Independent All-Optical Switching in Co/Ho Multilayers, *Physical Review Applied*, **20**, 014068 (2023)

7.1 Sample optimization and magnetic properties

Wedge-shaped Glass/Ta(5)/Pt(5)/[Co(wedge, $0.5t_1$-$1.5t_1$)/Ho(wedge, $0.5t_2$-$1.5t_2$)]$_N$ /Pt(1)/Ta(5) multilayers with thicknesses given in nanometers were fabricated using dc magnetron sputtering. The wedge was spanned 50 mm, and t_1 and t_2 are the thicknesses at the position of 25mm for Co and Ho layers, respectively. N represents the number of repetitions of Co/Ho bilayers, as shown in Figure 7.1a. The Co and Ho layers are wedged in the same direction, maintaining a constant thickness ratio (t_1:t_2) across the entire wedge. The sample structure and thickness range for Co and Ho layers are listed in Table 7.1. Hereafter, We use Co(t_1)/Ho(t_2)-wedge to represent the samples with different Co and Ho layer thicknesses. The magnetic properties of the samples were characterized at room temperature using the static polar Kerr magnetometer with a magnetic field applied perpendicular to the film plane. All samples exhibit perpendicular anisotropy, displaying high squareness of hysteresis loops and 100% remanence (Figure 7.1b for Co(0.86 nm)/Ho(0.96 nm)). The positive sign of the Kerr rotation at a high positive field shows that the multilayer is dominated by the Co sublattice, despite the Ho layer being thicker than the Co layer.

Sample name	**Structure**	**Co wedge(nm)**	**Ho wedge(nm)**
Co/Ho-I	[Co(0.8, wedge)/Ho(0.9, wedge)]$_4$	0.4 - 1.2	0.45 - 1.35
Co/Ho-II	[Co(1, wedge)/Ho(0.9, wedge)]$_4$	0.5 - 1.5	0.45 - 1.35
Co/Ho-III	[Co(1.2, wedge)/Ho(0.9, wedge)]$_4$	0.6 - 1.8	0.45 - 1.35
Co/Ho-IV	[Co(1, wedge)/Ho(1.2, wedge)]$_4$	0.5 - 1.5	0.6 - 1.8

Table 7.1: Description of four Co/Ho wedge samples with different Co and Ho thickness combinations and range for N = 4.

Figure 7.1c shows the evolution of the coercivity with different Co and Ho thickness combinations. Each data point represents a specific combination of Co and Ho thicknesses. The axes represent the respective thickness values for Co and Ho layers, while the color of each data point represents the coercivity value. The red color indicates high coercivities around 300 Oe, and the blue color indicates low coercivities around 40 Oe. The coercivities of various Ho (Co) thicknesses with Co (Ho) thickness fixed at 1 nm have been extracted from Figure 7.1c and shown in Figure 7.1d. For the case of t_{Ho} = 1 nm, the coercivity decreases from 164 Oe to 64 Oe as Co thickness increases from 0.86 nm to 1.33 nm. Considering the coercivity for perpendicular anisotropy,

$$H_{\mathrm{Keff}} = \frac{2K_{\mathrm{u}}}{\mu_0 M_{\mathrm{s}}} - M_{\mathrm{s}} \tag{7.1}$$

where the coercivity is inversely proportional to M_s, the decrease in H_C leads to the increase in M_s. While for the case of t_{Co} = 1 nm, the coercivity increases as Ho thickness increases.

The saturation magnetization M_s, and coercive field H_C, have been characterized as a function of temperature T, shown in Figure 7.2. Here, the measure-

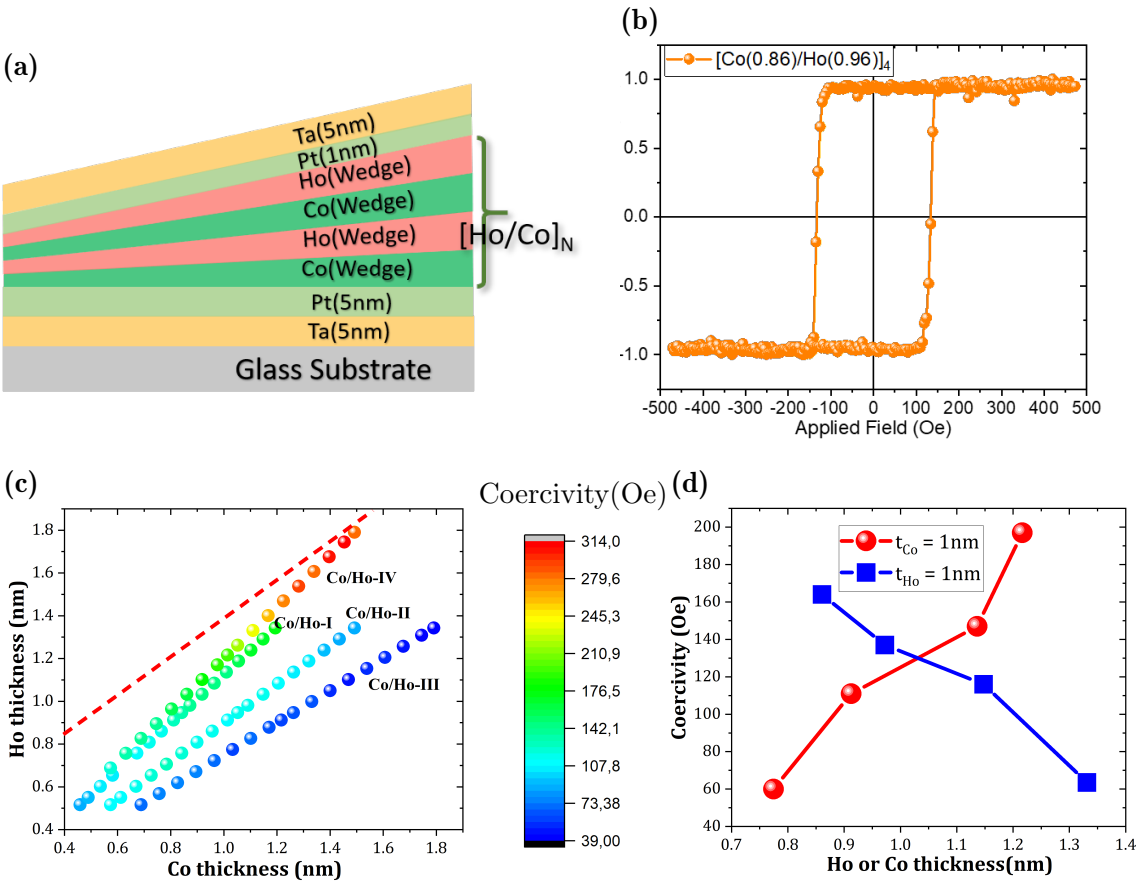

Figure 7.1: a): Schematic of the wedged $[Co/Ho]_N$. The Co and Ho layers are wedged in the same direction with graded monolayer thickness spanning $0.5t_1 < t_{Co} < 1.5t_1$ and $0.5t_2 < t_{Ho} < 1.5t_2$. The square brackets contain the bilayer structure that is repeated N times within each sample. b): Polar magneto-optical Kerr effect measurement performed at room temperature on $[Co(0.86)/Ho(0.96)]_4$; (c): Coercivity map of the four samples listed in Table 7.1. Each data point represents a specific combination of Co and Ho thicknesses. The x and y axes represent the respective thickness values for Co and Ho layers, while the color of each data point represents the coercivity value. The red dots indicate strong coercivities around 300 Oe, the blue dots indicate weak coercivities around 40 Oe, and the red dashed line shows the estimated thickness compensation line. (d): The coercivity as various Ho (Co) thicknesses with Co (Ho) thickness is fixed at 1 nm.

ments with temperature between 20 K and 400 K have been performed on three positions with different Co and Ho thicknesses of Co/Ho-I, $[Co(0.46)/Ho(0.52)]_4$, $[Co(0.6)/Ho(0.7)]_4$ and $[Co(0.81)/Ho(0.91)]_4$, respectively. All the stacks show a compensation temperature T_{comp} below room temperature, indicating that Co-sublattice dominates the sample. The existence of compensation temperature verifies that antiferromagnetic coupling exists between the Co and Ho layers. The compensation temperature T_{comp} is 210 K for $[Co(0.81)/Ho(0.91)]_4$, which is closer to the room temperature, while it is 115 K for $[Co(0.46)/Ho(0.52)]_4$. These measurements are consistent with the coercivity map results in Figure 7.1c.

For samples Co/Ho-I and Co/Ho-IV where the thickness ratio of Ho and Co layer are 1:1.13 and 1:1.2 through the entire wedge, respectively, the coercivities are higher with larger thicknesses corresponding to lower M_s. The increase in the thickness of the two layers leads to an increase in their respective magnetic moments. But the magnetic moment of the Ho sublattice grows faster, and more magnetic moments compensate for the magnetic moment of the Co sublattice, resulting in a decrease

in the net magnetic moment and making the whole system closer to the compensation point. On the contrary, coercivity decreases when the thicknesses increase for Co/Ho-III, where the thickness ratio of Ho and Co keeps 1:0.75, indicating the system is further from the compensation point with larger thicknesses of the two layers. A remarkable finding emerges in the case of Co/Ho-II, where the Co and Ho layers have a thickness ratio of 1.11:1. The coercivities of this system remain constant at approximately 110 Oe, regardless of the exact thickness values.

The coercivity for Co(1.5nm)/Ho(1.8nm) is 313 Oe; this high value suggests that the magnetic moments of the Co and Ho layers almost compensate. Taking the thickness ratio of Co/Ho-II, where the coercivity remains a constant, and Co(1.5nm)/Ho(1.8nm), which shows a high coercivity and is close to the compensation, the thickness compensation line, which represents a region where the Co and Ho layer thicknesses are finely compensated, can be roughly estimated as:

$$t_{\mathrm{Ho}} = 0.9t_{\mathrm{Co}} + 0.5$$

which is shown by the red dashed line in Figure7.1c. The net magnetization is dominated by the Ho sublattice on the left side, while it is dominated by the Co sublattice on the right side. Despite Ho possessing a higher atomic magnetic moment of $10.6\mu_{\mathrm{B}}$ at low temperature, surpassing that of Gd and Tb (7.5 μ_{B} and 9.34 μ_{B}, respectively)[53,150], the multilayer is still dominated by Co even when the thickness of Ho is higher than that of Co. This behavior is mainly attributed to the low Curie temperature of the Ho element, which is approximately 19K[151].

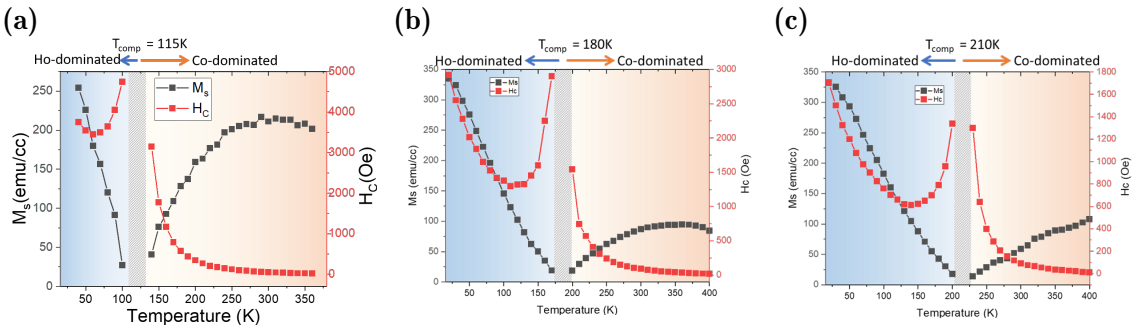

Figure 7.2: Saturation magnetization M_S and coercivity H_C as a function of temperature, (a) $[Co(0.46)/Ho(0.52)]_4$; (b): $[Co(0.6)/Ho(0.7)]_4$; (c): $[Co(0.81)/Ho(0.91)]_4$. All the stacks show a compensation temperature T_{comp} below room temperature. The compensation temperatures are 115 K, 180 K, and 210 K, and M_S at 300 K are 210 emu/cc, 87 emu/cc, and 59 emu/cc for the case of (a), (b) and (c). The temperature-dependent coercivity for all the cases shows a similar trend, where the coercivity diverges at compensation temperature; in the meantime, it increases as temperature decreases when the temperature is below a certain value. The temperatures where the minimum coercivity occurs below compensation temperature are 60 K, 110 K, and 150 K for the case of (a), (b), and (c), respectively.

The temperature-dependent coercivity for all the cases shows a similar trend, where the coercivity diverges at compensation temperature; in the meantime, it increases as temperature decreases when the temperature is below a certain value. For ferrimagnet, the coercivity as a function of temperature shows a trend that diverges at the compensation temperature [152–155], where the net magnetization of the ferrimagnetic material becomes zero according to equation 7.1. The coercivity generally decreases as the temperature moves farther away from T_{comp}. For ferro-

magnet, the coercivity exhibits a different trend from ferrimagnet. The coercivity generally decreases as the temperature increases, and conversely, it increases as the temperature decreases. The nucleation of the magnetization and/or domain wall motion is limited with lower temperatures due to the thermal effect, resulting in a higher coercivity [156, 157]. In the case of artificially synthesized ferrimagnetic materials, the temperature-dependent coercivity is influenced by two main factors: 1) the compensation effect; 2) the thermal effects. Above the compensation temperature, the compensation and thermal effects synergistically affect the coercivity, which decreases with the temperature increase. Below the compensation temperature, the compensation and thermal effects are opposite of the coercivity. Below and close to the compensation temperature, the increase of M_S has a larger effect on the coercivity, so the coercivity decreases rapidly as temperature decreases. However, when the temperature drops to a certain value, the more difficult nucleation and/or domain wall motion leads to a rapid increase in the coercivity.

7.2 Switching quality(area) vs Different thickness combinations

Single-shot HI-AOS of the magnetization in the Co/Ho multilayer has been explored in different regions, where the thickness of either Co or Ho is maintained at a fixed value of 1 nm, while the thickness of the other material (Ho or Co) is systematically varied. By altering the thickness of one of the materials while keeping the other constant, we can study the influence of varying layer thickness on the single shot switching behaviors. Since Co-sublattice dominates all the samples, samples with larger Ho thickness are closer to the compensation point for a fixed Co thickness of 1 nm. On the contrary, samples with larger Co thickness are further away from the compensation point for a fixed Ho thickness of 1 nm.

Firstly, let us examine the magnetization-switching behavior of samples with varying Ho thickness and a fixed Co thickness of 1 nm. We assess the switching domain, represented by the blue domain area, compared to the spot area above a critical fluence, indicating the presence of observable domains after laser pulse irradiation. For Ho thickness of 0.77 nm, the blue domain area is 67% of the circular area after the first pulse, while the blue domain area reduces to around 50% after the second, third, and fourth pulses, implying that no single switching occurs with this specific thickness combination. However, with larger Ho thickness, it is noteworthy that the blue domain area is larger (More than 50%) by the first and third pulses, while it is smaller (Less than 50%) by the second and fourth pulses, indicating partial switching of the magnetization in area.

The switching behavior is significantly influenced by the Co thickness when the Ho thickness is fixed at 1 nm. Figure 7.3b and 7.3d illustrate that when the Co thickness is 1.33 nm, there is only 50% of the blue domain area after each pulse, suggesting the absence of switching. Conversely, with a lower Co thickness, bringing the sample closer to the compensation point, alternating percentages of 70% and 40% for the blue domain areas after odd and even pulses suggest partial magnetization switching.

However, it is important to note that the percentage of the blue domain area alone does not fully represent the actual quality of the switching. Of course, 50% of the blue domain after each pulse, for example, $[Co(1)/Ho(0.77)]_4$ and $[Co(1.33)/Ho(1)]_4$, indicates no switching. However, the switching and multidomain areas are different due to the different critical fluence for switching and demagnetization for different thickness combinations since the measurements were done with the same fluence.

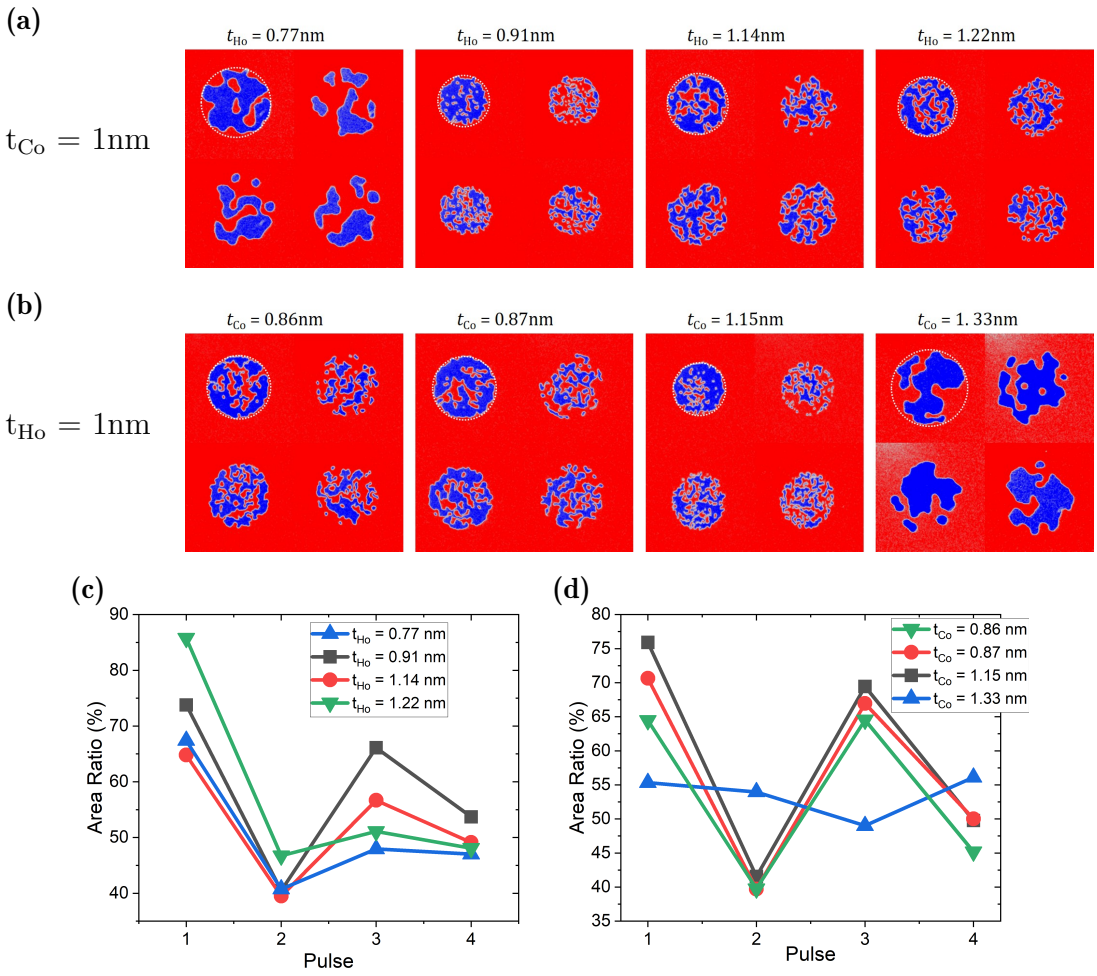

Figure 7.3: (a) and (b): AOS measurements performed on $[Co/Ho]_4$ stacks using a pulse duration of 50fs and a fluence of 11 mJ/cm^2. (c) and (d): The blue domain area was compared to the spot area above a critical fluence, which indicates the presence of observable domains after laser pulse irradiation. (a) and (c): Different Ho thicknesses were studied with a fixed Co thickness of 1nm. (b) and (d): Different Co thicknesses were examined with a fixed Ho thickness of 1nm. The dotted circles indicate the regions where the structure was excited by each individual laser pulse. The colors red and blue represent the net magnetization pointing up and down, respectively. In each image, the first line corresponds to pulse 1 and pulse 2, while the second line represents pulse 3 and pulse 4.

Thus, the percentage of the blue domain in the so-called switching region should be higher after an odd number of pulses and lower after an even number of pulses.

Based on the aforementioned single-shot switching tests, it is observed that there is no switching for thickness combinations significantly deviating from the compensation point. Furthermore, when either the Co or Ho thickness becomes too large, the entire multilayer film system no longer exhibits single-shot switching. By testing samples at different positions (that is, with different thicknesses), we focused the single switching on Co/Ho-I.

Figure 7.4 shows the measurement result performed on the Co/Ho-I stack, in which the sample is exposed to four subsequent laser pulses with F = 5.22 mJ/cm^2 and 9.38 mJ/cm^2 (50fs of the pulse duration). We can clearly observe a distinct region of magnetization switching after the first laser pulse in $[Co(0.46)/Ho(0.52)]_4$. After the second pulse, the magnetic moments reverse back to the initial state, indicating that the magnetic moments in the sample have undergone a reversal, which

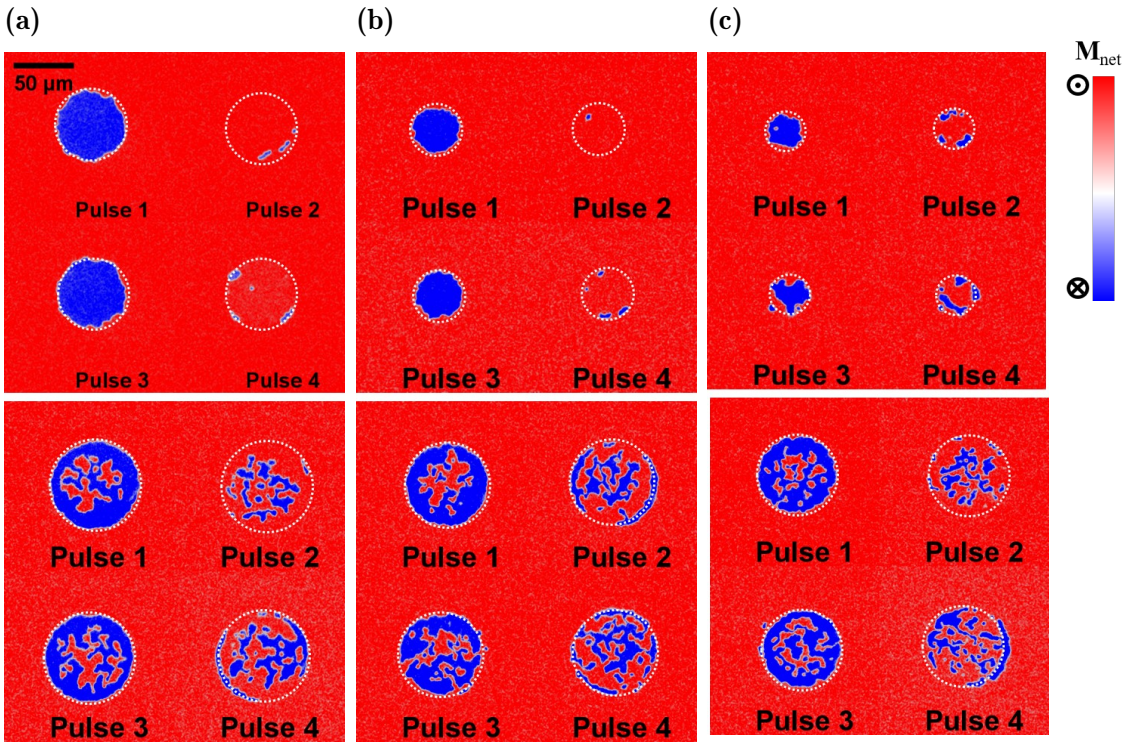

Figure 7.4: AOS measurements performed on $[Co/Ho]_4$ stacks with different Co and Ho thicknesses. (a): $[Co(0.46)/Ho(0.52)]_4$; (b): $[Co(0.6)/Ho(0.7)]_4$; (c): $[Co(0.81)/Ho(0.91)]_4$ (thickness in nm). The dotted circle regions correspond to the spots where the structure is excited by each single laser pulse (fluence 5.22 mJ/cm^2(top), 9.38 mJ/cm^2(bottom), pulse duration 50fs). Red and blue colors represent the net magnetization pointing up and down.

is a promising indication of toggle magnetization switching. Similar observations are made in samples with slightly thicker thicknesses, such as $[Co(0.6)/Ho(0.7)]_4$. In these cases, the magnetization switching area after the first laser pulse remains evident, indicating the robustness of the toggle magnetization switching phenomenon. However, as we further increase the thickness of both Co and Ho layers, a notable change in the behavior of magnetization switching is observed. For instance, in samples with a thickness of $[Co(0.81)/Ho(0.91)]_4$, the magnetization switching area after the first laser pulse becomes less smooth compared to the previous cases. This suggests that increased thickness makes the magnetization reversal process more challenging. Moreover, with subsequent laser pulses, a multidomain structure is formed in these thicker samples. This indicates a loss of magnetization toggle switching behavior when the thickness of Co and Ho reaches 0.8 nm and 0.9 nm, respectively. The appearance of multiple domains suggests that the magnetization is no longer uniformly switching, but instead, different regions within the material adopt different magnetic orientations.

Additionally, after an odd number of laser pulses, the shape of the domain is not perfectly circular, and some small domains at the rim appear after an even number of pulses. This can be attributed to two main factors. Firstly, the dipolar field, which is stronger close to the domain boundaries, influences the shape of the magnetization domains. Secondly, there may be a slight offset of the laser spot, which can introduce localized variations in the switching behavior.

Meanwhile, we also performed statistical analysis to assess the quality of magnetization switching. Specifically, we analyzed the area and domain wall length

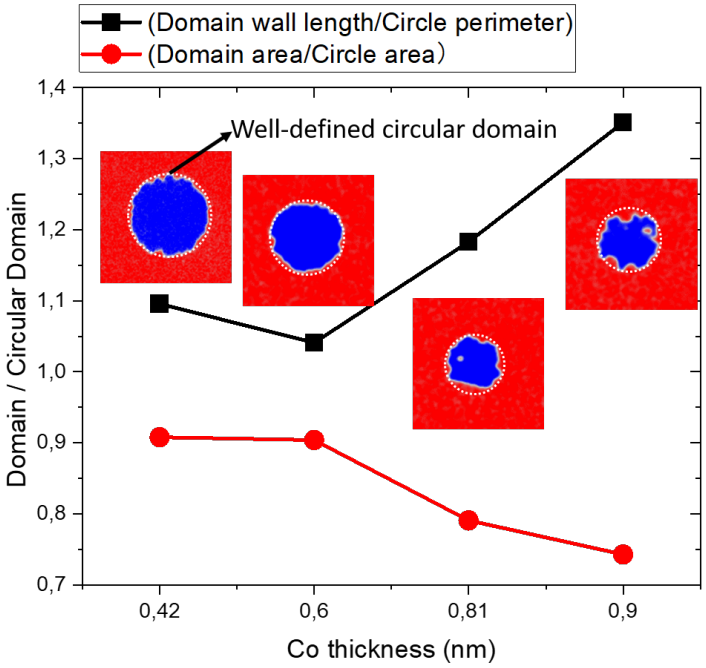

Figure 7.5: Analysis of the domain wall length and domain area compared to a well-defined circular domain. Insets are the domain pattern after the first pulse with different Co thicknesses (the thickness ratio of Co and Ho keeps 1: 1.1). An increase in the domain wall length is obviously associated with a decrease in the domain area.

ratio between the magnetization domain formed after the first laser pulse and a well-defined circular domain, which describes the quality of magnetization switching. The dependence of these ratios on the thickness of the Co layer is depicted in Figure 7.5. We observed that the domain area ratio, which compares the area of the actual domain to that of a perfect circle (shown by a white dashed circle), consistently remains below 1 and decreases further as the Co thickness increases. On the other hand, the domain wall length ratio, which measures the length of the domain wall relative to the perimeter of a perfect circle, consistently exceeds 1 and increases with increasing Co thickness. This domain area ratio and domain wall length ratio lead us to conclude that the thicknesses of both the Co and Ho layers play a critical role in achieving successful single-shot switching. Specifically, for a repetition number (N) of 4, the Co layer thickness should not exceed 0.8 nm, while the Ho layer thickness should be below 0.9 nm. Otherwise, the resulting domain shape tends to become dendritic, with irregular and branching structures.

7.3 Repetition numbers and thicknesses

Based on the above results, we proceeded to conduct a series of samples with fixed thicknesses of Co layers ranging from 0.25 nm to 0.75 nm ($t_1 = 0.5$ nm) and Ho layers ranging from 0.28 nm to 0.83 nm ($t_2 = 0.55$ nm) while maintaining a thickness ratio of 1:1.1 between Co and Ho. Multiple samples were prepared with varying repetition numbers (N) of the bilayer, ranging from 2 to 5.

Single-shot all-optical switching measurements have been performed through the four entire wedges. The switching region for each multilayer with different repetition numbers has been extracted and shown by light red color in Figure 7.6. All of the samples exhibited remarkable and reliable single-pulse switching behavior. Specifi-

Repetition number	Co wedge(nm)	Ho wedge(nm)	Total thickness range (nm)
N = 2	0.25 - 0.75	0.28 - 0.83	1.06 - 3.16
N = 3	0.25 - 0.75	0.28 - 0.83	1.59 - 4.74
N = 4	0.25 - 0.75	0.28 - 0.83	2.12 - 6.32
N = 5	0.25 - 0.75	0.28 - 0.83	2.65 - 7.9

Table 7.2: Description of four Co/Ho double-wedge samples with fixed thicknesses of Co layers ranging from 0.25 nm to 0.75 nm ($t_1 = 0.5$ nm) and Ho layers ranging from 0.28 nm to 0.83 nm ($t_2 = 0.55$ nm) while maintaining a thickness ratio of 1:1.1 between Co and Ho.

cally, for N = 2, we observed that a clear toggle-switching phenomenon was evident above a certain critical Co monolayer thickness of approximately 0.56 nm and Ho monolayer thickness of approximately 0.62 nm. However, only a multidomain state was observed for lower thicknesses of both the Co and Ho layers. Expanding our investigation to N = 3, we found that the minimum Co monolayer thickness required for successful switching extended to approximately 0.31 nm, while the minimum Ho monolayer thickness extended to around 0.34 nm. For the cases of N = 4 and N = 5, We found that the reversal of magnetization occurred across the entire range of thicknesses within the wedged region, indicating that reliable switching was achieved for all combinations of Co and Ho layer thicknesses.

The switching images in Figure 7.6 clearly illustrate that when the sample is exposed to the laser pulse with the same fluence, the resulting sizes of the switching magnetic domains vary depending on the combinations of layer thicknesses. This can be attributed to the inherent Gaussian distribution of laser pulse energy. Consequently, the critical fluence required for magnetization switching, denoted as F_{Switch}, also varies for different thickness combinations. Furthermore, as the fluence surpasses a certain threshold, a multi-domain state emerges at the center of the laser spot where the fluence is the highest due to thermal demagnetization effects. This critical fluence is defined as F_{Multi}.

We conducted a comprehensive investigation to understand the influence of layer thickness on the critical fluence values, F_{Switch} and F_{Multi}, using a fixed pulse duration of 50 fs. In the case of N = 2, the specific combination $[Co(0.56)/Ho(0.62)]_2$ exhibits distinct values for F_{Switch} and F_{Multi}, measuring 3.5 mJ/cm^2 and 4.7 mJ/cm^2, respectively. As a result, the switching fluence range for this combination is relatively narrow, spanning only 1.2 mJ/cm^2. As the thicknesses of both Co and Ho layers increase, we observe a notable decrease in F_{Switch} and an increase in F_{Multi}. Consequently, the overall switching fluence range becomes wider. For instance, in the case of $[Co(0.74)/Ho(0.81)]_2$, the switching fluence range expands to approximately 2.5 mJ/cm^2, which is twice that of $[Co(0.56)/Ho(0.62)]_2$. This broader range is achieved due to the respective values of 3.2 mJ/cm^2 for F_{Switch} and 5.7 mJ/cm^2 for F_{Multi} associated with this particular combination.

In the case of N = 3, we observe an extension of the minimum thickness combination required for switching to $[Co(0.31)/Ho(0.34)]_3$. For this combination, F_{Switch} and F_{Multi} are measured 3.2 mJ/cm^2 and 4.6 mJ/cm^2, respectively. Comparing this with the previous case of N = 2, where we had $[Co(0.56)/Ho(0.62)]_2$ as the minimum thickness combination, it is interesting to note that the total thicknesses for both

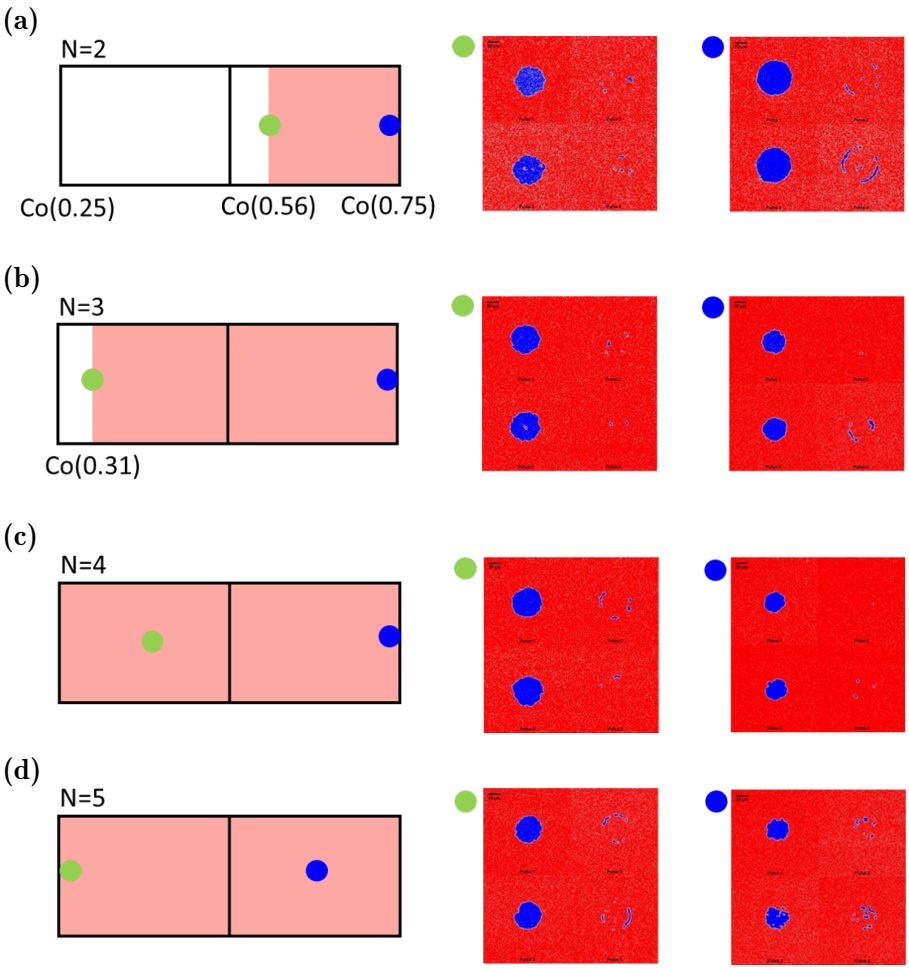

Figure 7.6: The range of Co and Ho layer thicknesses (shown by light red color) where single shot switching occurs in [Co/Ho]N multilayers and Single shot switching images which is exposed to consequent four single laser pulses with 3.75 mJ/cm^2 and pulse duration of 50 fs measured at different positions shown by green and blue dots. (a) N = 2, green dot: $[Co(0.56)/Ho(0.62)]_2$, blue dot: $[Co(0.74)/Ho(0.81)]_2$; (b) N = 3, green dot: $[Co(0.31)/Ho(0.34)]_3$, blue dot: $[Co(0.74)/Ho(0.81)]_3$; (c) N = 4, green dot: $[Co(0.38)/Ho(0.42)]_4$, blue dot: $[Co(0.74)/Ho(0.81)]_4$; (d) N = 5, green dot: $[Co(0.26)/Ho(0.29)]_5$, blue dot: $[Co(0.0.63)/Ho(0.69)]_5$; In each image, first line pulse 1 and pulse 2, second line pulse 3 and pulse 4.

combinations are 2.16 nm and 1.95 nm, respectively, which are very close. In the meantime, the value of F_{Switch} and F_{Multi} are very close, too. The F_{Switch} slightly increases as the Ho thickness increases to 0.5 nm and maintains a constant value around 3.7 mJ/cm^2 with larger Ho and Co thickness. Examining the behavior of F_{Multi}, we observe that it increases with a steeper slope when the Ho thickness is below 0.45 nm. As the Ho thickness ranges between 0.45 nm and 0.65 nm, F_{Multi} still increases but with a lower slope. However, when the Ho thickness exceeds 0.65 nm, F_{Multi} starts to decrease. In the case of N = 4 and N = 5, we observe a linear increase of F_{Switch} as Ho thickness increases and a similar trend of F_{Multi} as the case of N = 3.

A very interesting trend of F_{Switch} and F_{Multi} can be observed if we plot them as a function of the total thickness as shown in Figure 7.7b. We can clearly see that F_{Switch} increases almost linearly with an increasing total thickness of the multilayer. In the case of F_{Multi}, the variation with thickness is not monotonic, While F_{Multi}

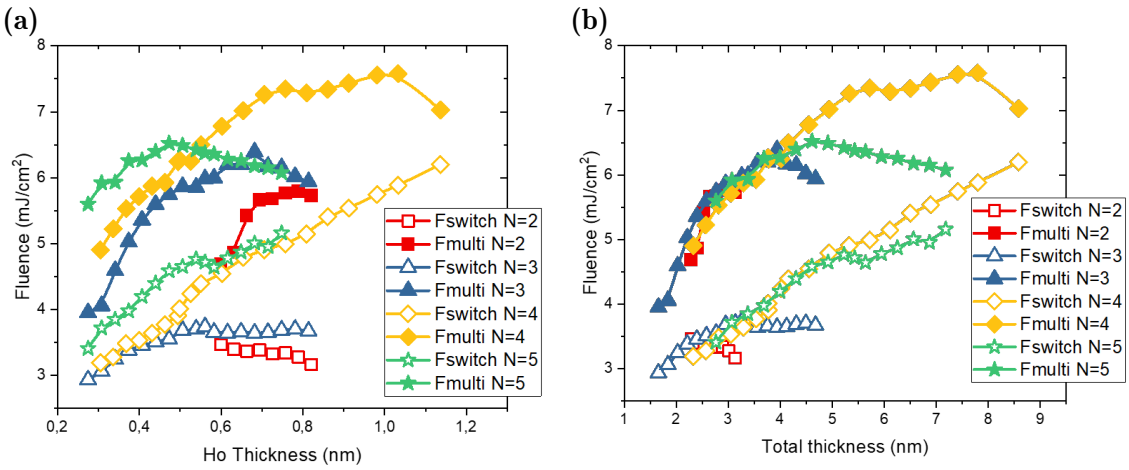

Figure 7.7: Variation of F_{Switch} and F_{Multi} as a function of thickness for different repetition numbers(pulse duration: 50 fs), (a): Monolayer thickness; (b): Total thickness.

increases when the total thickness is below 4.5 nm, it eventually saturates and can even decrease as the thickness further increases.

In the case of GdFeCo alloy, F_{Switch} significantly depends on the alloy composition and reaches a minimum around compensation points [94]. Our Co/Ho multilayers, which have been studied, are always in the Co-dominate region and along the compensation point line. Even though the compensation temperatures with different thickness combinations have been measured, it is hard to conclude the relationship between the F_{Switch} and the compensation point. However, Wei also pointed out that F_{Switch} scales with the layer thickness, which can be ascribed to the variation of the laser absorption and the domain volume. The energy absorption of a thin metallic film after exposure to a laser pulse is determined by its thickness and refraction index. The sample with a smaller thickness shows a higher absorption due to a lower reflectance. Moreover, with the same laser fluence, the thinner sample would be heated up to a higher temperature due to its smaller amount of materials. For the above reasons, the threshold switching fluence and demagnetizing fluence are expected to be lower for thinner samples.

Indeed, it is well known that a stable magnetic domain in a perpendicularly magnetized thin film strongly depends on the film thickness and saturation magnetization M_S[158–160]. This results from the competition between the dipolar energy that stabilizes small domains and the domain wall energy that tends to reduce the length of the domain walls and so stabilize big domains. It is, therefore, reasonable to infer that if the size of stable magnetic domains after the laser-induced heating is smaller than the size of the laser spot, thermal demagnetization will be observed because the system will break into small domains during cooling, resulting in a low F_{Multi}. As a result, even if a switch of magnetization occurs, only a demagnetized state could be observed. For example, in the cases of $[Co(1)/Ho(0.77)]_4$ and $[Co(1.33)/Ho(1)]_4$, which are further away from the compensation point, resulting in a large M_S, the critical fluences are much lower than the so-called F_{Switch} for the cases which are closer to the compensation point in Figure 7.3. This could explain why F_{Multi} decreases with larger thickness. However, I could not understand the magnetic larger domain size of the cases of $[Co(1)/Ho(0.77)]_4$ and $[Co(1.33)/Ho(1)]_4$ where the M_s should be higher than the other cases.

7.4 State diagram

In Chapters 4 and 5, we conducted an in-depth analysis of the state diagram associated with the single-shot switching of multilayers based on Tb and Dy elements. Notably, we found that this state diagram exhibits distinct characteristics compared to Gd-based materials. The results further highlight the differences in the switching mechanisms and timescales between these systems. Therefore, investigating the state diagram is a valuable approach to enhance our understanding of the intricate switching mechanisms involved in these materials. Figure 7.8 shows magneto-optical images obtained on a $[Co(0.46)/Ho(0.52)]_4$ multilayer after exposure to a single laser pulse for different pulse durations and different fluences. The film is initially saturated under an external magnetic field before exposure.

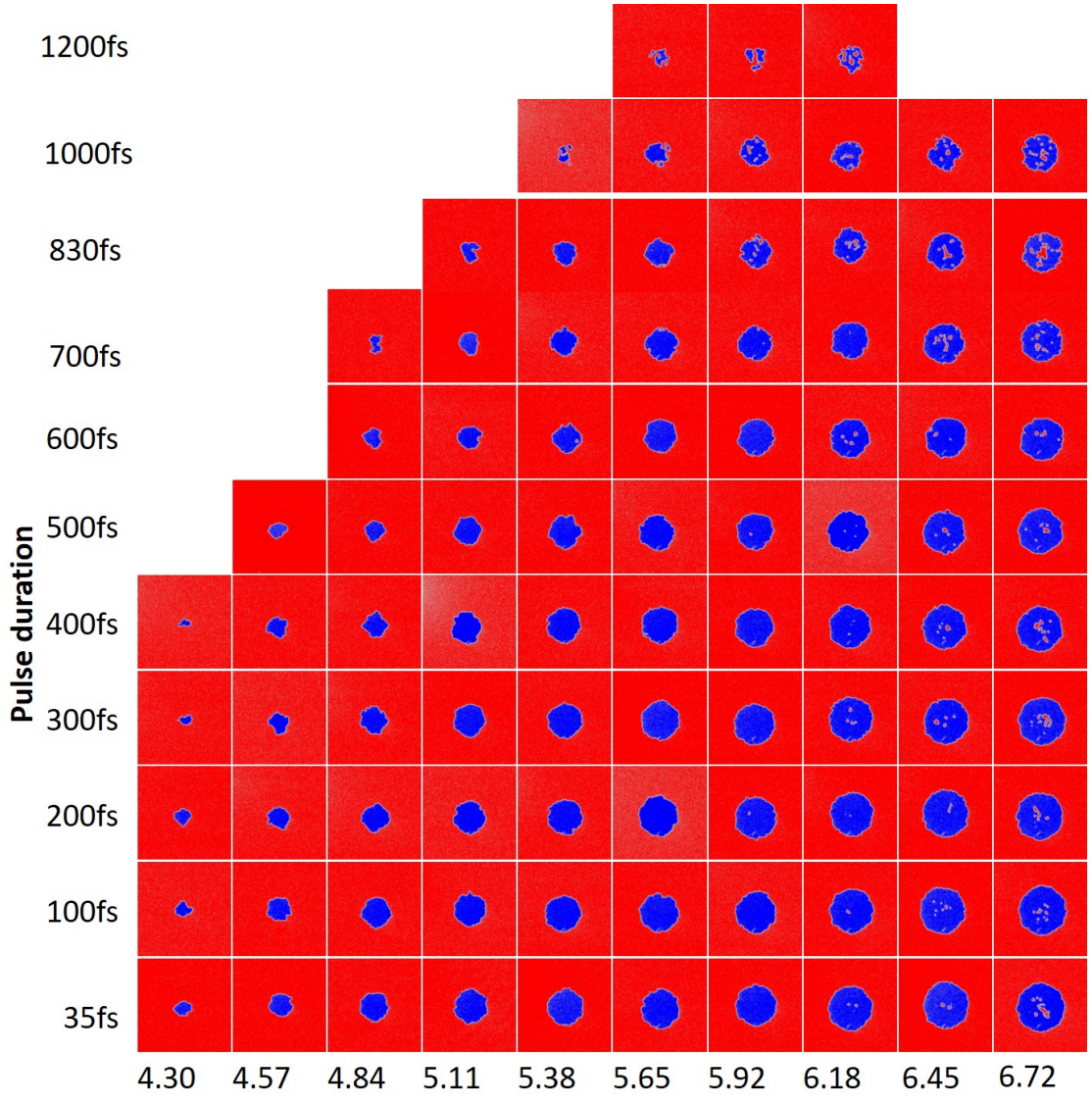

Figure 7.8: Background-subtracted images for AOS measurements performed on $[Co(0.46)/Ho(0.52)]_4$ sample with different Fluences and pulse durations.

The pulse duration and fluence of the single laser pulse significantly influence the size and characteristics of the switching domain. For example, when using a pulse duration of 35 fs, a small and localized switching domain is observed at a fluence of 4.3 mJ/cm^2, which we define as F_{Switch} above. Below this critical fluence, no observable changes occur on the sample upon laser pulse irradiation. As the fluence

increases, the switching domain expands within the laser spot. At a fluence of 6.2 mJ/cm^2, small domains begin to emerge in the central region of the laser spot, where the fluence is highest due to thermal demagnetization. This trend persists across various pulse durations, indicating the dependence of the switching domain on both fluence and pulse duration.

Furthermore, it is observed that as the pulse duration increases, the minimum fluence required for magnetization switching, F_{Switch}, also increases. For instance, at the same fluence of 5.4 mJ/cm^2, the switching domain size decreases with longer pulse durations, indicating a higher F_{Switch} due to the Gaussian distribution of the laser pulse energy. Conversely, a multidomain state in the central region occurs at lower fluences for longer pulse durations. As a result, the range of fluences capable of inducing switching becomes narrower with longer pulse durations. Only a multidomain state is observed when the pulse duration reaches 1200 fs.

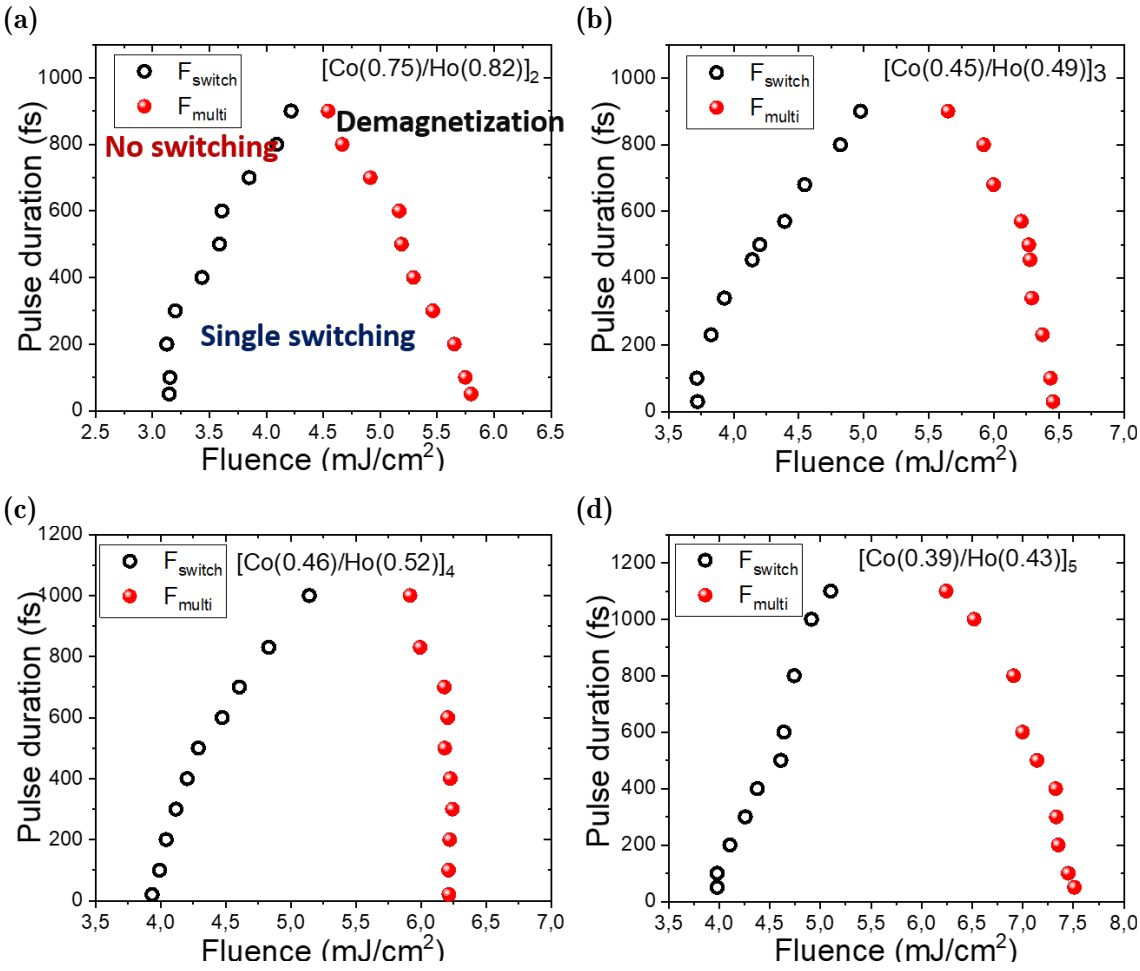

Figure 7.9: State diagram: switching fluence F_{switch} (open black circle) and multidomain fluence F_{multi} (full red sphere) as a function of the pulse duration for a single linearly polarized laser pulse. (a): $[Co(0.75)/Ho(0.82)]_2$; (b): $[Co(0.45)/Ho(0.49)]_3$; (c): $[Co(0.46)/Ho(0.52)]_4$; (d): $[Co(0.39)/Ho(0.43)]_5$.

To study the state diagram, the evolution of both F_{Switch} and F_{Multi} as a function of laser pulse durations have been extracted from the Kerr images. The state diagram classifies the magnetic states obtained after one laser pulse irradiation into three distinct regions: No switching, single switching, and demagnetization. Interestingly, F_{Switch} and F_{Multi} exhibit distinct dependencies on pulse duration. Let's consider the example of $[Co(0.75)/Ho(0.82)]_2$ with 2 repetitions of the bilayer. At a

pulse duration of 35 fs, F_{Switch} and F_{Multi} are measured to be 3.1 mJ/cm^2 and 5.8 mJ/cm^2, respectively, resulting in a fluence range of 2.7 mJ/cm^2 for single switching. However, when the pulse duration is increased to 500 fs, we observe an increase in F_{Switch} to 3.6 mJ/cm^2, while F_{Multi} decreases to 5.2 mJ/cm^2, resulting in a narrower switching fluence range of 1.6 mJ/cm^2. As the pulse duration continues to increase, we observe a further increase in F_{Switch} and a further decrease in F_{Multi}. This trend persists until $F_{Switch} = F_{Multi}$, which defines the maximum pulse duration (τ_{max}) below which the phenomenon of all-optical helicity-independent switching can be observed. Beyond this maximum pulse duration, only a multidomain state could be observed without single switching. Similar trends are observed in the relationship between F_{Switch}, F_{Multi}, and pulse duration in the case of other stacks with varying repetition numbers of the bilayer. As the pulse duration increases, F_{Switch} tends to increase, while F_{Multi} decreases, resulting in a triangular shape of the state diagram. This triangular pattern is consistently observed across different stacks with varying repetition numbers and thickness combinations. For stacks with N = 2, the maximum pulse duration (τ_{max}) falls around 900 fs, slightly increasing as the number of bilayer repetitions increases. The overall behavior of F_{Switch}, F_{Multi}, and pulse duration in forming the state diagram remains consistent across these different stack configurations.

The observed state diagram in the Co/Ho samples exhibits a triangular shape, similar to that found in GdFeCo alloys, despite the absence of Gd in the samples. Instead, the samples contain a heavy rare-earth element (RE) with strong spin-orbit couplings, such as Tb and Dy. However, the state diagram of Co/Ho differs significantly from the state diagrams reported in other multilayers that include Tb, TbCo, DyCo, TbFe, and a transition metal (TM) layer consisting of Co, Fe, CoFeB, and Py. This indicates that the current understanding of the helicity-independent all-optical switching (HI-AOS) process in Gd, which suggests that low spin-orbit/damping materials are necessary, does not fully explain the behavior observed in Ho.

7.5 Time-resovled MOKE dynamics

So far, we demonstrated the AO-HIS in Co/Ho multilayers by means of static microscopy measurements. As a new kind of material showing magnetization switching, it is necessary to test the time-dependent magnetization evolution, which can figure out the switching time scales, consequently helping us understand the switching mechanism.

The dynamics were done on the samples with a thickness combination of [Co(0.38) /Ho(0.42)]$_4$, where it shows a relatively larger switching window for pulse duration and fluence. First, static single shot switching has been checked with a fluence of 7.1 mJ/cm$_2$ to ensure the fluence is in the switching window. Before doing the dynamics, we tested the thermal heating of the laser with 10 kHz of the repetition rate for more than 30 minutes. The sample is still alive with these conditions and shows single-shot switching after the test. The measurements were done for positive and negative external fields of 550 Oe. Here, we show some time-dependent MOKE images where we subtracted data for opposite external magnetic field directions, and a common background was subtracted at each delay.

At low fluence, we observe standard ultrafast demagnetization curves with a fast reduction of magnetization followed by a rather fast but still slower recovery. With lower fluence, for example, 2.6 mJ/cm^2, a fast demagnetization takes place within 0.5 ps, and it is followed by a pronounced magnetization recovery toward its

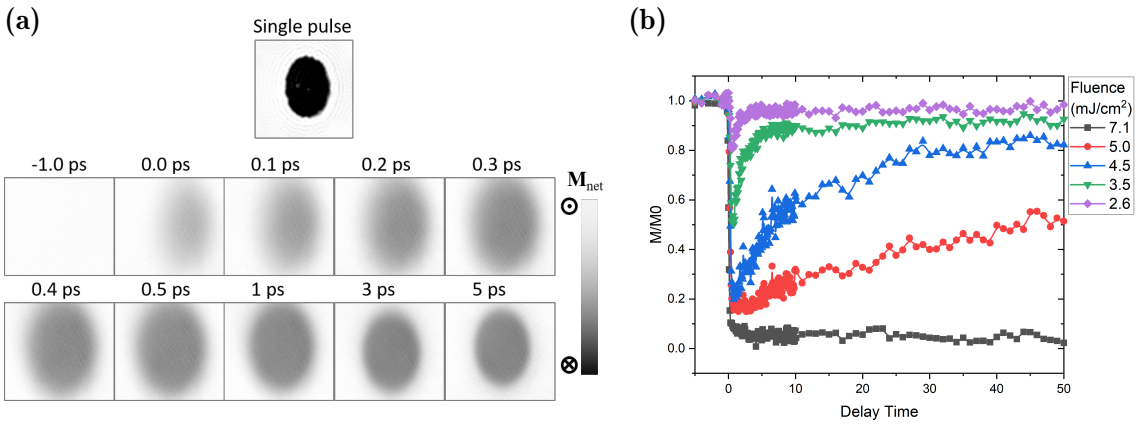

Figure 7.10: The magnetization dynamics $[Co(0.38)/Ho(0.42)]_4$ are investigated by measuring the evolution of magnetization as a function of delay time with the laser fluence of 7.1 mJ/cm_2. (a): top: static switching image shows that the single shot switching could be observed with the laser fluence of 7.1 mJ/cm_2; bottom: TR-MOKE images where we subtracted data for opposite external magnetic field (550 Oe) directions, and a common background was subtracted at different delay times. (b): The evolution of magnetization as a function of delay time, which is extracted from the TR-MOKE images. The curves corresponding to different fluences were extracted at a specific position located at a certain distance from the center. According to the Gaussian distribution of the laser pulse, we can get the fluences at a certain distance from the center.

initial state. The magnetization aligned along the initial state around 4 ps. With higher fluence, the magnitude of demagnetization becomes larger. Meanwhile, the magnetization recovery is slower due to the enhanced thermal effect of higher laser fluence. A long-lived full demagnetized state is observed when the fluence increases to 7.1 mJ/cm^2. In this case, the magnetization reaches zero and cannot cross zero to reverse its direction.

We have measured the transient hysteresis loops at various time delays to confirm that we only observe the full demagnetization state rather than magnetization switching. The hysteresis loops are measured on the sample $[Co(0.46)/Ho(0.52)]_4$ [2] with a fluence of 7.9 mJ/cm^2. In order to measure the hysteresis loops at different delay times, the dynamics have been done on the TR-MOKE set-up without images.

As shown in Figure 7.11, these hysteresis loops were obtained by fixing the time delay between the pump and probe beams. Meanwhile, we captured the evolution of the TRMOKE signal by varying the external magnetic fields along the out-of-plane direction. In this case, we can record the hysteresis loops at different timescales by moving the delay line. For instance, we observe a square hysteresis loop when there is no pump beam, in agreement with that measured by static MOKE. When t = -10 ps, the coercivity and the squareness are reduced, suggesting that the accumulated heating of the pump pulses plays a role. Once t = 0.5 ps, the magnetization signal almost disappears, indicated by the loss of hysteresis loops. It is the same case for t = 10 ps and longer delay time. These results are consistent with the dynamic results where the magnetization is fully demagnetized at the same timescale.

[2]Because of the wedged sample, we don't have more samples to do the dynamics after cutting the sample for temperature-dependent magnetic property measurements. The dynamics of other samples have been measured, and they show similar behavior.

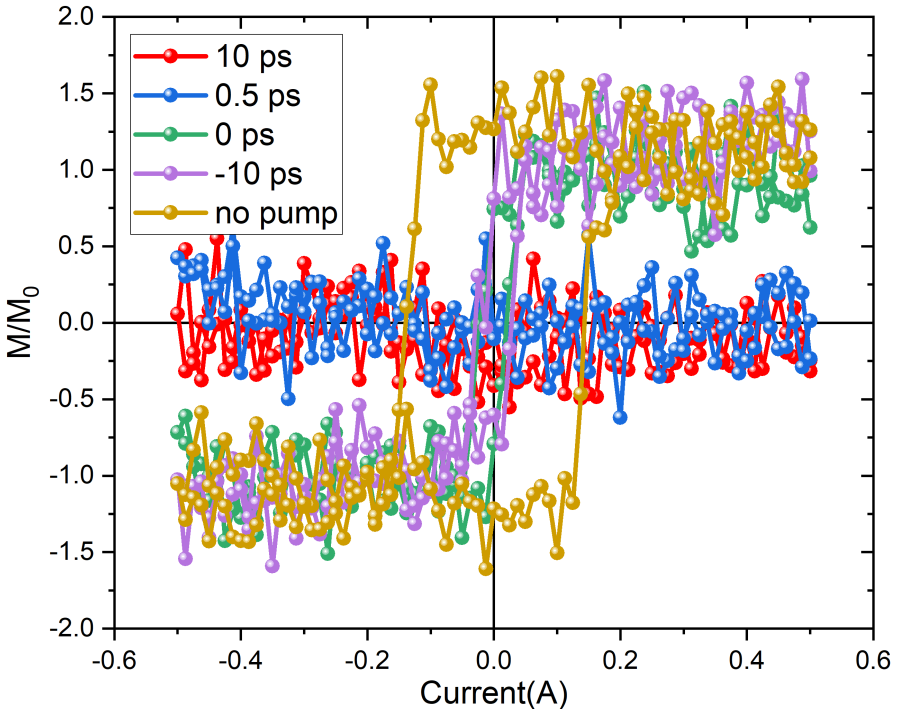

Figure 7.11: Hysteresis loops measured at different delay times with the pump fluence of 7.9 mJ/cm^2 on the sample $[Co(0.46)/Ho(0.52)]_4$.

7.6 Annealing

The magnetic properties and the single-shot switching behavior have been studied after thermal annealing of the multilayers. The multilayers with N=4 and 5 were annealed at 200°C for 1 h without any applied field. After the annealing process, interesting variations in the magnetic properties of Co/Ho multilayers were observed. In the case of N = 4, lower Co and Ho thickness combinations exhibited a distinct perpendicular magnetic anisotropy, as evident from the MOKE hysteresis loops. Conversely, higher thickness combinations displayed hysteresis loops with a remanence equal to one and prominent high-field tails. Moving on to N = 5, the hysteresis loops took on a strip-like pattern. Notably, the annealing process does not change the polarity of the hysteresis loops, which are still dominated by Co-sublattice. While the shape of the hysteresis loop ranges from square hysteresis to hysteresis loop characteristic of stripe/bubble domains [131, 133] when the total thickness increases.

Then, the single shot switching behavior of the annealed samples has been checked. After the first and second laser shot pulse with a pulse duration of 50 fs, Kerr images show that single pulse switching no longer holds and is replaced by the formation of small domains and a demagnetized state. The effect of the annealing on the interfaces and crystalline structure has to be more deeply checked. However, if interface alloying is considered, a decrease in saturation magnetization is expected by the increase of Ho momentum. So, only a decrease in the domain wall energy can explain the behavior observed by a decrease in the exchange constant or of the magnetic anisotropy. These results in annealed samples could be a piece of evidence that the magnetic properties play a role in the single pulse switching.

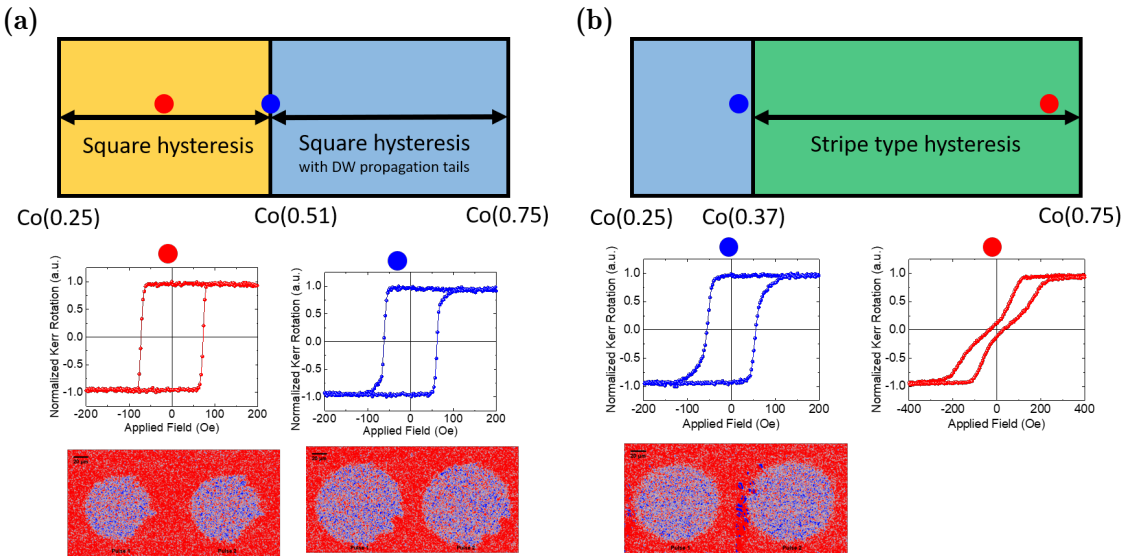

Figure 7.12: Hysteresis loops and single pulse reversal measurements in (a) [Co(0.5, wedge)/Ho(0.55, wedge)]$_4$ and (b) [Co(0.5, wedge)/Ho(0.55, wedge)]$_5$ after annealing at 200°C. Top line: region of thickness showing different hysteresis loops: orange: square hysteresis, blue: remanence equal to one with high field tails, green: hysteresis loop characteristic of stripe domains. Middle line: hysteresis loop measured at the location of blue and red dots, characteristic of the 3 thickness regions. Bottom line: Kerr image after first and second laser shot pulse with pulse duration of 50 fs (blue areas are magnetized down, red areas are magnetized up).

7.7 Conclusions and perspectives

In this chapter, we investigated the properties of Co/Ho multilayers, which is a novel material system with the expectation of higher spin-orbit coupling compared to Tb and Dy [161]. We made several significant observations throughout our investigation. Firstly, Co/Ho multilayers exhibited perpendicular magnetic anisotropy with a compensation temperature below room temperature. Furthermore, we observed single-shot switching behavior in Co/Ho multilayers with varying monolayer thicknesses depending on the repetition numbers of the bilayer. Interestingly, the total thickness of the multilayer played a crucial role in determining the switching capability, with F_{Switch} and F_{Multi} showing a strong correlation with the overall thickness. This emphasizes the importance of carefully designing the multilayer structure to optimize its switching performance.

Furthermore, we observed that the switching behavior of Co/Ho multilayers resembled that of GdFeCo alloys, deviating from that observed in Tb-based and Dy-based multilayers. Unlike the latter systems, Co/Ho multilayers displayed a state diagram with a distinct triangle shape strongly influenced by the pulse duration. However, it is worth noting that switching was not observed in the dynamics, indicating an unclear understanding of the switching mechanism in this system.

Considering the scope of our study, we focused solely on the Co-rich region of the multilayers. Exploring the switching behavior in the Ho-rich region would be valuable to understanding the system more comprehensively. Moreover, in terms of dynamics, we typically applied an external magnetic field to initialize the magnetization before each pulse. It would be interesting to investigate the dynamics without applying an external field to observe the intrinsic behavior of the system.

Sample list

- 665 V/Ta(5)Pt(5)[Co(1, wedge)/Ho(0.9, wedge)]*4Pt(1)Ta(5)
- 667 V/Ta(5)Pt(5)[Co(0.8, wedge)/Ho(0.9, wedge)]*4Pt(1)Ta(5)
- 668 V/Ta(5)Pt(5)[Co(1.2, wedge)/Ho(0.9, wedge)]*4Pt(1)Ta(5)
- 670 V/Ta(5)Pt(5)[Co(1, wedge)/Ho(1.2, wedge)]*4Pt(1)Ta(5)
- 675 V/Ta(5)Pt(5)[Co(0.5, wedge)/Ho(0.55, wedge)]*4Pt(1)Ta(5)
- 679 V/Ta(5)Pt(5)[Co(0.5, wedge)/Ho(0.55, wedge)]*3Pt(1)Ta(5)
- 680 V/Ta(5)Pt(5)[Co(0.5, wedge)/Ho(0.55, wedge)]*5Pt(1)Ta(5)
- 681 V/Ta(5)Pt(5)[Co(0.5, wedge)/Ho(0.55, wedge)]*2Pt(1)Ta(5)

Chapter 8

Conclusion

We first briefly reviewed the magnetization manipulation based on magnetic random access memory (MRAM) and introduced the ultrafast magnetization switching induced by pure laser pulses, including helicity-dependent all-optical switching (HD-AOS) and helicity-independent all-optical switching (HI-AOS). We mostly focus on the single-pulse all-optical switching and its mechanism in different materials. It is intended to serve as a reference and comparison for discussing subsequent work.

The next part focused on sample deposition techniques and four types of MOKE setups involving static and dynamic measurements. Since we mostly used wedge samples, we introduced the thickness and concentration determination of wedge samples. Moreover, the details of laser characterization, especially the spatial energy distribution and the laser beam size, have been shown.

The remaining part of this thesis focused on the experimental results of three parts of the works, including sample optimization, magnetic properties characterization, static and dynamic pump-probe measurements, and some simulation works.

Firstly, $Co_{100-x}Lu_x$ alloy thin films have been studied, where Lu has the same properties as Gd with small spin-orbit coupling (L=0). We optimized the PMA from scratch by depositing a series of $Co_{100-x}Lu_x$ thin films with various thicknesses and concentrations. The static magnetic properties were carefully studied, including saturated magnetization and coercivity as a function of temperature, sample thickness, and concentrations. As a result, perpendicular magnetic anisotropy can be obtained in 3 nm of $Co_{100-x}Lu_x$ alloy with x varies between 22% and 42%. Besides, single-shot switching measurements in full film and only a multidomain state can be observed after sending a femtosecond laser pulse. The increase in domain size with higher Lu concentration reminds us that the film can be fabricated into nanodots to bring the structure size below the domain size. However, around 50% of the reversal dots indicate no deterministic magnetization reversal in CoLu alloy. The results can be attributed to the low magnetization and, consequently, too-small angular momentum carried by the Lu element by atomistic simulations.

The next part of the work is based on the pioneer single shot-switching in Tb/Co multilayer-based electrodes. Starting with wedged $[Tb/Co]_5$ and $[Tb/Fe]_4$ multilayers, single-shot switching has successfully been reproduced by a femtosecond laser pulse. Surprisingly, concentric ring domain structures are induced at high laser intensities, resulting in multiple threshold fluences. The complex ring structure with magnetization pointing in opposite directions is neither caused by the dipole field nor the laser spot size. Each threshold fluence only depends on the local fluence absorbed by the sample. Besides, single-shot switching can be obtained with a pulse duration of up to at least 10 ps or even longer. More importantly, the threshold

fluences are mostly independent of the pulse duration, which differs from the Gd-based materials case. Moreover, by testing the impact of the magnetic structure in RE layer, the anisotropy of TM layer, as the RE/TM interface, we can figure out the ingredients to design the structure to show single-shot switching, where the anisotropy of the TM layer can not be too strong. By duplicating the RE (or RE alloy)/TM bilayer to construct a multilayer stack, on the one hand, the perpendicular anisotropy of the Co layer is reduced due to the absence of a Pt/Co interface; on the other hand, the RE/TM exchange coupling interface is integrated. Based on these concepts, more than 30 [1] types of multilayers, trilayers, and bilayers have been studied and show single-shot switching.

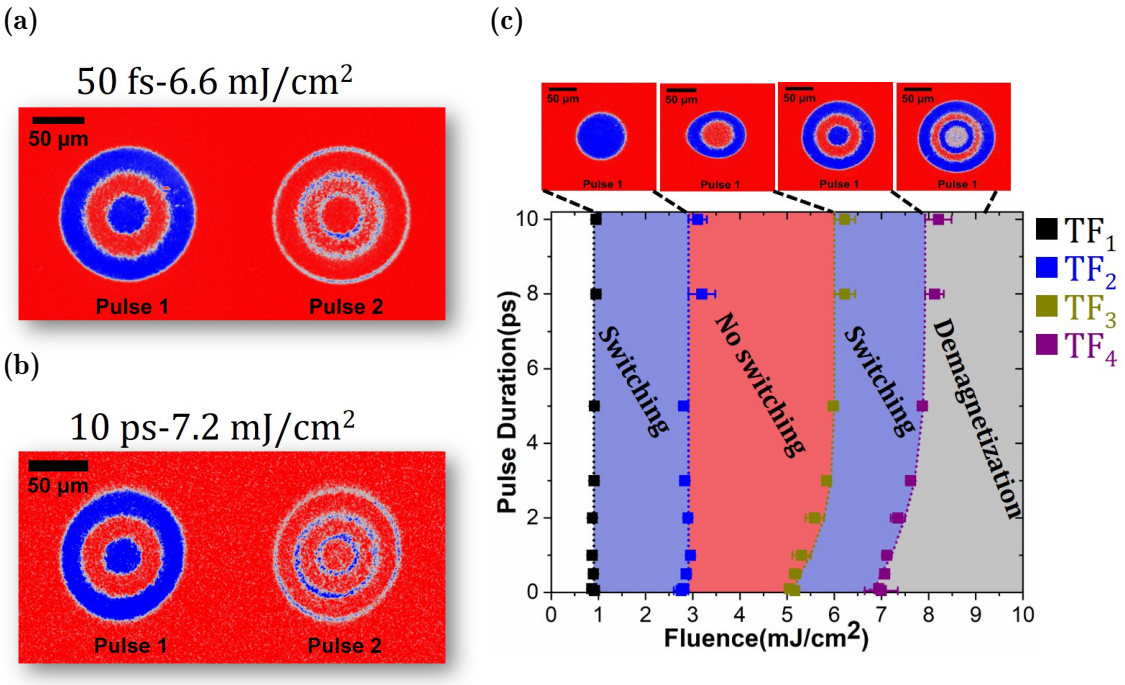

Figure 8.1: AOS measurements and State diagram in $[Tb(1.31\ nm)/Fe(1.89\ nm)]_4$ multilayers. AOS measurements with (a): 50 fs and (b): 10 ps of pulse durations with similar fluence. (c): State diagram of reversal pulse duration versus fluence. One switching ring (blue) corresponds of two threshold fluences, for example, the first switching ring corresponds to TF_1 and TF_2, and the second switching ring corresponds to TF_3 and TF_4... Here, TF_1 and TF_4 are the F_{switch} and F_{multi}, respectively. The dotted lines are guides for the eyes.

The switching mechanism and switching process have been discussed to be an in-plane reorientation precessional reversal. A macrospin model based on the LLG equation has been developed and reproduces the ring structure, which confirms that the magnetization processes toward the in-plane due to the fast reduction of the perpendicular anisotropy after being excited by the laser pulse. Furthermore, we successfully observed two types of single-shot switching in $TbCo/Gd_xCo_{100-x}/TbCo$ trilayer structure by tunning the Gd concentration from 22% to 3.6%, GdCo-like switching with $x > 12.3\%$ and multilayer-like switching (in-plane reorientation precessional switching) with $x < 7.5\%$. Which type of switching occurs is related to the Gd concentration and, consequently, the in-plane reorientation transition temperature.

[1] 19 types of wedged samples were shown in the chapter 5

When we tested different types of multilayers, we also studied Co/Ho multilayers, which is a novel material system with the expectation of higher spin-orbit coupling compared to Tb and Dy. We observed single-shot switching behavior in Co/Ho multilayers with varying monolayer thicknesses depending on the repetition numbers of the bilayer. Interestingly, the total thickness of the multilayer played a crucial role in determining the switching capability, with F_{Switch} and F_{Multi} showing a strong correlation with the overall thickness. This emphasizes the importance of carefully designing the multilayer structure to optimize its switching performance. Furthermore, we observed that the switching behavior of Co/Ho multilayers resembled that of GdFeCo alloys, deviating from that observed in Tb-based and Dy-based multilayers. Unlike the latter systems, Co/Ho multilayers displayed a state diagram with a distinct triangle shape strongly influenced by the pulse duration. However, it is worth noting that switching was not observed in the dynamics, indicating an unclear understanding of the switching mechanism in this system.

Bibliography

[1] Arne Brataas, Andrew D Kent, and Hideo Ohno. Current-induced torques in magnetic materials. Nature materials, 11(5):372–381, 2012.

[2] Eric Beaurepaire, J-C Merle, A Daunois, and J-Y Bigot. Ultrafast spin dynamics in ferromagnetic nickel. Physical review letters, 76(22):4250, 1996.

[3] Claudiu D Stanciu, Fredrik Hansteen, Alexey V Kimel, Andrei Kirilyuk, Arata Tsukamoto, Achioshi Itoh, and Th Rasing. All-optical magnetic recording with circularly polarized light. Physical review letters, 99(4):047601, 2007.

[4] K Vahaplar, AM Kalashnikova, AV Kimel, Denise Hinzke, Ulrich Nowak, R Chantrell, A Tsukamoto, A Itoh, A Kirilyuk, and Th Rasing. Ultrafast path for optical magnetization reversal via a strongly nonequilibrium state. Physical review letters, 103(11):117201, 2009.

[5] Maarten Beens, Mark LM Lalieu, Rembert A Duine, and Bert Koopmans. The role of intermixing in all-optical switching of synthetic-ferrimagnetic multilayers. AIP Advances, 9(12), 2019.

[6] 1956: FIRST COMMERCIAL HARD DISK DRIVE SHIPPED. `https://www.computerhistory.org/storageengine/first-commercial-hard-disk-drive-shipped/`.

[7] Kazuo Goda and Masaru Kitsuregawa. The history of storage systems. Proceedings of the IEEE, 100(Special Centennial Issue):1433–1440, 2012.

[8] Florin Radu and Jaime Sánchez-Barriga. Ferrimagnetic heterostructures for applications in magnetic recording. In Novel Magnetic Nanostructures, pages 267–331. Elsevier, 2018.

[9] Juan Antonio González, Juan Pedro Andrés, and Ricardo López Antón. Applied trends in magnetic rare earth/transition metal alloys and multilayers. Sensors, 21(16):5615, 2021.

[10] Andreas Moser, Kentaro Takano, David T Margulies, Manfred Albrecht, Yoshiaki Sonobe, Yoshihiro Ikeda, Shouheng Sun, and Eric E Fullerton. Magnetic recording: advancing into the future. Journal of Physics D: Applied Physics, 35(19):R157, 2002.

[11] Liang Pan and David B Bogy. Heat-assisted magnetic recording. Nature Photonics, 3(4):189–190, 2009.

[12] Robert E Rottmayer, Sharat Batra, Dorothea Buechel, William A Challener, Julius Hohlfeld, Yukiko Kubota, Lei Li, Bin Lu, Christophe Mihalcea, Keith Mountfield, et al. Heat-assisted magnetic recording. IEEE Transactions on Magnetics, 42(10):2417–2421, 2006.

[13] Mark H Kryder, Edward C Gage, Terry W McDaniel, William A Challener, Robert E Rottmayer, Ganping Ju, Yiao-Tee Hsia, and M Fatih Erden. Heat assisted magnetic recording. Proceedings of the IEEE, 96(11):1810–1835, 2008.

[14] Kirill Rivkin, Mourad Benakli, Ned Tabat, and Huaqing Yin. Physical principles of microwave assisted magnetic recording. Journal of Applied Physics, 115(21), 2014.

[15] Jian-Gang Zhu, Xiaochun Zhu, and Yuhui Tang. Microwave assisted magnetic recording. IEEE Transactions on Magnetics, 44(1):125–131, 2007.

[16] Satoshi Okamoto, Nobuaki Kikuchi, Masaki Furuta, Osamu Kitakami, and Takehito Shimatsu. Microwave assisted magnetic recording technologies and related physics. Journal of Physics D: Applied Physics, 48(35):353001, 2015.

[17] Ronald B Goldfarb, Bernard Dieny, and Kyung-Jin Lee. Introduction to magnetic random-access memory. John Wiley & Sons, 2016.

[18] Ricardo C Sousa and I Lucian Prejbeanu. Non-volatile magnetic random access memories (mram). Comptes Rendus Physique, 6(9):1013–1021, 2005.

[19] Bernard Dieny and I Lucian Prejbeanu. Magnetic random-access memory. Introduction to Magnetic Random-Access Memory, pages 101–164, 2017.

[20] Jagadeesh Subbaiah Moodera, Lisa R Kinder, Terrilyn M Wong, and R Meservey. Large magnetoresistance at room temperature in ferromagnetic thin film tunnel junctions. Physical review letters, 74(16):3273, 1995.

[21] Mario Norberto Baibich, Jean Marc Broto, Albert Fert, F Nguyen Van Dau, Frédéric Petroff, P Etienne, G Creuzet, A Friederich, and J Chazelas. Giant magnetoresistance of (001) fe/(001) cr magnetic superlattices. Physical review letters, 61(21):2472, 1988.

[22] Grünberg Binasch, Peter Grünberg, F Saurenbach, and W Zinn. Enhanced magnetoresistance in layered magnetic structures with antiferromagnetic interlayer exchange. Physical review B, 39(7):4828, 1989.

[23] Shunichi Iwasaki. Past and present of perpendicular magnetic recording. Journal of magnetism and magnetic materials, 320(22):2845–2849, 2008.

[24] SN Piramanayagam. Perpendicular recording media for hard disk drives. Journal of Applied Physics, 102(1), 2007.

[25] Y Shiroishi, K Fukuda, I Tagawa, H Iwasaki, S Takenoiri, H Tanaka, H Mutoh, and N Yoshikawa. Future options for hdd storage. IEEE Transactions on Magnetics, 45(10):3816–3822, 2009.

[26] Daniel C Ralph and Mark D Stiles. Spin transfer torques. Journal of Magnetism and Magnetic Materials, 320(7):1190–1216, 2008.

[27] Takayuki Kawahara, Kenchi Ito, Riichiro Takemura, and Hideo Ohno. Spin-transfer torque ram technology: Review and prospect. Microelectronics Reliability, 52(4):613–627, 2012.

[28] C-Y Hung and Luc Berger. Exchange forces between domain wall and electric current in permalloy films of variable thickness. Journal of applied physics, 63(8):4276–4278, 1988.

[29] Luc Berger. Emission of spin waves by a magnetic multilayer traversed by a current. Physical Review B, 54(13):9353, 1996.

[30] John C Slonczewski. Current-driven excitation of magnetic multilayers. Journal of Magnetism and Magnetic Materials, 159(1-2):L1–L7, 1996.

[31] Taehui Na, Kyungho Ryu, Jisu Kim, Seung H Kang, and Seong-Ook Jung. A comparative study of stt-mtj based non-volatile flip-flops. In 2013 IEEE International Symposium on Circuits and Systems (ISCAS), pages 109–112. IEEE, 2013.

[32] Prashanth Barla, Vinod Kumar Joshi, and Somashekara Bhat. Design and analysis of she-assisted stt mtj/cmos logic gates. Journal of Computational Electronics, 20(5):1964–1976, 2021.

[33] Rajagopalan Ramaswamy, Jong Min Lee, Kaiming Cai, and Hyunsoo Yang. Recent advances in spin-orbit torques: Moving towards device applications. Applied Physics Reviews, 5(3), 2018.

[34] Jairo Sinova, Sergio O Valenzuela, Jörg Wunderlich, CH Back, and T Jungwirth. Spin hall effects. Reviews of modern physics, 87(4):1213, 2015.

[35] Aurelien Manchon, Hyun Cheol Koo, Junsaku Nitta, Sergey M Frolov, and Rembert A Duine. New perspectives for rashba spin–orbit coupling. Nature materials, 14(9):871–882, 2015.

[36] CH Back, R Allenspach, W Weber, SSP Parkin, D Weller, Edward L Garwin, and HC Siegmann. Minimum field strength in precessional magnetization reversal. Science, 285(5429):864–867, 1999.

[37] CH Back, D Weller, J Heidmann, D Mauri, D Guarisco, EL Garwin, and HC Siegmann. Magnetization reversal in ultrashort magnetic field pulses. Physical Review Letters, 81(15):3251, 1998.

[38] Shehzaad Kaka and Stephen E Russek. Precessional switching of submicrometer spin valves. Applied Physics Letters, 80(16):2958–2960, 2002.

[39] HW Schumacher, C Chappert, P Crozat, RC Sousa, PP Freitas, J Miltat, J Fassbender, and B Hillebrands. Phase coherent precessional magnetization reversal in microscopic spin valve elements. Physical review letters, 90(1):017201, 2003.

[40] Th Gerrits, HAM Van Den Berg, J Hohlfeld, L Bär, and Th Rasing. Ultrafast precessional magnetization reversal by picosecond magnetic field pulse shaping. Nature, 418(6897):509–512, 2002.

[41] Ioan Tudosa, Ch Stamm, AB Kashuba, F King, HC Siegmann, J Stöhr, G Ju, B Lu, and D Weller. The ultimate speed of magnetic switching in granular recording media. Nature, 428(6985):831–833, 2004.

[42] CD Stanciu, AV Kimel, F Hansteen, A Tsukamoto, A Itoh, Andrei Kirilyuk, and Th Rasing. Ultrafast spin dynamics across compensation points in ferrimagnetic gdfeco: The role of angular momentum compensation. Physical Review B, 73(22):220402, 2006.

[43] Ganping Ju, Julius Hohlfeld, Bastiaan Bergman, Rene JM van de Veerdonk, Oleg N Mryasov, Jai-Young Kim, Xiaowei Wu, Dieter Weller, and Bert Koopmans. Ultrafast generation of ferromagnetic order via a laser-induced phase transformation in ferh thin films. Physical review letters, 93(19):197403, 2004.

[44] AV Kimel, A Kirilyuk, PA Usachev, RV Pisarev, AM Balbashov, and Th Rasing. Ultrafast non-thermal control of magnetization by instantaneous photomagnetic pulses. Nature, 435(7042):655–657, 2005.

[45] Fredrik Hansteen, Alexey Kimel, Andrei Kirilyuk, and Theo Rasing. Femtosecond photomagnetic switching of spins in ferrimagnetic garnet films. Physical review letters, 95(4):047402, 2005.

[46] CD Stanciu, F Hansteen, AV Kimel, A Tsukamoto, A Itoh, Andrei Kirilyuk, and Th Rasing. Ultrafast interaction of the angular momentum of photons with spins in the metallic amorphous alloy gdfeco. Physical review letters, 98(20):207401, 2007.

[47] Alexey V Kimel and Mo Li. Writing magnetic memory with ultrashort light pulses. Nature Reviews Materials, 4(3):189–200, 2019.

[48] Elena Yu Vedmedenko, Roland Kenji Kawakami, Denis D Sheka, Pietro Gambardella, Andrei Kirilyuk, Atsufumi Hirohata, Christian Binek, Oksana Chubykalo-Fesenko, Stefano Sanvito, Brian J Kirby, et al. The 2020 magnetism roadmap. Journal of Physics D: Applied Physics, 53(45):453001, 2020.

[49] Jun-Yang Chen, Li He, Jian-Ping Wang, and Mo Li. All-optical switching of magnetic tunnel junctions with single subpicosecond laser pulses. Physical Review Applied, 7(2):021001, 2017.

[50] Luding Wang, Houyi Cheng, Pingzhi Li, Youri LW van Hees, Yang Liu, Kaihua Cao, Reinoud Lavrijsen, Xiaoyang Lin, Bert Koopmans, and Weisheng Zhao. Picosecond optospintronic tunnel junctions. Proceedings of the National Academy of Sciences, 119(24):e2204732119, 2022.

[51] L Avilés-Félix, L Álvaro-Gómez, G Li, CS Davies, A Olivier, Miguel Rubio-Roy, S Auffret, A Kirilyuk, AV Kimel, Th Rasing, et al. Integration of tb/co multilayers within optically switchable perpendicular magnetic tunnel junctions. Aip Advances, 9(12):125328, 2019.

[52] L Avilés-Félix, Aurélien Olivier, Guanqiao Li, Carl S Davies, Laura Álvaro-Gómez, Miguel Rubio-Roy, Stéphane Auffret, Andrei Kirilyuk, AV Kimel, Th Rasing, et al. Single-shot all-optical switching of magnetization in tb/co multilayer-based electrodes. Scientific reports, 10(1):5211, 2020.

[53] Luis Avilés-Félix, Louis Farcis, Zebin Jin, Laura Álvaro-Gómez, Gunqiao Li, Kihiro T Yamada, Andrei Kirilyuk, Aleksey V Kimel, Th Rasing, Bernard Dieny, et al. All-optical spin switching probability in [tb/co] multilayers. Scientific Reports, 11(1):6576, 2021.

[54] D Salomoni, Y Peng, L Farcis, S Auffret, M Hehn, G Malinowski, S Mangin, B Dieny, LD Buda-Prejbeanu, RC Sousa, et al. Field-free all-optical switching and electrical read-out of tb/co-based magnetic tunnel junctions. arXiv preprint arXiv:2305.15135, 2023.

[55] M Lakshmanan. The fascinating world of the landau–lifshitz–gilbert equation: an overview. Philosophical Transactions of the Royal Society A: Mathematical, Physical and Engineering Sciences, 369(1939):1280–1300, 2011.

[56] Burkard Hillebrands and Kamel Ounadjela. Spin dynamics in confined magnetic structures I, volume 83. Springer Science & Business Media, 2003.

[57] E Lifshitz and LD Landau. On the theory of the dispersion of magnetic permeability in ferromagnetic bodies. Phys. Z. Sowjetunion, 8(135), 1935.

[58] Thomas L Gilbert. A phenomenological theory of damping in ferromagnetic materials. IEEE transactions on magnetics, 40(6):3443–3449, 2004.

[59] Andrei Kirilyuk, Alexey V Kimel, and Theo Rasing. Ultrafast optical manipulation of magnetic order. Reviews of Modern Physics, 82(3):2731, 2010.

[60] William Brown. Thermal fluctuation of fine ferromagnetic particles. IEEE Transactions on Magnetics, 15(5):1196–1208, 1979.

[61] P Shiktorov, E Starikov, V Gruzinskis, Tomás González, Javier Mateos, Daniel Pardo, L Reggiani, L Varani, and JC Vaissière. Langevin forces and generalized transfer fields for noise modeling in deep submicron devices. IEEE Transactions on Electron Devices, 47(10):1992–1998, 2000.

[62] G Grinstein and RH Koch. Coarse graining in micromagnetics. Physical review letters, 90(20):207201, 2003.

[63] Unai Atxitia, Oksana Chubykalo-Fesenko, Natalia Kazantseva, Denise Hinzke, Ulrich Nowak, and Roy W Chantrell. Micromagnetic modeling of laser-induced magnetization dynamics using the landau-lifshitz-bloch equation. Applied physics letters, 91(23), 2007.

[64] Bert Koopmans, JJM Ruigrok, Francesco Dalla Longa, and WJM De Jonge. Unifying ultrafast magnetization dynamics. Physical review letters, 95(26):267207, 2005.

[65] U Atxitia, O Chubykalo-Fesenko, Jakob Walowski, A Mann, and M Münzenberg. Evidence for thermal mechanisms in laser-induced femtosecond spin dynamics. Physical Review B, 81(17):174401, 2010.

[66] T Roth, AJ Schellekens, S Alebrand, O Schmitt, D Steil, B Koopmans, M Cinchetti, and M Aeschlimann. Temperature dependence of laser-induced demagnetization in ni: A key for identifying the underlying mechanism. Physical Review X, 2(2):021006, 2012.

[67] SI Anisimov, BL Kapeliovich, TL Perelman, et al. Electron emission from metal surfaces exposed to ultrashort laser pulses. Zh. Eksp. Teor. Fiz, 66(2):375–377, 1974.

[68] H Hopster, R Raue, and R Clauberg. Spin-flip stoner excitations in a ferromagnet observed by inelastic spin-polarized electron scattering. Physical review letters, 53(7):695, 1984.

[69] M Plihal, DL Mills, and J Kirschner. Spin wave signature in the spin polarized electron energy loss spectrum of ultrathin fe films: theory and experiment. Physical review letters, 82(12):2579, 1999.

[70] R Vollmer, M Etzkorn, PS Anil Kumar, H Ibach, and J Kirschner. Spin-polarized electron energy loss spectroscopy of high energy, large wave vector spin waves in ultrathin fcc co films on cu (001). Physical review letters, 91(14):147201, 2003.

[71] Wen-Xin Tang, Yu Zhang, I Tudosa, J Prokop, M Etzkorn, and Jurgen Kirschner. Large wave vector spin waves and dispersion in two monolayer fe on w (110). Physical review letters, 99(8):087202, 2007.

[72] J Prokop, Wen-Xin Tang, Y Zhang, I Tudosa, TRF Peixoto, Kh Zakeri, and Jurgen Kirschner. Magnons in a ferromagnetic monolayer. Physical review letters, 102(17):177206, 2009.

[73] B Koopmans, Grégory Malinowski, F Dalla Longa, D Steiauf, M Fähnle, T Roth, M Cinchetti, and M Aeschlimann. Explaining the paradoxical diversity of ultrafast laser-induced demagnetization. Nature materials, 9(3):259–265, 2010.

[74] C Stamm, T Kachel, N Pontius, R Mitzner, T Quast, K Holldack, S Khan, C Lupulescu, EF Aziz, M Wietstruk, et al. Femtosecond modification of electron localization and transfer of angular momentum in nickel. Nature materials, 6(10):740–743, 2007.

[75] M Cinchetti, M Sánchez Albaneda, D Hoffmann, T Roth, J-P Wüstenberg, M Krauß, O Andreyev, HC Schneider, M Bauer, and M Aeschlimann. Spin-flip processes and ultrafast magnetization dynamics in co: Unifying the microscopic and macroscopic view of femtosecond magnetism. Physical review letters, 97(17):177201, 2006.

[76] Hiroyuki Awano, Satoru Ohnuki, Hiroshi Shirai, Norio Ohta, Atushi Yamaguchi, Satoshi Sumi, and Kenji Torazawa. Magnetic domain expansion readout for amplification of an ultra high density magneto-optical recording signal. Applied physics letters, 69(27):4257–4259, 1996.

[77] P Hansen, C Clausen, G Much, M Rosenkranz, and K Witter. Magnetic and magneto-optical properties of rare-earth transition-metal alloys containing gd, tb, fe, co. Journal of applied physics, 66(2):756–767, 1989.

[78] J Hohlfeld, Th Gerrits, M Bilderbeek, Th Rasing, H Awano, and N Ohta. Fast magnetization reversal of gdfeco induced by femtosecond laser pulses. Physical Review B, 65(1):012413, 2001.

[79] Sabine Alebrand, Matthias Gottwald, Michel Hehn, Daniel Steil, Mirko Cinchetti, Daniel Lacour, Eric E Fullerton, Martin Aeschlimann, and Stéphane Mangin. Light-induced magnetization reversal of high-anisotropy tbco alloy films. Applied Physics Letters, 101(16), 2012.

[80] Sabine Alebrand, Ute Bierbrauer, Michel Hehn, Matthias Gottwald, Oliver Schmitt, Daniel Steil, Eric E Fullerton, Stéphane Mangin, Mirko Cinchetti, and Martin Aeschlimann. Subpicosecond magnetization dynamics in tbco alloys. Physical Review B, 89(14):144404, 2014.

[81] Alexander Hassdenteufel, Birgit Hebler, Christian Schubert, Andreas Liebig, Martin Teich, Manfred Helm, Martin Aeschlimann, Manfred Albrecht, and Rudolf Bratschitsch. Thermally assisted all-optical helicity dependent magnetic switching in amorphous fe100–xtbx alloy films. Advanced Materials, 25(22):3122–3128, 2013.

[82] Stéphane Mangin, M Gottwald, CH Lambert, D Steil, V Uhlíř, L Pang, Michel Hehn, S Alebrand, M Cinchetti, Grégory Malinowski, et al. Engineered materials for all-optical helicity-dependent magnetic switching. Nature materials, 13(3):286–292, 2014.

[83] G Kichin, M Hehn, J Gorchon, G Malinowski, J Hohlfeld, and S Mangin. From multiple-to single-pulse all-optical helicity-dependent switching in ferromagnetic co/pt multilayers. Physical Review Applied, 12(2):024019, 2019.

[84] Marco Berritta, Ritwik Mondal, Karel Carva, and Peter M Oppeneer. Ab initio theory of coherent laser-induced magnetization in metals. Physical review letters, 117(13):137203, 2016.

[85] Robin John, Marco Berritta, Denise Hinzke, Cai Müller, Tiffany Santos, Henning Ulrichs, Pablo Nieves, Jakob Walowski, Ritwik Mondal, Oksana Chubykalo-Fesenko, et al. Magnetisation switching of fept nanoparticle recording medium by femtosecond laser pulses. Scientific reports, 7(1):4114, 2017.

[86] I Radu, K Vahaplar, C Stamm, T Kachel, N Pontius, HA Dürr, TA Ostler, J Barker, RFL Evans, RW Chantrell, et al. Transient ferromagnetic-like state mediating ultrafast reversal of antiferromagnetically coupled spins. Nature, 472(7342):205–208, 2011.

[87] Natalia Kazantseva, Ulrich Nowak, Roy W Chantrell, Julius Hohlfeld, and Adnan Rebei. Slow recovery of the magnetisation after a sub-picosecond heat pulse. Europhysics Letters, 81(2):27004, 2007.

[88] TA Ostler, J Barker, RFL Evans, RW Chantrell, U Atxitia, O Chubykalo-Fesenko, S El Moussaoui, LBPJ Le Guyader, E Mengotti, LJ Heyderman, et al. Ultrafast heating as a sufficient stimulus for magnetization reversal in a ferrimagnet. Nature communications, 3(1):666, 2012.

[89] Amal El-Ghazaly, Brandon Tran, Alejandro Ceballos, Charles-Henri Lambert, Akshay Pattabi, Sayeef Salahuddin, Frances Hellman, and Jeffrey Bokor. Ultrafast magnetization switching in nanoscale magnetic dots. Applied Physics Letters, 114(23), 2019.

[90] Jon Gorchon, Richard B Wilson, Yang Yang, Akshay Pattabi, JY Chen, Li He, JP Wang, Mo Li, and Jeffrey Bokor. Role of electron and phonon temperatures in the helicity-independent all-optical switching of gdfeco. Physical Review B, 94(18):184406, 2016.

[91] Yong Xu, Michel Hehn, Weisheng Zhao, Xiaoyang Lin, Grégory Malinowski, and Stéphane Mangin. From single to multiple pulse all-optical switching in gdfeco thin films. Physical Review B, 100(6):064424, 2019.

[92] Yong Xu, Marwan Deb, Grégory Malinowski, Michel Hehn, Weisheng Zhao, and Stéphane Mangin. Ultrafast magnetization manipulation using single femtosecond light and hot-electron pulses. Advanced Materials, 29(42):1703474, 2017.

[93] Danny Petty Gweha Nyoma, Maxime Vergès, Michel Hehn, Daniel Lacour, Julius Hohlfeld, Sebastiaan van Dijken, Grégory Malinowski, Stéphane Mangin, and François Montaigne. Size effect on single pulse all-optical helicity-independent switching in gdfeco disk arrays. Applied Physics Letters, 123(5), 2023.

[94] Jiaqi Wei, Boyu Zhang, Michel Hehn, Wei Zhang, Gregory Malinowski, Yong Xu, Weisheng Zhao, and Stéphane Mangin. All-optical helicity-independent switching state diagram in gd-fe-co alloys. Physical Review Applied, 15(5):054065, 2021.

[95] Quentin Remy, Junta Igarashi, Satoshi Iihama, Grégory Malinowski, Michel Hehn, Jon Gorchon, Julius Hohlfeld, Shunsuke Fukami, Hideo Ohno, and Stéphane Mangin. Energy efficient control of ultrafast spin current to induce single femtosecond pulse switching of a ferromagnet. Advanced Science, 7(23):2001996, 2020.

[96] Quentin Remy. Ultrafast spin dynamics and transport in magnetic metallic heterostructures. PhD thesis, Université de Lorraine, 2021.

[97] Jun-Xiao Lin, Michel Hehn, Thomas Hauet, Yi Peng, Junta Igarashi, Yann Le Guen, Quentin Remy, Jon Gorchon, Gregory Malinowski, Stéphane Mangin, et al. Single laser pulse induced magnetization switching in in-plane magnetized gdco alloys. arXiv preprint arXiv:2308.10516, 2023.

[98] Wei Zhang, Jun Xiao Lin, Tian Xun Huang, Gregory Malinowski, Michel Hehn, Yong Xu, Stéphane Mangin, and Weisheng Zhao. Role of spin-lattice coupling in ultrafast demagnetization and all optical helicity-independent single-shot switching in gd 1- x- y tb y co x alloys. Physical Review B, 105(5):054410, 2022.

[99] Alejandro Ceballos, Akshay Pattabi, Amal El-Ghazaly, Sergiu Ruta, Christian P Simon, Richard FL Evans, Thomas Ostler, Roy W Chantrell, Ellis Kennedy, Mary Scott, et al. Role of element-specific damping in ultrafast, helicity-independent, all-optical switching dynamics in amorphous (gd, tb) co thin films. Physical Review B, 103(2):024438, 2021.

[100] MLM Lalieu, MJG Peeters, SRR Haenen, R Lavrijsen, and B Koopmans. Deterministic all-optical switching of synthetic ferrimagnets using single femtosecond laser pulses. Physical review B, 96(22):220411, 2017.

[101] Maarten Beens, Mark LM Lalieu, Axel JM Deenen, Rembert A Duine, and Bert Koopmans. Comparing all-optical switching in synthetic-ferrimagnetic multilayers and alloys. Physical Review B, 100(22):220409, 2019.

[102] Julian Hintermayr, Pingzhi Li, Roy Rosenkamp, Youri LW van Hees, Junta Igarashi, Stéphane Mangin, Reinoud Lavrijsen, Grégory Malinowski, and Bert Koopmans. Ultrafast single-pulse all-optical switching in synthetic ferrimagnetic tb/co/gd multilayers. arXiv preprint arXiv:2306.01419, 2023.

[103] Pingzhi Li, Mark JG Peeters, Youri LW van Hees, Reinoud Lavrijsen, and Bert Koopmans. Ultra-low energy threshold engineering for all-optical switching of magnetization in dielectric-coated co/gd based synthetic-ferrimagnet. Applied Physics Letters, 119(25), 2021.

[104] Youri LW van Hees, Bert Koopmans, and Reinoud Lavrijsen. Toward high all-optical data writing rates in synthetic ferrimagnets. Applied Physics Letters, 120(25), 2022.

[105] Pingzhi Li, Johannes W van der Jagt, Maarten Beens, Julian Hintermayr, Marcel A Verheijen, René Bruikman, Beatriz Barcones, Roméo Juge, Reinoud Lavrijsen, Dafiné Ravelosona, et al. Enhancing all-optical switching of magnetization by he ion irradiation. Applied Physics Letters, 121(17), 2022.

[106] Luding Wang, Youri LW van Hees, Reinoud Lavrijsen, Weisheng Zhao, and Bert Koopmans. Enhanced all-optical switching and domain wall velocity in annealed synthetic-ferrimagnetic multilayers. Applied Physics Letters, 117(2), 2020.

[107] Satoshi Iihama, Yong Xu, Marwan Deb, Grégory Malinowski, Michel Hehn, Jon Gorchon, Eric E Fullerton, and Stéphane Mangin. Single-shot multi-level all-optical magnetization switching mediated by spin transport. Advanced Materials, 30(51):1804004, 2018.

[108] Junta Igarashi, Quentin Remy, Satoshi Iihama, Grégory Malinowski, Michel Hehn, Jon Gorchon, Julius Hohlfeld, Shunsuke Fukami, Hideo Ohno, and Stéphane Mangin. Engineering single-shot all-optical switching of ferromagnetic materials. Nano Letters, 20(12):8654–8660, 2020.

[109] Gyung-Min Choi and Byoung-Chul Min. Laser-driven spin generation in the conduction bands of ferrimagnetic metals. Physical Review B, 97(1):014410, 2018.

[110] Nicolas Bergeard, Michel Hehn, Stéphane Mangin, Gwladys Lengaigne, François Montaigne, MLM Lalieu, B Koopmans, and Grégory Malinowski. Hot-electron-induced ultrafast demagnetization in co/pt multilayers. Physical review letters, 117(14):147203, 2016.

[111] Junta Igarashi, Wei Zhang, Quentin Remy, Eva Díaz, Jun-Xiao Lin, Julius Hohlfeld, Michel Hehn, Stéphane Mangin, Jon Gorchon, and Grégory Malinowski. Optically induced ultrafast magnetization switching in ferromagnetic spin valves. Nature Materials, pages 1–6, 2023.

[112] EB Myers, DC Ralph, JA Katine, RN Louie, and RA Buhrman. Current-induced switching of domains in magnetic multilayer devices. Science, 285(5429):867–870, 1999.

[113] C Banerjee, N Teichert, KE Siewierska, Z Gercsi, GYP Atcheson, P Stamenov, K Rode, JMD Coey, and J Besbas. Single pulse all-optical toggle switching of magnetization without gadolinium in the ferrimagnet mn2ruxga. Nature communications, 11(1):4444, 2020.

[114] HÜSEYİN Kurt, Karsten Rode, Plamen Stamenov, Munuswamy Venkatesan, Y-C Lau, Emiliano Fonda, and JMD Coey. Cubic mn 2 ga thin films: Crossing the spin gap with ruthenium. Physical review letters, 112(2):027201, 2014.

[115] CS Davies, G Bonfiglio, K Rode, J Besbas, C Banerjee, P Stamenov, JMD Coey, AV Kimel, and A Kirilyuk. Exchange-driven all-optical magnetic switching in compensated 3 d ferrimagnets. Physical Review Research, 2(3):032044, 2020.

[116] C Banerjee, K Rode, G Atcheson, S Lenne, P Stamenov, JMD Coey, and J Besbas. Ultrafast double pulse all-optical reswitching of a ferrimagnet. Physical Review Letters, 126(17):177202, 2021.

[117] Zexiang Hu, Jean Besbas, Ross Smith, Niclas Teichert, Gwenael Atcheson, Karsten Rode, Plamen Stamenov, and JMD Coey. Single-pulse all-optical partial switching in amorphous dyxco1- x and tbxco1- x with random anisotropy. Applied Physics Letters, 120(11), 2022.

[118] John Kerr. Xliii. on rotation of the plane of polarization by reflection from the pole of a magnet. The London, Edinburgh, and Dublin Philosophical Magazine and Journal of Science, 3(19):321–343, 1877.

[119] P Weinberger. John kerr and his effects found in 1877 and 1878. Philosophical Magazine Letters, 88(12):897–907, 2008.

[120] ZJ Yang and MR Scheinfein. Combined three-axis surface magneto-optical kerr effects in the study of surface and ultrathin-film magnetism. Journal of applied physics, 74(11):6810–6823, 1993.

[121] Adrianus Johannes Schellekens. Manipulating spins: Novel methods for controlling magnetization dynamics on the ultimate timescale. 2014.

[122] T Ogasawara, N Iwata, Y Murakami, H Okamoto, and Y Tokura. Submicron-scale spatial feature of ultrafast photoinduced magnetization reversal in tbfeco thin film. Applied Physics Letters, 94(16), 2009.

[123] Kadir Vahaplar, AM Kalashnikova, AV Kimel, Stefan Gerlach, Denise Hinzke, Ulrich Nowak, Roy Chantrell, Arata Tsukamoto, A Itoh, Andrei Kirilyuk, et al. All-optical magnetization reversal by circularly polarized laser pulses: Experiment and multiscale modeling. Physical review B, 85(10):104402, 2012.

[124] V López-Flores, N Bergeard, V Halté, C Stamm, N Pontius, M Hehn, E Otero, E Beaurepaire, and C Boeglin. Role of critical spin fluctuations in ultrafast demagnetization of transition-metal rare-earth alloys. Physical Review B, 87(21):214412, 2013.

[125] Francoise Givord and Remy Lemaire. Proprietes cristallographiques et magnetiques des composes entre le cobalt et le lutecium. Solid State Communications, 9(5):341–346, 1971.

[126] Keizo Endo, Masanori Iijima, Akira Shinogi, and Kouichi Ishiyama. The metamagnetic transition in pseudobinary laves phase compounds lu (co1- xalx) 2. Journal of the Physical Society of Japan, 56(4):1316–1319, 1987.

[127] G Krill, JP Schillé, P Sainctavit, C Brouder, C Giorgetti, E Dartyge, and JP Kappler. Magnetic dichroism with synchrotron radiation. Physica Scripta, 1993(T49A):295, 1993.

[128] MSS Brooks, Olle Eriksson, and Börje Johansson. 3d-5d band magnetism in rare earth transition metal intermetallics: Lufe2. Journal of Physics: Condensed Matter, 1(34):5861, 1989.

[129] M Bersweiler, Karine Dumesnil, D Lacour, and Michel Hehn. Impact of buffer layer and pt thickness on the interface structure and magnetic properties in (co/pt) multilayers. Journal of Physics: Condensed Matter, 28(33):336005, 2016.

[130] J Kanak, M Czapkiewicz, T Stobiecki, M Kachel, I Sveklo, A Maziewski, and Sebastiaan Van Dijken. Influence of buffer layers on the texture and magnetic properties of co/pt multilayers with perpendicular anisotropy. physica status solidi (a), 204(12):3950–3953, 2007.

[131] M Hehn, S Padovani, K Ounadjela, and JP Bucher. Nanoscale magnetic domain structures in epitaxial cobalt films. Physical Review B, 54(5):3428, 1996.

[132] Senfu Zhang, Junwei Zhang, Yan Wen, Eugene M Chudnovsky, and Xixiang Zhang. Determination of chirality and density control of néel-type skyrmions with in-plane magnetic field. Communications Physics, 1(1):36, 2018.

[133] M Fattouhi, MY El Hafidi, M El Hafidi, A Kassiba, and N Yaacoub. Study of nucleation/annihilation process and vortices characteristics in co/py rectangular bilayers. Journal of Superconductivity and Novel Magnetism, 32:237–246, 2019.

[134] C Swindells, B Nicholson, O Inyang, Y Choi, T Hase, and D Atkinson. Proximity-induced magnetism in pt layered with rare-earth–transition-metal ferrimagnetic alloys. Physical Review Research, 2(3):033280, 2020.

[135] Young Chan Won and Sang Ho Lim. Interfacial properties of [pt/co/pt] trilayers probed through magnetometry. Scientific reports, 11(1):10779, 2021.

[136] V Gehanno, Y Samson, A Marty, B Gilles, and A Chamberod. Magnetic susceptibility and magnetic domain configuration as a function of the layer thickness in epitaxial fepd (0 0 1) thin films ordered in the l1o structure. Journal of Magnetism and Magnetic Materials, 172(1-2):26–40, 1997.

[137] U Atxitia, Denise Hinzke, Oksana Chubykalo-Fesenko, Ulrich Nowak, Hamid Kachkachi, Oleg N Mryasov, RF Evans, and Roy W Chantrell. Multiscale modeling of magnetic materials: Temperature dependence of the exchange stiffness. Physical Review B, 82(13):134440, 2010.

[138] Levente Rózsa, Unai Atxitia, and Ulrich Nowak. Temperature scaling of the dzyaloshinsky-moriya interaction in the spin wave spectrum. Physical Review B, 96(9):094436, 2017.

[139] Kazushi Yamauchi, Kazutaka Habu, and Noboru Sato. Magnetic structure of tb-fe films with an artificially layered structure. Journal of applied physics, 64(10):5748–5750, 1988.

[140] CS Davies, KH Prabhakara, MD Davydova, KA Zvezdin, TB Shapaeva, S Wang, AK Zvezdin, A Kirilyuk, Th Rasing, and AV Kimel. Anomalously damped heat-assisted route for precessional magnetization reversal in an iron garnet. Physical review letters, 122(2):027202, 2019.

[141] LA Shelukhin, VV Pavlov, PA Usachev, P Yu Shamray, RV Pisarev, and AM Kalashnikova. Ultrafast laser-induced changes of the magnetic anisotropy in a low-symmetry iron garnet film. Physical Review B, 97(1):014422, 2018.

[142] VN Kats, TL Linnik, AS Salasyuk, AW Rushforth, M Wang, P Wadley, Andrey V Akimov, SA Cavill, V Holy, AM Kalashnikova, et al. Ultrafast changes of magnetic anisotropy driven by laser-generated coherent and noncoherent phonons in metallic films. Physical Review B, 93(21):214422, 2016.

[143] Jean-Yves Bigot and Mircea Vomir. Ultrafast magnetization dynamics of nanostructures. Annalen der Physik, 525(1-2):2–30, 2013.

[144] Philippe Scheid, Quentin Remy, Sébastien Lebègue, Gregory Malinowski, and Stéphane Mangin. Light induced ultrafast magnetization dynamics in metallic compounds. Journal of Magnetism and Magnetic Materials, 560:169596, 2022.

[145] A Mekonnen, AR Khorsand, M Cormier, AV Kimel, A Kirilyuk, Ales Hrabec, Laurent Ranno, A Tsukamoto, A Itoh, and Th Rasing. Role of the intersublattice exchange coupling in short-laser-pulse-induced demagnetization dynamics of gdco and gdcofe alloys. Physical review B, 87(18):180406, 2013.

[146] Kshiti Mishra, Thomas GH Blank, CS Davies, L Avilés-Félix, D Salomoni, LD Buda-Prejbeanu, RC Sousa, IL Prejbeanu, Bert Koopmans, Th Rasing, et al. Dynamics of all-optical single-shot switching of magnetization in tb/co multilayers. Physical Review Research, 5(2):023163, 2023.

[147] Marcel Hennes, Aladine Merhe, Xuan Liu, David Weder, Clemens von Korff Schmising, Michael Schneider, Christian Michael Günther, Benoît Mahieu, Grégory Malinowski, Michel Hehn, et al. Laser-induced ultrafast demagnetization and perpendicular magnetic anisotropy reduction in a co 88 tb 12 thin film with stripe domains. Physical Review B, 102(17):174437, 2020.

[148] Sergei Ovcharenko, Mikhail Gaponov, Alexey Klimov, Nicolas Tiercelin, Philippe Pernod, Elena Mishina, Alexander Sigov, and Vladimir Preobrazhensky. Ultrafast manipulation of magnetic anisotropy in a uniaxial intermetallic heterostructure tbco2/feco. Journal of Physics D: Applied Physics, 55(17):175001, 2022.

[149] Agne Ciuciulkaite, Kshiti Mishra, Marcos V Moro, Ioan-Augustin Chioar, Richard M Rowan-Robinson, Sergii Parchenko, Armin Kleibert, Bengt Lindgren, Gabriella Andersson, Carl S Davies, et al. Magnetic and all-optical switching properties of amorphous tb x co 100- x alloys. Physical Review Materials, 4(10):104418, 2020.

[150] Daniele Gerion, Armand Hirt, and André Châtelain. High curie temperature and possible canted magnetism in free gd clusters. Physical review letters, 83(3):532, 1999.

[151] BL Rhodes, S Legvold, and FH Spedding. Magnetic properties of holmium and thulium metals. Physical Review, 109(5):1547, 1958.

[152] Thomas A Ostler, Richard FL Evans, Roy W Chantrell, Unai Atxitia, Oksana Chubykalo-Fesenko, Ilie Radu, Radu Abrudan, Florin Radu, Arata Tsukamoto, A Itoh, et al. Crystallographically amorphous ferrimagnetic alloys: Comparing a localized atomistic spin model with experiments. Physical Review B, 84(2):024407, 2011.

[153] Kai Chen, Dieter Lott, Florin Radu, Fadi Choueikani, Edwige Otero, and Philippe Ohresser. Observation of an atomic exchange bias effect in dyco4 film. Scientific reports, 5(1):18377, 2015.

[154] Andreas Donges, Sergii Khmelevskyi, Andras Deak, Radu-Marius Abrudan, Detlef Schmitz, Ilie Radu, Florin Radu, László Szunyogh, and Ulrich Nowak. Magnetization compensation and spin reorientation transition in ferrimagnetic dyco 5: Multiscale modeling and element-specific measurements. Physical Review B, 96(2):024412, 2017.

[155] Robin Bläsing, Tianping Ma, See-Hun Yang, Chirag Garg, Fasil Kidane Dejene, Alpha T N'Diaye, Gong Chen, Kai Liu, and Stuart SP Parkin. Exchange coupling torque in ferrimagnetic co/gd bilayer maximized near angular momentum compensation temperature. Nature communications, 9(1):4984, 2018.

[156] EF Kneller and FE Luborsky. Particle size dependence of coercivity and remanence of single-domain particles. Journal of Applied Physics, 34(3):656–658, 1963.

[157] Xavier Batlle, M Garcia del Muro, Javier Tejada, H Pfeiffer, Peter Görnert, and Ekkehard Sinn. Magnetic study of m-type doped barium ferrite nanocrystalline powders. Journal of applied physics, 74(5):3333–3340, 1993.

[158] Charles Kittel. Theory of the structure of ferromagnetic domains in films and small particles. Physical Review, 70(11-12):965, 1946.

[159] A Maziewski, V Zablotskii, and M Kisielewski. Analysis of magnetic domain sizes in ultrathin ferromagnetic films. physica status solidi (a), 189(3):1001–1005, 2002.

[160] Mohammed Salah El Hadri, Michel Hehn, Philipp Pirro, Charles-Henri Lambert, Grégory Malinowski, Eric E Fullerton, and Stéphane Mangin. Domain size criterion for the observation of all-optical helicity-dependent switching in magnetic thin films. Physical review B, 94(6):064419, 2016.

[161] KV Shanavas, Zoran S Popović, and S Satpathy. Theoretical model for rashba spin-orbit interaction in d electrons. Physical Review B, 90(16):165108, 2014.